

5. SITE 1096¹

Shipboard Scientific Party²

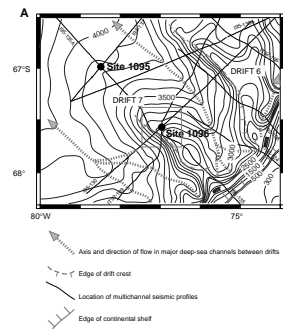
BACKGROUND AND SCIENTIFIC OBJECTIVES

Site 1096 (Fig. F1A) is the more elevated and proximal of two sites on a sediment drift on the continental rise off the northwestern Pacific margin of the Antarctic Peninsula. This site lies in 3152 m of water close to the top of the gentle, northeast-facing slope of the drift (Drift 7). It was drilled to sample the shallow part of the stratigraphic section within the drift, where it is thick and undisturbed. The deeper section was drilled 75 km to the northwest, on the northwestern flank of Drift 7 at Site 1095 (3840 m), where the youngest sediments are thinner.

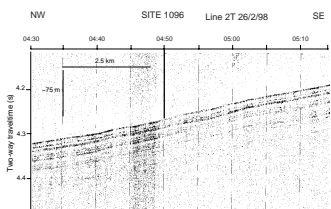
Site 1096 was located near the crest of the drift (Fig. F2), on a gentle slope ($<1^\circ$) elevated more than 700 m above the large, dendritic channel systems that develop at the foot of the Antarctic continental slope and extend northwest to the abyssal plain. The channel systems are maintained by turbidity currents originating on the continental slope, loaded with the unstable component of unsorted, largely terrigenous sediment, glacially transported to the continental shelf edge. We anticipated that the difference in elevation between the site and the turbidity-current channels would limit direct turbidite deposition. This would allow the mainly fine-grained terrigenous component, which had been suspended and entrained as a nepheloid layer within ambient bottom currents, to accumulate. According to the results of shallow piston coring, a barren, terrigenous silty clay representing glacial deposition would alternate downcore with mainly biosiliceous, pelagic silty clay deposited during interglacials.

The sedimentary cover, more than 3 km thick, rests on oceanic basement dated at ~ 40 Ma by magnetic anomalies (Barker, 1982). The magnetic profile obtained on passage between Sites 1095 and 1096 has allowed basement at both sites to be dated more precisely (Fig. F3). Basement is dated at 36.7 Ma at Site 1096 and at 42.7 Ma at Site 1095 (using the time scale of Cande and Kent, 1995). Upon crossing the site,

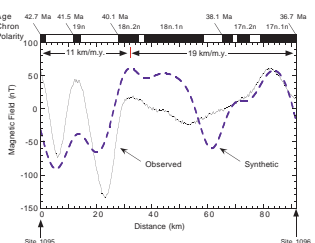
F1. Location of Site 1096 on two crossing MCS reflection profiles, p. 38.



F2. 3.5-kHz sub-bottom profile across Site 1096, p. 40.



F3. Magnetic total-field profile between Sites 1095 and 1096, p. 41.



¹Examples of how to reference the whole or part of this volume.

²Shipboard Scientific Party addresses.

the 3.5-kHz sub-bottom profile (Fig. F2) showed up to 75 ms two-way traveltime (TWT) penetration (corresponding to 50–60 m) through continuous reflectors parallel to the seafloor. The alternation of stronger reflectors and acoustically transparent sediment suggested the occurrence of three depositional cycles in the upper part of the section, possibly reflecting glacial-interglacial variation.

Multichannel seismic (MCS) profiles across the site (I95-135, I95-130A, and IT92-109 [Figs. F4, F1B; also see “[Appendix](#),” p. 24, and Fig. AF1, p. 59, both in the “Leg 178 Summary” chapter]) show that the sedimentary sequence corresponding to Units M1 and M2 of Rebisco et al. (1997) comprise continuous and parallel reflectors with a change in amplitude across the unit boundary: low amplitude in Unit M1 above 400 ms and high amplitude in Unit M2 beneath. The total thickness of Units M1 and M2 here is 740 ms, compared with 300 ms at the distal drift Site 1095. The deeper Units M3 and M4 cored at Site 1095, underlying the two upper units, here lie below a bottom-simulating reflector (BSR) that we have interpreted provisionally as the result of silica diagenesis (opal-A to opal-CT). This might adversely affect diatom preservation.

Drilling at Site 1096 was intended to examine the variation of this hemipelagic component of glacially derived sedimentation in a highly expanded Pliocene–Pleistocene section. Penetration to ~650 m would sample only the upper part of the drift (Units M1 and M2, the “drift maintenance” stage of sedimentation), presumably extending back about 5 m.y. The principal objectives were

1. To see if the pronounced cyclicity apparent in the topmost 5–10 m of drift deposits (and thus accessible to piston coring [Camerlenghi et al., 1997; Pudsey and Camerlenghi, 1998]) would persist downsection and therefore be capable of providing information about the glacial state of the adjacent continent; and
2. If so, to use the drift sediment record to examine at high time resolution the Pliocene–Pleistocene history of Antarctic glaciation.

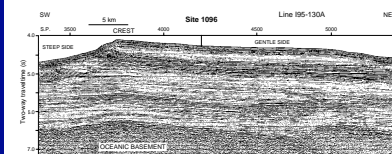
OPERATIONS

Upon leaving Site 1095, we deployed the proton precession magnetometer while looping back over the site. Continuous total field magnetic and 3.5-kHz profiles were obtained that extended over and just to the southeast of Site 1096. We averaged 8.1 kt during the 58-nmi transit to Site 1096.

Hole 1096A

Hole 1096A was spudded at 1130 hr on 25 February with the advanced hydraulic piston corer (APC) at a seafloor depth estimated from recovery as 3152.0 m (3163.2 meters below rig floor [mbrf]). APC coring advanced to refusal at a depth of 140.7 meters below seafloor (mbsf) (Core 15H) with 84.2% recovery (Table T1). The bit cleared the seafloor at 0145 hr on 26 February, and the *JOIDES Resolution* was offset 20 m west of Hole 1096A.

F4. Part of MCS reflection profile I95-130A across Site 1096, [p. 42](#).



T1. Site 1096 coring summary,
[p. 101](#).

Hole 1096B

Before spudding Hole 1096B, a water-sampling temperature probe sample of bottom water was obtained. Hole 1096B was spudded with the APC at 0700 hr on 26 February at a seafloor depth of 3152.5 m (3163.7 mbrf). Piston coring advanced to 108.3 mbsf (Core 12H) without incident but on Core 13H encountered a change in the formation and only advanced 7.6 m. We switched to extended core barrel (XCB) for the next two cores (115.9 to 135.2 mbsf) but recovered virtually nothing. The hole was then deepened with the APC to refusal at 166.9 mbsf. The interval from ~110 to 170 mbsf, besides causing some coring difficulties, marks a zone where physical properties change and where a lithologic boundary occurs, as discussed in subsequent sections of this chapter. Adara tool temperature measurements were obtained at the mudline, 32.2 mbsf (Core 4H), 60.8 mbsf (Core 7H), and 89.3 mbsf (Core 10H). Orientation data were obtained for Cores 4H, 5H, and 6H.

Coring continued in Hole 1096B with the XCB advancing steadily to 212.5 mbsf, where a Davis-Villinger Temperature Probe (DVTP) was deployed on the wireline to measure formation temperature. Thereafter, circulation was poor and recovery reduced. At 260.6 mbsf, after a second DVTP deployment, the drill string was tripped, and three of the four bit nozzles were found to be plugged with clay and glacial drop-stones. The nozzles were cleared and the bit seal replaced. From DVTP data and other data collected during APC coring, an initial temperature gradient of about 80°C/km was estimated.

Hole 1096C

Hole 1096C was started 20 m west of Hole 1096B by first drilling to 114.0 mbsf. We then alternated between coring and drilling in the interval from 114.0 to 231.4 mbsf, taking two APC and four XCB cores to fill gaps in recovery from the first two holes (Table T1).

Continuous XCB coring began at 255 mbsf and advanced to 588.6 mbsf (Core 41X) without incident and with generally good recovery (82.7%). During the cutting of Core 42X (588.6 to 598.1 mbsf), the hard-formation cutting shoe failed downhole. Because of the need to ensure that sediments producing a prominent seismic reflector had been sampled, an additional core (43X) was obtained (598.1 to 607.7 mbsf), in which a small piece of ground-up cutting shoe was recovered.

In preparation for logging, a 20-bbl high-viscosity mud sweep was circulated and the pipe pulled back to 97.3 mbsf. The triple combination tool string was deployed at 0115 hr on 4 March but was retrieved without logging because of an electronic problem. The integrated porosity-lithology tool (IPLT) was then run into the pipe at 0600 hr and encountered an obstruction at 353 mbsf. The hole was logged from this depth up to the bit, with a short repeat section. During logging, additional tight spots were observed at 170 and 240 mbsf. In many parts of the hole, the diameter exceeded 18 in.

At noon the tool was recovered, and a wiper trip was conducted from 97 to 578 mbsf. The region from 578 to 607 mbsf was washed and reamed. After a 20-bbl mud flush was circulated, the bit was pulled back to 356 mbsf. The IPLT was deployed again and advanced from 356 to 556 mbsf, where an obstruction prevented further penetration. The hole was logged from 556 mbsf up to the bit.

At midnight on 4 March, the first tool string was recovered and the second tool (geological high-sensitivity magnetic tool [GHMT]) deployed. The GHMT logged the hole from 510 to 356 mbsf and was recovered and rigged down by 0930 hr on 5 March. The drill string was recovered, but the positioning beacon failed to release and was therefore not retrieved. The vessel departed for Site 1097 at 1530 hr on 5 March. For a summary of drilling at Site 1096, see Table T1, p. 54, in the “Leg 178 Summary” chapter.

LITHOSTRATIGRAPHY

Holes 1096A, 1096B, and 1096C penetrated to a maximum depth of 607.7 mbsf, recovering predominantly fine-grained and terrigenous sediments. They can be divided into three lithostratigraphic units (I, II, and III; Table T2; Fig. F5), although further subdivision of Unit III may ultimately be justified.

Unit I (0–32.8 mbsf) consists of laminated and massive, commonly intensely bioturbated, diatom-bearing silty clays. Sedimentation rates averaged 7 cm/k.y. The top of Unit II is placed at the first appearance downcore of common parallel-laminated silt and mud turbidites. Unit II is partly a turbidite succession ~140 m thick (32.8–173.0 mbsf), with generally low biogenic content. Sedimentation rates averaged 9 cm/k.y. Although the turbidite silts are thin and subordinate to muds, two coarsening-upward sequences may be discerned in the upper part of Unit II. A massive, well-sorted sand turbidite occurs at 112 mbsf. Unit III extends from 173 mbsf to the bottom of the hole at 607.7 mbsf. It is composed of (1) very thinly laminated and generally nonbioturbated clays deposited from muddy turbidity currents, and (2) intensely bioturbated homogenous silty clays. Overall, Unit III has a sedimentation rate of 18 cm/k.y., although variations in deposition rates may be recorded by intervals of intense bioturbation with abundant ice-raftered debris.

In Units II and III, the alternation of laminated turbidite facies and bioturbated hemipelagic facies records cyclic fluctuations in sediment supply and transport processes. Some of these fluctuations may be related to glacial–interglacial (Milankovich) cycles along the Antarctic Peninsula margin similar to those identified within Unit I, but longer period cycles also exist.

Unit I

Interval: Cores 178-1096A-1H through 4H; Core 178-1096B-1H through Section 5H-1, 50 cm

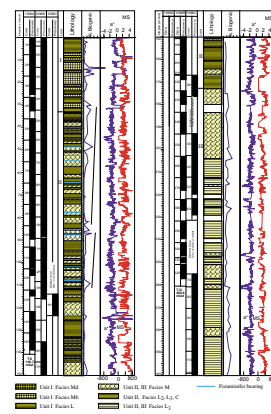
Age: Holocene to late Pleistocene (0.0–0.48 Ma)

Depth: 0–32.8 mbsf

Unit I consists of laminated and massive, commonly intensely bioturbated, clay and diatom-bearing silty clay. Weak bottom (contour) current activity influenced depositional patterns, although much fine-grained sediment was probably delivered from the margin by turbidity currents. Sedimentation rates averaged 7 cm/k.y. (see “**Sedimentation Rates**,” p. 30). Unit I shows a well-defined alternation of biogenic-rich and terrigenous horizons that are the stratigraphic expression of late Quaternary glacial cycles.

T2. Summary of lithostratigraphic units identified at Site 1096, p. 103.

F5. Lithostratigraphy at Site 1096, p. 43.



Description

Three facies are recognized in Unit I: two massive facies (diatom rich and diatom poor) and one laminated facies consisting mainly of clay with very rare silts.

Massive Facies

Facies Md (massive, diatomaceous), comprising diatomaceous silty clay and diatom-bearing silty clay, occurs at the core top and in three units downcore (Fig. F6). It is dark grayish brown to brown and olive brown (10YR 4/2, 4/3, 5/3, 6/4; 2.5Y 4/2) and is intensely mottled by burrows, with original depositional structures having been obliterated (Fig. F7). Diatoms are well preserved, and foraminifers, radiolarians, and calcareous nannofossils are also present. Scattered sand grains and granules occur. This facies corresponds to high values of the chromaticity parameters a^* and b^* and to low magnetic susceptibility (Fig. F6). There is a thin (1 cm) vitric ash at 8.83 mbsf at the base of one interval of Facies Md (178-1096B-2H-4, 53 cm).

Facies Mb (massive, barren) consists of silty clay containing few, poorly preserved diatoms. Bioturbation is common to rare, and colors are generally lighter than Facies Md (grayish brown, pale brown, and olive gray: 2.5Y 5/2, 10 YR 6/3, 5Y 5/2), locally darkening to dark gray (5Y 4/1). Very faint darker and lighter bands are the only primary structures seen, where bioturbation is less intense. Sand grains and granules occur in centimeter-thick burrowed layers, and also dispersed in layers up to 3 m thick.

Laminated Facies

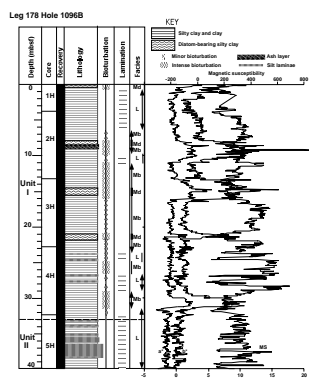
Facies L (laminated) is subordinate to the massive facies (Md and Mb), occurring as one thick interval from 0.6 to 6.0 mbsf and three thinner intervals downcore (Fig. F6). These consist of clay ($\leq 20\%$ silt, estimated from smear slides), with only a trace of biogenic material in the form of fragmented diatoms and foraminifers. Facies L is faintly color banded in shades of gray and dark gray (5Y 5/1, 5Y 4/1, N 4), becoming greener downcore to greenish gray (5GY 5/1) in Core 178-1096B-4H. Darker gray bands several centimeters thick are internally finely laminated with a few small bedding-parallel burrows (Fig. F8). Facies L has generally low values of chromaticity parameters a^* and b^* and high but variable magnetic susceptibility.

In the lowest 10 m of Unit I, the laminated facies includes four thin (5–10 cm) packets of interlaminated silt and clay. Although silt forms only 20%–30% of these packets, each is clearly visible as a trough in magnetic susceptibility (Fig. F6). The laminae in the packets at 23.7 and 24.6 mbsf are disrupted by minor bioturbation; in the lower two packets, the laminae have sharp bases and tops and form small thinning-upward sequences.

Interpretation

Unit I sediments are fine grained and record deposition mainly from hemipelagic settling in a regime of weak bottom currents. The rare thin packets of beds with sharp-based, parallel-laminated silts are interpreted as distal turbidites (compare Facies L₂, below). The more common clays showing weak, diffuse parallel lamination are interpreted as the deposits of bottom currents (contourites; similar to Facies C below). The intermixing of contourites and turbidites indicates a setting influenced mainly by weak bottom-current transport of fine sediment. Occasion-

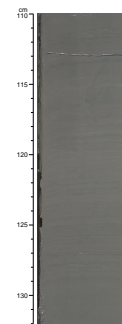
F6. Lithology of Unit I and correlation with color and magnetic susceptibility data, [p. 45](#).



F7. Facies Md in Unit I, [p. 46](#).



F8. Facies L in Unit I, [p. 47](#).



ally, dilute turbidity currents reached the site and deposited the silts. Dispersed sand grains and granules were transported to the area by ice rafting. The massive diatomaceous facies records periods of seasonally open water allowing diatom productivity; these periods may represent warm oxygen isotope Stages 1 (seafloor sediment = Holocene), 5e, 7 (occurrence of *Hemidiscus karstenii*; see “**Biostratigraphy**,” p. 12), and 9. Stage 11 and additional warm stages down to the Brunhes/Matuyama boundary at 55 mbsf (see “**Paleomagnetism**,” p. 15) are not represented by diatom-bearing layers.

Unit II

Interval: Cores 178-1096A-5H through 13H; Section 178-1096B-5H-1, 50 cm, through Core 22X; Core 178-1096C-1H through Section 2H-4

Age: late Pleistocene to late Pliocene (0.48–2.1 Ma)

Depth: 32.8–173.0 mbsf

Unit II is a partly turbiditic succession 140 m thick. The top of Unit II is placed at 32.8 mbsf at the first appearance downcore of common parallel-laminated silt and mud couplets (Core 178-1096B-5H-1, 50 cm). This corresponds to a downcore increase in high-frequency variability of magnetic susceptibility (Fig. F6). Although the turbidite silt beds are thin and subordinate to muds, two coarsening-upward trends (first-order cycles) may be discerned in the upper part of Unit II. A massive, well-sorted sand turbidite bed occurs at 112 mbsf.

The sediments can be divided into four facies that record regimes where mud was deposited by different processes. Two related laminated facies are characterized by a well-developed repetitive internal organization of sedimentary structures. The first, L₃ (we retain the numbering scheme of Site 1095 where the same facies were seen), consists of thinly laminated silty clays. The second and less common, L₂, shows sharp-based, parallel-laminated silts and laminated silty clays.

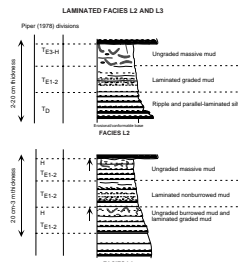
The other two facies show no consistent internal organization of structures and occur in beds that are poorly defined and commonly moderately to intensely bioturbated. Facies C (not seen at Site 1095) comprises faintly laminated bioturbated silty clays with starved ripples; Facies M consists of massive silty clay, commonly with foraminifers or diatoms. Ice-raftered debris is present throughout Unit II but is most abundant in Facies M.

Description

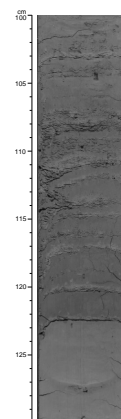
Facies L₂: Silt and Silty Clay

Facies L₂ is distinguished by the presence of sharp-based, commonly graded silt laminae. Silts are 1–12 mm thick, and gray, dark gray, or very dark gray (5Y 5/1, 4/1, 3/1). The base of silt laminae are generally sharp, although thicker laminae may have slightly erosional bases. Internally, the thicker silts (>3 mm) show parallel lamination or slightly wavy lamination. Bed tops are sharp or gradational into overlying laminated or massive silty clay (Figs. F9, F10). The silty clay is gray to dark gray (5Y 5/1, 4/1; N 4) and faintly parallel laminated. Bioturbation is not extensive and is limited to small *Chondrites* and *Planolites* burrows, belonging to the deep-water bathyal *Nereites* ichnofacies assemblage. Facies L₂ accounts for ~9% of the thickness of Unit II. It occurs either as

F9. Descriptive scheme used for muddy turbidite Facies L₂ and L₃, p. 48.



F10. Muddy turbidite Facies L₂ in Unit II, p. 49.



isolated silt laminae grading up into laminated mud or as packets 10–60 cm thick of interlaminated to thinly interbedded silt and silty clay (Fig. F10). Some of these packets are thinning-upward sequences (e.g., in Core 178-1096A-5H), with silts typically 10 mm thick at the base and 1 mm thick at the top; silt forms 10%–20% of each packet. From 70 to 101 mbsf, there are packets of silt laminae partly cemented by aragonite (Fig. F10). Ice-raftered debris is rare in Facies L₂, although isolated pebbles occur.

Facies L₃: Laminated Silty Clay

This facies is distinguished by the presence of well-defined lamination and only minor bioturbation. It consists of thinly laminated (millimeter scale) and laminated (<1 cm) silty clay, with thin bioturbated layers at bed tops (Fig. F9). The lamination is visible as subtle color changes or as partings within drilling biscuits. Small-scale color banding is common, and upward transitions from dark to light hues in the silty clays suggest normal grading in grain size. Greenish gray to dark greenish gray (5GY 5/1, 4/1) colors are characteristic. Bioturbation is not extensive in this facies and is limited to small *Chondrites* and *Planolites* burrows, belonging to the deep-water bathyal *Nereites* ichnofacies assemblage. This facies accounts for ~40% of Unit II. Ice-raftered debris is rare in Facies L₃, although isolated pebbles and lenses of sand grains and granules occur.

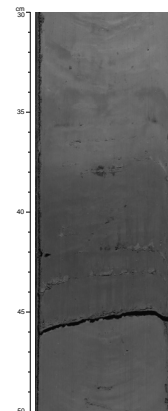
Facies C: Faintly Laminated Bioturbated Silty Clay

Facies C is distinguished by faint lamination (generally visible as diffuse color banding) and minor to moderate bioturbation, together with very thin discontinuous silt laminae that occur in isolation instead of in packets. Facies C accounts for <5% of the total stratigraphic thickness of Unit II and occurs as intervals up to 40 cm thick, which are transitional from underlying hemipelagic intervals (T_{E3-H}) of Facies L₂ and L₃, rather than as discrete, well-defined beds (Fig. F11). Facies C shows a weak lamination, commonly wavy, with isolated (starved) silty ripples, irregular and discontinuous silt laminae (Fig. F12), and variable bioturbation by *Planolites*, *Chondrites*, and *Zoophycos* ichnofauna. A distinctive color mottling caused by bioturbation and mixing of dark greenish gray, locally glauconitic clay (5GY 4/1) and dark gray (5Y 4/1) silt laminae with prominent gray burrows is also observed. Ice-raftered debris occurs locally, in the form of dispersed sand grains and granules, as well as isolated pebbles.

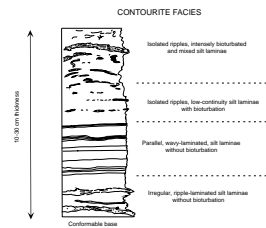
Facies M: Bioturbated Silty Clay

Facies M is distinguished by moderate to intense bioturbation that has obliterated most primary sedimentary structures. It occurs in intervals up to 6 m thick (more commonly 0.5–2 m thick) and accounts for ~45% of the thickness of Unit II. The base of Facies M is usually poorly defined as a result of mixing by bioturbation and typically shows large (1 cm) *Planolites* burrows; interval tops are commonly the sharp bases of overlying Facies L₂ silts. Colors include gray, dark gray, and dark greenish gray (N 5/0, N 4/0, 5Y 4/1, 5GY 4/1). Facies M includes silty clay and diatom-bearing silty clay; diatom preservation is poor to moderate. Most intervals are homogeneous, but the greener layers show very faint color banding on a 5- to 15-cm scale. Color changes are gradational and burrow mottles (*Planolites* and *Zoophycos*) are easiest to observe where there are color contrasts (Fig. F13). Ten thin (0.2–1.0 m) intervals of foraminifer-bearing to foraminiferal silty clay occur be-

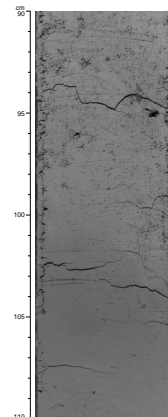
F11. Silty clay in Unit II showing diffuse, poorly defined lamination, p. 50.



F12. Schematic drawing of contourite facies from Unit II, p. 51.



F13. Facies M in Unit II: silty clay coarsening upward, p. 52.



tween 48 and 123 mbsf (shown in blue in Fig. F5, illustrated in Fig. F13; see “[Organic Geochemistry](#),” p. 16). Ice-raftered debris is common in Facies M and includes scattered sand grains and angular granules, a few thin (1–2 cm) sandy layers, and isolated pebbles as much as 2–3 cm in diameter.

In addition to these four facies, Unit II contains a single bed of massive sand, 68 cm thick, at 112 mbsf (178-1096B-13H-2, 147 cm, to 13H-3, 62 cm; Fig. F14). The sand is well sorted and medium grained, with subangular to subrounded grains. The base and top are sharp, and the bed shows no internal sedimentary structures. It is a quartz-lithic sand, and most of the lithic grains are low-grade metasediments.

Depositional Cycles

In the upper part of Unit II (33–110 mbsf), the occurrence of silt-based turbidites (Facies L₂) delineates two coarsening-upward sequences, shown as thin arrows in Figure F5. In the lower sequence, Facies L₂ forms 4% of the sediment in Core 178-1096B-13H, 9% in Core 178-1096B-12H, and 16% in Core 178-1096B-11H. Core 178-1096D-10H, the base of the upper sequence, contains no silt beds; Facies L₂ forms 11% of the sediment in Cores 178-1096B-9H, 8H, and 7H, 15% in Core 178-1096B-6H, and 31% in Core 178-1096B-5H.

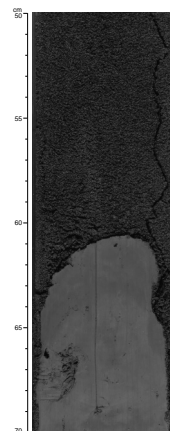
Interpretation

Laminated silts and silty clays similar to those of Unit II (Facies L₂, L₃) are described in the literature as “parallel silt-laminated muds,” “mud turbidites,” and “thin-bedded turbidites” (see reviews by Stow and Piper, 1984; Stow and Wetzel, 1990). These facies are characteristic of deep-marine depositional environments dominated by muddy sediment gravity flows (e.g., Pickering et al., 1988; Alonso and Maldonado, 1990) and are interpreted as being those recognized at Site 1095 (see “[Lithostratigraphy](#),” p. 3, in the “Explanatory Notes” chapter).

Facies C and M clearly record very different depositional regimes from the turbidite Facies L₂ and L₃. The lack of clear lamination and of well-defined bedding sequences, the occurrence of dispersed ice-raftered debris (sand grains and granules), and more intense bioturbation are distinguishing characteristics. Facies C probably records deposition of hemipelagic mud from weak bottom currents and is transitional upward from the T_{E3-H} hemipelagic division of Facies L₂ and L₃. Rare “starved” silt ripples and discontinuous silt laminae indicate limited current reworking. Current velocities were insufficient to generate significant size sorting, continuous silt laminae, or ripple cross-lamination. This is consistent with a regime dominated by hemipelagic settling of mud in an area affected by weak bottom currents. Facies C is therefore interpreted as contourites. Commonly, a waning low-density turbidity current supplies suspended fine sediment to the lower water column (benthic nepheloid layer), where it is redistributed by bottom currents. Such processes are well described by Stow and Wetzel (1990). Contourite facies typically show pervasive bioturbation (e.g., Gonthier et al., 1984). However, some deposits attributed to muddy contourites at Site 1096 are not uniformly intensely bioturbated. This can be attributed to a high input of hemipelagic mud.

Facies M is closely related to Facies C and results from hemipelagic settling of mud from the benthic nepheloid layer. The nepheloid layer can be supplied with suspended sediment by low-density turbidity currents and by biogenic components settling from the sea surface. Supply

F14. Sharp-based, well-sorted massive sand bed, [p. 53](#).



of fine sediment from sinking glacial meltwater plumes is another possibility because the continental shelf edge (the nearest possible position of the grounded ice margin) is ~100 km from the site. Facies M differs from C in being almost structureless as a result of intense bioturbation, which suggests deposition rates low enough to allow the benthic fauna to rework seafloor sediments. A high proportion of coarse ice-rafted debris in this facies is also consistent with a reduction in the supply of fine-grained sediment (although it may also record a greater influx of ice-rafted debris).

In the massive sand bed, the absence of sedimentary structures such as cross-stratification may rule out deposition from a traction current (i.e., a strong bottom current). Beds of massive sand in deep-sea deposits may also be interpreted as sediment gravity flows, and a wide variety of terms has been employed (fluxoturbidite, grain flow, fluidized flow, liquefied flow, and hyperconcentrated flow).

Unit III

Interval: Cores 178-1096B-23X through 32X; Section 178-1096C-2H-5 through Core 42X

Age: late Pliocene to early Pliocene (2.1–4.7 Ma)

Depth: 173.0–607.7 mbsf

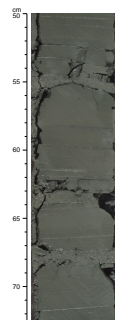
Unit III extends from 173 mbsf to the bottom of the hole and is dominantly fine grained. It is composed of thinly laminated and generally nonbioturbated silty clays (Facies L₃) and intensely bioturbated homogenous silty clays (Facies M). Diatom content increases downward. The sedimentation rate of 18 cm/k.y. is twice as high as in Unit II. Intervals of intense bioturbation with abundant ice-rafted debris may record fluctuations in deposition rates. Cyclicity in sedimentation is present on various scales.

Description

Unit III is mainly composed of two of the facies previously described, L₃ (laminated silty clay) and M (massive, bioturbated silty clay). Silty turbidite facies (L₂) and fine-grained contourite facies (C) are extremely rare. The contact between Units II and III occurs at 173 mbsf in Section 178-1096C-2H-4, 150 cm, at the top of a very thick interval of Facies M (Fig. F5). This stratigraphic level also coincides with a downward increase in the siliceous biogenic component (Fig. F5) and marked changes in physical properties of the sediments (see “Physical Properties,” p. 21), which confirms a change in depositional style between Units II and III.

Facies L₃ lamination is seen very clearly within drilling biscuits (Fig. F15). Biogenic content increases downcore. Facies M in Unit III shows some differences from Unit II and thus is described separately. It is distinguished by moderate to intense bioturbation that has obliterated most primary sedimentary structures. It occurs in intervals 0.5–30 m thick (generally <8 m thick) and constitutes 52% of the recovered thickness of Unit III. The biogenic content increases downcore from silty clay through diatom-bearing silty clay to diatom silty clay, with some muddy diatom ooze intervals below 450 mbsf (Fig. F5). Foraminifers are absent. In the upper part of Unit III (above 225 mbsf), Facies M shows diffuse color banding (gray to dark gray and greenish gray; 5Y 5/1, 4/1,

F15. Muddy turbidite Facies L₃ in Unit III showing sharply defined lamination, [p. 54](#).



5GY 5/1). Elsewhere, Facies M is dark greenish gray (5G 4/1) and appears conspicuously green compared with the dark greenish gray (5GY 4/1) of surrounding Facies L₃. Ice-raftered debris in the form of scattered sand grains and angular granules is very common in Facies M (Fig. F16). It occurs throughout some intervals but in others is concentrated in decimeter- to meter-thick layers.

Massive and laminated facies alternate downcore on a 0.3- to 20-m scale (Fig. F5). Because of incomplete core recovery, it is not known whether the 30 m of Facies M at the top of Unit III and the 55 m of Facies L₃ from 395 to 450 mbsf are continuous. Facies M occurs from 173 to 204 mbsf at the top of Unit III and is then very subordinate to Facies L₃ until 450 mbsf. From 450 to 524 mbsf, Facies M forms nearly half the cored thickness; there is a clear correspondence between sediment facies, spectral reflectance, and magnetic susceptibility in this interval (Fig. F5). Texturally, Unit III is quite uniform downcore as shown by sand:silt:clay ratios estimated from smear slides (Fig. F17). Below 524 mbsf, the alternations of Facies M and L₃ are generally thin (0.3–5 m).

The massive facies generally has lower magnetic susceptibility than the laminated facies (Fig. F5), perhaps because of dilution of ferromagnetic minerals by biogenic silica. The magnetic susceptibility curve also exhibits a low-frequency cyclicity of ~1 cycle per 40 m (~200 ka; see “Physical Properties,” p. 21). The high-frequency variability in magnetic susceptibility cannot be related to any visible features in the cores, in contrast to Unit I.

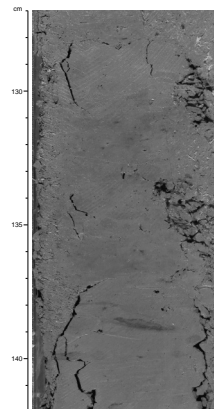
Interpretation

As described above for Unit II, the laminated Facies L₃ can be attributed to distal turbidite flows. The massive Facies M records a setting dominated by hemipelagic deposition and ice rafting. Although more intense bioturbation in Facies M would suggest a lower deposition rate of mud allowing complete sediment reworking by the benthos, there appears to be no significant difference in high sedimentation rate (18 cm/k.y.; see “Sedimentation Rates,” p. 30) between the parts of Unit III dominated by Facies L₃ and the part below 450 mbsf, where Facies L₃ and M alternate.

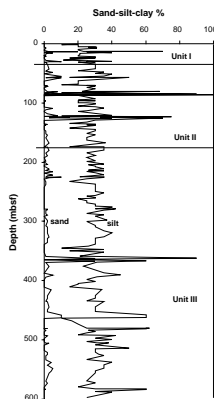
Ice-Rafted Debris

Ice-raftered debris occurs throughout Units I, II, and III at Site 1096 (Fig. F18). It is present as scattered sand grains and granules, as isolated pebbles (limestone), and as lenses of granules and sand. An average of 1.9 pebbles (0.5–6 cm in diameter) per core was observed on split-core surfaces from Holes 1096A, 1096B, and 1096C. Pebble abundance is lowest in Unit I, averaging 0–2 pebbles per core (Fig. F18). In Unit II, ice-raftered pebbles reach a peak in abundance at 112–114 mbsf. Unit III appears to have a cyclic trend in pebble abundance that peaks several times downhole. To understand the flux in ice-raftered debris at this site through time, it is necessary to quantify the contribution of the sand and granule ice-raftered debris fraction and to compare ice-raftered debris concentrations with sedimentation rates and facies. Ice-raftered debris lithologies are primarily volcanic (basalt and rhyolite), volcaniclastic, and intrusive igneous (granite and granodiorite), with smaller contributions of metamorphic (granitic gneiss) and sedimentary rocks (silt-

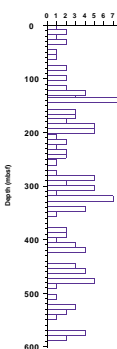
F16. Facies M; mottled, intensely bioturbated silty clay in Unit III, p. 55.



F17. Sand-silt-clay percentage in major lithologies at Site 1096, p. 56.



F18. Abundance of pebbles 0.5–6.0 cm in diameter at Site 1096, p. 57.



stone). Most or all rock types have local sources on the Antarctic Peninsula.

The concentration of ice-raftered debris at Site 1096 appears to be more than twice as high as at Site 1095. The total accumulation rate is three times higher at Site 1096 than 1095, even further increasing the difference in ice-raftered debris between Sites 1095 and 1096. A detailed study of ice-raftered debris at both Sites 1095 and 1096 should yield important information about the iceberg flux from the continental shelf over time.

Depositional Setting of Site 1096

The elevated position of Site 1096 (water depth of 3152.5 m) near the crest of Drift 7, ~600 m above the channel to the southwest and 380 m above the smaller channel to the southeast, indicates that turbidity currents derived from the continental margin may bypass the site. This possibly has been the case throughout the drift-maintenance stage, as a considerable difference in height between paleodrift crest and paleo-channel floor has been maintained (Rebesco et al., 1996). Probably the finest fractions of suspended flows were available for redistribution over the drift by gentle bottom currents. In the long term, the occurrence of the laminated (turbidites) and massive (hemipelagic) facies may be related to the history of channel development on either side of the drift (see "[Seismic Stratigraphy](#)," p. 31). The southwestern channel is a very long-lived feature and has existed throughout the 4.7 m.y. represented by Site 1096 sediments. Although there is a deeply buried channel northeast of the drift, the northeastern channel in its present position appears to be younger. Reflectors at 400 ms TWT below the seafloor (320 mbsf and deeper) can be traced beneath it, which suggests that it did not exist for much of Unit III time. The young channel margins truncate reflectors at 200 ms TWT below the seafloor (i.e., 155 mbsf), which is in the lower part of Unit II. The occurrence of distal turbidites in Unit II may be related to reactivation of the northeastern channel, which in turn may be a reflection of greater sediment supply from the margin related to climatic changes. The possibility of a local sedimentological, not a regional, climatic explanation for changes in sedimentation, as here, was part of the rationale for sampling a different sediment drift (see "[Lithostratigraphy](#)," p. 2, in the "Site 1101" chapter).

The upward decrease and disappearance of silt-based turbidites from Unit II to Unit I could have resulted from a reduction in sediment supply in the late Pleistocene. The alternation of hemipelagic facies (C and M) with turbidite facies (L_2 and L_3) at Site 1096 could be the stratigraphic "overprint" of glacial-interglacial climate cycles along the Antarctic Peninsula. In Unit III, the sedimentation rate appears to be uniformly high (see "[Sedimentation Rates](#)," p. 30), and the reasons for the apparent changes in cycle length (L_3/M alternations varying from meters to tens of meters; Fig. F5) are not yet completely understood. Very thick (tens of meters) cycles probably do not bear a simple relationship to glacial-interglacial cycles; however, the interval from 525 to 560 mbsf has eight cycles (i.e., 1/44 k.y.), close to the obliquity period of 41 k.y.

Cyclic, climatically driven changes of sedimentary facies are well known along the Antarctic continental margin. Ehrmann and Grobe (1991) and Ehrmann et al. (1991) described significant changes in ice-raftered debris content, grain size, and biogenic components from glacials to interglacials at Sites 745 and 746 in the Australian-Antarctic Basin

drilled during Ocean Drilling Program (ODP) Leg 119 (Barron, Larsen, et al., 1991). They recognized two facies. Facies A (interglacial) had a high content of siliceous microfossils and a relatively low content of fine terrigenous sediment and ice-rafted debris. Facies B (glacial) was distinguished by a smaller biogenic silica content and enhanced terrigenous sedimentation. Here, probably because of proximity to the continental shelf edge, the direct terrigenous sediment supply (Facies L) is dominant during glacials, leading to a greater ice-rafted debris component within the much more slowly deposited interglacial sediments (Facies C and M).

BIOSTRATIGRAPHY

Compared to Site 1095, Site 1096 reveals both faster sedimentation and better biogenic preservation. Calcareous nannofossils appeared somewhat unexpectedly in material recovered from this site within the upper 174 mbsf. Below this depth, the biostratigraphy is based on the biogenic silica record. The change at 174 mbsf coincides with the lithologic change from Unit II to Unit III, which continues to the base of Hole 1096C (see “[Lithostratigraphy](#),” p. 4). The high sedimentation rate of this lower section has expanded the biostratigraphic zones to approximately three times their thickness at Site 1095. The bottom of Hole 1096C is believed to be early Pliocene in age.

Diatoms

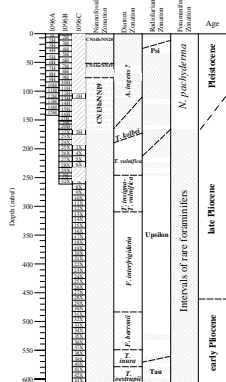
Diatoms are generally rare to barren in sediments from Hole 1096A and the upper parts of Holes 1096B and 1096C. The exception to this is in brown, possibly interglacial, sediments found in the lower portion of Cores 178-1096A-2H and 178-1096B-2H and 3H, in which diatoms are common and the assemblage is dominated by *Fragilariopsis kerguelensis*, *Thalassionema* spp., and *Thalassiothrix* spp. fragments. The presence of *Hemidiscus karstenii* also suggests that those intervals are within the interval 0.19 to 0.49 Ma (Shipboard Scientific Party, 1999).

The zonal boundaries in the upper part of the diatom zonal scheme used on this leg are based on last occurrence (LO) datums. The zonal determinations for Holes 1096A, 1096B, and 1096C are shown in Figure F19. The extensive reworking that happens in glacial environments makes the task of identifying these datums more difficult. The sporadic Pliocene diatom species, including *Thalassiosira torokina*, *T. inura*, *T. vulnifica*, and *T. oliverana* with neritic diatom *Paralia sulcata* in Hole 1096A and the upper part of Holes 1096B and 1096C, was considered reworked because of the presence of well-preserved calcareous nannofossils of a younger age (<1.69 Ma). Table T3 summarizes the diatom datums for this site.

The co-occurrence of *Thalassiosira complicata* and *T. inura* without *T. vulnifica* in samples from Cores 178-1096B-21H, 22H, and 24H through 26X suggests placement of those samples in the *Thalassiosira kolbei* Zone. The upper zonal boundary marker species, *T. kolbei*, was not observed at this site. The topmost occurrence of *T. vulnifica* observed in Sample 178-1096B-23X-3, 70 cm (177.6 mbsf), defines the base of the *T. kolbei* Zone.

The presence of *T. vulnifica* and the absence of *Thalassiosira insigna* in Samples 178-1096B-27X-CC through 30X-1, 82 cm (242 mbsf), suggest placement of those samples in the *T. vulnifica* Zone. The LO of *T.*

F19. Occurrence of calcareous nannofossils, diatoms, radiolarians, and planktonic foraminifers at Site 1096, [p. 58](#).



insignia, indicating the base of the *T. vulnifica* Zone, is noted between Samples 178-1096B-30X-1, 82 cm, and 30X-2, 72 cm (243.5 mbsf).

The co-occurrence of *T. insignia* and *T. vulnifica* in Samples 178-1096B-30X-2, 72 cm, through 32X-CC and Samples 178-1096C-7X-CC through 13X-1, 10 cm, implies that those samples are within the *T. insignia/T. vulnifica* Zone. The base of this zone is defined by the first occurrence of *T. vulnifica* in Sample 178-1096C-13X-1, 10 cm (308.9 mbsf).

The *Fragilariopsis interfrigidaria* Zone extends over the largest depth interval of any zone at this site, including 17 cores (from 178-1095C-30X through 14X). The base is defined by the first occurrence (FO) of *F. interfrigidaria*, in Sample 178-1096C-30X-CC (482.5 mbsf). The FO of *Fragilariopsis barronii* (base of the *F. barronii* Zone) is in Sample 178-1096C-37X-CC (550.3 mbsf). Two cores down, in Sample 178-1096C-40X-CC (579.1 mbsf), the base of the *T. inura* Zone is indicated by the FO datum of *T. inura*. Although the diatoms in Core 178-1096C-41X were not well preserved, they did not contain any *T. inura*, restricting the lowest part of the cored section to the *Thalassiosira oestrupii* Zone.

Radiolarians

Radiolarians sampled at Site 1096 ranged in age from Pleistocene (Psi Zone) to early Pliocene (Tau Zone) (Fig. F19). The younger sediments were dominated by calcareous microfossils and lacked sufficient siliceous biogenic material to determine radiolarian zonal boundaries. In the upper Pliocene, below ~ 220 mbsf, preservation of radiolarians improved. This portion of the section down to the bottom of Hole 1096C is greatly expanded compared to Site 1095. Interestingly, a specimen of the subpolar-subtropical *Dictyocoryne* genus was found in Sample 178-1096A-21H-CC.

Because of the sparseness of fauna and absence of age-diagnostic species, Pleistocene to late Pliocene zones cannot be distinguished. The youngest discernible age is 0.610 Ma, suggested by the presence of *Antarctissa cylindrica* in Sample 178-1096A-4H-CC (36.2 mbsf). This implied an age of at least 0.610 Ma, placing it in the Psi Zone. From 36.2 to ~220 mbsf, no other biostratigraphic markers occur, preventing the determination of the Chi and Phi Zones.

The presence of *Helotholus vema* at 222 mbsf (Samples 178-1096A-27H-CC and 178-1096C-5X-CC) indicates an age of at least 2.421 Ma within the Upsilon Zone. The 50-m barren interval above 222 mbsf precludes the location of the upper boundary of the Upsilon Zone. Two events within the Upsilon Zone were noted at this site. The earliest observed appearance of *Prunopyle titan* (3.489 Ma) was at 232 mbsf; *Lamproxymene coronata* (3.705 m.y.), at 531 mbsf. Both occur after 10-m barren intervals in which the actual top occurrences may exist. Neither the top (last occurrence datum [LOD]) of *Desmospyris spongiosa* nor the bottom (first occurrence datum) of *Cycladophora davisiana* was observed, even though these two events occur above the top (LOD) of *P. titan*. The assemblage within the Upsilon Zone is consistent downcore and similar to that observed at Site 1095. In the lower part of the section (Cores 178-1096C-13X through 38X, 308.8 to 559.8 mbsf), the >63-µm fraction was extremely diluted by mud. It contained common to abundant radiolarians and a small proportion of mineral grains, however.

Sample 178-1096C-38X-CC contains the lowest occurrence of *H. vema*, and the following core recovered no sediment. Consequently, we conclude that the boundary between the Upsilon and Tau Zones is in

the interval from 560 to 570 mbsf (Core 178-1096C-39X). Abundance and preservation diminished from ~560 mbsf to the bottom of the hole. The top common occurrence of *Lychnocanium grande* (5.018 m.y.) was not encountered.

Calcareous Nannofossils

Occurrences of calcareous nannofossils were confined to the upper 170 m of Holes 1096A and 1096B (Fig. F19). The acme of *Emiliania huxleyi* that marks the base of the CN15/NN20 Zone was not observed. The youngest nannofossils allow a determination of the CN14b/NN19 Zone, with *E. huxleyi* present and *Pseudoemiliania lacunosa* absent. The base of this zone is in an interval barren of nannofossils, which extends to the lower portion of Core 178-1096A-6H. Below this depth *P. lacunosa* is a consistent but never dominant part of the assemblage, indicating the upper boundary of CN14a/NN19 at Sample 178-1096A-6H-CC (55.2 mbsf). Intermittent intervals of well-preserved calcareous nannofossils characterize the CN13b/NN19 Zone (see Fig. F19), bounded above by the reentry of the medium *Gephyrocapsa* spp. This zone continues from Sample 178-1096B-9H-6, 61 cm, to 22H-CC (78.3–174 mbsf), where occurrences of calcareous nannofossils begin. Below this depth in the hole, all observed samples are barren of well-preserved nannofossils. A few core-catcher samples contain very dissolved specimens of *Coccolithus pelagicus* and *Sphenolithus* spp., but they are never comparable in preservation to the assemblages from the upper sections.

The species *C. pelagicus* is a dominant member of assemblages in several samples (178-1096A-9H-6, 130 cm; 14H-1, 132 cm; 14H-2, 44 cm; 15H-5, 117 cm; 178-1096B-10H-1, 68 cm). Beaufort and Aubry (1992) suggested that Miocene fluctuations in *C. pelagicus* from Site 747 on the Kerguelen Plateau were dependent on water temperature. They note that *C. pelagicus* is a stenothermal species, adapted to temperatures ranging from 0° to 15°C, with optimal abundance between 2° and 12°C. They found five such intervals of increased *C. pelagicus* abundance in the Miocene but none from the Pliocene or Pleistocene.

Foraminifers and Bolboforma

At Site 1096, selected core catchers and many core samples were examined for foraminifers. Planktonic foraminifers are abundant to rare at Site 1096. In addition, both calcareous and agglutinated benthic foraminifers are present in small numbers. An unidentified species of *Bolboforma* is abundant in one core-catcher sample, 178-1096C-14X-CC (328 mbsf). The size and amount of the sand fraction containing foraminifers is highly variable at Site 1096. Some samples contain almost no sand, whereas others contain abundant, well-sorted, coarse or fine sand, or larger sized ice-rafterd detritus. The most common lithologies of ice-rafterd pebbles are basalts and green volcaniclastics. The abundance of foraminifers does not appear to be related to the amount of sand fraction, and foraminifers are present in equal numbers in both sand-rich and sand-poor samples. Beneath 350 mbsf, samples were indurated and difficult to process, and fewer samples were examined.

Planktonic foraminifers are present throughout Holes 1096A, 1096B, and 1096C. In the upper 174 mbsf, planktonic foraminifers are abundant to rare, but from 174 to 598 mbsf they are only rare. All samples contain *Neogloboquadrina pachyderma* sinistral (Fig. F19). In the upper interval there are several samples of foraminiferal ooze, including Sam-

ples 178-1096B-7H-1, 100–104 cm (52.3 mbsf); 178-1096A-14H-2, 47–49 cm (123.6 mbsf); and 178-1096B-20H-2, 134–136 cm (160.5 mbsf). In these samples, more than 90% of the assemblage consists of *N. pachyderma* sinistral with rare occurrences of *N. pachyderma* dextral and *Globigerina bulloides*, which is consistent with a Pleistocene to late Pliocene age for this interval (Pujol and Bourrouilh, 1991). Reworked planktonic foraminiferal faunas are present in several samples. Both Samples 178-1096B-12H-CC (108 mbsf) and 13H-CC (115.8 mbsf) contain excellently preserved middle to late Miocene planktonic foraminifers including *Globoturborotalita woodi* and *Neogloboquadrina continuosa*.

Benthic foraminifers are rare in scattered samples throughout Site 1096. Shallow-water shelf species, including *Globocassidulina subglobosa*, are more common than deep-water species. Only Sample 178-1096B-20H-2, 134–136 cm (160.5 mbsf), contains an excellently preserved deep-water benthic foraminiferal assemblage, including *Nuttallites umbonifer*, *Oridorsalis umbonatus*, *Cibicidoides mundulus*, and *Epistominella exigua*. Samples where siliceous microfossils were especially abundant, 178-1096C-7X-CC (262 mbsf), 28X-CC (464 mbsf), and 33X-CC (509 mbsf), contained agglutinated foraminifers, including *Martinottiella nodulosa* and *Karreriella* sp.

PALEOMAGNETISM

Split-Core Measurements

Archive halves of APC (down to ~170 mbsf) and XCB (down to ~588 mbsf) cores recovered at Site 1096 were measured at 5-cm intervals. Measurement of the natural remanent magnetization (NRM) of Cores 178-1096A-1H through 15H, 178-1096B-1H through 22X, and 178-1096C-1H through 9X was done after stepwise alternating field (AF) demagnetization at 0 (NRM), 10, and 20 mT (Tables T4, T5, T6, T7, T8, T9, T10, T11, T12, T13, T14, T15, T16, all also in ASCII format in the TABLES directory). Cores 178-1096B-23X through 32X and Cores 178-1096C-10X through 41X were demagnetized up to 30 mT because of the higher coercivity of the drill-string overprint for these cores. The distribution of inclination values obtained after demagnetization at 20 mT reflects the overall good quality of the magnetic record. It can be clearly defined as the combination of two log-normal distributions centered respectively at -74° and $+76^{\circ}$ and approaching the geocentric axial dipole values of $\pm 78^{\circ}$ expected at 67°S (Fig. F20).

Discrete Samples

Analysis of the data collected from discrete samples followed the methods described in “Paleomagnetism,” p. 16, in the “Site 1095” chapter (Tables T17, T18, T19, all also in ASCII format in the TABLES directory). Stepwise AF demagnetization of discrete samples taken from the working halves of cores revealed that the drill-string overprint was dominantly vertically downward, as observed at Site 1095 (see “Paleomagnetism,” p. 16, in the “Site 1095” chapter). The drill-string overprint was mostly or wholly removed by partial AF demagnetization of the NRM at 20 or 30 mT. Samples from the upper 18 m of cores from Site 1096 had a very “hard” magnetization, as AF demagnetization up to 80 mT only removed 30%–60% of the intensity of remanence (Fig. F21). Samples from the underlying sediments had “softer” magnetiza-

T4. Split-core paleomagnetic measurements for Hole 1096A before demagnetization, [p. 106](#).

T5. Split-core paleomagnetic measurements for Hole 1096A after 10-mT demagnetization, [p. 107](#).

T6. Split-core paleomagnetic measurements for Hole 1096A after 20-mT demagnetization, [p. 108](#).

T7. Split-core paleomagnetic measurements for Hole 1096A after processing results from 20-mT demagnetization, [p. 109](#).

T8. Split-core paleomagnetic measurements for Hole 1096B before demagnetization, [p. 110](#).

T9. Split-core paleomagnetic measurements for Hole 1096B after 10-mT demagnetization, [p. 111](#).

T10. Split-core paleomagnetic measurements for Hole 1096B after 20-mT demagnetization, [p. 112](#).

T11. Split-core paleomagnetic measurements for Hole 1096B after 30-mT demagnetization, [p. 113](#).

T12. Split-core paleomagnetic measurements for Hole 1096B after processing results from 20-mT demagnetization, [p. 114](#).

T13. Split-core paleomagnetic measurements for Hole 1096C before demagnetization, [p. 115](#).

tion, with 80%–90% of the remanence removed after demagnetization at 80 mT (Fig. F22). In both cases, the direction of the characteristic remanent magnetization (ChRM) vector was very stable up to 60 mT. A small number of samples had no stable direction of magnetization.

Inclinations calculated from principal component analysis (PCA) of the discrete sample measurements agreed very well with the inclinations from the magnetically cleaned split cores (Fig. F23A; Table T20, also in ASCII format in the TABLES directory). For the 118 samples analyzed, 85 gave maximum angular deviations between 0° and 5°, 13 gave angles between 5° and 10°, and 20 gave angles >10° (Fig. F23C; Tables T8, T9, T10, T11, T12). In general, samples with low intensities gave larger maximum angular deviation angles and more uncertain ChRM directions (Fig. F23D).

Magnetostratigraphy

Results obtained from Holes 1096A, 1096B, and 1096C provide a near-continuous paleomagnetic data set down to 588 mbsf. The magnetostratigraphy has been constructed from records of the inclination and intensity of remanence (Figs. F24, F25; Table T21). Declination was not used in the magnetostratigraphic record because the cores were not oriented. The Brunhes/Matuyama (0.78 Ma) reversal occurs in Hole 1096A between 54.60 and 55.40 mbsf, and in Hole 1096B between 54.94 and 54.99 mbsf. The Jaramillo (0.99–1.07 Ma) and the Olduvai (1.77–1.95 Ma) Subchrons are seen in Holes 1096A and 1096B, but their boundaries remain difficult to determine accurately and correspond to intervals of very low intensities of remanence (Fig. F26). These intervals of low intensity are also related to low values of magnetic susceptibility (Fig. F26) and may be understood in terms of local changes in the nature or concentration of the magnetic minerals. The rest of the stratigraphic column displays a succession of polarity intervals, starting in Hole 1096B with the termination of Chron C2An.1n (2.581 Ma) between 215.35 and 217.25 mbsf and ending in Hole 1096C with the onset of Chron C3n.2n (4.62 Ma) between 583.85 and 584.05 mbsf.

ORGANIC GEOCHEMISTRY

At Site 1096, hydrocarbon gases were measured in every core recovered. Inorganic carbon concentration was first measured on approximately one sample per section, with additional sampling later. Elemental analyses were performed on one sample per core. Solvent extraction of organic matter was applied on a subset of five samples. Rock-Eval pyrolysis was performed on five carbonate samples.

Volatile Hydrocarbons

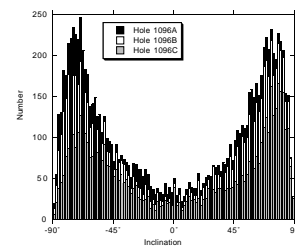
For gas monitoring at Site 1096, both headspace and vacutainer sampling were used (Table T22). At Hole 1096A, headspace concentration of methane (C_1) exceeded the background level below 50 mbsf and increased downhole (Fig. F27), small amounts of ethane (C_2) were present, and propane (C_3) occurred below 123 mbsf (Fig. F28). The gas composition remained relatively constant through most of Hole 1096B. Upon recovery of Section 178-1096B-23X-2 (176 mbsf), gas pockets were discovered, and vacutainer sampling was initiated. Vacutainer sampling continued in parallel with headspace sampling during the

T14. Split-core paleomagnetic measurements for Hole 1096C after 10-mT demagnetization, [p. 116](#).

T15. Split-core paleomagnetic measurements for Hole 1096C after 20-mT demagnetization, [p. 117](#).

T16. Split-core paleomagnetic measurements for Hole 1096C after 30-mT demagnetization, [p. 118](#).

F20. Histogram of inclinations for Holes 1096A, 1096B, and 1096C, [p. 59](#).



T17. Discrete sample NRM and AF demagnetization results for Hole 1096A, [p. 119](#).

T18. Discrete sample NRM and AF demagnetization results for Hole 1096B, [p. 120](#).

T19. Discrete sample NRM and AF demagnetization results for Hole 1096C, [p. 121](#).

remainder of Site 1096 operations. Hydrocarbons isobutane (C_4) and isopentane (C_5) first appeared in Section 178-1096C-11X-3 (293 mbsf) and increased slowly with depth, whereas propane increased more rapidly (Table T22; Fig. F28). The methane:ethane ratio in vacutainer samples decreased downhole but never reached the safety limit of 100.

The increasing amount of C_{3+} hydrocarbons in Hole 1096C indicates a thermogenic origin of this portion of the gas. This hypothesis is supported by the presence of hydrogen sulfide that forms at temperatures of 130°–140°C. The shallow depth and estimated temperature of 40°–45°C (see “Physical Properties,” p. 21) at the bottom of Hole 1096C suggest that the observed heavy hydrocarbons and hydrogen sulfide formed at a greater depth and migrated upward.

Inorganic Carbon and Elemental Analyses

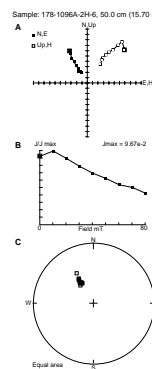
Site 1096 is divided into three lithostratigraphic units (see “**Lithostratigraphy**,” p. 4). Unit I (0–33 mbsf) consists of diatom-bearing silty clays and contains low concentrations of inorganic and organic carbon, with mean values of 0.12 and 0.13 wt%, respectively. Unit II comprises mainly mud and silt turbidites and thin foraminifer-bearing laminae. Unit II was recovered in Holes 1096A and 1096B, with ~80 m of overlap. Initial routine sampling for carbonate analyses included only one of the foraminifer-bearing laminae in Hole 1096A. Subsequent sampling was targeted directly at eight more of these layers in the upper part of Holes 1096A and 1096B. These thin laminae account for all of the sharp peaks observed in the inorganic carbon data from Site 1096 (Fig. F29). The stratigraphic correlation between Holes 1096A and 1096B is good (see “**Composite Depths**,” p. 29), and a correlation between specific inorganic carbon peaks should be possible; however, the widely spaced sampling interval precludes such an effort for now. Total organic carbon concentrations remain low throughout Unit II (Fig. F30), increase sharply at ~180 mbsf at the boundary between Units II and III, and continue to increase downhole, although with large fluctuations. In Unit III, total organic carbon averages 0.36 wt%, but inorganic carbon remains low, 0.10 wt%, except in carbonate-cemented layers that occur in Hole 1096C (Fig. F29; Table T23). The increase of total organic carbon also coincides with the increase of biosiliceous material, which indicates a higher primary productivity by diatoms (see “**Biostratigraphy**,” p. 12).

Elevated amounts of sulfur occur below 340 mbsf (Table T23) and reflect pyrite occurrences (see “**Inorganic Geochemistry**,” p. 18) and possibly adsorption of sulfur to organic matter in a reducing environment.

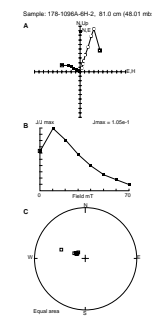
Organic Matter

Five samples that contain ~0.5% total organic carbon were selected for organic solvent extraction and gas chromatographic analysis of lipid compounds. Overall, lipid fraction recovery was low, the chromatograms are complex, and the analytical capabilities onboard are limited, which makes interpretation tentative. Nonetheless, all samples show a marine fingerprint, with some differences evident among samples. Samples 178-1096C-16X-4, 64–68 cm; 21X-6, 80–84 cm; and 28X-4, 63–66 cm, show a clear marine algal origin, whereas Samples 178-1096A-2H-1, 100–104 cm, and 178-1096C-35X-4, 59–61 cm, indicate a mixed origin.

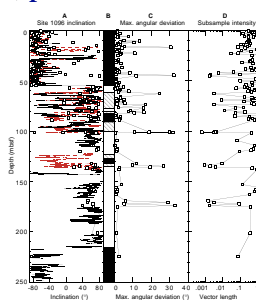
F21. Orthogonal projection, change in intensity, and equal-area projection of the remanence vector, Sample 178-1096A-2H-6, p. 60.



F22. Orthogonal projection, change in intensity, and equal-area projection of the remanence vector, Sample 178-1096A-6H-2, p. 61.



F23. Inclination measured on archive halves of Holes 1096A and 1096B, p. 62.



T20. Results from the principal component analysis of discrete paleomagnetic samples, p. 123.

Samples from Hole 1096C show signs of organic matter maturation and biodegradation by the presence of short carbon chains and increasingly complex and poorly resolved chromatograms.

Rock-Eval pyrolysis was performed on five carbonate samples that contain ~0.5 wt% total organic carbon (Table T24). The values obtained using Rock-Eval compare reasonably well with those calculated from total carbon and inorganic carbon, but the total organic carbon values remain too low (<0.5%) to allow a reliable evaluation of the data.

INORGANIC GEOCHEMISTRY

Interstitial Water Chemistry

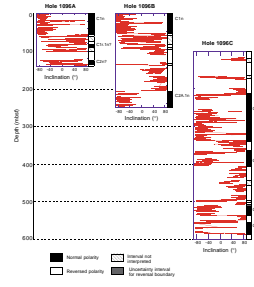
We squeezed 35 whole-round core samples for interstitial water at Site 1096. Two samples were taken from each of the first six cores in Hole 1096A, one sample from each of the next six cores, and one sample from every third core from Holes 1096B and 1096C (Table T25). We also obtained a single seawater sample from just above the mudline in Hole 1096B. Chloride concentrations in the upper 100 mbsf (Fig. F31) exceed the modern bottom-water value by as much as 2.8% and could reflect the global increase in ocean salinity during the last glaciation (McDuff, 1985); however, the slightly increased variability of the chloride data within this interval may represent an artifact of sample processing or storage, thus limiting the strength of such an inference. Below 100 mbsf, chloride concentrations decrease steadily with depth by ~6%.

Organic Matter Degradation

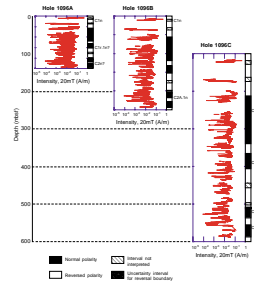
The interstitial water chemistry at Site 1096 exhibits patterns similar to those observed at Site 1095, although generally with more pronounced concentration gradients (Fig. F31). Decaying organic matter exerts a stronger influence at Site 1096, probably because the sediment has accumulated more rapidly (7 cm/k.y. in the upper 200 m) and contains slightly more organic carbon (0.1–0.4 wt%), particularly below 180 mbsf (see “**Sedimentation Rates**,” p. 30, and “**Organic Geochemistry**,” p. 16). Dissolved manganese increases sharply with depth to a maximum concentration (196 µM) at 15 mbsf, reflecting dissolution of Mn oxides under suboxic conditions. Directly below this zone, dissolved sulfate and manganese decrease steadily with depth as a result of sulfate reduction and accompanying precipitation of sulfide minerals. Sulfate decreases to zero at 60 mbsf, where significant concentrations of methane and ethane first arise (see “**Organic Geochemistry**,” p. 16; Fig. F27), and manganese reaches a minimum concentration (9 µM) near 160 mbsf.

Other dissolved byproducts of organic matter decay, such as alkalinity, ammonium, and phosphate, all increase with depth in the upper sediment column (Fig. F31). Alkalinity reaches a sharp maximum (>8.0 mM) at 42 mbsf, a distinct minimum (4.0 mM) at 126 mbsf, and a broader maximum (>10.0 mM) between 200 and 400 mbsf, whereas ammonium increases steadily with depth to a maximum concentration (>2 mM) at 460 mbsf, then decreases slightly at greater depths. Unlike alkalinity and ammonium, dissolved phosphate increases to a maximum (>13.0 µM) at shallow depths, between 5 and 25 mbsf, then decreases somewhat erratically to 200 mbsf. At depths >200 mbsf,

F24. Inclination of the magnetization vector vs. depth for Holes 1096A, 1096B, and 1096C, [p. 63](#).

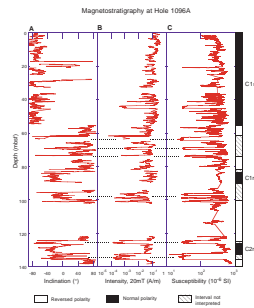


F25. Intensity of the magnetization vector vs. depth for Holes 1096A, 1096B, and 1096C, [p. 64](#).



T21. Depths of geomagnetic reversals in Holes 1096A, 1096B, and 1096C, [p. 125](#).

F26. Inclination, intensity of the NRM, and magnetic susceptibility at Hole 1096A vs. depth, [p. 65](#).



T22. Gas components measured in headspace and vacutainer samples, [p. 126](#).

phosphate remains relatively constant ($\approx 1.0 \mu\text{M}$). Dissolved fluoride decreases sharply in the upper 50 mbsf and also remains constant ($\approx 20 \mu\text{M}$) at greater depths (Fig. F31). As at Site 1095, the phosphate and fluoride profiles suggest that apatite precipitates authigenically within the sediment, although probably in disseminated amounts too small to detect. The constant phosphate and fluoride concentrations at depth could correspond to equilibrium values with respect to this mineral phase (Jahnke et al., 1983; Schuffert et al., 1994). Note, however, that fluoride reaches a constant concentration at a shallower depth than phosphate, and the inferred equilibrium values differ slightly between Sites 1095 and 1096.

Dissolved iron concentrations remain near zero throughout most of the sediment column at Site 1096, but a small peak in dissolved iron occurs between 300 and 360 mbsf (Table T25), well below the zone where organic-matter diagenesis should dissolve the oxidized iron solid phases. This dissolved iron may relate, however, to the pyritized silt laminae that occur just below 360 m in Hole 1096C (intervals 178–1096C-19X-4, 110–115 cm, and 21X-2, 10–13 cm; see “[Lithostratigraphy](#),” p. 4). Also, total sulfur concentrations increase at 357 mbsf and persist from 390 mbsf to the bottom of Hole 1096C (see “[Organic Geochemistry](#),” p. 16; Table T23).

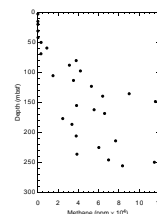
Silica, Carbonate, and Silicate Diagenesis

Other inorganic processes such as dissolution of biogenic silica and carbonate, reprecipitation of authigenic silica and carbonate phases, and diagenesis of clay and feldspar minerals probably influence the chemical composition of interstitial water at Site 1096. Dissolved silica increases considerably in the upper 5 to 50 mbsf (Fig. F31) and eventually attains maximum concentrations of $\sim 1100 \mu\text{M}$, essentially the solubility limit of opal-A (Kastner et al., 1977), at depths below 300 mbsf. Slightly lower dissolved silica concentrations occur between 100 and 150 mbsf, coincident with the interval of decreased alkalinity. We infer that biogenic opal dissolves principally between 0 and 50 mbsf, with substantial dissolution occurring in the uppermost meter of sediment because the first interstitial water sample contains much more dissolved silica ($> 500 \mu\text{M}$) than the bottom-water sample ($150 \mu\text{M}$).

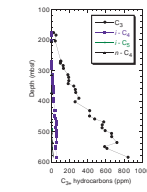
Overall, dissolved calcium increases slightly with depth in the upper 100 mbsf (Fig. F31), but a distinct minimum in the calcium profile occurs at 50 mbsf, near the base of the sulfate reduction zone and coincident with a sharp reversal of the alkalinity gradient. Calcium remains fairly constant ($\sim 14 \text{ mM}$) between 100 and 400 mbsf, then increases below to a maximum value (25 mM) at the bottom of the hole. In contrast, dissolved magnesium decreases by $> 40\%$ through the upper 150 mbsf (Fig. F31) with a noticeable inflection at 50 mbsf, then remains constant ($\sim 30 \text{ mM}$) to 300 mbsf before decreasing further to a minimum value (14 mM) at the bottom of the hole. Similarly, dissolved potassium decreases by $> 60\%$ through the upper 150 mbsf (Fig. F31) with an inflection near 50 mbsf, but then remains constant (4 mM) to 500 mbsf before decreasing slightly to a minimum value (3 mM) at the bottom of the hole. Strontium remains constant at its seawater value ($\sim 90 \mu\text{M}$) in the upper 30 mbsf (Fig. F31), then increases steadily with depth to a constant value ($\sim 150 \mu\text{M}$) below 300 mbsf.

From the profiles described above, we identify the base of the sulfate reduction zone as a particularly active horizon of mineral diagenesis at Site 1096. Dissolution of biogenic calcium carbonate and subsequent

F27. Methane occurrence in headspace samples, [p. 66](#).

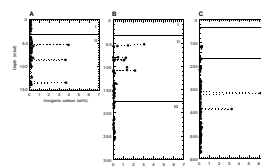


F28. C₃₊ hydrocarbons measured in gas pockets, [p. 67](#).

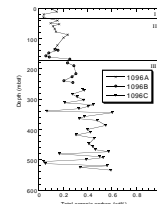


1096-G-2.EPS

F29. Inorganic carbon occurrences in Holes 1096A, 1096B, and 1096C, [p. 68](#).



F30. TOC concentrations for Holes 1069A, 1096B, and 1096C, [p. 69](#).



T23. Analyses of inorganic carbon, total carbon, and sulfur, [p. 128](#).

T24. Summary of Rock-Eval pyrolysis measurements, [p. 131](#).

T25. Interstitial water analyses for Holes 1096A, 1096B, and 1096C, [p. 132](#).

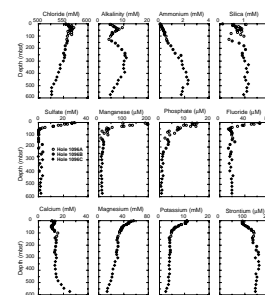
precipitation of authigenic carbonate phases could cause the observed release of strontium, the decrease in alkalinity, and the uptake of calcium and perhaps some magnesium. The occurrence near this horizon and at greater depths of narrow silt layers cemented partially by aragonite (see “[Lithostratigraphy](#),” p. 4) provides direct evidence of authigenic carbonate precipitation. Although the loss of dissolved sulfate enhances the possibility for replacement of calcite by dolomite (Baker and Kastner, 1981), we have not yet detected any direct evidence of dolomite formation at Site 1096. We speculate further that the silt layers could act as preferential pathways for upward diffusion of dissolved methane that could subsequently reoxidize to dissolved bicarbonate and conceivably trigger carbonate mineral growth at the base of the sulfate reduction zone, much as it does around methane seeps at the seafloor (Paull et al., 1992). If so, the carbonate-cemented silts should possess extremely light carbon-isotope signatures. By extrapolating the observed magnesium gradient beyond the maximum depth penetrated, we calculate that magnesium concentrations would decrease to zero at a depth of ~800 mbsf, well above the inferred basement depth of ~3500 mbsf (see “[Seismic Stratigraphy](#),” p. 31); therefore, magnesium uptake probably results mostly from clay mineral diagenesis within the sediment column instead of from alteration of basaltic basement rocks (cf. Lawrence et al., 1975; Gieskes and Lawrence, 1976; Perry et al., 1976). In fact, clay mineral reactions probably exert the strongest influence on the observed calcium, magnesium, potassium, and perhaps strontium profiles.

X-Ray Diffraction Mineralogy

A total of 28 samples were analyzed by X-ray diffraction for clay mineralogy at Site 1096. All but one of these were also analyzed for their bulk mineralogy. In three cores, two samples were taken where alternating colors were interpreted as possible barren glacial and biogenic interglacial intervals. Most unpaired samples were taken from presumed glacial intervals. Bulk and clay mineralogies at Site 1096, which were similar to those found at Site 1095, consist primarily of quartz, feldspar, and a mixture of clay minerals, including chlorite, illite, and a mixed-layer clay, most likely mixed smectite-illite of varying proportions. Traces of amphibole were also detected in all samples.

The relative abundances of quartz and feldspar, as measured by the ratio of their principal diffraction peaks, remain nearly constant among all samples, but clay mineral abundances vary significantly. In all but a few bulk mineral samples, the 3.19-Å plagioclase diffraction peak ranges between 30% and 45% of the height of the 3.34-Å quartz peak (Table [T26](#)). Considerable variability among the clays, however, is demonstrated by the widely varying ratios between their diffraction intensities (Table [T27](#); Fig. [F32](#)). This is particularly evident in the relative intensity of the mixed-layer peak, which varies among samples by an order of magnitude relative to chlorite. In general, the greatest abundances of chlorite and mixed-layer clay relative to illite occur below 200 mbsf. As at Site 1095, however, the greatest variability among clays occurs between alternating sediment types instead of as a function of age or burial depth.

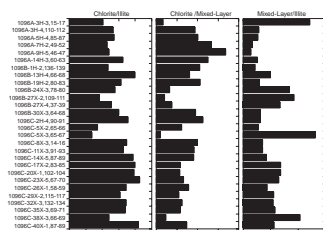
F31. Interstitial water chemistry in Holes 1096A, 1096B, and 1096C, p. 70.



T26. Relative intensities of selected X-ray diffraction peaks from bulk mineral samples of Site 1096 sediments, p. 133.

T27. Relative intensities of selected X-ray diffraction peaks from clay mineral samples of Site 1096 sediments, p. 134.

F32. Ratios between X-ray diffraction intensities of peaks for chlorite, illite, and mixed-layer clays, p. 71.



X-Ray Fluorescence and Trace-Element Chemistry

Trace-element concentrations were measured by X-ray fluorescence on splits of the 27 bulk-sediment samples analyzed by X-ray diffraction. These results (Table T28) are similar to those obtained from Site 1095. For most elements analyzed, peak concentrations occur in the uppermost 150 mbsf, typically between 40 and 150 mbsf, and then decrease by ~30% with greater depth. For example, Rb concentrations increase from 90 to 120 ppm between 20 and 60 mbsf and then decrease to ~75 ppm at 320 mbsf, a value typical of the lower 250 m in Hole 1096C. These trends imply that similar factors influenced the bulk-sediment chemistry at Sites 1095 and 1096. At both sites, the trend toward lower concentrations of lithophile trace elements (e.g., Rb, Cr) occurs in sediments of similar age ~1.5 Ma (see “[Sedimentation Rates](#),” p. 30; also see “[Sedimentation Rates](#),” p. 32, in the “Site 1095” chapter). This change in composition correlates poorly with interstitial water chemistry profiles. For example, much sharper interstitial concentration gradients occur at Site 1096 than at Site 1095, reflecting the shallower occurrence of sulfate reduction and other redox-related reactions. In contrast, sharper bulk-sediment chemical gradients are found at Site 1095. Based on these observations, we conclude that the sedimentary trace-element gradients at these two sites result primarily from changes in sediment source (i.e., provenance) rather than from reactions with interstitial water. The peak concentration of Ba (1250 ppm) in the shallowest interglacial sample implies high surface-water productivity during deposition of this interval (Dymond et al., 1992), whereas the absence of high barium concentrations in older interglacial intervals may reflect dissolution of barium under anoxic conditions (Brumsack and Gieskes, 1983; von Breymann et al., 1990).

T28. Trace-element chemistry of bulk sediment from Holes 1096A, 1096B, and 1096C, [p. 135](#).

PHYSICAL PROPERTIES

Whole-Core Measurements

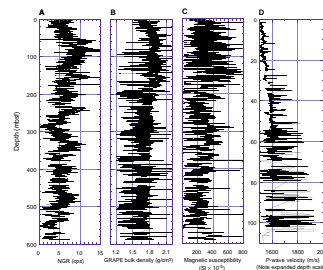
Multisensor Track (MST)

Natural gamma-ray (NGR) activity, gamma-ray attenuation porosity evaluator (GRAPE) density, magnetic susceptibility, and *P*-wave velocity were measured on whole-round samples (see “[Physical Properties](#),” p. 20, in the “Explanatory Notes” chapter). All measurements were made to the base of APC coring in Holes 1096A and 1096B, at depths of 140.7 mbsf (Core 178-1096A-15H) and 166.7 mbsf (Core 178-1096B-20H), respectively. *P*-wave velocity measurements were not made on the XCB cores because of poor core quality, but the other properties were measured down to 588.6 mbsf (Core 178-1096C-41X).

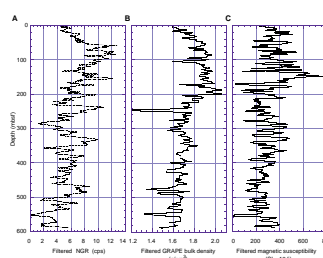
Magnetic Susceptibility

Whole-core magnetic susceptibility was measured at 2-cm intervals (averaged over 2 s). The raw data are provided [on CD-ROM and the World Wide Web](#) and are shown in Figure F33. The spurious data associated with the ends of sections at Site 1095 were minimized at Site 1096 by not measuring the upper and lower 6 cm of each section. After low-pass filtering (Fig. F34), depth-scaled susceptibility shows a positive correlation with the GRAPE density. The average susceptibility and the susceptibility’s variance also increase between ~100 and 160 mbsf (Fig. F34). This trend may be the result of a downward increase in silt con-

F33. Spliced raw data for NGR, GRAPE density, magnetic susceptibility, and *P*-wave velocity, [p. 72](#).



F34. NGR, GRAPE density, and magnetic susceptibility vs. depth, [p. 73](#).



tent toward the base of lithostratigraphic Unit II and the high silt variability of the unit. Unit II is composed mainly of fine-grained silt and mud turbidites (see “[Lithostratigraphy](#),” p. 4). Paleomagnetic polarity reversals were used to convert the data to the age scale shown in Figure [F35](#).

GRAPE Bulk Density

Density was measured by gamma-ray attenuation at 2-cm intervals (averaged over 2 s at each point). The raw data are provided [on CD-ROM and the World Wide Web](#) and are shown before (Fig. [F33](#)) and after (Figs. [F34](#), [F35](#)) low-pass filtering.

GRAPE density values rise to ~2.0 g/cm³ at ~160 mbsf, then fall to ~1.5 g/cm³ at ~580 mbsf. The greater part of this density drop corresponds closely to the base of lithostratigraphic Unit II (see “[Lithostratigraphy](#),” p. 4), which coincides with the beginning of XCB coring. However, the decrease in density at the base of Unit II occurs over an interval of ~40 m, which suggests that it is not caused solely by the change in coring method. It reflects a physical properties change that was also noted in the index properties and magnetic susceptibility (see below). Superimposed on the broad trends of the filtered data are peaks that show a positive correlation with the magnetic susceptibility data and correspond to lithostratigraphic changes.

P-wave Velocities

Whole-core P-wave measurements were only recorded continuously down to 106.3 mbsf (Core 178-1096A-12H-3) in Hole 1096A and to 107.48 mbsf (Core 178-1096B-12H-6) in Hole 1096B. Below, core disturbance related to XCB coring was too great for measurements to be reliable. The anomalously high values associated with the ends of core sections at Site 1095 were removed from Site 1096 data sets by omitting data within 10 cm of the beginning and end of each section. The raw data can be found [on CD-ROM and the World Wide Web](#) and are presented in Figure [F33](#). The main features in this data set are the increase in P-wave velocity downhole and the correlation between the peaks in the filtered P-wave velocities and sediment layers with high silt content (see “[Lithostratigraphy](#),” p. 4).

Natural Gamma Radiation

Whole-core natural gamma-ray emissions (averaged over 15 s) were counted at 15-cm intervals. The change to XCB coring did not cause any change in the signal. The raw data set is provided [on CD-ROM and the World Wide Web](#) and presented in Figure [F33](#).

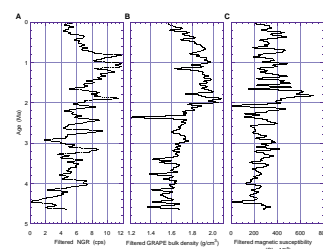
The filtered gamma-ray count (Figs. [F34](#), [F35](#)) shows an increase with depth in the first 60 mbsf, followed by a broad decrease with depth to the base of Hole 1096C at ~580 mbsf, possibly with a weak 50-m cyclicity. There is an inverse correlation between the MST measurements (GRAPE density, magnetic susceptibility, and NGR data) and the biogenic component of the sediments.

Split-Core Measurements

Index Properties

Gravimetric and volumetric determinations of index properties were made for 36 samples in Hole 1096A (Cores 178-1096A-1H through 15H), 30 samples in Hole 1096B (Cores 178-1096B-13H through 32X), and 102 samples in Hole 1096C (Cores 178-1096C-1H through 41X).

F35. NGR, GRAPE density, and magnetic susceptibility data vs. age, [p. 74](#).



One sample was taken every first, third, and fifth section per core where possible.

Samples were not taken from the reconstituted sediment surrounding the “biscuits” in the XCB cores or in regions of flow-in in APC cores. Wet mass, dry mass, and dry volume were measured, and from these measurements, percentage water weight, porosity, dry density, bulk density, and grain density were calculated (see “Physical Properties,” p. 20, in the “Explanatory Notes” chapter; see **CD-ROM and the World Wide Web** for raw data).

Index properties bulk density and GRAPE density agree well in the upper 220 m. Below, they show a similar decrease with depth to the base of the hole (Fig. F36). The index properties grain density shows a similar decrease with depth from 170 mbsf, as does the bulk density. High grain density coincides with lithostratigraphic Unit II (see “**Lithostratigraphy**,” p. 4), but grain density does not show the sharp increase with depth of the bulk density, within the upper 100 mbsf. The trend of porosity and percentage bulk water content (Fig. F37) is the inverse of that shown by the bulk density. After the initial decrease down to 100 mbsf, porosity and water content increase steadily downward from 52% to 60% and from 27% to 37%, respectively. These results were not expected, as porosity normally decreases with depth because of compaction. A possible explanation is the increase in biogenic silica content (Fig. F37A), seen previously to inhibit compaction (Bryant and Rack, 1990). The highest values of porosity and water content are found in the upper 30 mbsf, corresponding to lithostratigraphic Unit I, where there is a high biogenic content but also a low lithostatic load.

Yield Strength

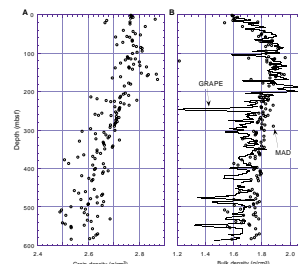
The yield strength of the sediments was measured using the vane shear and pocket penetrometer equipment. Residual strengths were also obtained from the vane shear equipment. The raw data are presented in Figure F38A and provided **on CD-ROM and the World Wide Web**. The most notable features in the data sets are the decreased strengths found with the vane shear equipment below 140 mbsf and the change in the pocket penetrometer data variability at 210 mbsf.

Down to 140 mbsf, the peaks in the vane-determined shear strengths coincide with the lowest biogenic abundances in the sediments (Fig. F38B) and with the minimum porosity (Fig. F38C) and water contents. Below this level, the relationships are not as clear, which suggests that the yield strength peak at 140 mbsf may represent the highest reliable measurement possible with the equipment. However, the general relationship of higher porosity and lower strengths remains valid below 140 mbsf.

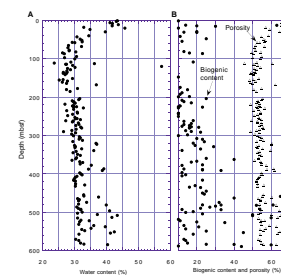
The change in variability of the pocket penetrometer data (at ~200 mbsf) is likely to reflect a stiffening of the sediment to a level at which remolding became obvious and disturbed areas were sampled less. The vane shear equipment has a larger footprint than the pocket penetrometer and is therefore less likely to record the effect of remolded areas on the average behavior of the sediment.

Yield strength normalized by the overburden stress (see raw data **on CD-ROM and the World Wide Web**) gives an empirical estimate of consolidation levels. Typically, values >0.5 suggest overconsolidation and <0.2 underconsolidation (Skempton, 1970). From Figure F38D, it may be seen that the material tested is underconsolidated, in agreement

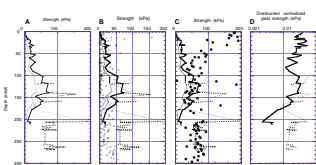
F36. Filtered GRAPE density, raw index properties bulk density, and grain density vs. depth, **p. 75**.



F37. Total biogenic content, index properties porosity, and bulk water content vs. depth, **p. 76**.



F38. Sediment strength, strength against biogenic content, strength against porosity, and yield strengths, **p. 77**.



with the proposed sedimentation mechanisms and rates (see “[Lithostratigraphy](#),” p. 4, and “[Sedimentation Rates](#),” p. 30).

Discrete P-wave Velocities

Discrete *P*-wave velocity measurements using all three sensors (PWS1, PWS2, and PWS3) of the velocity-strength (SV) system were made throughout Site 1096. The upper 40 m of Cores 178-1096B-1H through 5H were soft enough to use the penetrative transducer pairs of PWS1 (measurement direction = longitudinal; transducer spacing = 69.5 mm) and PWS2 (measurement direction = transverse; transducer spacing = 34.8 mm). Results of the transverse and longitudinal measurements are shown in Figure F39 (average measurement separation = 1.4 m). The curves are in close agreement, but no consistent velocity anisotropy is evident.

Hamilton Frame (PWS3) measurements (average measurement separation: 2.0 m) on Cores 178-1096B-5H through 32X and 178-1096C-1H through 38X cover the depth interval 40–554 mbsf, which is too compacted to be measured using the PWS1 and PWS2 transducers (Fig. F39B). The data from all three transducer pairs are provided on [CD-ROM and the World Wide Web](#).

Thermal Conductivity

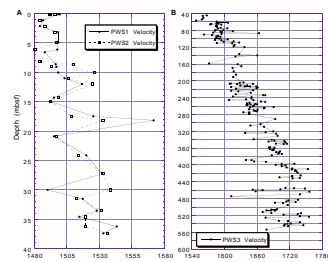
Thermal conductivity was measured once per core, on average, for all holes at Site 1096, usually in the middle of Section 3. Thermal conductivity was needed at Site 1096, in combination with downhole temperature measurements, to estimate heat flow and hence the temperature at the bottom of the hole and the depth to a theoretical methane hydrate BSR.

Above ~300 mbsf, measurements were taken by needle probe on the unsplit core, with the implicit assumption that the core was undisturbed before insertion of the needle and would remain so afterward. Most likely, this was not the case for much of the biscuited core recovered by XCB drilling below 167 mbsf in Hole 1096B and below 176 mbsf in Hole 1096C.

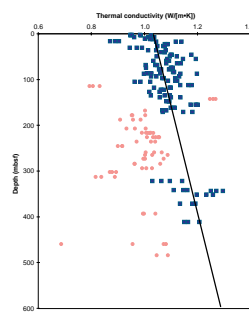
The other available method is appropriate for hard sediment or rock. It uses a different (“half-space”) geometry, in which the needle is embedded at the flat surface of a plastic block of known thermal properties (see “[Physical Properties](#),” p. 20, in the “Explanatory Notes” chapter). The block is clamped to a flat surface of the specimen, and thermal contact is assured by use of a proprietary thermal joint compound. The operator is advised to submerge block and specimen in water, to provide a more stable thermal environment. However, it was clear that sediment from below 300 mbsf, too indurated for measurement by needle insertion, was too soft for immersion in water. To take the measurement in air was to expose the specimen to larger changes in ambient temperature than the (TK04) software would accept in default mode; a valid measurement could be achieved only by doubling the acceptable limit of standard deviation of the decay curve fit. This may have biased, or increased the scatter of, measurements on deeper samples.

Measurements on cored material from all three holes at Site 1096 are combined in Figure F40. Each needle insertion produced three values, which show an internal scatter of about 5%. In addition, sediment thermal conductivity, measured by whatever means as a part of marine geothermal heat flow determinations, shows scatter of up to 10% within

F39. PWS1, PWS2, and PWS3 measurements vs. depth, [p. 78](#).



F40. Thermal conductivity measurements at Site 1096, [p. 79](#).



apparently uniform cores. The origin of this scatter is uncertain, and it has become common practice to determine an average value or (for longer sections) to fit a straight line by least squares. At Site 1096, however, even allowing for this scatter, a dependence of the thermal conductivity values on the methods of measurement and coring is apparent in Figure F40.

Thermal conductivity in fine-grained sediments is to first approximation a bulk property and therefore a linear combination of the conductivities of the grains and the interstitial water. It therefore depends upon porosity and lithology. The thermal conductivity of water is ~ 0.6 W/(m·K), and of most sediment-forming minerals is much higher. Thus, lithology aside, thermal conductivity should increase downhole as porosity decreases. The gradient in thermal conductivity in the uppermost 170 m in Figure F40 illustrates this, although it has been argued that APC coring compacts sediments, particularly at depth, so that the gradient might be artificially high. GRAPE and grain density measured on discrete samples both decrease downward around 170 mbsf, where there is a lithostratigraphic boundary and a change from a calcareous to a siliceous biofacies. However, the reduction in thermal conductivity below 170 mbsf is considered in large part an artifact of the change from APC to XCB. During this transition, it is possible that the needle probe has been inserted into the higher porosity drilling matrix surrounding a biscuit, or has split a biscuit during insertion, allowing the crack to fill with water or air.

Below 300 mbsf it was possible to find larger biscuits, apparently intact after coring and splitting, which could be measured by the half-space method. There is a slight concern here, however, that the search for a measurable piece might in fact result in a bias toward the more indurated components of the rock so that measurement would be biased toward higher values. Anomalously low values might result, on the other hand, if thermal contact was inadequate, or the specimen was either too small or had hidden cracks that would not have been open in situ.

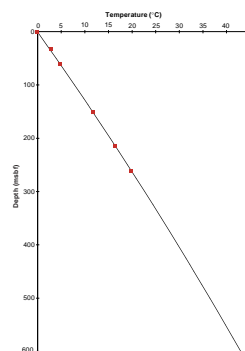
For all these reasons, it was considered best to fit a simple straight line to the main body of data, neglecting values anomalously high and low and, in particular, ignoring the low values associated with needle probe measurements on unsplit XCB cores below 170 mbsf. The straight line gives a thermal conductivity equal to $1.0325 + 0.00043x$ W/(m·K), where x is in meters.

Downhole Temperatures and Geothermal Heat Flow

Six valid temperature measurements were obtained at Site 1096. The Adara tool was used at the mudline and after firing APC Cores 178-1096B-4H and 7H, and the Davis-Villinger tool was used after cutting Cores 178-1096B-17X, 26X, and 32X. The Adara deployment during Core 178-1096B-4H was subject to corer motion during the thermal decay period but can be used; an additional Adara deployment with Core 178-1096B-10H recovered no data because the batteries failed. Temperatures are plotted against depth in Figure F41.

The downhole increase in thermal conductivity is incompatible with a constant temperature gradient downhole, if heat flow is constant. The assumption of constant heat flow means that heat generation within the upper sediments by radioactive decay is neglected, which is reasonable: the logs show only minor radioactivity downhole (see “[Down-hole Measurements](#),” p. 26). The straight-line fit to thermal

F41. Downhole temperature measurements at Site 1096, [p. 80](#).



conductivity measurements (Fig. F40) can be combined with downhole temperatures to determine geothermal heat flow and to extrapolate in situ temperature to the base of the hole. The result is a logarithmic curve, shown in Figure F41 as a line through the measured temperatures and extrapolated to 600 mbsf. The line is a good fit, except perhaps for the temperature from Core 178-1096B-4H, mentioned above. The extrapolated temperature at the base of Hole 1096B (607 mbsf) is 43.4°C.

Heat flow at this site is 83 mW/m². To make a comparison with the theoretical value of heat flow for ocean floor of this age, it is necessary to make an allowance for developments in the Magnetic Reversal Time Scale (MRTS) since the original empirical relationship was derived (Parsons and Sclater, 1977). These authors used the time scale of Heitzler et al. (1968). The site lies on ocean floor dated by marine magnetic anomalies at ~37 Ma (Cande and Kent, 1995; “**Background and Scientific Objectives**,” p. 1), or at ~42.5 Ma by the MRTS of Heitzler et al. (1968). According to Parsons and Sclater (1977), the heat flow appropriate to this age (from a global average, bearing in mind oceanic lithospheric evolution) is 72 mW/m², so the measured heat flow is ~15% higher than expected. This is considered a valid determination, however, because neither the temperatures nor the thermal conductivity measurements are in error to that extent. No allowance has been made for the effects of sedimentation (e.g., Hutchison, 1985).

The average temperature gradient downhole of about 80°/km gives a depth for the base of the methane hydrate stability zone of 300 mbsf using the ODP Pollution Prevention and Safety Panel (PPSP) hydrate stability equation (PPSP, 1992). Any BSR associated with that base would therefore lie at ~340 ms on seismic reflection profiles through the site and could not be linked to the observed BSR at 6–700 ms, which we attribute to silica diagenesis (see “**Background and Scientific Objectives**,” p. 1, and “**Seismic Stratigraphy**,” p. 31).

DOWNHOLE MEASUREMENTS

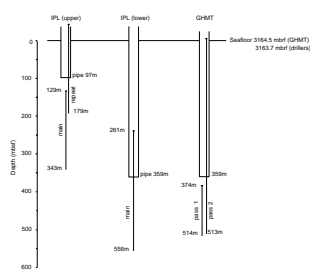
Logging Operations

After coring had reached maximum depth at 607.7 mbsf, Hole 1096C was filled with viscous mud, and the pipe pulled to 97 mbsf. We ran the IPLT (natural gamma, porosity, density) and the GHMT (natural gamma, magnetic susceptibility, and total magnetic field) strings (see Fig. F42; also “**Downhole Measurements**,” p. 25, in the “Explanatory Notes” chapter). Logging operations started at 0030 hr on 4 March and finished at 0930 hr on 5 March (Table T29). The wireline heave compensator was used for all passes.

During the first run of the IPLT, we encountered a hole blockage at 353 mbsf that was not passable with the tool string. The hole was then logged up to the pipe, with a repeat section from 179 mbsf to seafloor. The hole conditions were unstable, and further constrictions were met at 170 and 240 mbsf. After a wiper trip, the end of the pipe was positioned below the blockage of the upper run and the IPLT was lowered downhole, but it was stopped 50 m above the bottom. For the two GHMT passes, the tool string could not pass below 514 mbsf because of continued hole fill.

While logging Hole 1096C, we contended with several tool malfunctions. Before the IPLT reached the borehole on the first attempted run,

F42. Summary of downhole logging operations at Hole 1096C, p. 81.



T29. Summary of logging operations, Site 1096, p. 136.

the run had to be aborted and the tool returned to the ship from the seafloor to have its telemetry unit replaced. The long-spaced gamma-ray detector on the hostile environment lithodensity sonde (HLDS) could not lock into its control signal for the upper IPLT run because the hole was excessively wide; thus, the density and photoelectric effect (PEF) logs were invalid for this pass. The caliper measurements saturated at 14.5 in (37 cm), whereas the maximum caliper extent measured on the surface was 18.5 in (47 cm); the Schlumberger engineer concluded that the caliper had been returning a systematically low reading and reprocessed the gamma-ray and porosity measurements accordingly. The dual induction tool remained unusable after its failure at Site 1095.

Log Quality

Hole 1096C was very wide: it exceeded the maximum 18.5 in (47 cm) of the caliper for ~80% of the logged interval. Thus, the density and porosity logs should be regarded with caution, although neither displays the wide spikes that are characteristic of bad contact of the tool with the borehole wall. The deeper penetrating logs, such as magnetic susceptibility, are much less affected by borehole diameter.

The open hole natural gamma logs contain apparently anomalously high values through the bridged zones at 170–180 and 234–246 mbsf, partly caused by the sediment being adjacent to the detector. Cores from these intervals show corresponding highs in the natural gamma measurements obtained using the MST, which implies some lithologic control. However, the natural gamma emissions measured through the pipe by the natural gamma-ray tool (NGT) during the GHMT run were not anomalous. Two different tools were used to measure natural gamma emission: the hostile environment natural gamma-ray sonde (HNGS) on the IPLT (more accurate) and the NGT on the GHMT. Both logs are shown in Figures F43 and F44. The NGT logs are slightly noisier than the HNGS logs because of the downhole processing that the HNGS performs. The match between core and log natural gamma is patchy.

The absolute values of density and density-derived porosity match well the index physical properties of the cores, apart from the anomalous log density lows in intervals of excessive hole diameter (Fig. F43). The array porosity (APLC) porosity estimate is high compared to the index properties porosity values because of clay-bound water. The pattern in the susceptibility log matches closely the MST susceptibility record but is ~5 m deeper than the core depth scale.

Logging Units

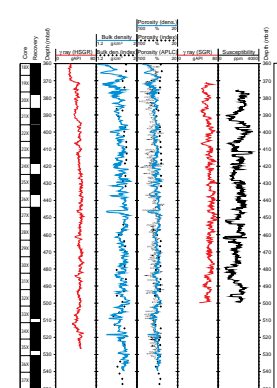
Because of the interrupted logged depth intervals, we did not attempt to divide the formation into units on the basis of the logs alone.

Logs and Lithology

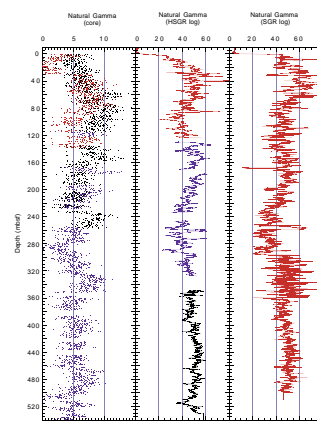
Several logs directly represent lithologic variation (Table T30). Figure F45 illustrates that the logs can be rich in variability even in the moderately homogenous lithostratigraphic Unit III (see “**Lithostratigraphy**,” p. 4).

Computed gamma ray (the natural gamma resulting from K and Th), is typically used as an estimate of the sediment’s clay content because K

F43. Downhole logs of hole diameter, HSGR, RHOM, APLC, SGR, and RMGS from Hole 1096C, p. 82.

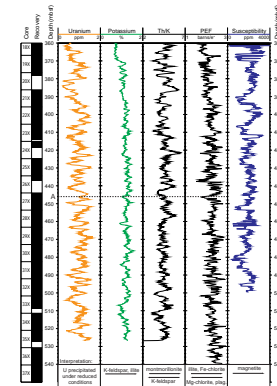


F44. Gamma-ray logs in Hole 1096C from the IPLT and GHMT tool strings, p. 83.



T30. Chemical and nuclear parameters for common minerals, p. 137.

F45. Downhole logs of uranium, potassium, thorium/potassium ratio, and PEF from Hole 1096C, p. 84.



and Th are present in the clays. However, both K-feldspar and micas also contain K and both are present at Site 1096, so simple interpretation with respect to clays is not possible here. Uranium is precipitated under reducing conditions and can occur associated with organic matter. The uranium log (~3–4.5 Ma) has a strongly cyclic character, with a periodicity of ~40 k.y.

The ratio Th/K can be taken to indicate the abundance of mixed-layer clay compared with illite (higher Th/K indicates relatively more mixed-layer clay). The presence of K-feldspar decreases the Th/K ration.

Each element, and hence each mineral, has a characteristic PEF (absorption of low-energy gamma rays) (Table T30). The Hole 1096C PEF log values mostly lie between 3.2 (illite) and 2 barns/e⁻ (montmorillonite). The presence of Mg chlorite (1.39 barns/e⁻) will lower the overall PEF, and Fe chlorite (12.36 barns/e⁻) will raise the PEF. The low PEF log indicates that Fe chlorite is not present in significant amounts in Hole 1096C; this observation is compatible with the average grain density of 2.76 g/cm³ (see “Physical Properties,” p. 21), which is much less than that of Fe-chlorite (3.42 g/cm³) (Fig. F46).

The neutron-capture cross section (Σ_f), like the PEF, is characteristic for each element. However, its use for lithologic purposes is limited by the very high Σ_f of chlorine, which is present in the seawater that fills the borehole. The average log value is shifted upward to 35 capture units (c.u.) by the dominance of chlorine.

Magnetic susceptibility is governed mainly by the concentration of magnetic minerals in the sediment, the most important of which is magnetite, which occurs mostly in the nonclay detrital fraction of the sediment. In example A of Figure F45, the small trough in the K log indicates a reduction in illite abundance at this level, which is also partly responsible for the low in PEF and high in the Th/K ratio. An associated U low is of uncertain origin, and no clear magnetic susceptibility anomaly is present at this level.

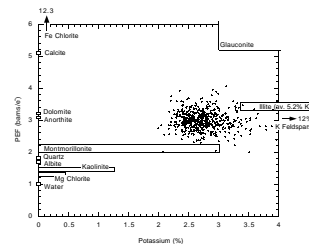
Natural Gamma

Natural gamma was logged through the pipe twice at Hole 1096C. The gamma rays are attenuated in proportion to the thickness of the pipe and bottom-hole assembly (BHA): the lowermost 64 m of the BHA is ~5.1 cm thick, and the pipe above is 1.75 cm thick, with thicker pipe joints spaced every 9.5 m. The through-pipe HSGR and SGR (the [standard] total gamma-ray measurements of the HNGS and NGT, respectively) logs were normalized to give the same amplitude as the open-hole HSGR at the same depth. The two modified logs have similar long- and short-wavelength features, which indicates that the normalization was successful (Fig. F44). The original HSGR and SGR logs are shown in Figure F43.

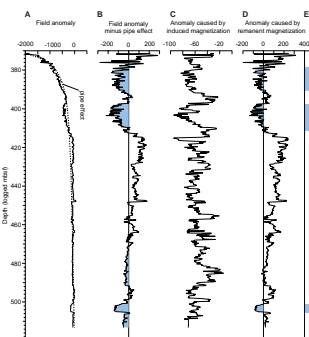
Magnetic Polarity Stratigraphy from the GHMT

Total magnetic field and magnetic susceptibility (RMGS) measurements from the GHMT tool string were used to construct a downhole magnetic polarity stratigraphy (see “Downhole Measurements,” p. 25, in the “Explanatory Notes” chapter). This GHMT-derived polarity sequence matches quite well the polarities derived from half-core inclination measurements (see “Paleomagnetism,” p. 15), after the 5-m downward shift of the core depth scale is considered (Fig. F47).

F46. PEF vs. potassium for the interval 360–525 mbsf in Hole 1096C, p. 85.



F47. Polarity stratigraphy in Hole 1096C from the GHMT tool string, p. 86.



Temperature Log

The Lamont-Doherty temperature-logging tool recorded the temperature of the fluid in Hole 1096C during the upper and lower passes of the IPT tool string. The results of the lower pass are presented here. The uphole curve has a quite constant temperature gradient of $\sim 24^{\circ}\text{C}/\text{km}$ (Fig. F48). The downhole and uphole curves show a constant offset of $\sim 1.5^{\circ}\text{C}$ because the borehole continued to re-equilibrate during acquisition. These temperatures are not considered to represent in situ formation temperatures, although the temperature tool rested in the fill at the bottom of the hole before logging. Thus, some equilibration would have occurred. The temperature measured at bottom (16.7°C) is therefore a lower bound on the true formation temperature (see also Fig. F41).

COMPOSITE DEPTHS

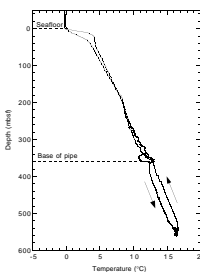
A continuous sedimentary sequence at Site 1096 was recovered for the upper 260.96 mbsf (263.58 meters composite depth [mcd]), extending from the early Pliocene to present. Hole 1096C was drilled to 114.06 mbsf (118.03 mcd). Cores 178–1096C-1H through 6X were collected between 114.0 and 231.4 mbsf to bridge recovery gaps in Holes 1096A and 1096B.

At Site 1096, whole-core, high-resolution measurements were made every 2 cm for magnetic susceptibility and GRAPE density and every 15 cm (standard size) for NGR for all cores in Holes 1096A, 1096B, and 1096C. The MST was used with no change in the measurements at the onset of XCB. *P*-wave velocity was measured down to 107.48 mbsf because the signal was poor; however, it was not used to build the composite depth scale. Color spectral reflectance was measured on the split core at a 5-cm interval.

Initially, all data sets for each hole were visually and quantitatively compared to check for consistency. Subsequently, color spectral reflectance and magnetic susceptibility (as the most continuous and consistent data sets) were employed as the primary parameters to determine depth offsets for the composite depth section. The offsets that comprise the composite depth section at Site 1096 are given in Table T31. See also “**Composite Depths**,” p. 23, in the “Explanatory Notes” chapter.

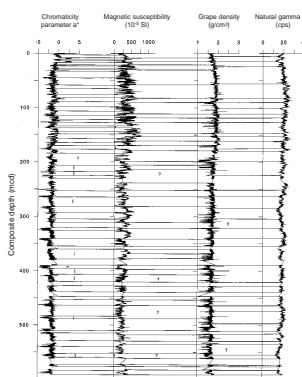
Natural gamma radiation and GRAPE density measurements from the MST were used to confirm the hole-to-hole correlations. GRAPE density, NGR, and magnetic susceptibility correlated positively except in two intervals at ~ 300 – 325 and 530 – 550 mcd for GRAPE density vs. NGR and in four intervals at ~ 220 – 240 , 410 – 425 , 470 – 480 , and 552 – 560 mcd for magnetic susceptibility vs. GRAPE density (Fig. F49). Color spectral reflectance (chromaticity parameter a^*) and magnetic susceptibility show an excellent correlation except for two intervals (180–210 and 552–560 mcd). In the lowermost interval (552–560 mcd), the chromaticity parameter a^* is well correlated with GRAPE density values. The correlation between chromaticity parameter a^* and magnetic susceptibility is mostly positive, except for intervals at about 10–30, 210–225, 270–280, 360–380, 395–425, and 480–485 mcd, in which it became negative (Fig. F49). It was found that all related parameters show an evident cyclic pattern. The relative independence of GRAPE density and chromaticity parameter a^* data made it possible to resolve and correlate sedimentary features in the record of one hole that were not apparent

F48. Temperature log from Hole 1096C, taken during the lower IPT run, p. 87.



T31. Depth offsets of the Site 1096 mcd scale relative to mbsf depth, p. 138.

F49. Correlation of chromaticity parameter a^* , magnetic susceptibility, GRAPE density, and natural gamma radiation data, p. 88.



in the other. Magnetic susceptibility and chromaticity parameter a^* records that were used for correlation are displayed on the mcd scale in Figure F50. The base of the composite depth section is at 263.58 mcd. The remainder of the Hole 1096C cores have been appended to the composite section below this depth without adjustment of relative depths. The mcd scale growth relative to the mbsf scale was about 2% over the range of the composite section (Fig. F51). This section was checked and refined using a paleontological and paleomagnetic correlated tie point in Core 178-1096B-27H vs. Core 178-1096C-5H.

After construction of the composite depth section for Site 1096, a single spliced record for all parameters was developed (see “**Composite Depths**,” p. 23, in the “Explanatory Notes” chapter). The tie points between the cores used to construct the splice are given in Table T32. The spliced GRAPE density and magnetic susceptibility data are displayed in Figure F52.

SEDIMENTATION RATES

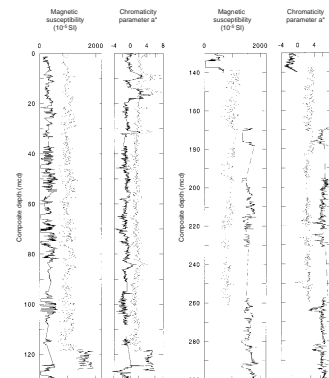
A sedimentary section 607.7 m thick extending from the Holocene to the lower Pliocene was recovered at Site 1096. Sedimentation rates were calculated for the upper 569 mbsf over intervals of continuous recovery. The depth-age relationship (Fig. F53; Table T33) was based on diatom and radiolarian datums in combination with geomagnetic reversals from Holes 1096A, 1096B, and 1096C. Sedimentation rates are assumed to be constant between geomagnetic reversals and are calculated by taking the slope of the depth-age line between successive points (Fig. F54; Table T34). By extrapolation, the age of the base of the hole (607.7 mbsf) was estimated as 4.7 Ma.

The depth of a magnetic polarity transition is defined as the depth at which the inclination changes sign. Many transitions were assigned a large uncertainty where the transition itself was lost in a gap between cores or within a disturbed interval (see Table T21; Figs. F24, F25). The center of the uncertainty interval was used in calculating sedimentation rates. Biostratigraphic datums were assigned when a clear FO or LO could be determined through examination of sediment samples. No FO or LO was determined when the occurrence bordered an interval barren of biogenic material.

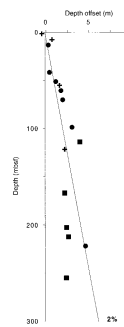
Calcareous nannofossils were present in the upper 170 mbsf at this site, but the relatively short intervals in which they occurred alternated with barren intervals, making it impossible to assign depths to any datums. Siliceous biostratigraphic datums (Table T33), which mostly occur in the lower 437 m of Site 1096, were less abundant than in Site 1095.

Depth-age relationships based on paleomagnetic data show two main intervals with different slopes (Fig. F53). From the bottom of the hole to a depth of 216 mbsf (2.58 Ma), the sedimentation rate averages ~18 cm/k.y. From 216 mbsf to the top of the hole, the sedimentation rate is ~9 cm/k.y. This upper interval is not as well constrained as the lower because of the absence of a clearly defined Matuyama reversed polarity chron (see “**Paleomagnetism**,” p. 15).

F50. Magnetic susceptibility and chromaticity parameter a^* data from Site 1096, [p. 89](#).

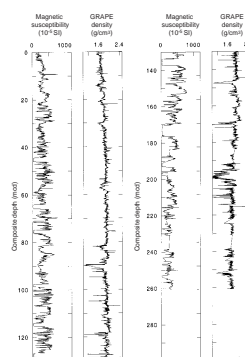


F51. Depth offsets of the Site 1096 mcd scale relative to mbsf depth, [p. 90](#).



T32. Spliced cores for Holes 1096A, 1096B, and 1096C, [p. 140](#).

F52. Spliced records of magnetic susceptibility and GRAPE density data for Site 1096, [p. 91](#).



SEISMIC STRATIGRAPHY

Seismic reflection profiles across Site 1096, collected by the Osservatorio Geofisico Sperimentale of Trieste (see “[Seismic Stratigraphy](#),” p. 29, in the “Explanatory Notes” chapter; also see “[Appendix](#), p. 24, and Fig. AF1, p. 59, both in the “Leg 178 Summary” chapter), have been compared with data from Site 1096 to establish the seismic stratigraphy described below. Physical properties measurements from cores and data from downhole logging facilitated the construction of a synthetic seismogram for comparison with the seismic section.

Density/Velocity Model and Correlations

Bulk densities for the formation were derived from the MST GRAPE measurements (2-cm separation downcore), index properties samples (averaging 3.7-m separation), and lithodensity logging (HLDS, spatial resolution ~15 cm) for the depth interval 360 to 540 mbsf (Fig. F55). The index properties measurements and the MST data are in better agreement than at Site 1095 (Fig. F55). However, above 174 mbsf, the index properties density is slightly lower than the MST density; below 174 mbsf, it is an average of 0.04 g/cm³ higher. This can be explained by the final change from the APC to the XCB coring method at this depth. Two major negative MST density excursions at 200 and 250 mbsf are not represented within the index properties data. Zones of core disturbance at these depth intervals are probably responsible for this phenomenon. The limited available in situ densities from the downhole logging are within the range of the MST and index properties data. For a first modeling approach, only the index properties densities have been used.

Two differently derived velocities are available. The MST P-wave logger provided continuous data (4-cm spatial resolution) down to 125 mbsf (within the APC-cored part of the hole) but no data between 125 and 580 mbsf. Single Hamilton Frame (PWS3) measurements (one every section) provide high-quality data from 40 to 580 mbsf. The SV longitudinal and transverse data sets (PWS1 and PWS2) for the upper 40 m are combined in the apparent absence of velocity anisotropy. A comparison of the “cleaned” MST data (see “[Physical Properties](#),” p. 20, in the “Explanatory Notes” chapter) with the combined SV velocity measurements is shown in Figure F56. Most of the MST-derived P-wave velocities are higher than SV values. This may be a result of the influence of the core liner. For a first modeling approach, only the SV velocities have been used.

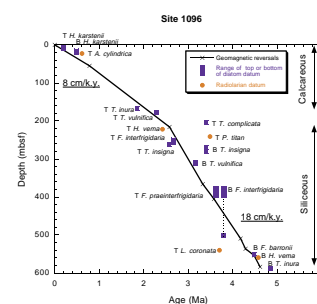
Source Signals

The digital far-field signal of the Generator Injector air gun and a sea-floor reflection have been used for convolution with the reflectivity coefficient series (see “[Seismic Stratigraphy](#),” p. 33, in the “Site 1095” chapter).

Time-Depth Functions

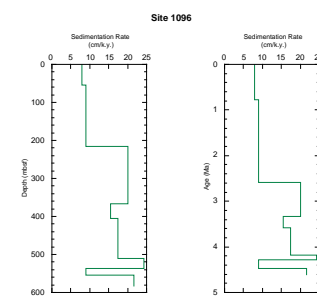
Both velocity data sets have been used to produce time-depth curves (Fig. F57). The SV and MST time-depth relationships are compared with the Carlson et al. (1986) standard time-depth relationship and with the

F53. Depth-age relationship for Site 1096 based on geomagnetic reversals, biostratigraphic diatom ranges, and radiolarian datums, p. 92.



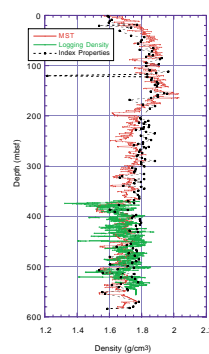
T33. Depths of geomagnetic polarity transitions and diatom and radiolarian datum events at Site 1096, p. 142.

F54. Sedimentation rates vs. depth and age, p. 93.



T34. Depths of geomagnetic reversals for Site 1096, p. 143.

F55. Comparison of MST, down-hole logging, and index properties densities, Site 1096, p. 94.



polynomial regression of Site 1095 vertical seismic profile data. In spite of sedimentation rates about three times higher at Site 1096, there is a substantial similarity between the three data sets, which support a model in which the velocity-depth relationship is dominated by compaction. Nevertheless, a less-pronounced curvature of the time-depth curve of Site 1096 may reflect undercompaction (see also “[Physical Properties](#),” p. 21).

Synthetic Seismograms

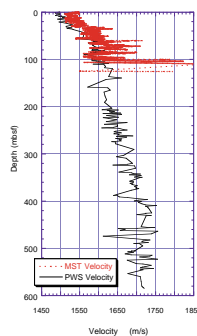
The raw velocity and density data were reviewed and cleaned. Only four and one data points, respectively, were removed from the SV and index properties data sets. The generation of a complete synthetic seismic trace using index properties densities and SV velocities for Site 1096 is depicted in Figure F58. In general, there is a positive correlation between the density and velocity curves. The two data sets were adjusted to the same length and sample interval using a linear interpolation. After applying a 5-point moving average filter, the data were again subsampled with a 1.5-m spacing to provide better contrast between adjacent impedance values. Two unfiltered synthetic traces (one for the far-field wavelet and one for the seafloor reflection) are displayed in Figure F58.

Correlation of the Synthetic Seismogram and Digital Traces of Survey Line IT95-130

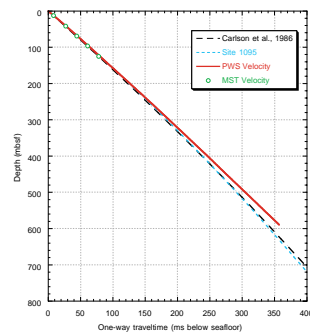
All four calculated synthetic traces were interpolated to a 1-ms resolution (1000 Hz) and subsequently filtered using a high-order, zero-phase equi-ripple band-pass filter (pass band = 20–110 Hz; attenuation = 60–70 dB; filter order = 170–220). Five of these traces are shown together with 42 traces of the field seismic profile in Figures F59 and F60. A zero-phase Butterworth band-pass filter (pass band = 10–110 Hz) and a 150-ms automatic gain recovery window were applied to the sorted and stacked data set. Additionally, the total time window and the delay were reduced, and the 2-ms field data were interpolated to 1 ms to fit the time resolution of the synthetic trace. The optimal filter parameters were adjusted to values used during the actual processing of the seismic survey data. Different amounts of time-invariant gain were applied to equalize the overall amplitude appearance of the field and synthetic traces.

The synthetic and survey traces correlate only in the lower and middle parts. Correlation of the synthetic and the survey traces allows the time equivalent of the total penetration depth to be determined (700 ms TWT below seafloor). A unique zone of reflectors occurs at ~150 ms, which is not represented in the synthetic traces. At its base lie three closely spaced wiggles with positive amplitudes and a 50-ms transparent interval. Timewise, this section could be correlated with an upper BSR (Fig. F61) visible below the scarp slope of the drift to the southwest. However, this reflector cannot be associated with a gas hydrate stability zone (see “[Physical Properties](#),” p. 21). In Figure F61, the boundaries of the major seismostratigraphic units are correlated with the major lithostratigraphic units.

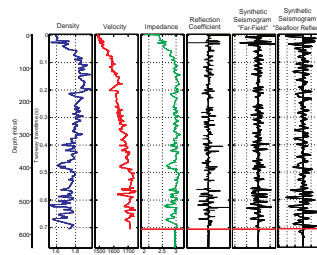
F56. Comparison of MST and PWS P-wave velocities, Site 1096, p. 95.



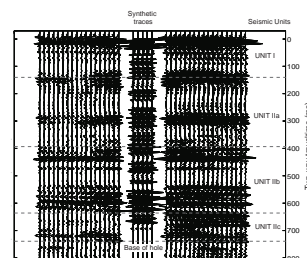
F57. Traveltime depth models for Site 1096 compared with Site 1095 and Carlson approximation, p. 96.



F58. Site 1096 synthetic seismograms and corresponding density/velocity model, p. 97.



F59. Site 1096 synthetic seismogram (using far-field wavelet) and field survey traces, p. 98.



Seismic Units

Seismic units defined at Site 1095 have been traced across the MCS profiles to Site 1096 in a preliminary way. Changes in the seismic character and thickness of the different units from the distal (Site 1095) to the proximal (Site 1096) parts of the sediment drift are noted below. Drilling at Site 1096 reached a depth of 607 mbsf and probably penetrated seismic Unit I and Subunits IIa, IIb, and IIc, previously defined at Site 1095.

Seismic Unit I (0–110 mbsf)

In the MCS profiles, the top 80 m of seismic Unit I consists of parallel and subparallel high-amplitude and continuous reflectors (Fig. F61). The sub-bottom 3.5-kHz seismic profile, obtained during the site approach, penetrated the upper 60 m of seismic Unit I. This profile shows reflector packages with a marked cyclic variation of amplitude (Fig. F4). The lower part of seismic Unit I, as imaged in MCS profiles, consists of lower amplitude continuous reflectors that alternate with disrupted and transparent reflectors (Fig. F61). Although the overall external geometry of seismic Unit I at Site 1096 is of a sheet drape, changes in thickness occur in directions parallel and perpendicular to the margin. From the distal part of the drift at Site 1095 to the proximal part at Site 1096, there is an increase in thickness of this younger sequence of ~50 m. In a direction parallel to the continental margin, thickness increases from 100 m at the crest of the drift to 150 m at the base of the gentler flank.

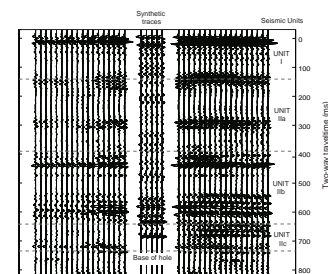
Seismic Unit II (110 to >607 mbsf)

At Site 1096, it seems likely that only three of the five seismic sub-units defined at Site 1095 were drilled. Subunit IIa (110–316 mbsf) is characterized by parallel and subparallel low-amplitude to transparent reflectors (Fig. F61). The acoustic character corresponds to low-amplitude traces in the synthetic seismogram (Fig. F59). Thickness of Subunit IIa increases considerably from Site 1095 to Site 1096. In a direction parallel to the margin, thickness decreases toward the base of the gentler flank of the drift where reflectors are partly truncated by channel cutting. The base of Subunit IIa is marked by a reflector with moderate amplitude, which correlates with a higher amplitude reflector of the synthetic seismogram (Fig. F59). Subunit IIb (316–519 mbsf) consists of a package of high-amplitude and continuous reflectors that correspond to a series of high-amplitude reflectors in the synthetic seismogram (Fig. F59). The thickness of Subunit IIb appears to change from 40 m at Site 1095 to ~200 m at Site 1096. In a direction parallel to the margin, Subunit IIb increases in thickness to the southwest, where reflectors diverge below the crest of the drift. Subunit IIc (519–>607 mbsf) is the lowest seismic unit penetrated at this site. This subunit is bounded by two high-amplitude reflectors. Reflectors within this subunit are rare at the site but are present below the crest of the drift where the subunit thickens (Fig. F61).

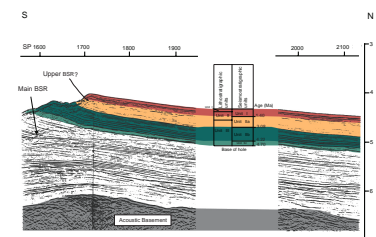
Interpretation

Several general observations can be made from the seismic profile across Site 1096.

F60. Site 1096 synthetic seismogram (using seafloor reflection wavelet) and field survey traces, p. 99.



F61. Integration of seismic reflection profile IT92-109 with seismic-stratigraphic and lithostratigraphic units, p. 100.



Seismic Unit I comprises lithostratigraphic Unit I and the upper half of lithostratigraphic Unit II (see “[Lithostratigraphy](#),” p. 4). Lithostratigraphic Unit I (0–33 mbsf) is characterized by a well-defined alternation of biogenic-rich and terrigenous horizons. This cyclic pattern can be recognized in the sub-bottom 3.5 kHz profile (Fig. [F4](#)). Lithostratigraphic Unit II (33–172 mbsf) is characterized by a repetitive succession of laminated and massive facies. Seismic Subunits IIa, IIb, and IIc include the lower half of lithostratigraphic Unit II and the whole of lithostratigraphic Unit III. Lithostratigraphic Unit III (172 to 607.7 mbsf) is an alternation of laminated turbidite contourite facies and bioturbated hemipelagic facies. A possible BSR at 170 ms TWT (~125 mbsf) near shotpoint 1710 on profile IT92-109 (Fig. [F61](#)) cannot be attributed to the base of the hydrate stability zone, which lies at ~340 m (see “[Physical Properties](#),” p. 21).

The increase in thickness of units between Site 1095 and Site 1096 indicates an expanded section in Site 1096, in accord with the higher sedimentation rates (see “[Sedimentation Rates](#),” p. 30). External geometry (mainly sheet drape) and regular reflection patterns of the seismic units at Site 1096 suggest sedimentation from turbidity currents, weak bottom currents, and hemipelagic deposition. The observed change in thickness of seismic Unit I toward the northeast channel is compatible with its being a major sediment source during a “drift maintenance” stage (Rebesco et al., 1996, 1997). The increased thickness toward the southwest of sediments below Unit IIb is a feature of the earlier “drift growth” stage. The considerable thickening of sedimentary units from Site 1095 to 1096 supports the view that the terrigenous component originates at the nearby continental margin.

The ages assigned to the seismic units recognized at Site 1096 (Table [T35](#); Fig. [F61](#)) are based on preliminary paleomagnetic data from drilled cores (see “[Paleomagnetism](#),” p. 15). Seismic Unit I is Pleistocene in age (0–1.4 Ma). The rest of the drilled sediments are early Pleistocene and Pliocene in age (1.4–4.7 Ma).

T35. TWT and depth to base of seismic units at Site 1096, [p. 144](#).

REFERENCES

- Alonso, B., and Maldonado, A., 1990. Late Quaternary sedimentation of the Ebro turbidite systems (Northwestern Mediterranean): two styles of deep-sea deposition. *Mar. Geol.*, 95:353–377.
- Baker, P.A., and Kastner, M., 1981. Constraints on the formation of sedimentary dolomite. *Science*, 213:215–216.
- Barker, P.F., 1982. The Cenozoic subduction history of the Pacific margin of the Antarctic Peninsula: ridge crest-trench interactions. *J. Geol. Soc. London*, 139:787–801.
- Barron, J., Larsen, B., et al., 1991. *Proc. ODP, Init. Repts.*, 119: College Station (Ocean Drilling Program).
- Beaufort, L., and Aubry, M.-P., 1992. Paleoceanographic implications of a 17-m.y.-long record of high-latitude Miocene calcareous nannoplankton fluctuations. In Wise, S.W., Jr., Schlich, R., et al., *Proc. ODP, Sci. Results*, 130: College Station, TX (Ocean Drilling Program), 539–549.
- Berggren, W.A., Kent, D.V., Swisher, C.C., III, and Aubry, M.-P., 1995. A revised Cenozoic geochronology and chronostratigraphy. In Berggren, W.A., Kent, D.V., Aubry, M.-P., and Hardenbol, J. (Eds.), *Geochronology, Time Scales and Global Stratigraphic Correlation*. Spec. Publ.—Soc. Econ. Paleontol. Mineral. (Soc. Sediment. Geol.), 54:129–212.
- Brumsack, H.J., and Gieskes, J.M., 1983. Interstitial water trace element chemistry of laminated sediments from the Gulf of California, Mexico. *Marine Chem.*, 14: 89–106.
- Bryant, W.R., and Rack, F.R., 1990. Consolidation characteristics of Weddell Sea sediments: results of ODP Leg 113. In Barker, P.F., Kennett, J.P., et al., *Proc. ODP, Sci. Results*, 113: College Station, TX (Ocean Drilling Program), 211–223.
- Camerlenghi, A., Rebisco, M., and Pudsey, C.J., 1997. High resolution terrigenous sedimentary record of the sediment drifts on the Antarctic Peninsula Pacific margin. In Ricci, C.A. (Ed.), *The Antarctic Region: Geological Evolution and Processes*. Init. Results, SEDANO Progr., *Terra Antarct.*, 705–710.
- Cande, S.C., and Kent, D.V., 1995. Revised calibration of the geomagnetic polarity timescale for the Late Cretaceous and Cenozoic. *J. Geophys. Res.*, 100:6093–6095.
- Carlson, R.L., Gangi, A.F., and Snow, K.R., 1986. Empirical reflection travel time versus depth and velocity versus depth functions for the deep-sea sediment column. *J. Geophys. Res.*, 91:8249–8266.
- Dymond, J., Suess, E., and Lyle, M., 1992. Barium in deep-sea sediment: a geochemical proxy for paleoproductivity. *Paleoceanography*, 7:163–181.
- Ehrmann, W.U., and Grobe, H., 1991. Cyclic sedimentation at Sites 745 and 746, Leg 119. In Barron, J., Larsen, B., et al., *Proc. ODP, Sci. Results*, 119: College Station, TX (Ocean Drilling Program), 225–238.
- Ehrmann, W.U., Grobe, H., and Fütterer, D.K., 1991. Late Miocene to Holocene glacial history of East Antarctica as revealed by sediments from Sites 745 and 746. In Barron, J., Larsen, B., et al., *Proc. ODP, Sci. Results*, 119: College Station, TX (Ocean Drilling Program), 239–262.
- Gersonde, R., and Bárcena, M.A., 1998. Revision of the late Pliocene–Pleistocene diatom biostratigraphy for the northern belt of the Southern Ocean. *Micropaleontology*, 44:1–15.
- Gieskes, J.M., and Lawrence, J.R., 1976. Interstitial water studies, Leg 35. In Hollister, C.D., Craddock, C., et al., *Init. Repts. DSDP*, 35: Washington (U.S. Govt. Printing Office), 407–426.
- Gonthier, E.G., Faugeres, J.C., and Stow, D.A.V., 1984. Contourite facies of the Faro Drift, Gulf of Cadiz. In Stow, D.A.V., and Piper, D.J.W. (Eds.), *Fine-Grained Sediments: Deep Water Processes and Facies*: Geol. Soc. Spec. Publ. London, 15:275–292.
- Harwood, D.M., and Maruyama, T., 1992. Middle Eocene to Pleistocene diatom biostratigraphy of Southern Ocean sediments from the Kerguelen Plateau, Leg 120. In

- Wise, S.W., Jr., Schlich, R., et al., *Proc. ODP, Sci. Results*, 120: College Station, TX (Ocean Drilling Program), 683–733.
- Heirtzler, J.R., Dickson, G.O., Herron, E.M., Pitman, W.C. III, and Le Pichon, X., 1968. Marine magnetic anomalies, geomagnetic field reversals, and motions of the ocean floor and continents. *J. Geophys. Res.*, 73:2119–2136.
- Hutchison, I., 1985. The effect of sedimentation and compaction on oceanic heat flow. *Geophys. J. R. Astron. Soc.*, 82:439–459.
- Jahnke, R.A., Emerson, S.R., Roe, K.K., and Burnett, W.C., 1983. The present day formation of apatite in Mexican continental margin sediments. *Geochim. Cosmochim. Acta*, 47:259–266.
- Kastner, M., Keene, J.B., and Gieskes, J.M., 1977. Diagenesis of siliceous oozes, I. Chemical controls on the rate of opal-A to opal-CT transformation—an experimental study. *Geochim. Cosmochim. Acta*, 41:1041–1059.
- Lawrence, J.R., Gieskes, J.M., and Broecker, W.S., 1975. Oxygen isotope and cation composition of DSDP pore water and the alteration of layer II basalts. *Earth Planet. Sci. Lett.*, 27:1–10.
- McDuff, R.E., 1985. The chemistry of interstitial waters, Deep Sea Drilling Project Leg 86. In Heath, G.R., Burckle, L.H., et al., *Init. Repts. DSDP*, 86: Washington (U.S. Govt. Printing Office), 675–687.
- Parsons, B., and Sclater, J.G., 1977. An analysis of the variation of ocean floor bathymetry and heat flow with age. *J. Geophys. Res.*, 82:803–827.
- Paull, C.K., Chanton, J.P., Neumann, A.C., Coston, J.A., Martens, C.S., and Showers, W., 1992. Indicators of methane-derived carbonates and chemosynthetic organic carbon deposits: examples from the Florida Escarpment. *Palaios*, 7:361–375.
- Perry, E.A., Jr., Gieskes, J.M., and Lawrence, J.R., 1976. Mg, Ca and O¹⁸/O¹⁶ exchange in the sediment-pore water system, Hole 149, DSDP. *Geochim. Cosmochim. Acta*, 40:413–423.
- Pickering, K.T., Hiscott, R., and Hein, F.J., 1989. *Deep-marine Environments: Clastic Sedimentation and Tectonics*: London (Unwin Hyman).
- PPSP, 1992. Ocean drilling program guidelines for pollution prevention and safety. *JOIDES J.*, 18:1–24.
- Pudsey, C.J., and Camerlenghi, A., 1998. Glacial-interglacial deposition on a sediment drift on the Pacific margin of the Antarctic Peninsula. *Antarct. Sci.*, 10:286–308.
- Pujol, C., and Bourrouilh, R., 1991. Late Miocene to Holocene planktonic foraminifers from the subantarctic South Atlantic. In Ciesielski, P.F., Kristoffersen, Y., et al., *Proc. ODP, Sci. Results*, 114: College Station, TX (Ocean Drilling Program), 217–232.
- Rebesco, M., Camerlenghi, A., and Zanolla, C., in press. Bathymetry and morphogenesis of the continental margin west of the Antarctic Peninsula. *Terra Antarct.*
- Rebesco, M., Larter, R.D., Barker, P.F., Camerlenghi, A., and Vanneste, L.E., 1997. The history of sedimentation on the continental rise west of the Antarctic Peninsula. In Barker, P.F., and Cooper, A.K. (Eds.), *Geology and Seismic Stratigraphy of the Antarctic Margin* (Pt. 2). Am. Geophys. Union, Antarctic Res. Ser., 71:29–50.
- Schuffert, J.D., Jahnke, R.A., Kastner, M., Leather, J., Sturz, A., and Wing, M.R., 1994. Rates of formation of modern phosphorite off western Mexico. *Geochim. Cosmochim. Acta*, 58:5001–5010.
- Shipboard Scientific Party, 1999. Explanatory notes. In Gersonde, R., Hodell, D.A., Blum, P., et al., *Proc. ODP, Init. Repts.*, 177, 1–57 [CD-ROM]. Available from: Ocean Drilling Program, Texas A&M University, College Station, TX 77845-9547 U.S.A.
- Skempton, A.W., 1970. The consolidation of clays by gravitational compaction. *Q. J. Geol. Soc. London*, 125:373–411.
- Stow, D.A.V., and Piper, D.J.W., 1984. Deep-water fine-grained sediments: facies models. In Stow, D.A.V., and Piper, D.J.W. (Eds.), *Fine-Grained Sediments: Deep-Water Processes and Facies*. Geol. Soc. Spec. Publ. London, 15:611–645.

- Stow, D.A.V., and Wetzel, A., 1990. Hemiturbidite: a new type of deep-water sediment. In Cochran, J.R., Stow, D.A.V., et al., *Proc. ODP, Sci. Results*, 116: College Station, TX (Ocean Drilling Program), 25–34.
- von Breymann, M.T., Emeis, K.-C., and Camerlenghi, A., 1990. Geochemistry of sediments from the Peru upwelling area: results from Sites 680, 682, 685, and 688. In Suess, E., von Huene, R., et al., *Proc. ODP, Sci. Results*, 112: College Station, TX (Ocean Drilling Program), 491–503.

Figure F1. A. Bathymetric map (from Rebesco et al., *in press*) showing the main morphologic elements of Drifts 6 and 7 and the adjacent continental slope. Thin lines indicate the location of site-survey MCS reflection profiles. The box around Site 1096 refers to Figure **F1B**, p. 39. (Continued on next page.)

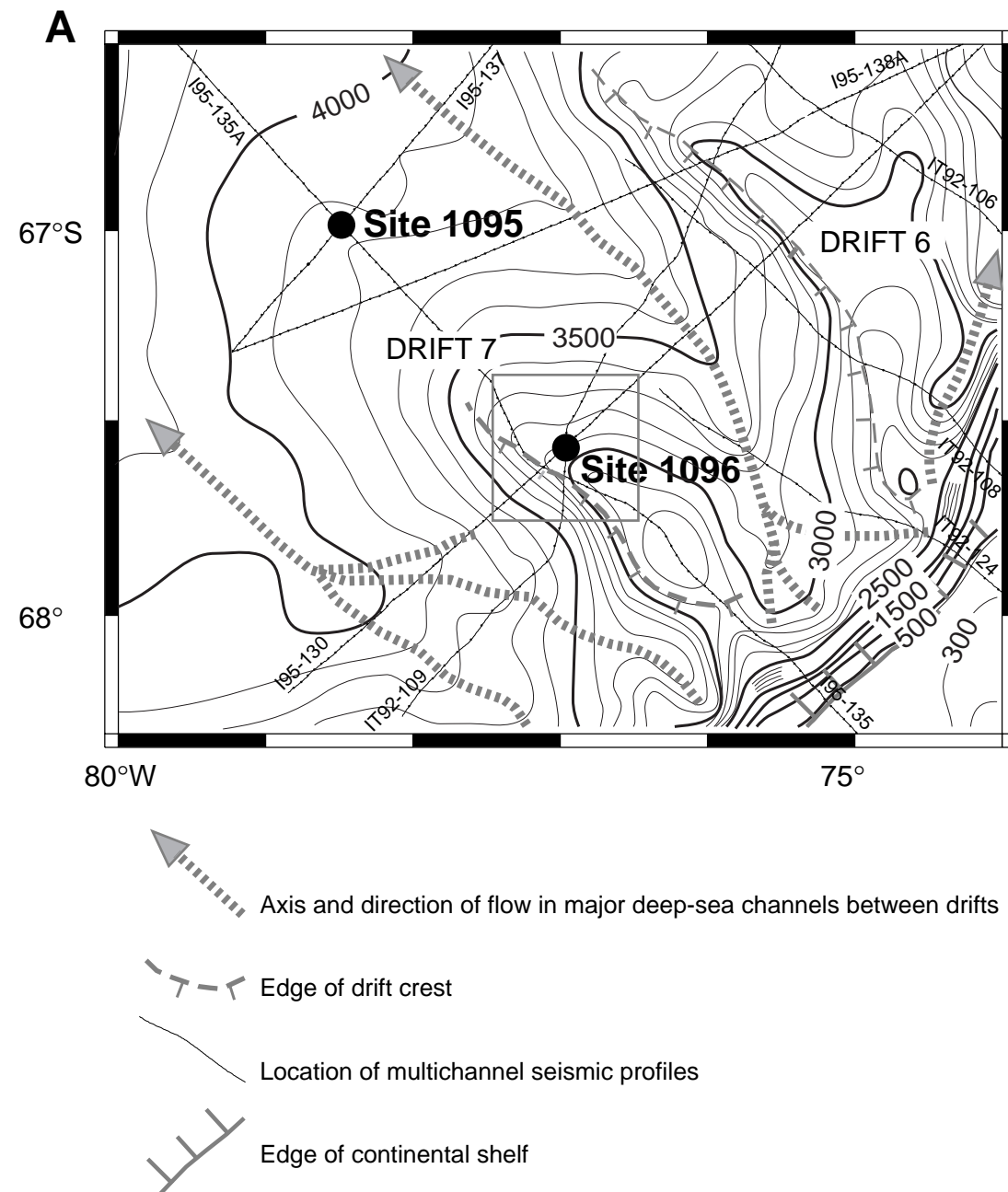


Figure F1 (continued). B. Location of Site 1096 on two crossing MCS reflection profiles (I95-130A and IT92-109) and the 3.5-kHz profile (bold line) acquired to locate the site after transit from Site 1095. See Figure F1, p. 43, in the "Site 1095" chapter, for location of this map.

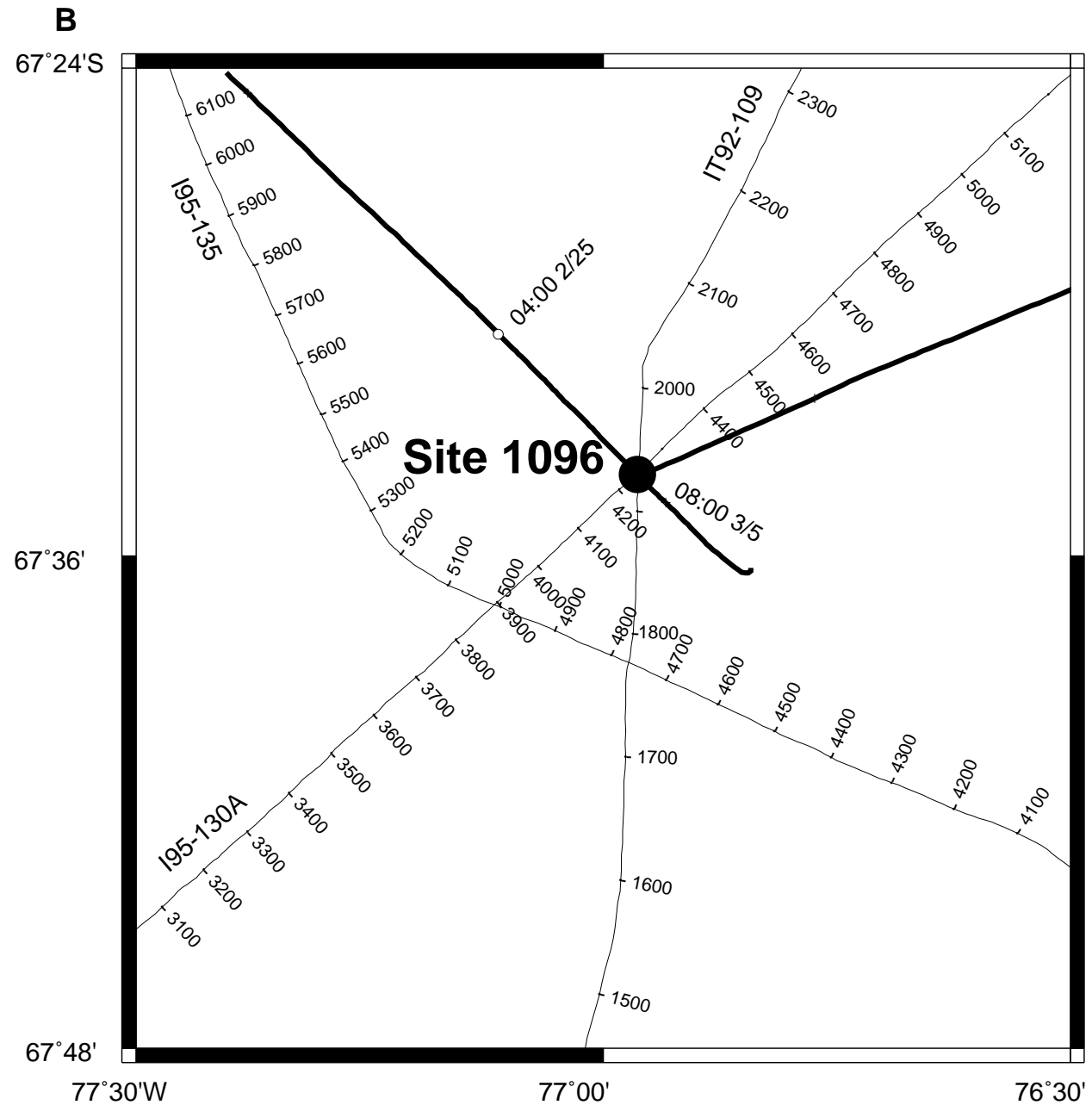


Figure F2. The 3.5-kHz sub-bottom profile across Site 1096, acquired during site approach (Fig. F1B, p. 39). The site is located on the gentle northwest flank of Drift 7 (note the strong vertical exaggeration of the profile). Bedding in the upper 40 m is parallel to the seafloor, and three similar beds, each ~12 m thick, are evident in the upper 35–40 m. A deeper weak reflector can be traced as deep as 80 ms two-way traveltime (TWT).

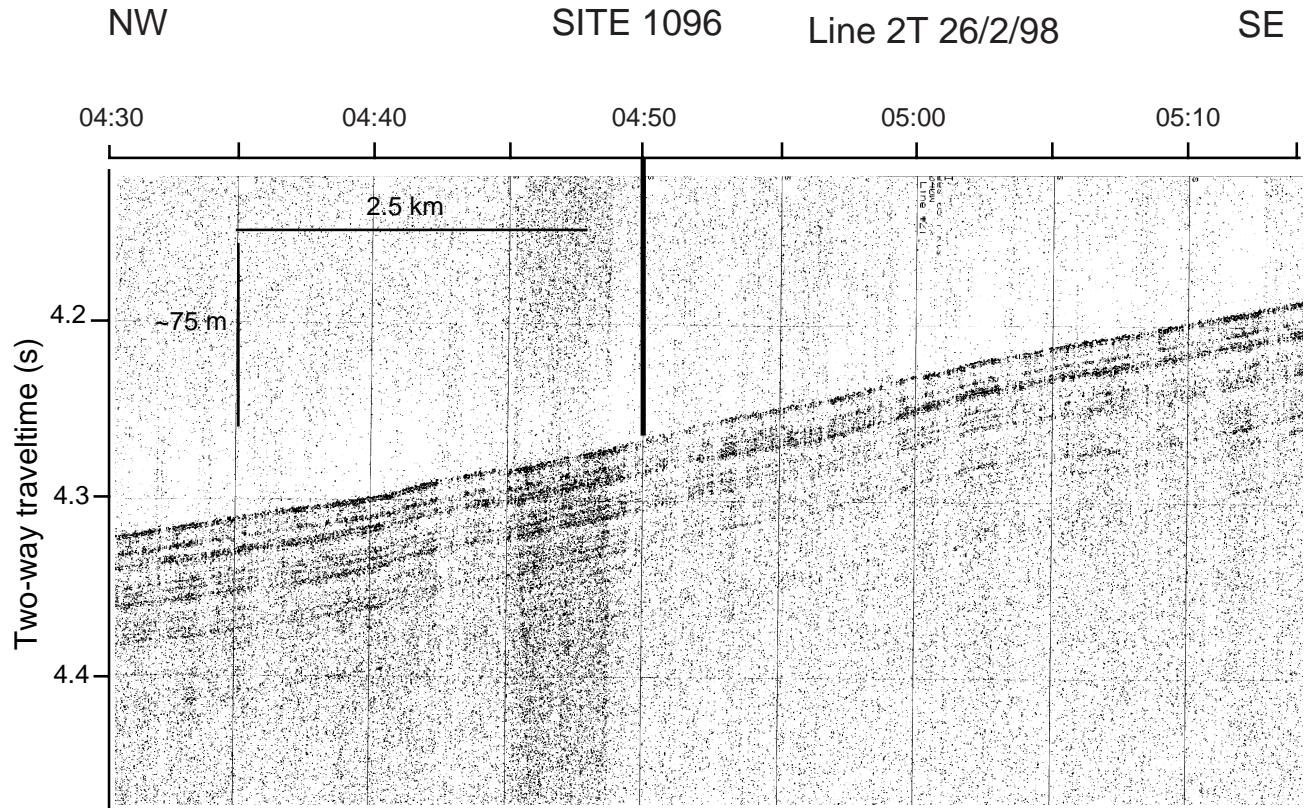


Figure F3. Magnetic total-field profile collected during transit between Sites 1095 and 1096. Identified magnetic anomalies show that basement age at Site 1095 is 42.7 Ma and at Site 1096 is 36.7 Ma (time scale of Cande and Kent, 1995).

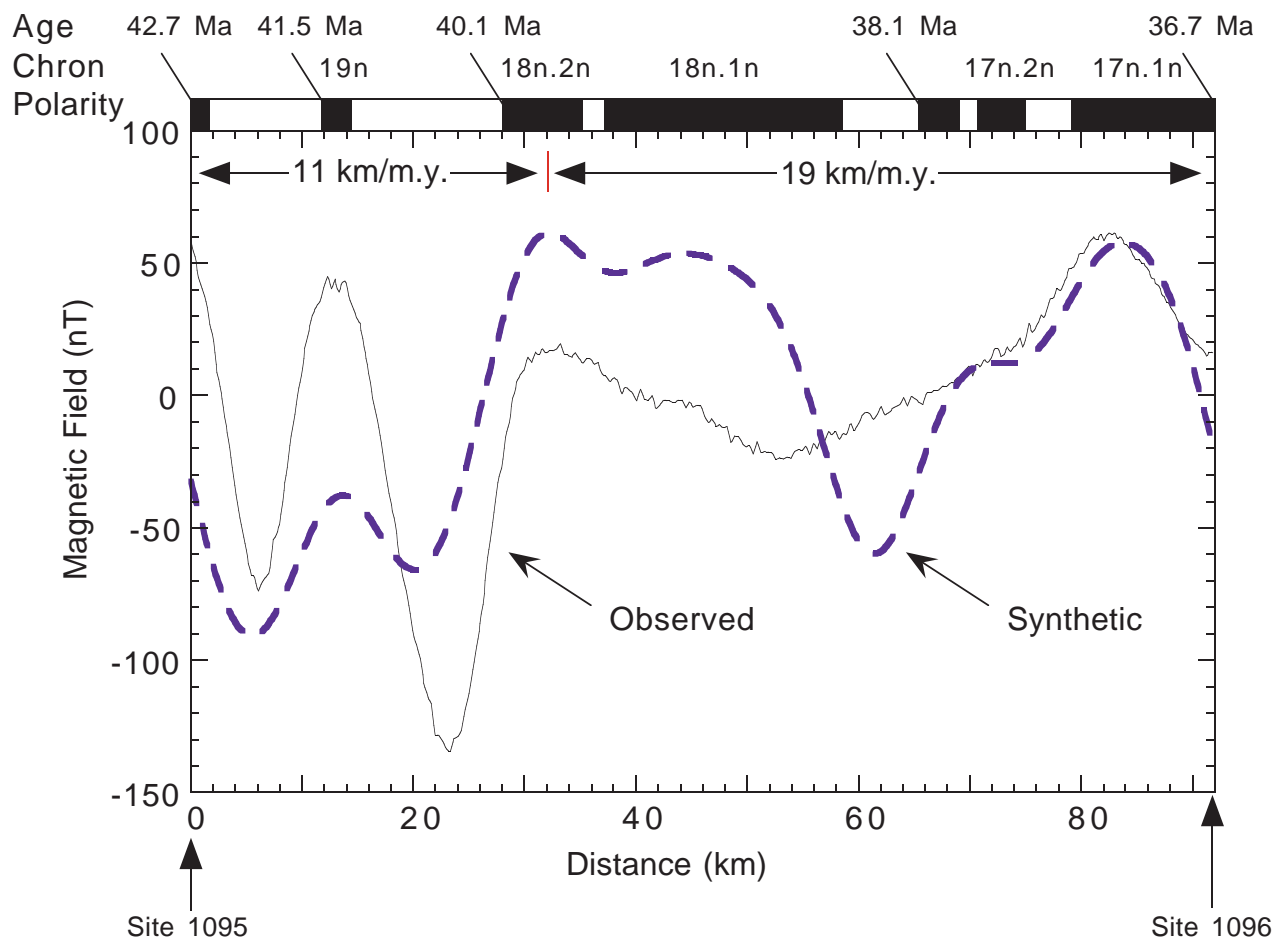


Figure F4. Part of MCS reflection profile I95-130A across Site 1096 (see location in Fig. F1, p. 38; also see Fig. F1A, p. 43, in the "Site 1095" chapter). Note the BSR at ~700 ms TWT below the seafloor, interpreted as the opal-A to opal-CT transition.

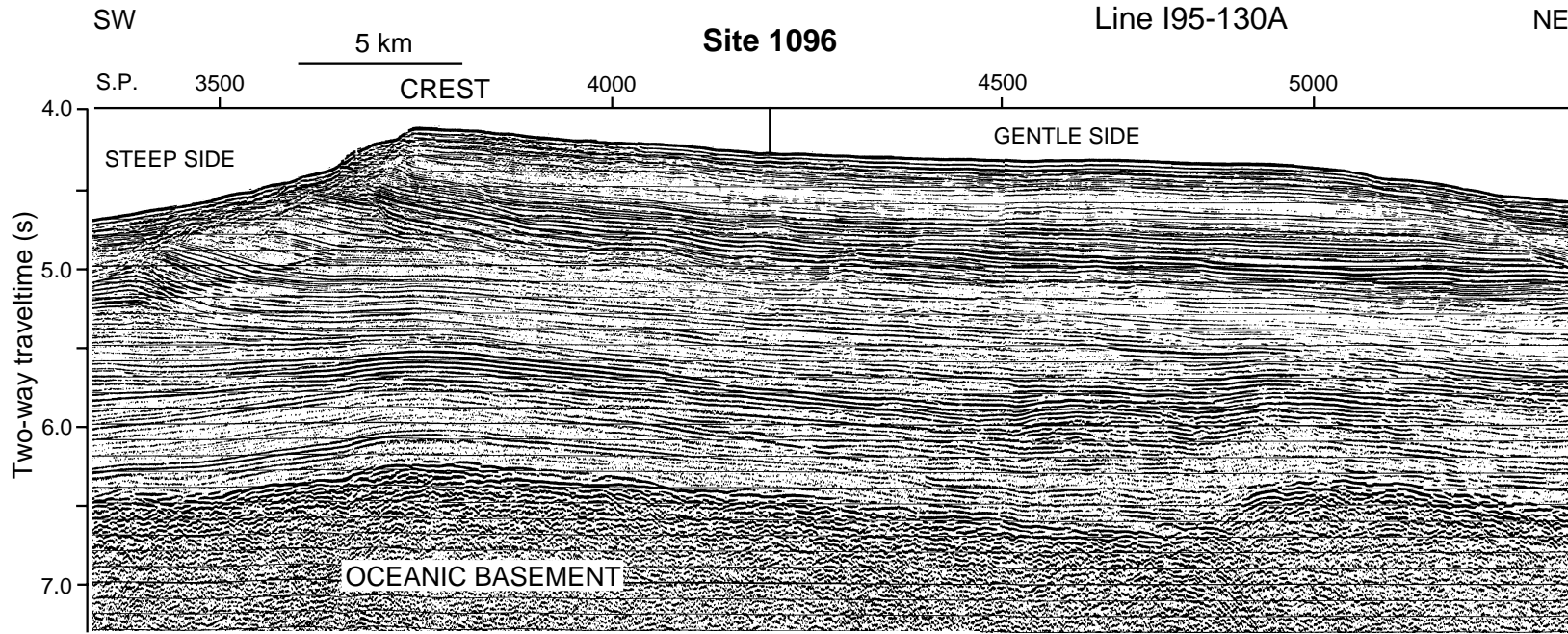


Figure F5. Lithostratigraphy at Site 1096: facies, biogenic content, chromaticity parameter a^* , and magnetic susceptibility. In Unit II, the laminated facies includes L₂ and L₃; in Unit III, L₃ only. Thin arrows in Unit II represent coarsening-upward sequences. T.D. = total depth. (Continued on next page.)

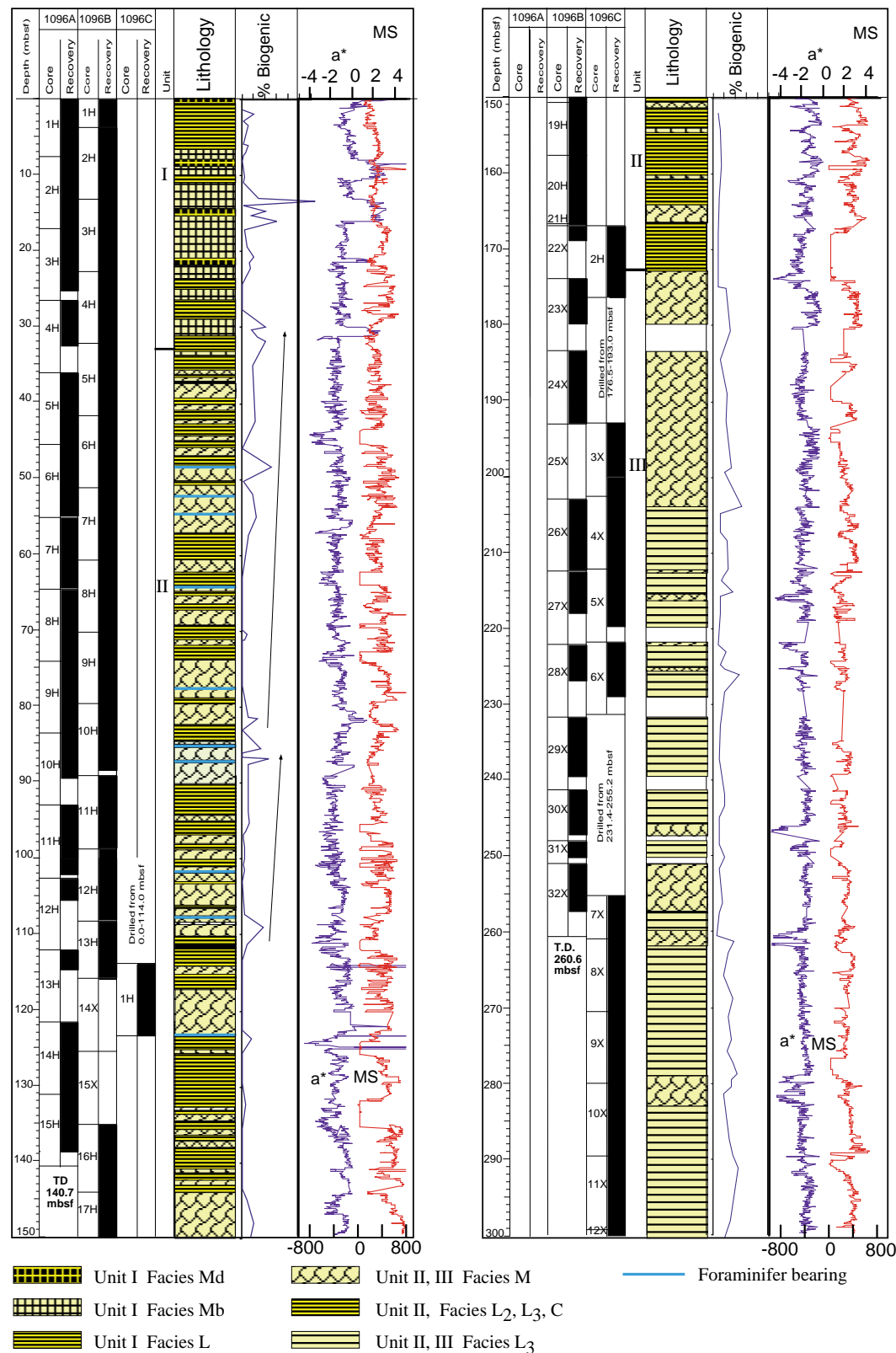


Figure F5 (continued).

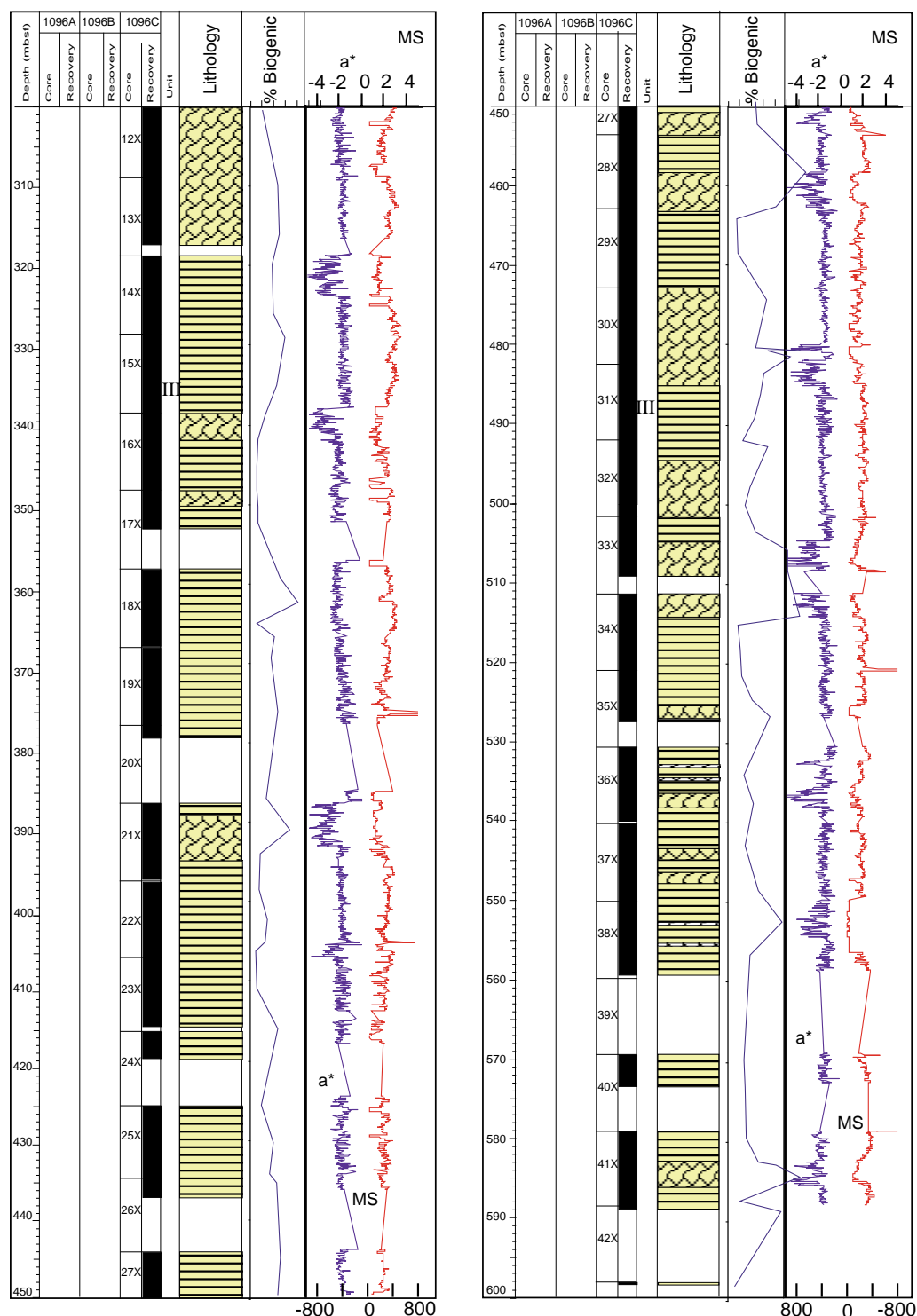


Figure F6. Lithology of Unit I and correlation with color and magnetic susceptibility data. Silt thicknesses exaggerated. The Unit I/II boundary is marked by a downward increase in high-frequency variability of magnetic susceptibility.

Leg 178 Hole 1096B

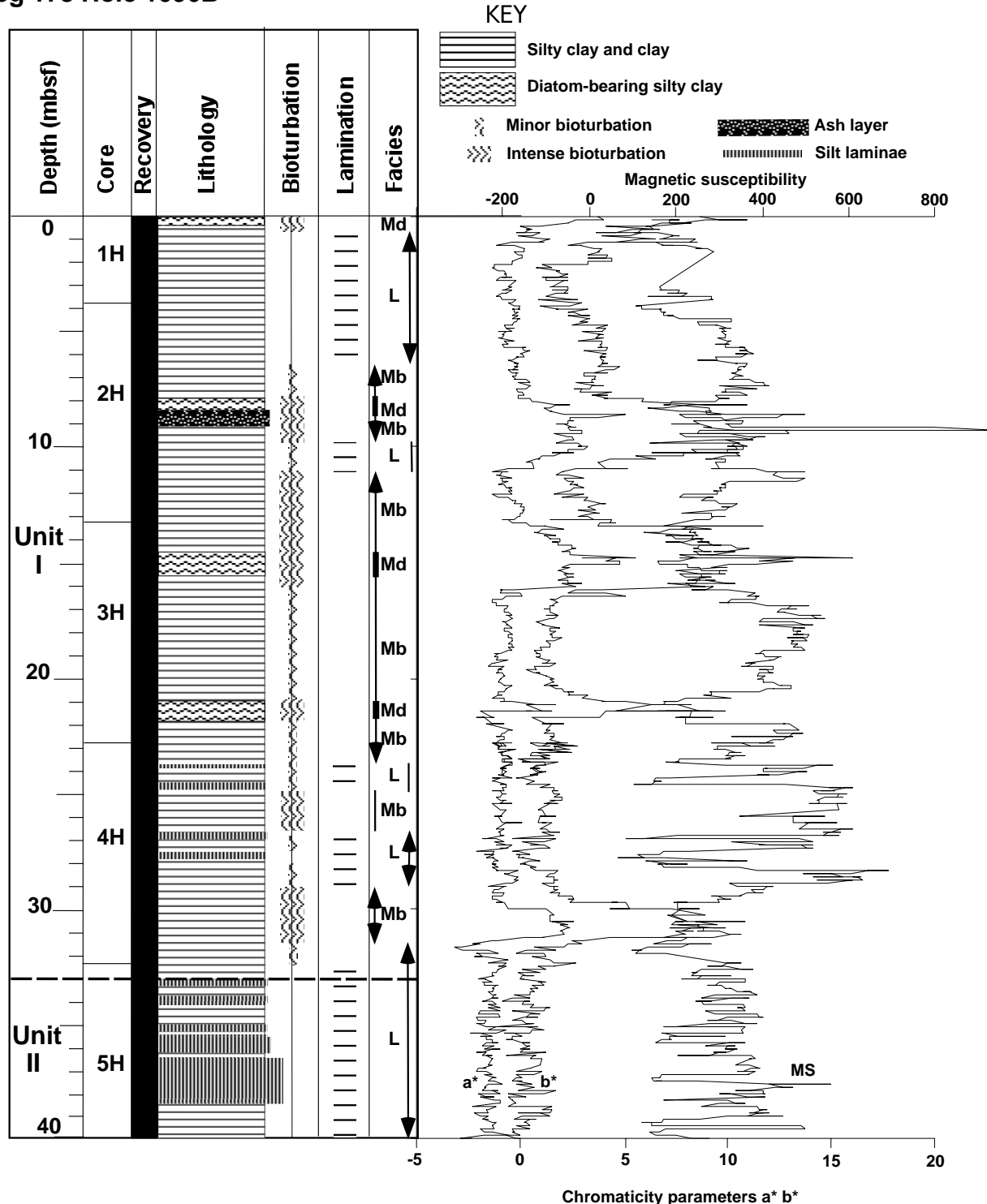


Figure F7. Facies Md in Unit I; olive brown diatomaceous silty clay, intensely mottled by burrows, with scattered sand grains and granules (interval 178-1096A-2H-6, 59–110 cm).

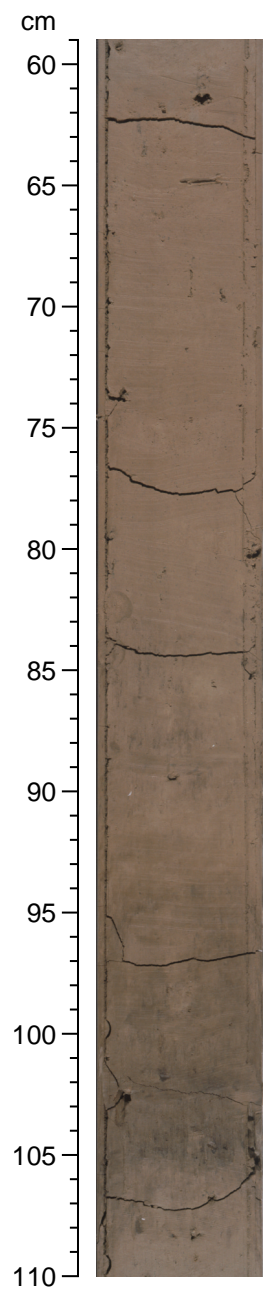


Figure F8. Facies L in Unit I; dark gray clay with millimeter-scale lamination and few small burrows (interval 178-1096A-1H-3, 110–132 cm).

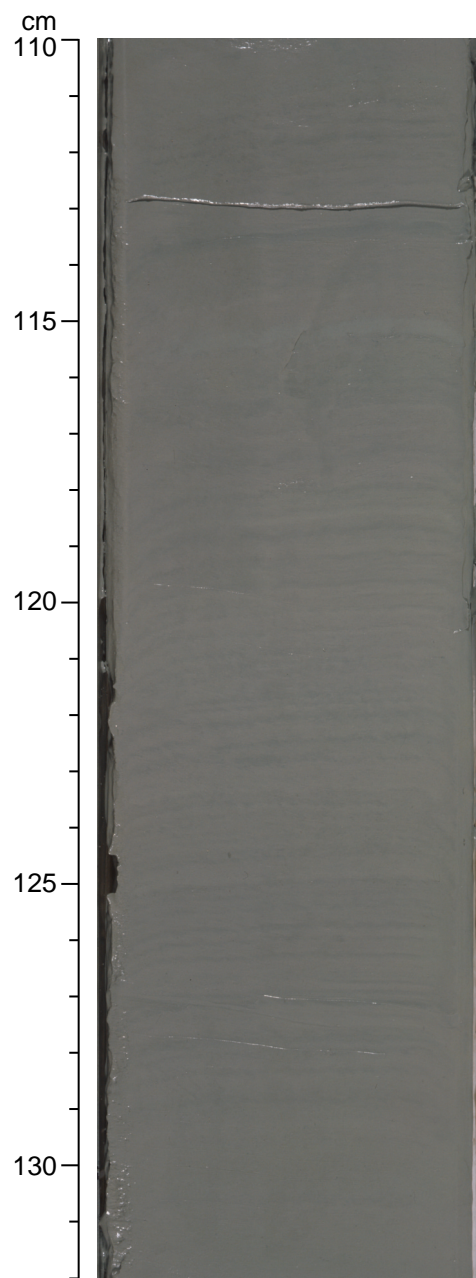


Figure F9. Descriptive scheme used for muddy turbidite Facies L₂ and L₃ (see also Fig. F3, p. 39, in the “Explanatory Notes” chapter, and Fig. F11, p. 57, in the “Site 1095” chapter). Intervals of L₂ and L₃ have sharp bases; tops are gradational to Facies C or Facies M.

LAMINATED FACIES L2 AND L3

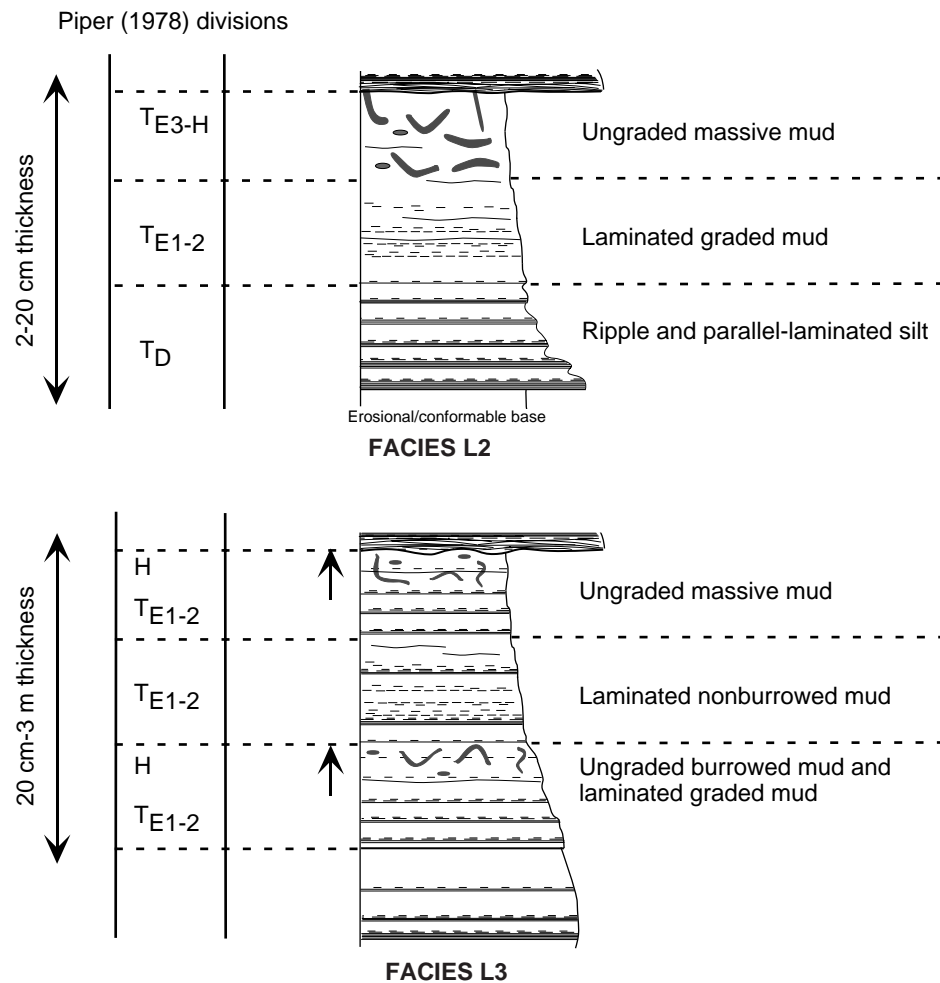


Figure F10. Muddy turbidite Facies L₂ (interval 178-1096B-11H-5, 100–130 cm) in Unit II. The turbiditic mud between the silt laminae is darker in color than the hemipelagic mud below 122.5 cm.

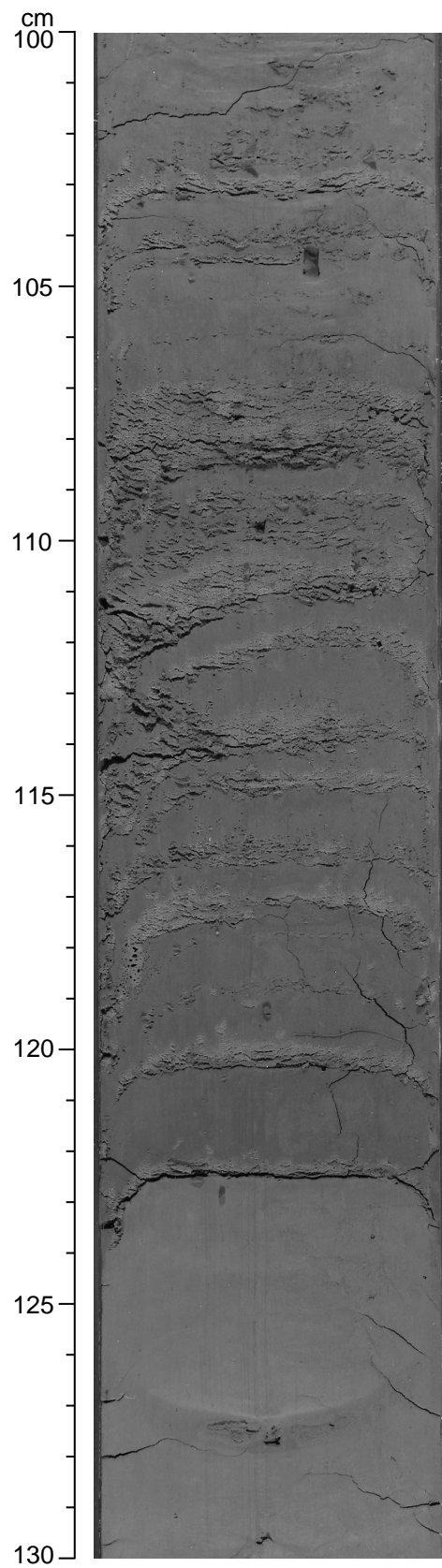


Figure F11. Silty clay (Facies C) in Unit II showing diffuse, poorly defined lamination with irregular, discontinuous silt laminae (between 42 and 43 cm and at 38 cm) and mottled bioturbated texture (interval 178-1096B-13H-4, 30–50 cm).

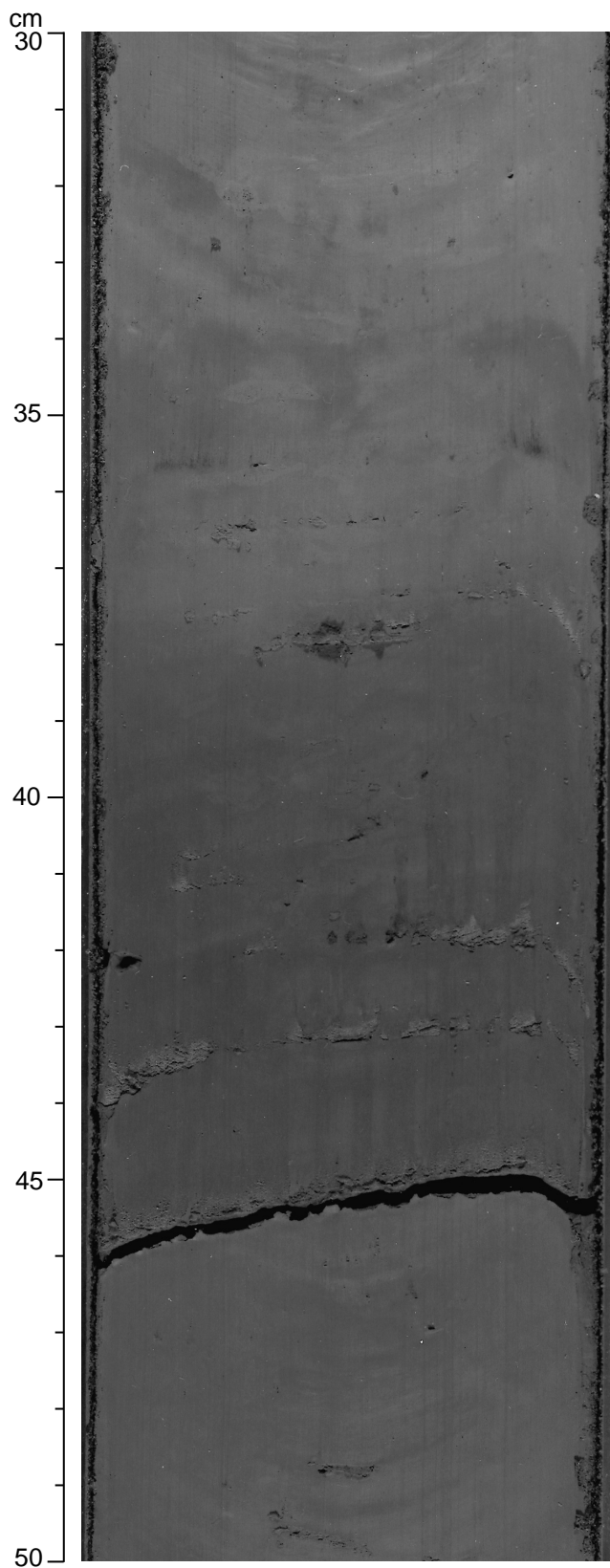


Figure F12. Schematic drawing of contourite facies (C) from Unit II. Facies C usually has gradational boundaries with Facies M or L₃.

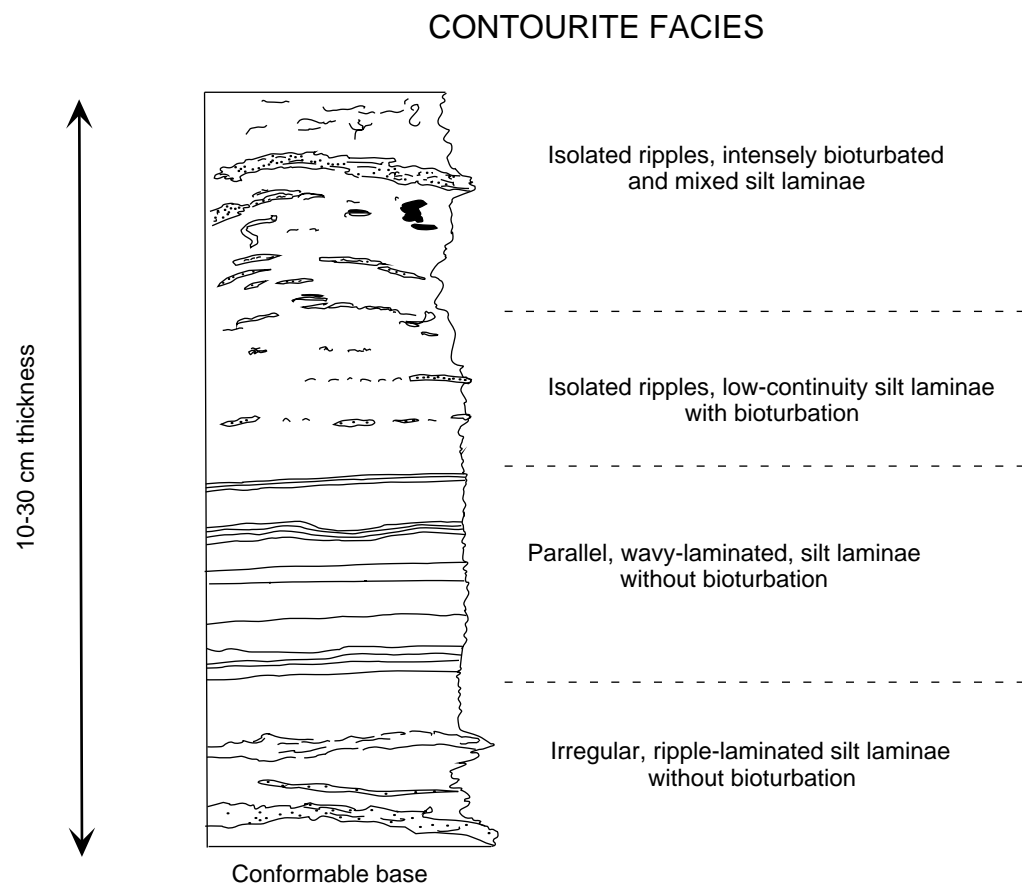


Figure F13. Facies M in Unit II: silty clay coarsening upward to foraminifer-bearing silty mud. Dispersed ice rafted debris up to granule size from 90 to 99 cm (interval 178-1096B-10H-5, 90–110 cm).

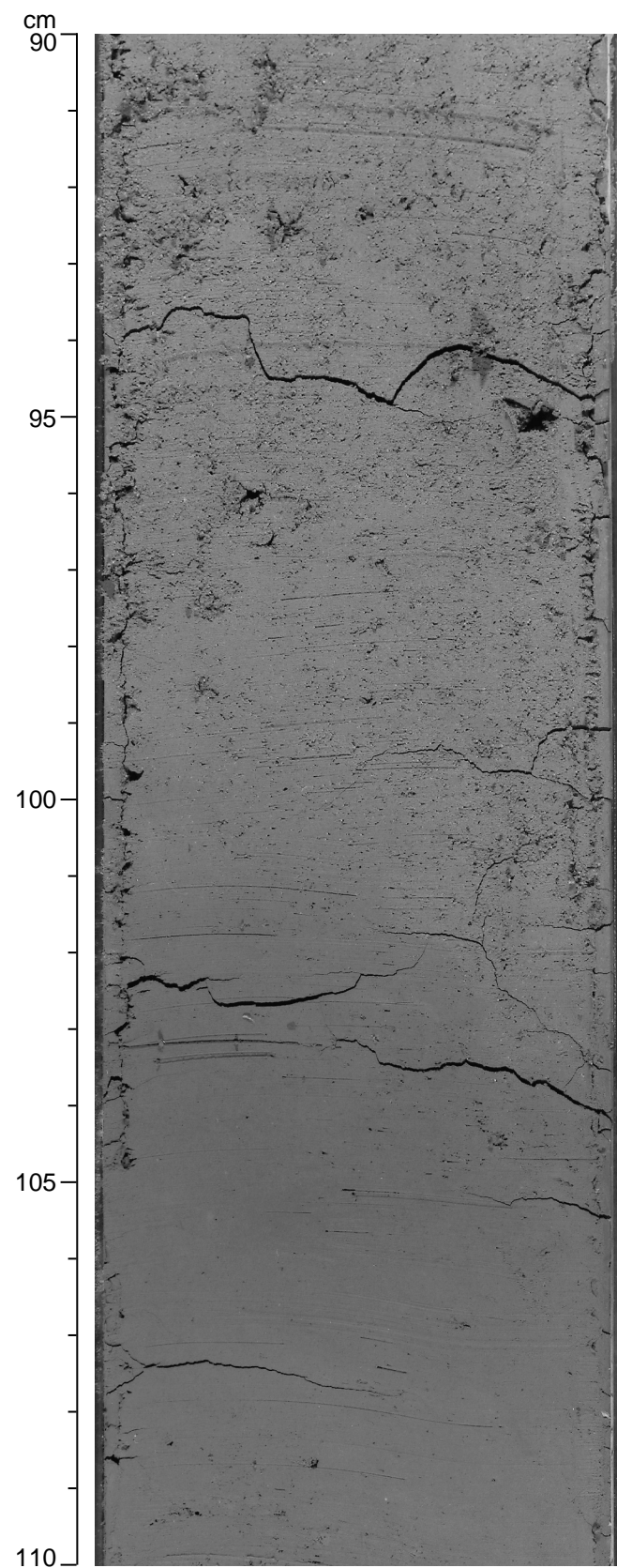


Figure F14. Sharp-based, well-sorted massive sand bed (interval 178-1096B-13H-3, 50–70 cm).

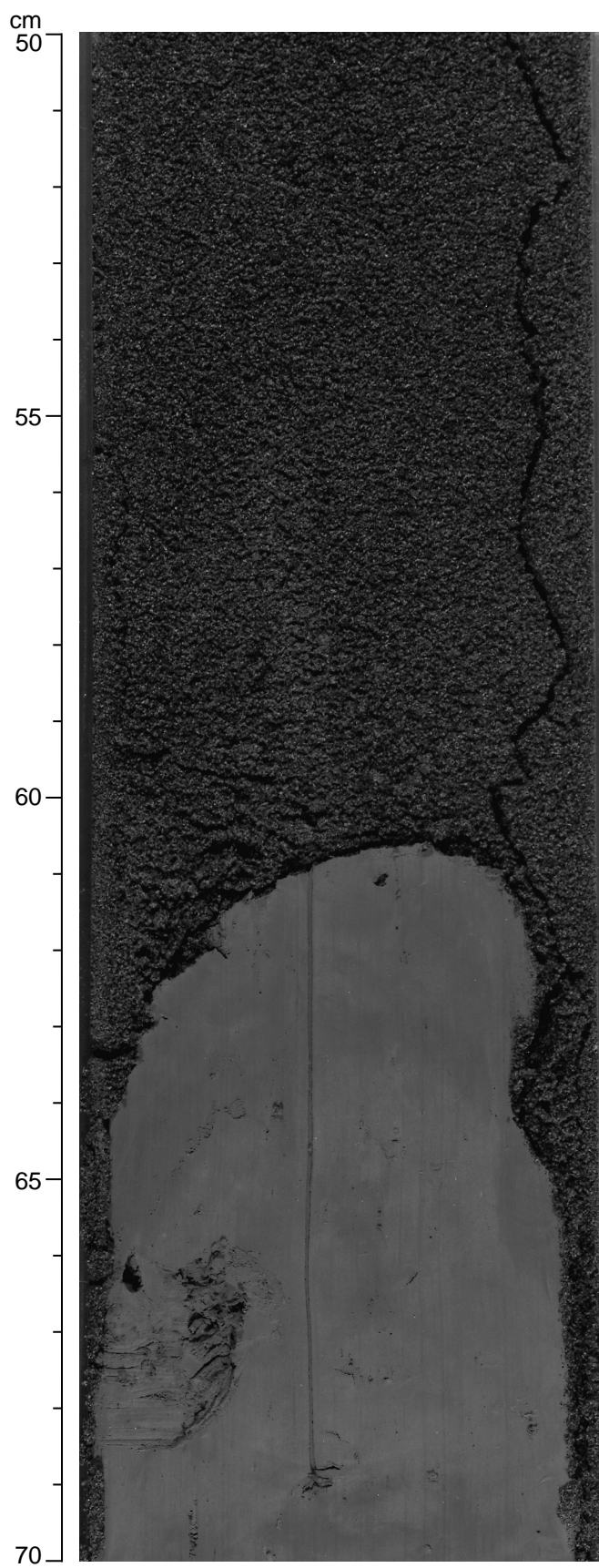


Figure F15. Muddy turbidite Facies L₃ in Unit III showing sharply defined lamination. The core has been fractured into large biscuits, with remolded mud at 55, 64, and 68 cm (interval 178-1096C-23X-6, 50-73 cm).

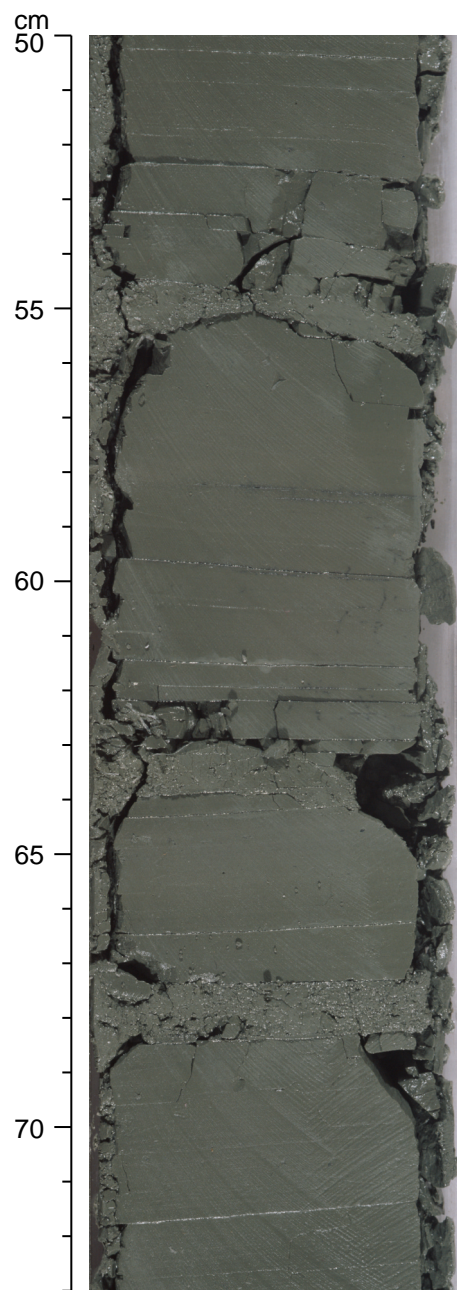


Figure F16. Facies M; mottled, intensely bioturbated silty clay (interval 178-1096C-21X-6, 127–142 cm) in Unit III. Note well-defined horizontal *Zoophycos* burrow with spreiten from 138 to 140 cm and oval *Planolites* burrows at far right of core at 140 cm.

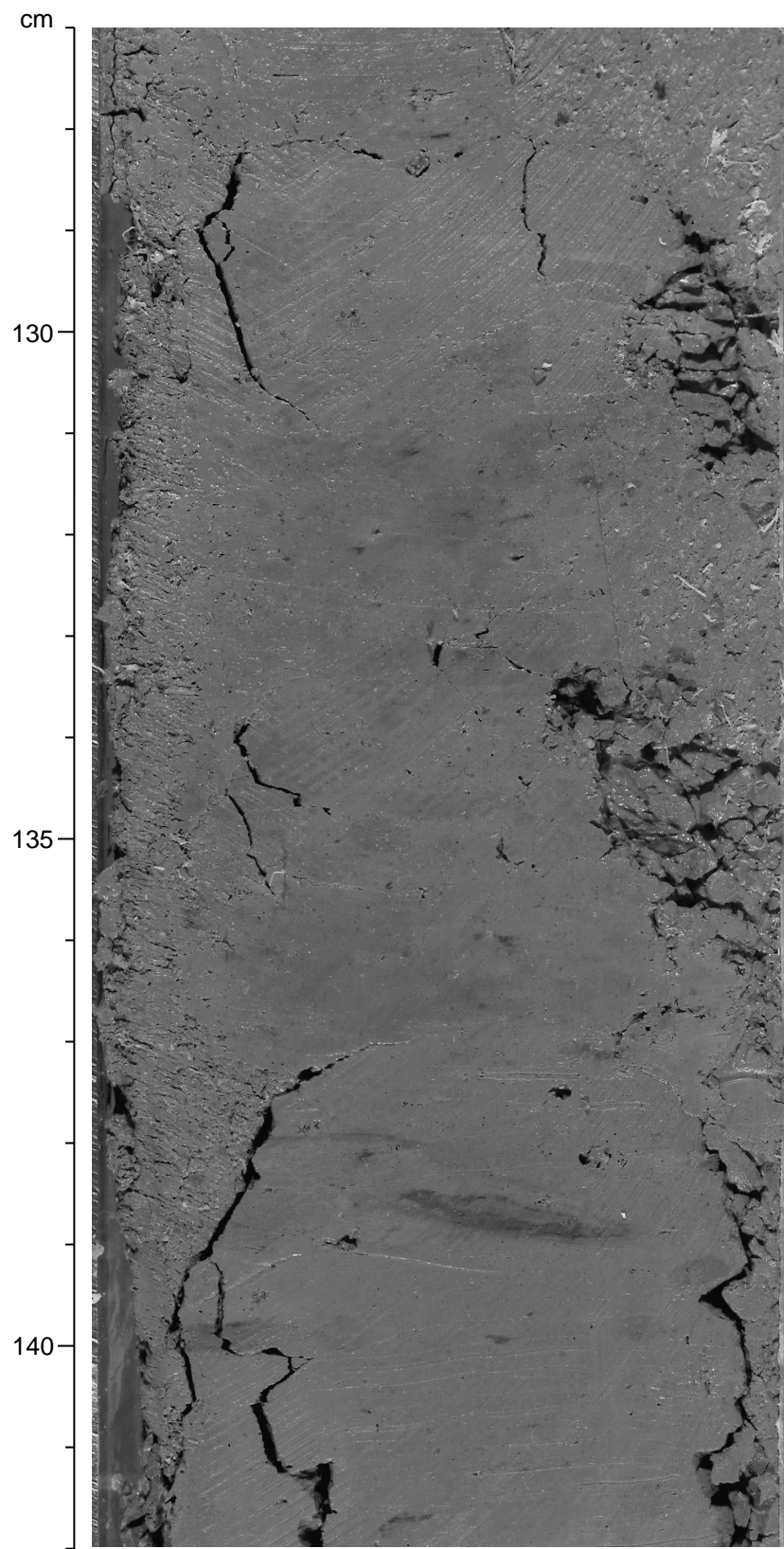


Figure F17. Sand-silt-clay percentage in major lithologies (silt laminae excluded) at Site 1096. Clay content is generally >65%.

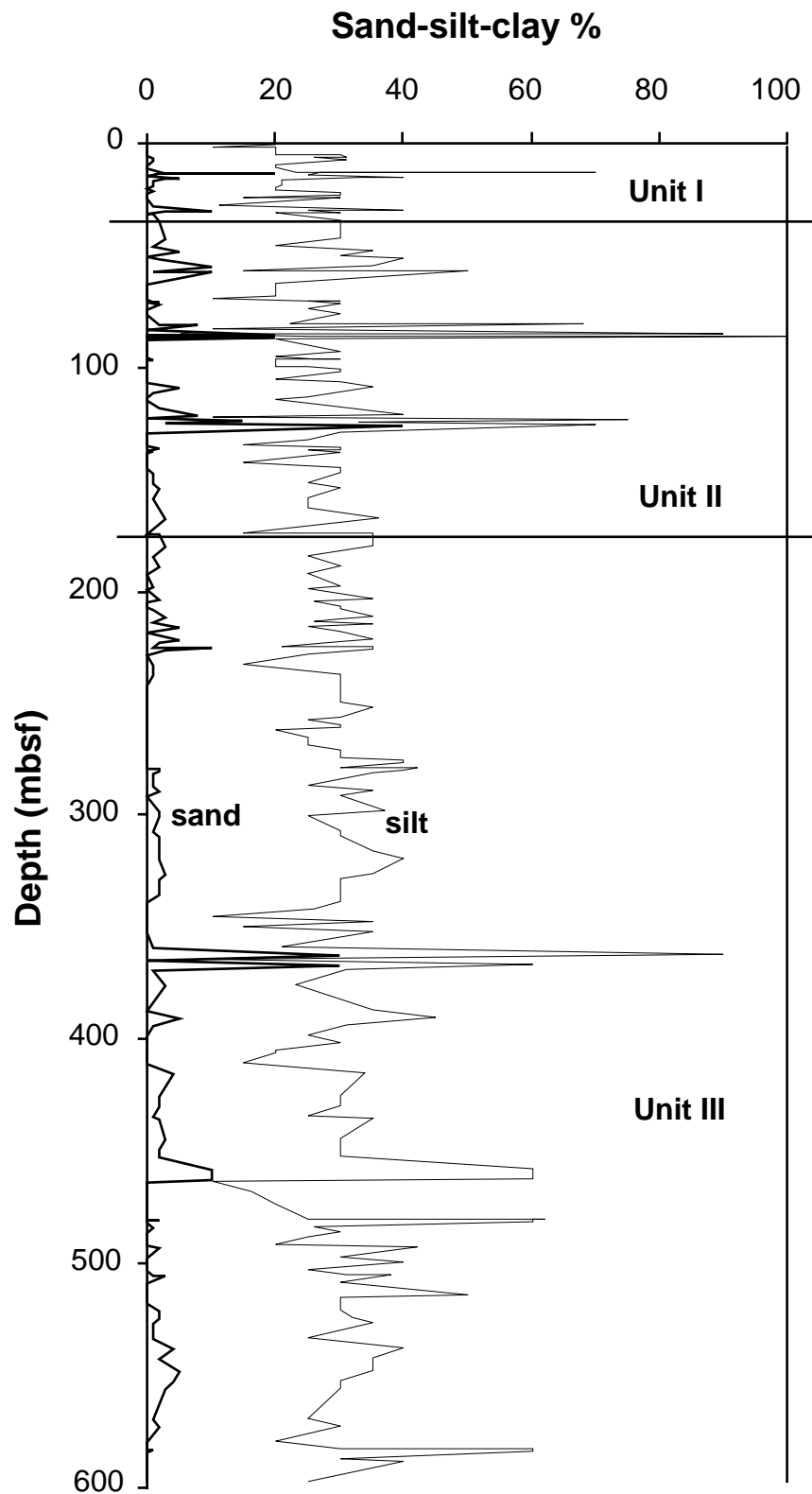


Figure F18. Abundance of pebbles 0.5–6.0 cm in diameter at Site 1096. Each bar represents one core.

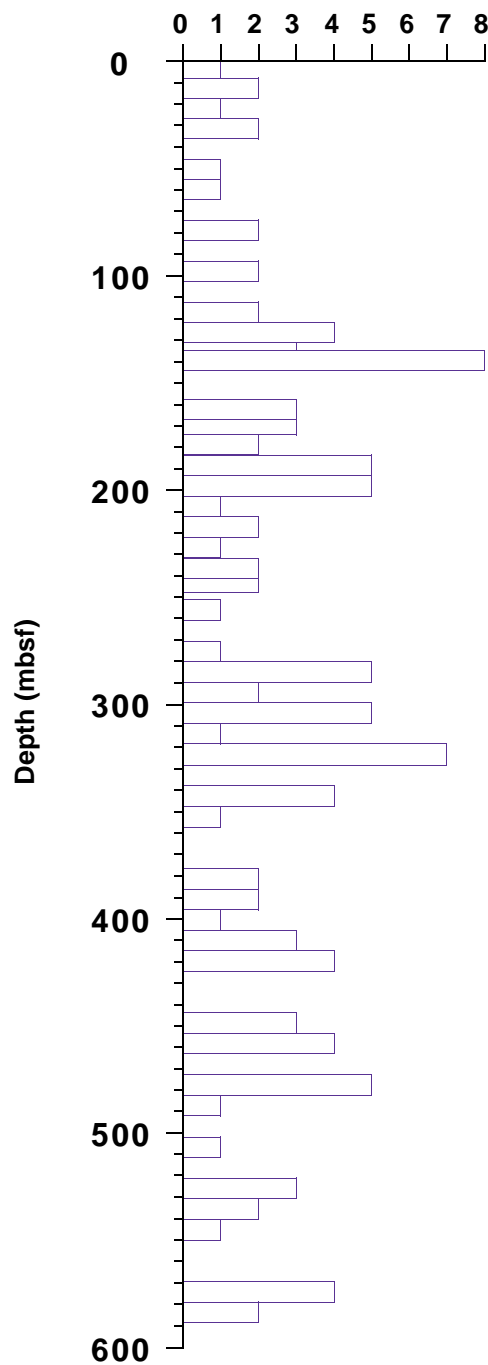


Figure F19. Occurrence of calcareous nannofossils, diatoms, radiolarians, and planktonic foraminifers at Site 1096. Stippled intervals = barren of microfossils except in the case of foraminifers, where the stippled pattern = scattered occurrences of *N. pachyderma* sinistral in the lower portion of Site 1096.

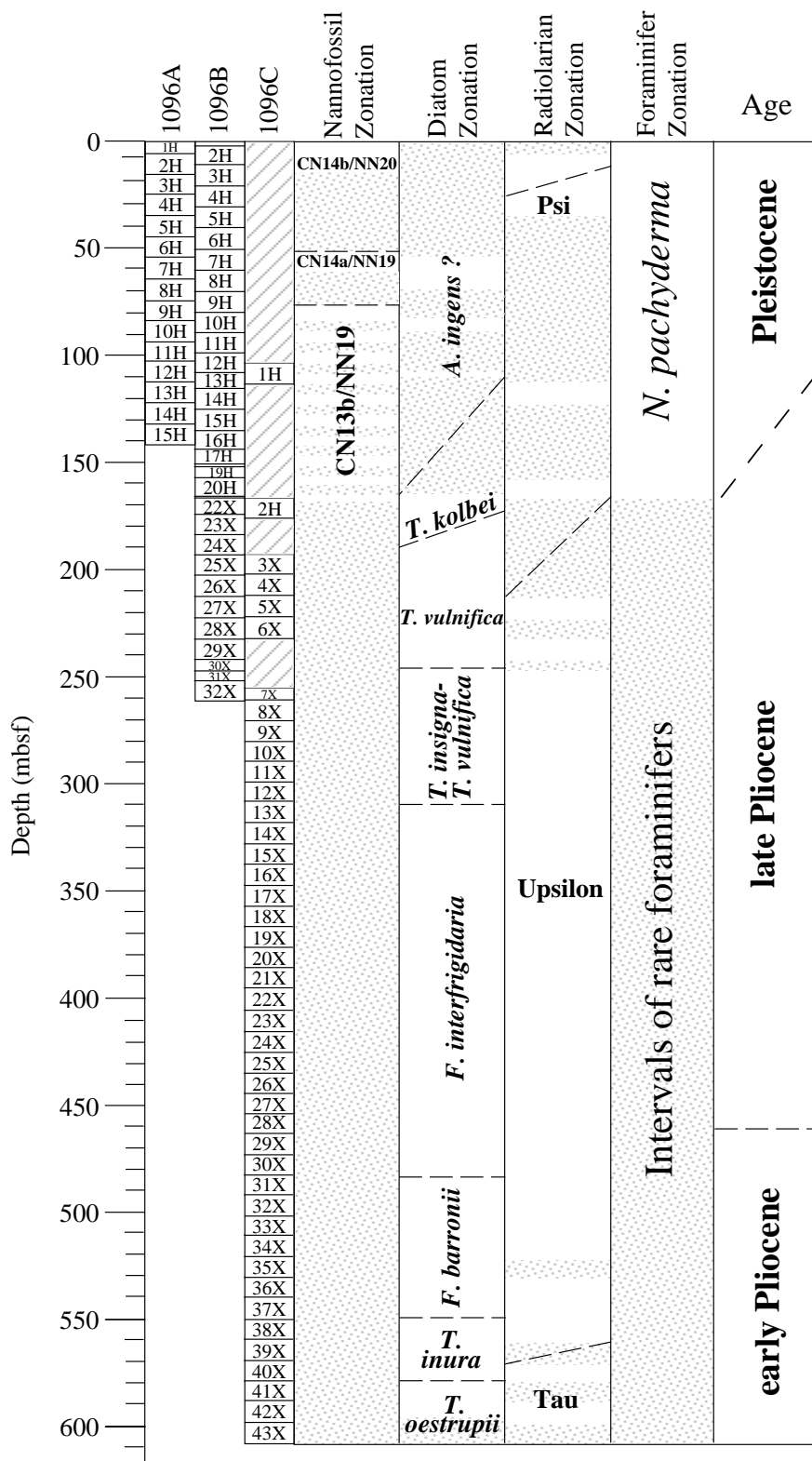


Figure F20. Histogram of inclinations for Holes 1096A, 1096B, and 1096C shown in black, white, and gray, respectively (after AF demagnetization of the NRM at 20 mT).

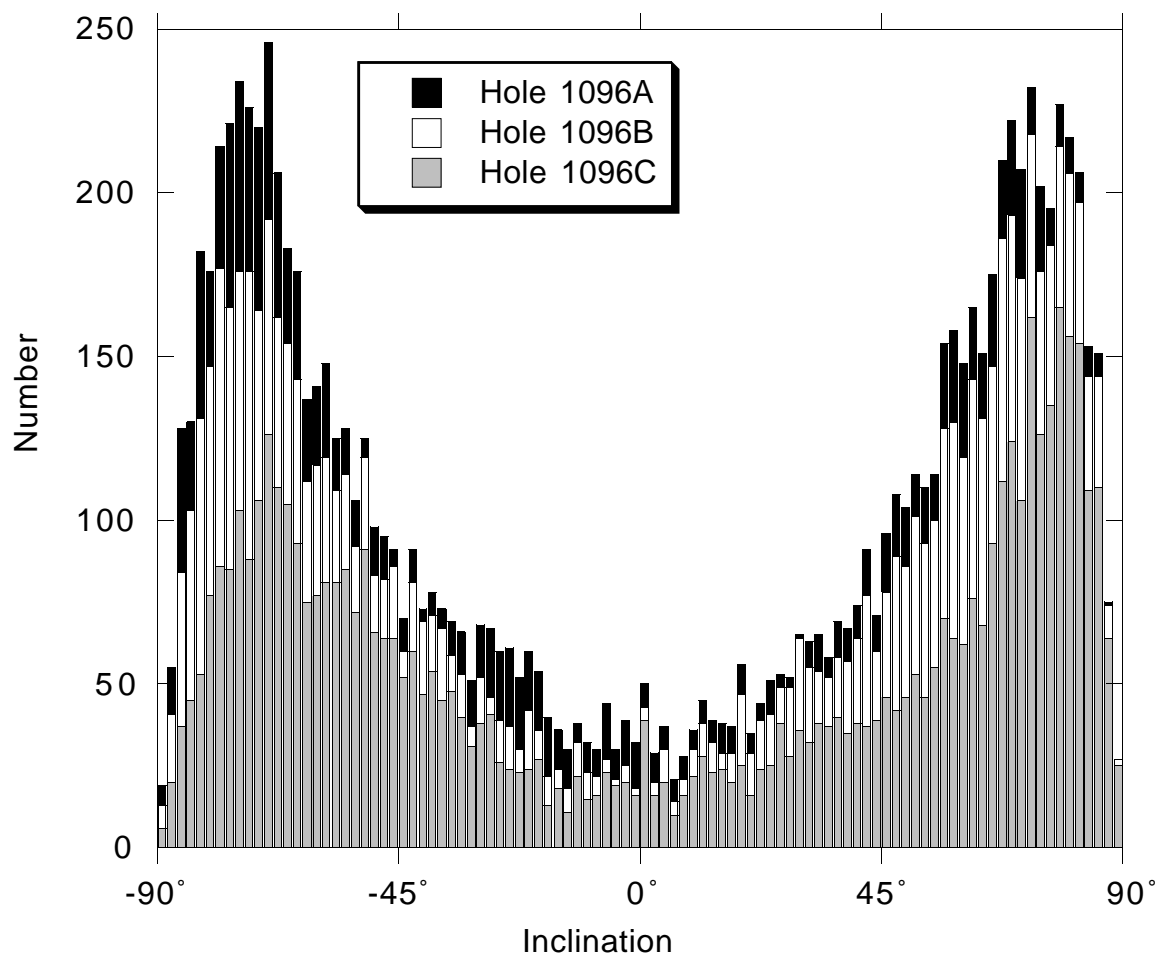


Figure F21. A. Orthogonal projection of the end-points of the remanence vector for Sample 178-1096A-2H-6, 50 cm. Open and solid symbols represent the vertical and horizontal projections, respectively. The steeply inclined drill-string overprint has been removed at the 10-mT demagnetization step. B. Change in the intensity of remanence, normalized to the 0-mT (NRM) intensity, during AF demagnetization. After demagnetization at 80 mT, this sample has ~40% of the intensity of remanence left. C. Equal-area projection of the remanence vector during AF demagnetization.

Sample: 178-1096A-2H-6, 50.0 cm (15.70 mbsf)

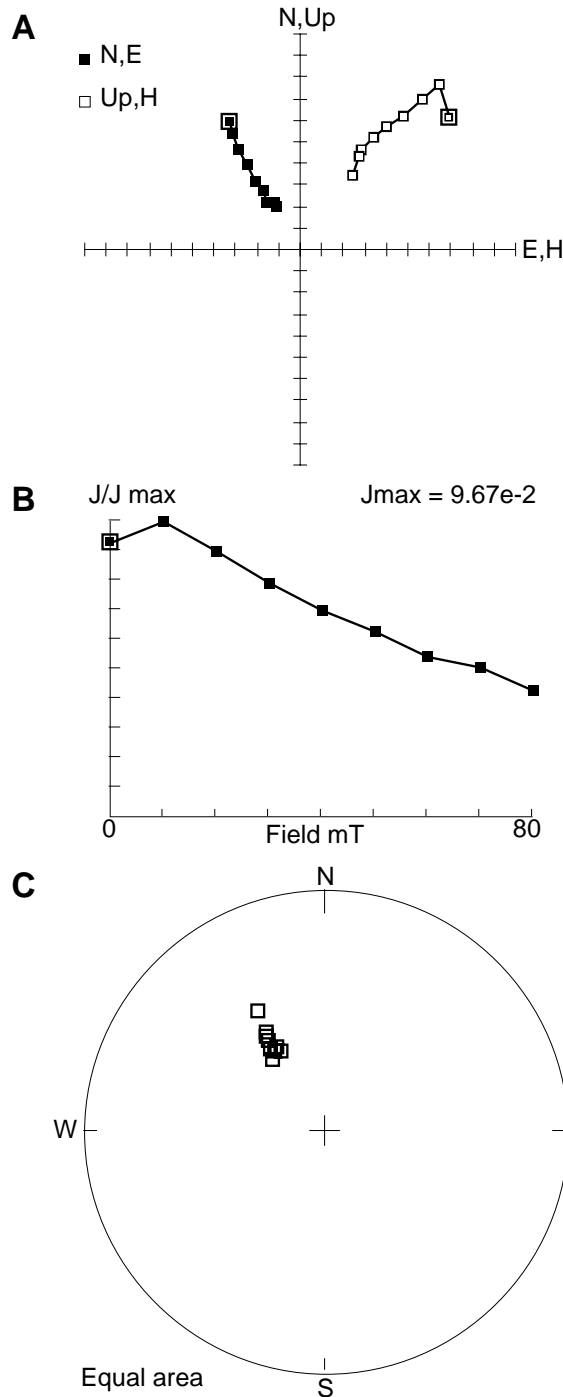


Figure F22. A. Orthogonal projection of the end-points of the remanence vector for Sample 178-1096A-6H-2, 81 cm. Open and solid symbols represent the vertical and horizontal projections, respectively. The steeply inclined drill-string overprint has been removed at the 10-mT demagnetization step. B. Change in the intensity of remanence, normalized to the 0-mT (NRM) intensity, during AF demagnetization. C. Equal-area projection of the remanence vector during AF demagnetization.

Sample: 178-1096A-6H-2, 81.0 cm (48.01 mbsf)

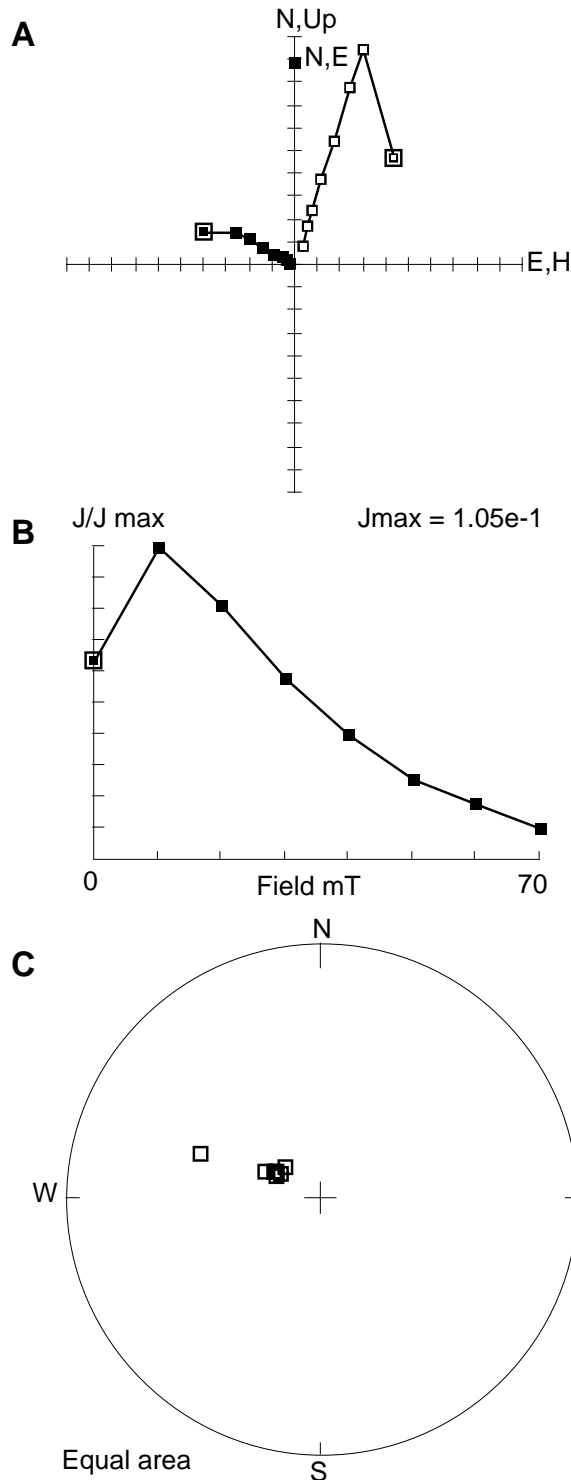


Figure F23. A. Inclination measured on archive halves of Holes 1096A (broken line) and 1096B (solid line), and discrete samples (open boxes). B. Interpreted magnetostratigraphy (see Fig. F24, p. 63, for legend). C. Maximum angular deviation angles for discrete samples. D. Vector length for discrete samples from PCA.

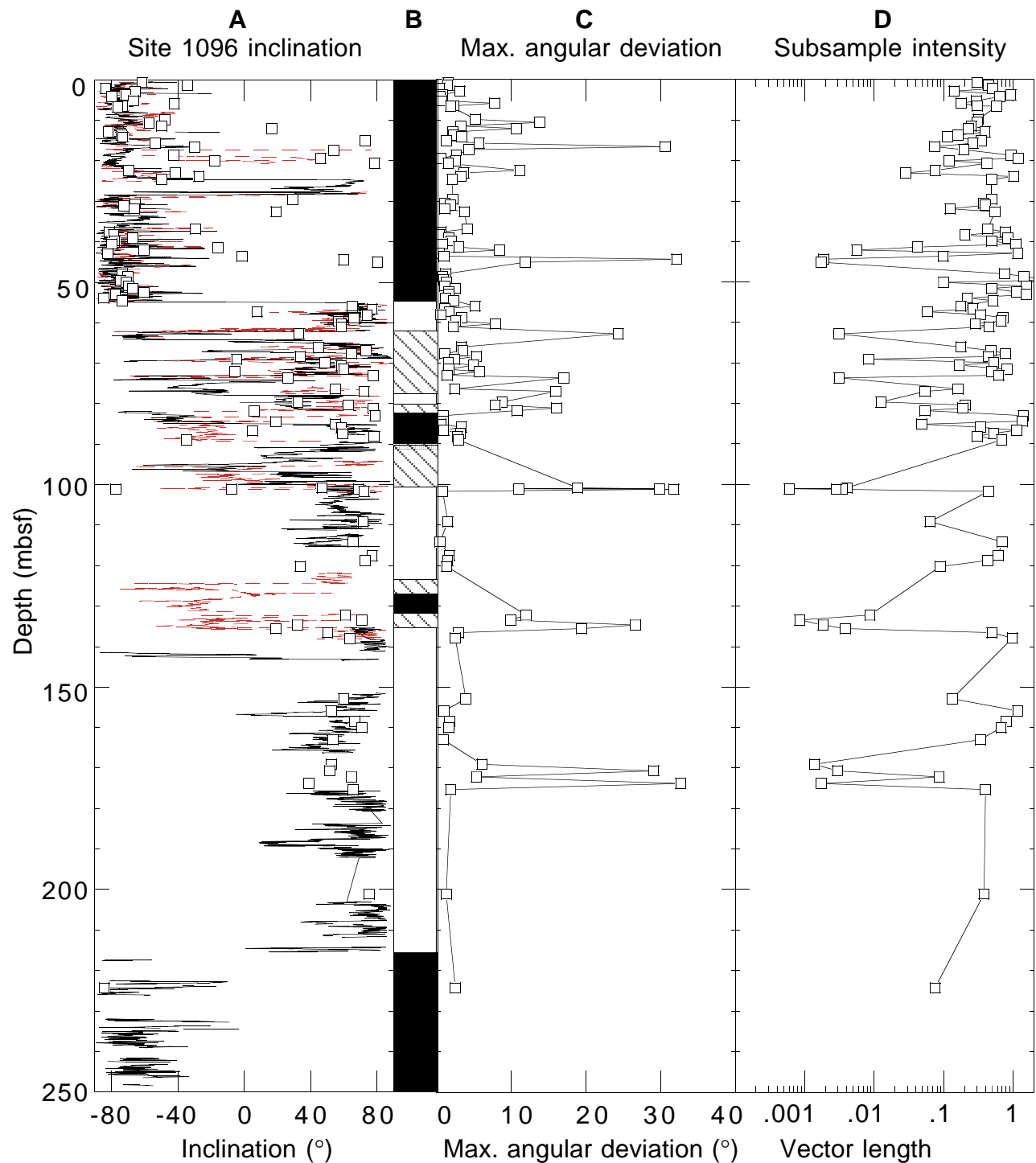


Figure F24. Inclination of the magnetization vector vs. depth (mbsf) for Holes 1096A, 1096B, and 1096C, after AF demagnetization at 20 mT. Magnetostratigraphy based on Berggren et al. (1995).

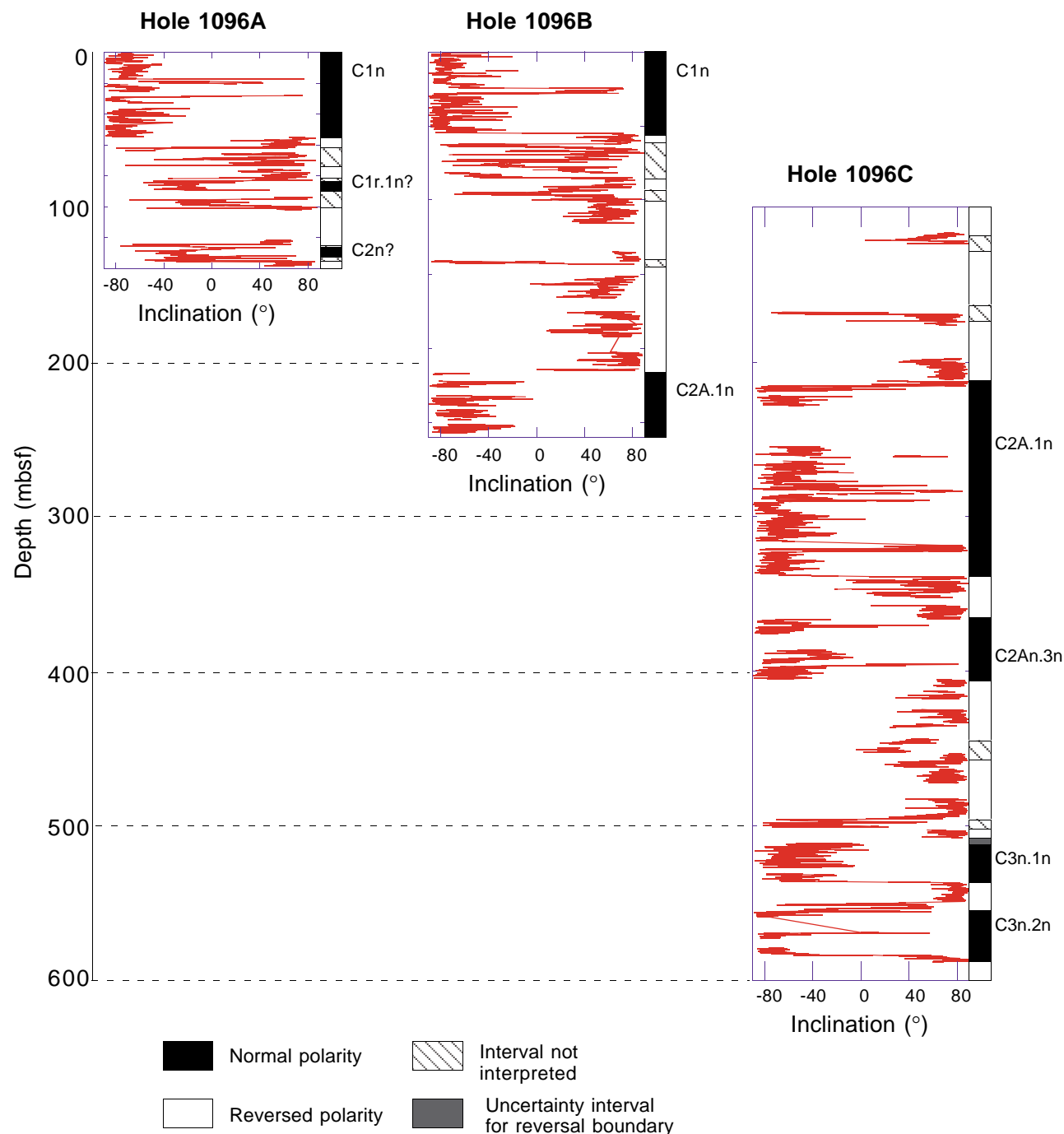


Figure F25. Intensity of the magnetization vector vs. depth (mbsf) for Holes 1096A, 1096B, and 1096C after AF demagnetization at 20 mT.

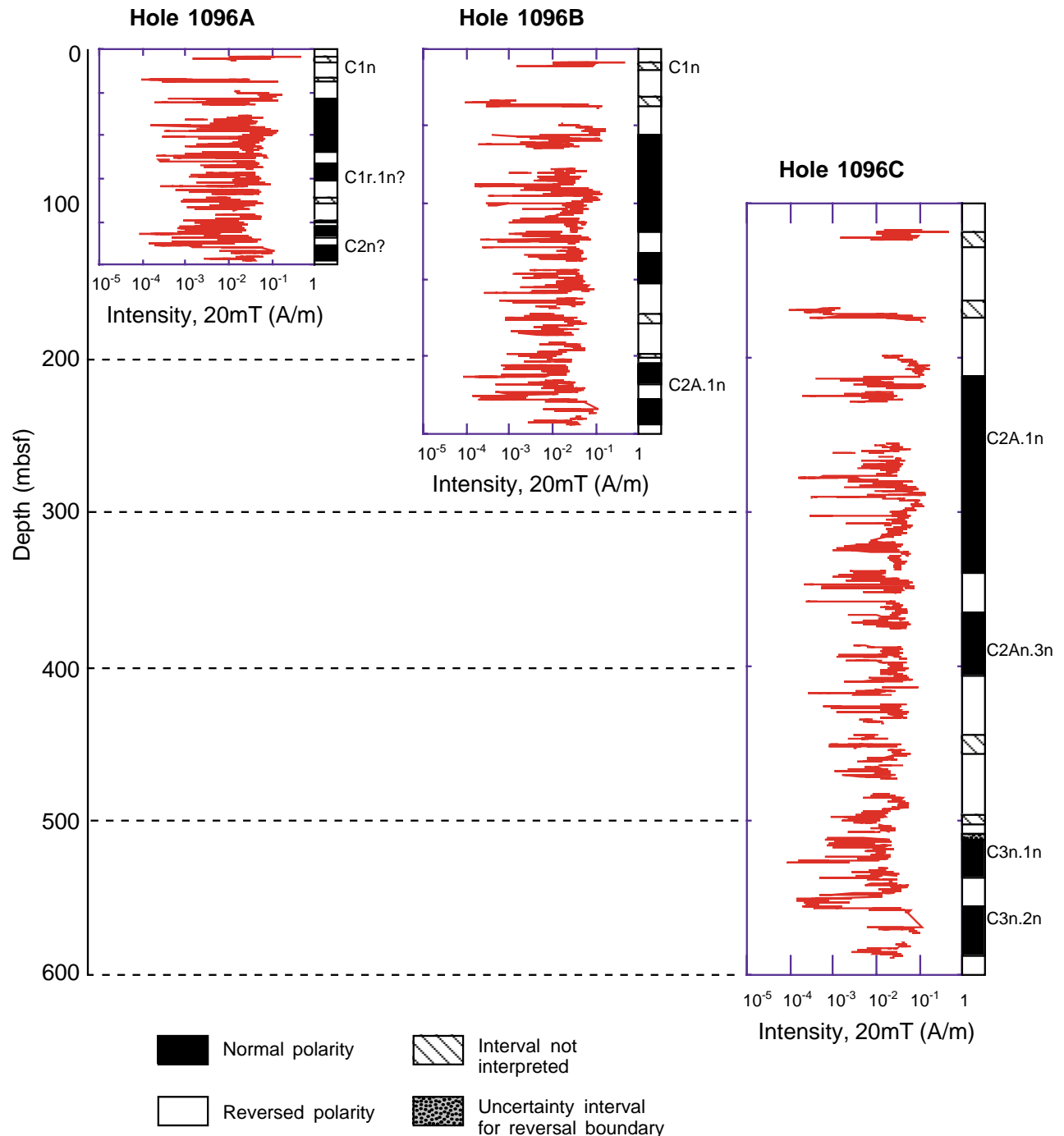


Figure F26. A. Inclination at Hole 1096A vs. depth (mbsf). B. Intensity of the NRM at 20 mT at Hole 1096A vs. depth. C. Magnetic susceptibility at Hole 1096A vs. depth (mbsf).

Magnetostratigraphy at Hole 1096A

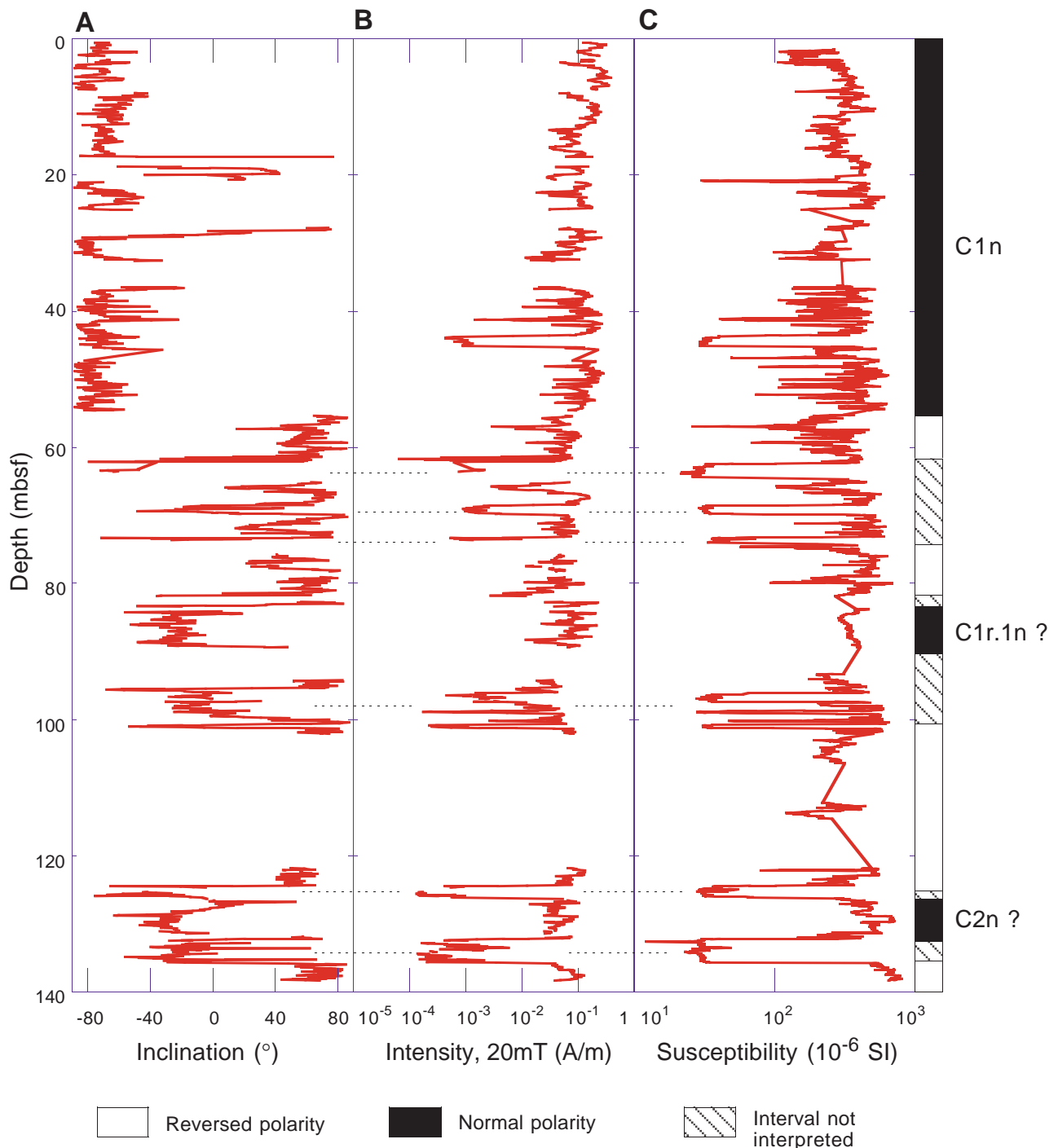


Figure F27. Methane occurrence in headspace samples, showing the first appearance of methane at 50 mbsf and a downhole increase.

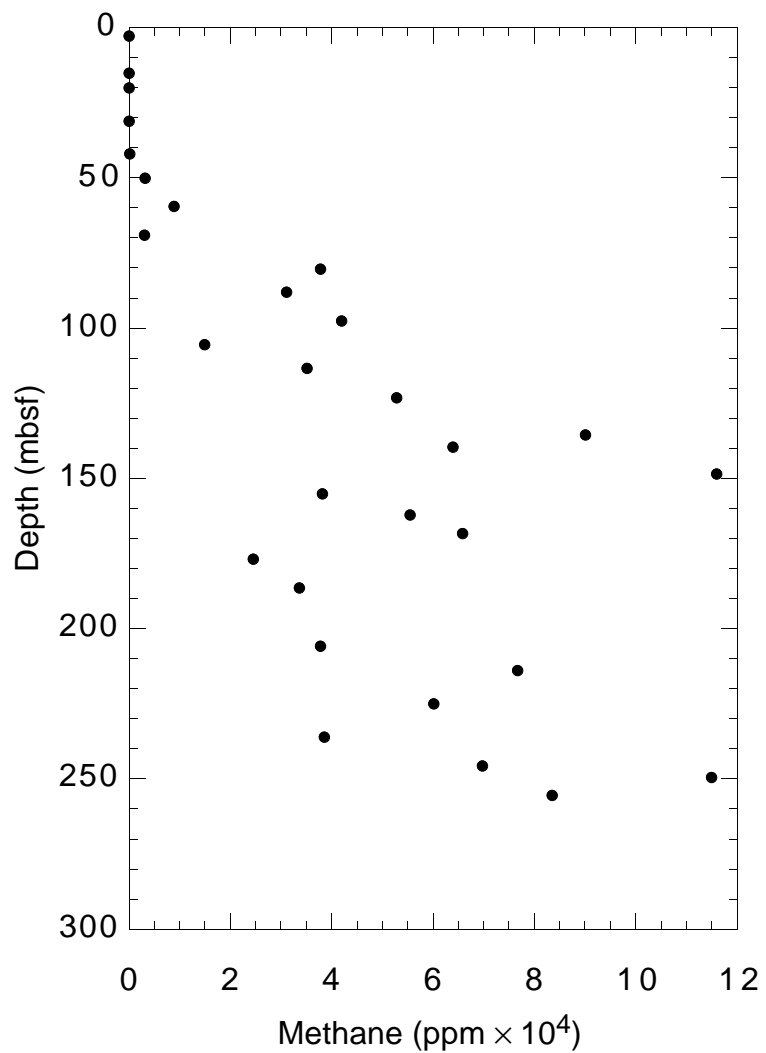


Figure F28. C_{3+} hydrocarbons measured in gas pockets by vacutainer sampling.

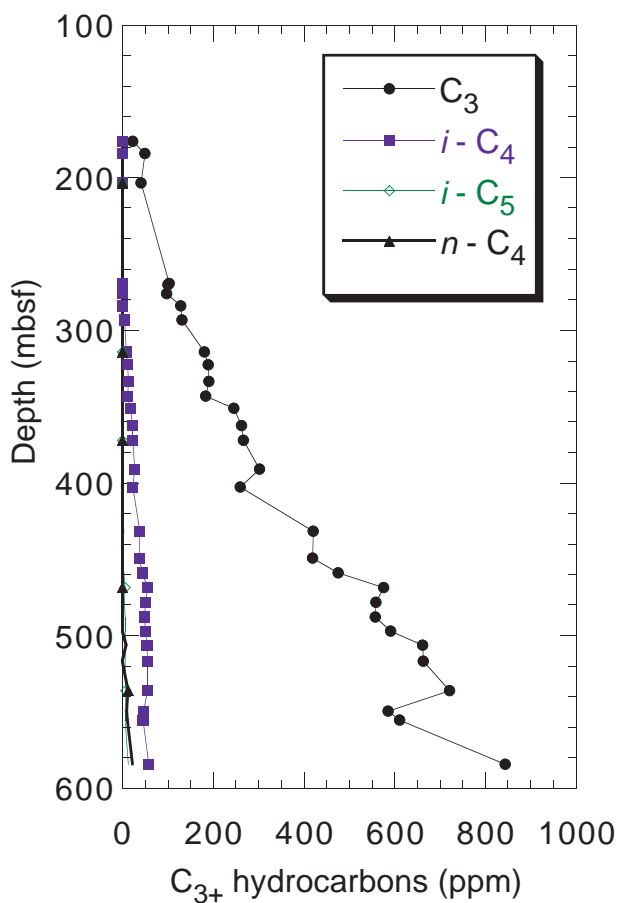


Figure F29. Inorganic carbon occurrences in (A) Hole 1096A, (B) Hole 1096B, and (C) Hole 1096C. Lithostratigraphic units are indicated by I, II, and III. Units I and III show mostly low concentrations of inorganic carbon, whereas Unit II has several peaks of higher inorganic carbon.

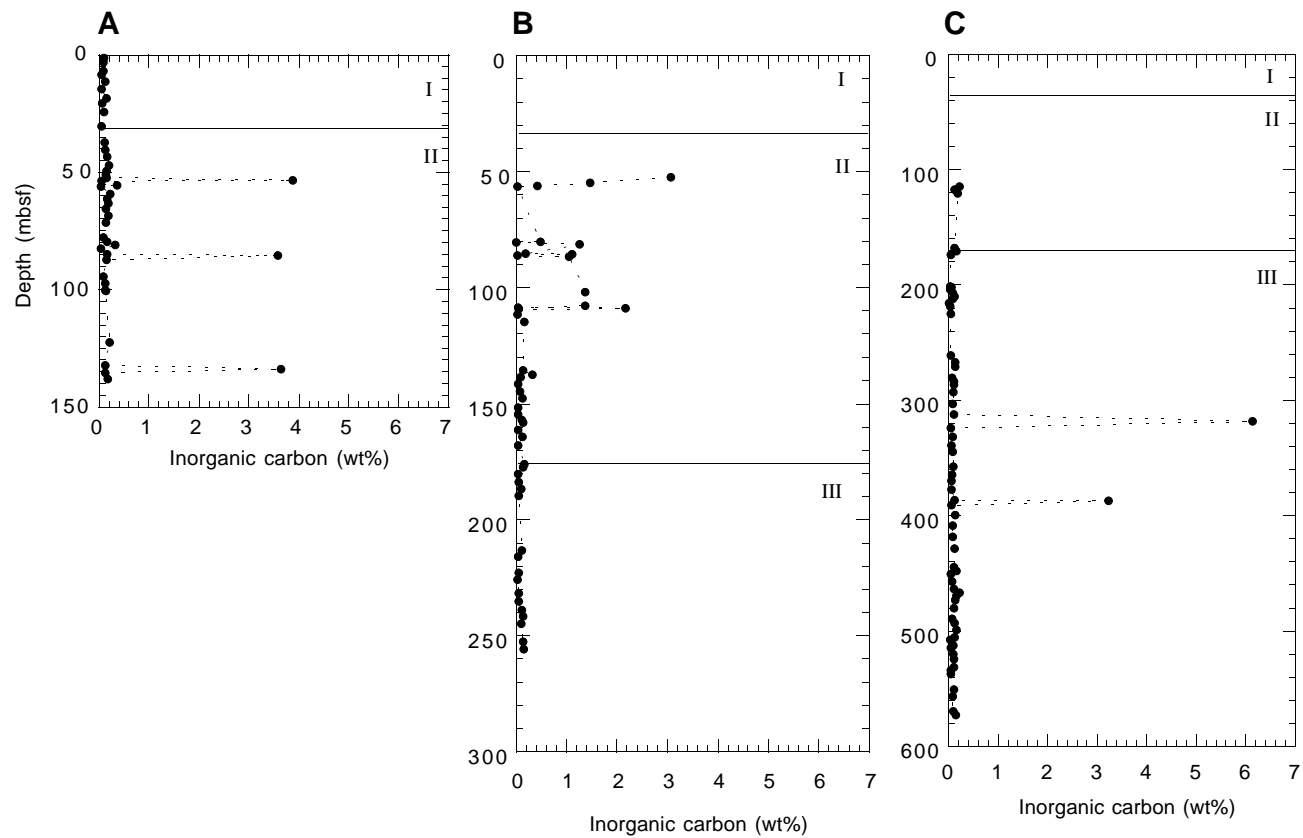


Figure F30. Total organic carbon concentrations for Holes 1096A, 1096B, and 1096C. Lithostratigraphic units are indicated by I, II, and III. Note shift to higher concentrations of total organic carbon at base of Unit II.

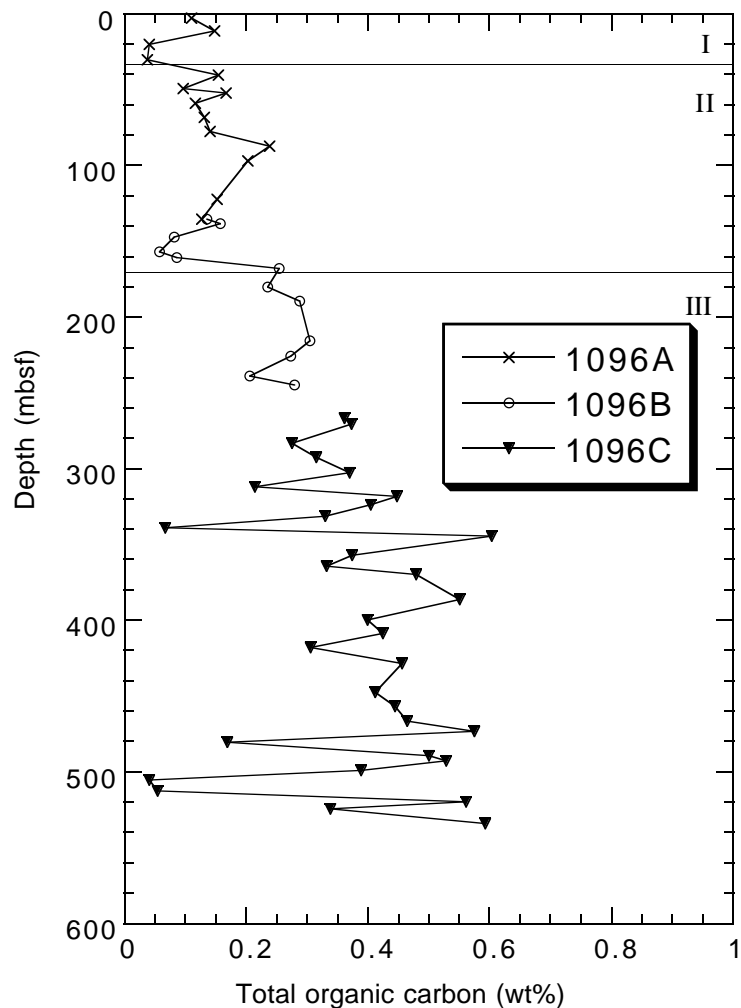


Figure F31. Profiles of interstitial water chemistry in Holes 1096A, 1096B, and 1096C.

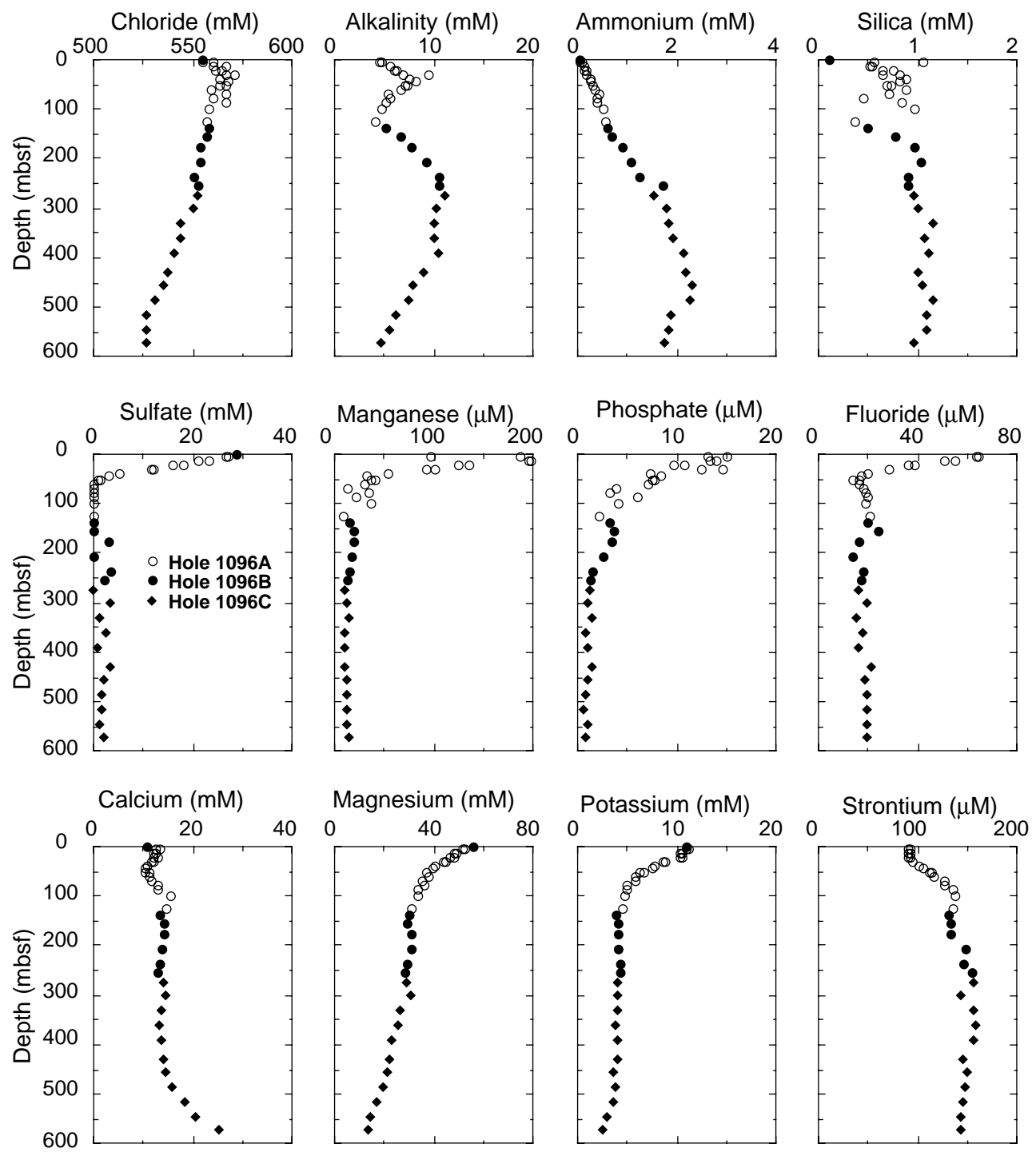


Figure F32. Ratios between X-ray diffraction intensities of selected peaks for chlorite (7 Å), illite (5 Å), and mixed-layer (~12 Å) clays in clay-sized sediment fractions from Site 1096. Peak height ratios do not reflect absolute concentrations.

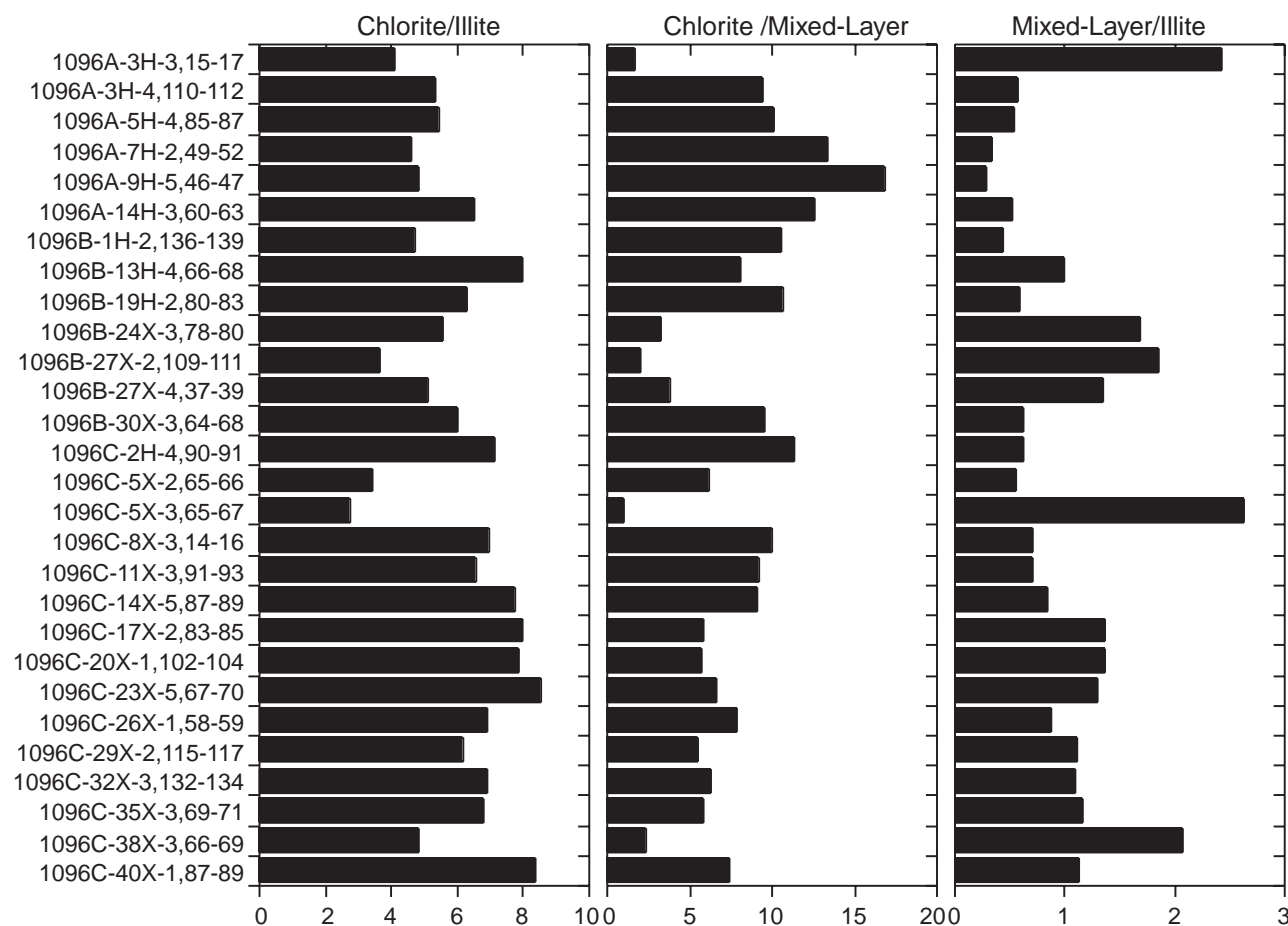


Figure F33. Spliced raw data for (A) NGR, (B) GRAPE density, (C) magnetic susceptibility, and (D) *P*-wave velocity. The GRAPE data were truncated at 1.2 g/cm³, and the susceptibility data were truncated at 0 to remove equipment noise.

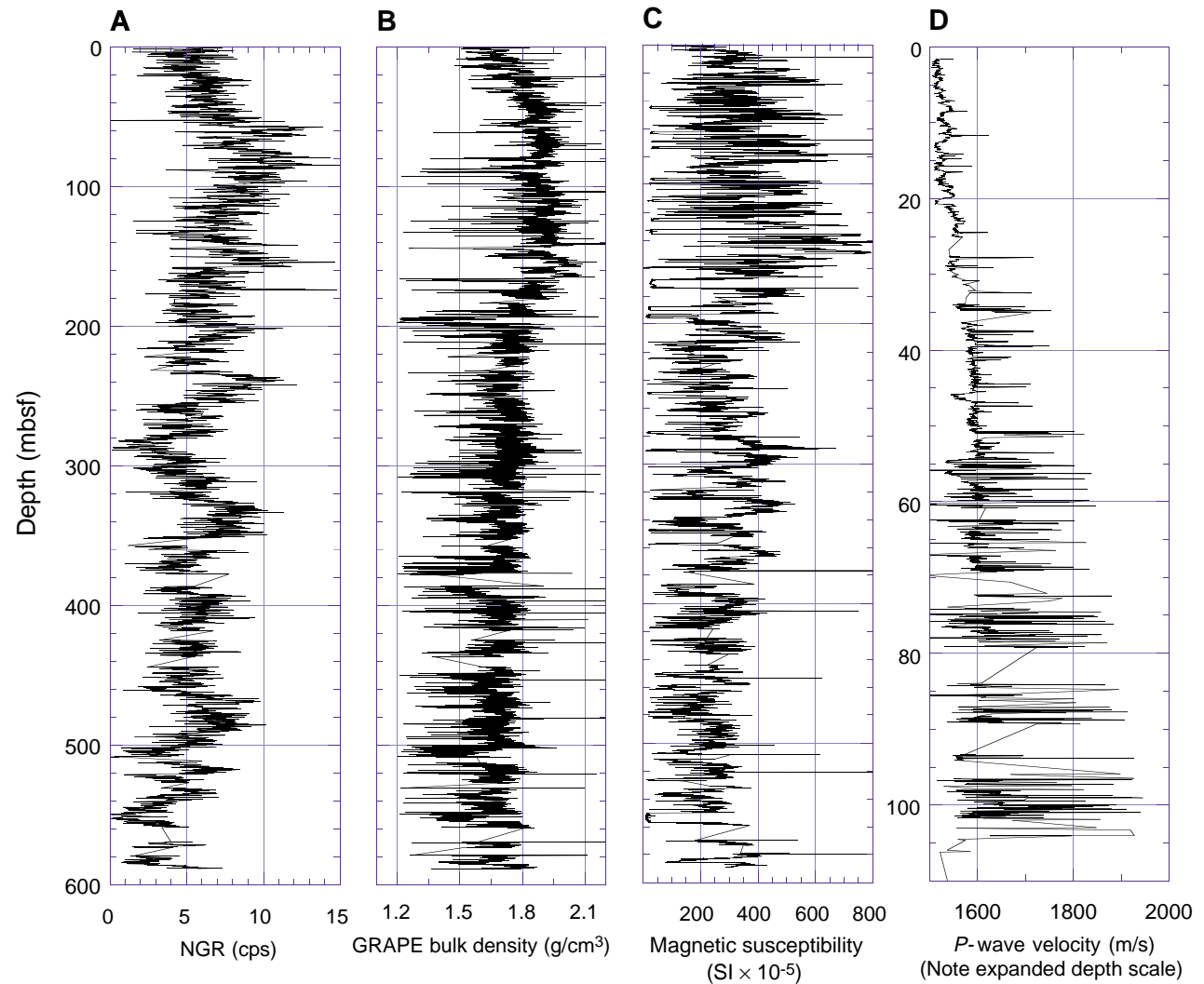


Figure F34. (A) NGR, (B) GRAPE density, and (C) magnetic susceptibility vs. depth. A Gaussian filter was applied to the data to remove high-frequency variability. The filter was centered around 10 m, with a high-frequency truncation point at ~1 m.

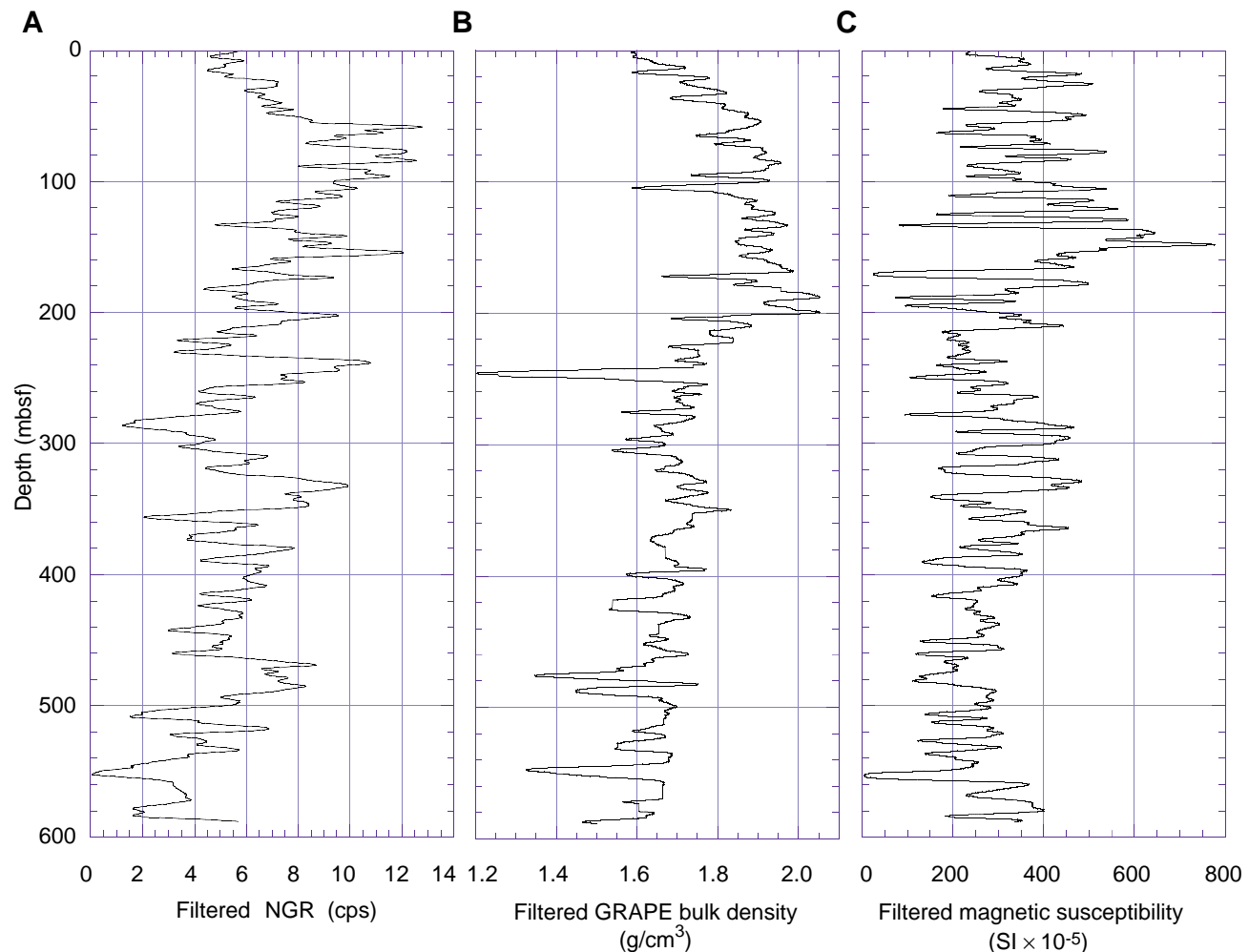


Figure F35. (A) NGR, (B) GRAPE density, and (C) magnetic susceptibility data vs. age. After age scaling, the data were filtered as in Figure F34, p. 82, in the "Site 1095" chapter.

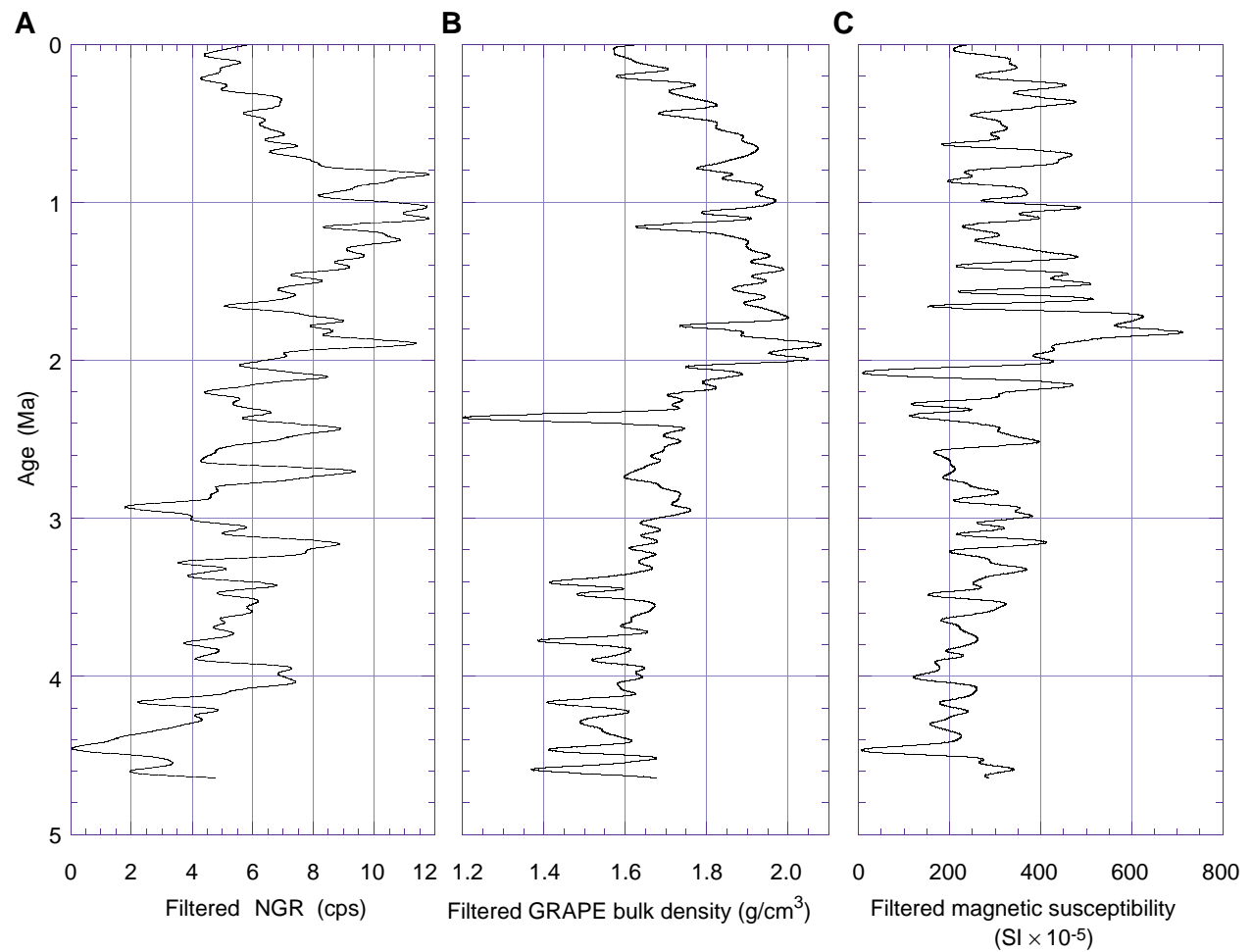


Figure F36. Filtered (A) grain density and (B) GRAPE density and raw index properties (MAD) bulk density vs. depth.

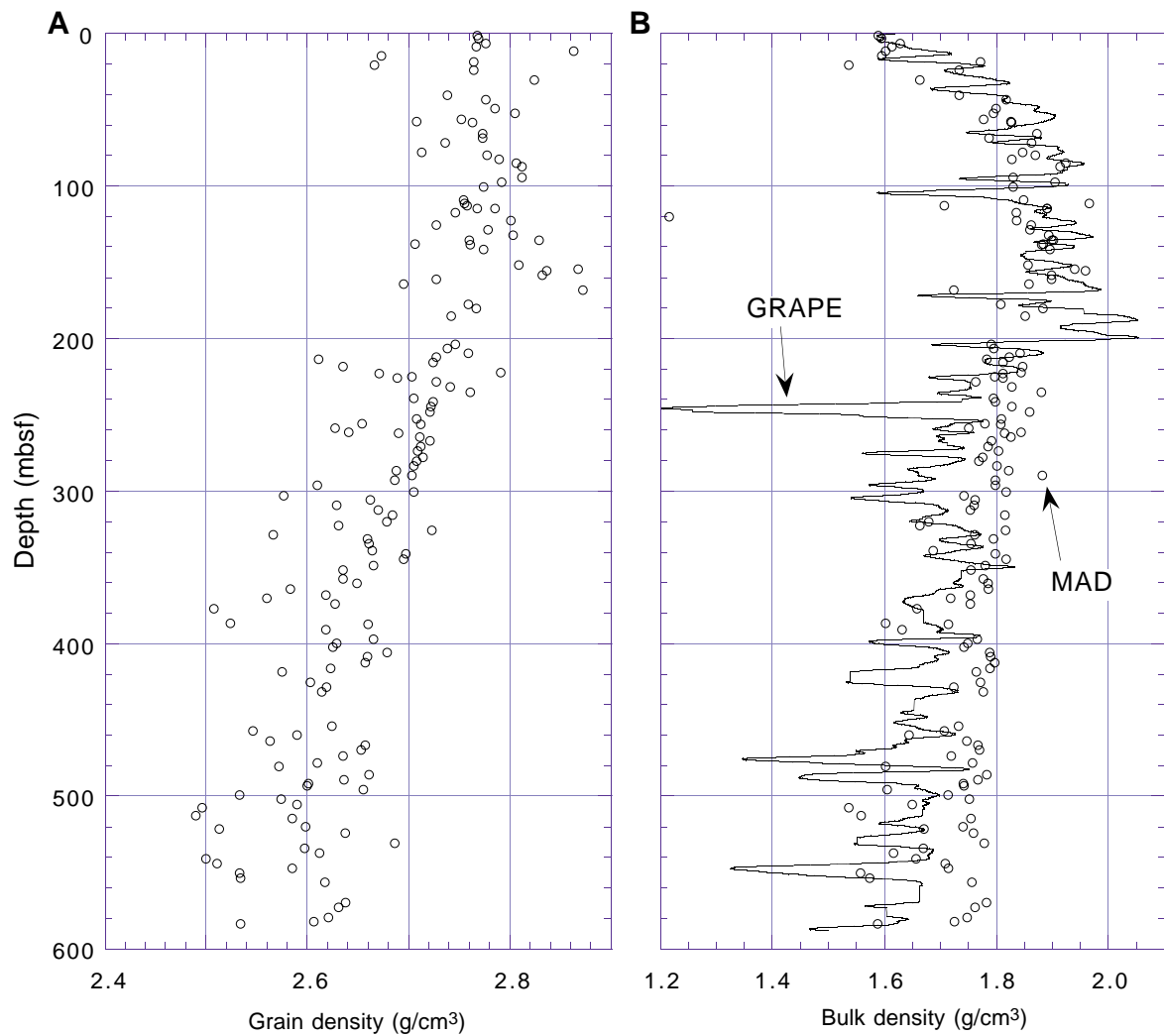


Figure F37. Total (A) bulk water content and (B) biogenic content and index properties porosity vs. depth. Only the major lithologic units are used for the total biogenic content plot.

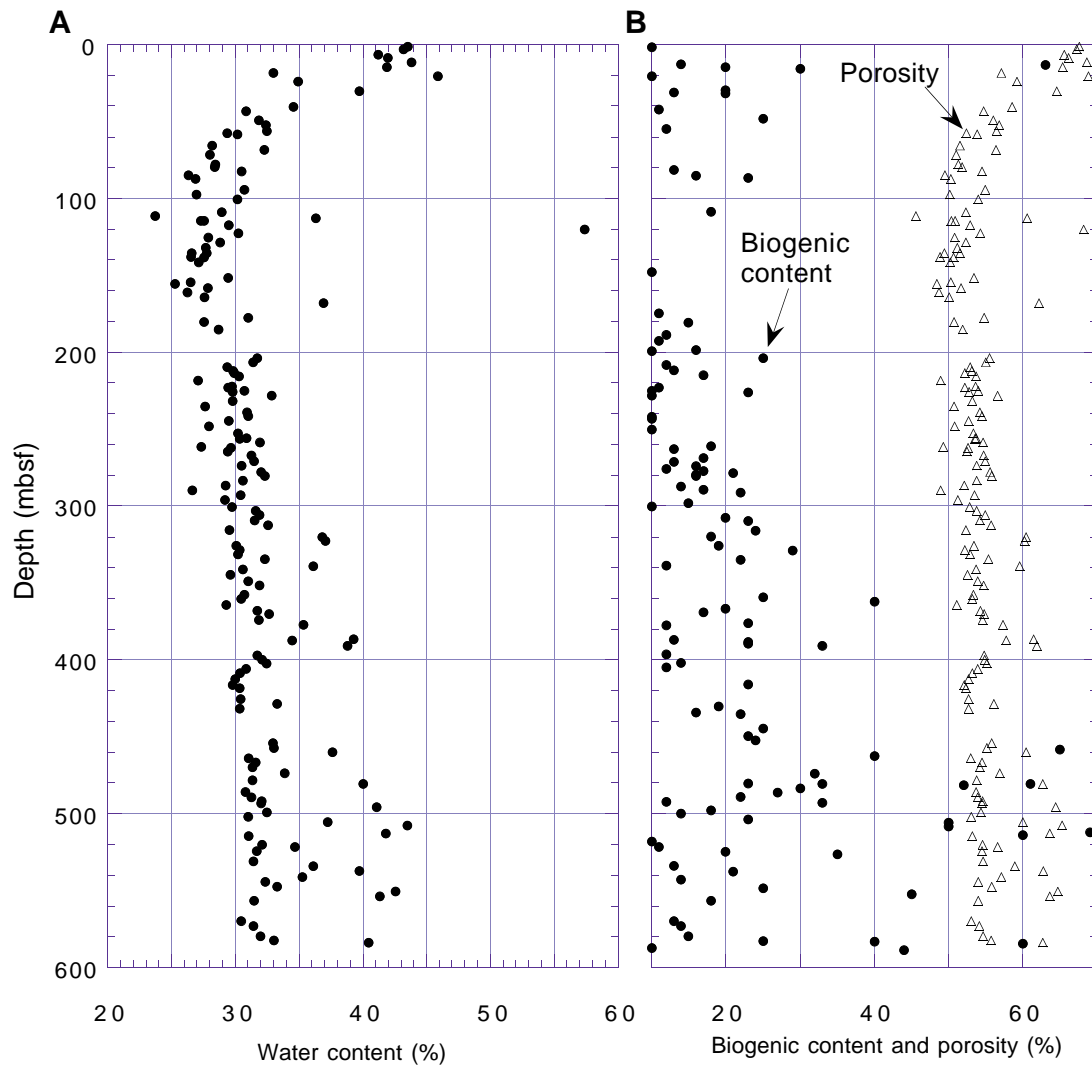


Figure F38. (A) Sediment strength, (B) strength compared with biogenic content, (C) strength compared with porosity, and (D) yield strengths normalized by overburden stress vs. depth. Thin solid lines = residual strengths of the sediments from the vane shear equipment, heavy solid lines = vane shear yield strengths, dashed lines = yield strengths obtained using the pocket penetrometer, diamonds = biogenic content, circles = porosity.

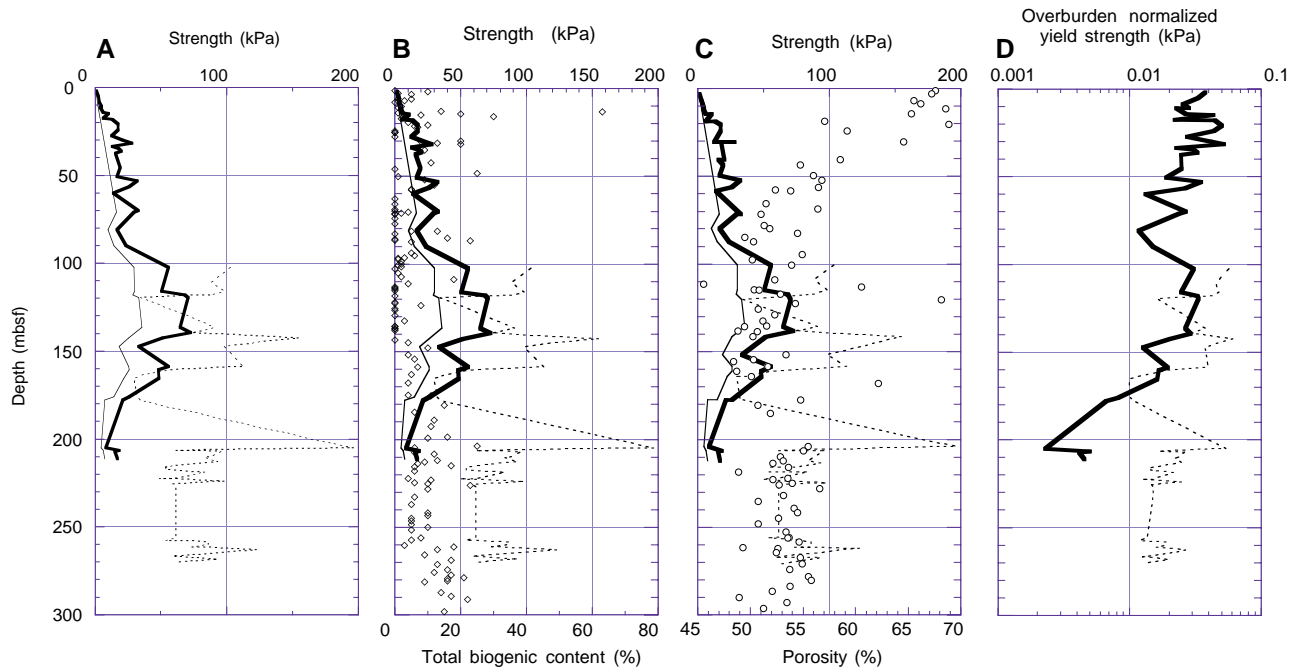


Figure F39. (A) PWS1, PWS2, and (B) PWS3 measurements vs. depth.

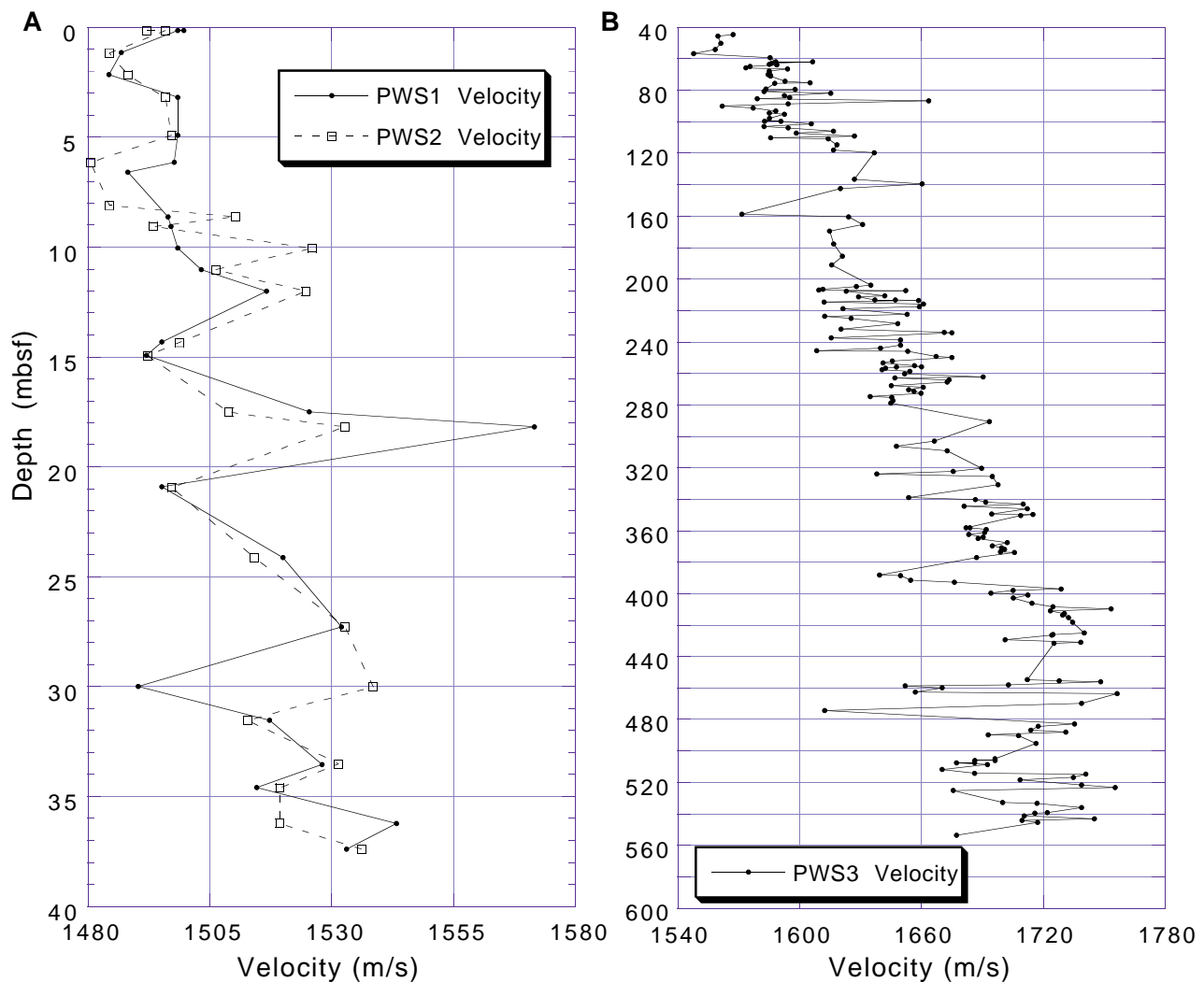


Figure F40. Thermal conductivity measurements at Site 1096. Squares = measurements considered unbiased and used in least-squares fit of conductivity model (black line), circles = those measurements not used.

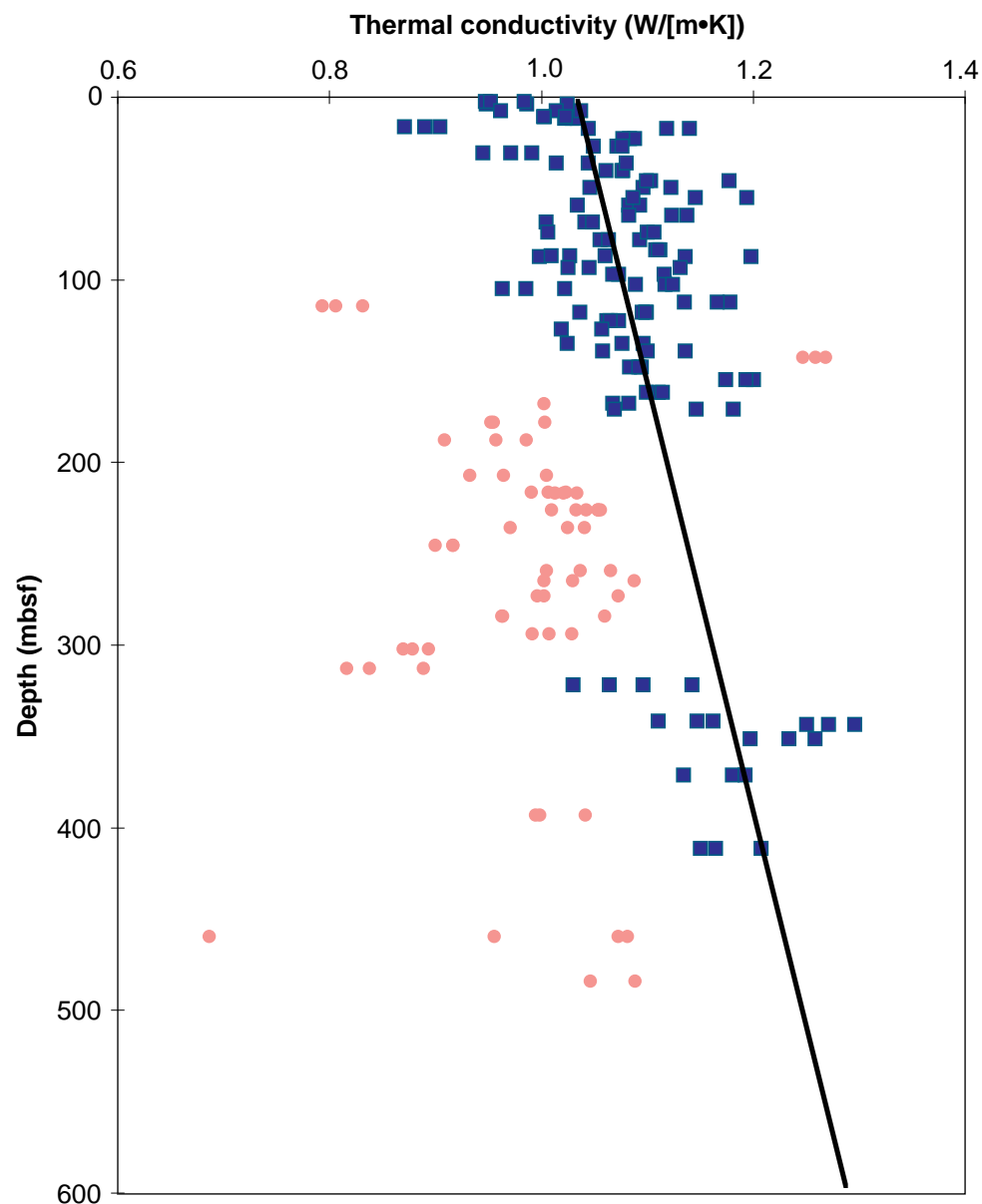


Figure F41. Downhole temperature measurements at Site 1096 with best-fitting logarithmic temperature-depth curve.

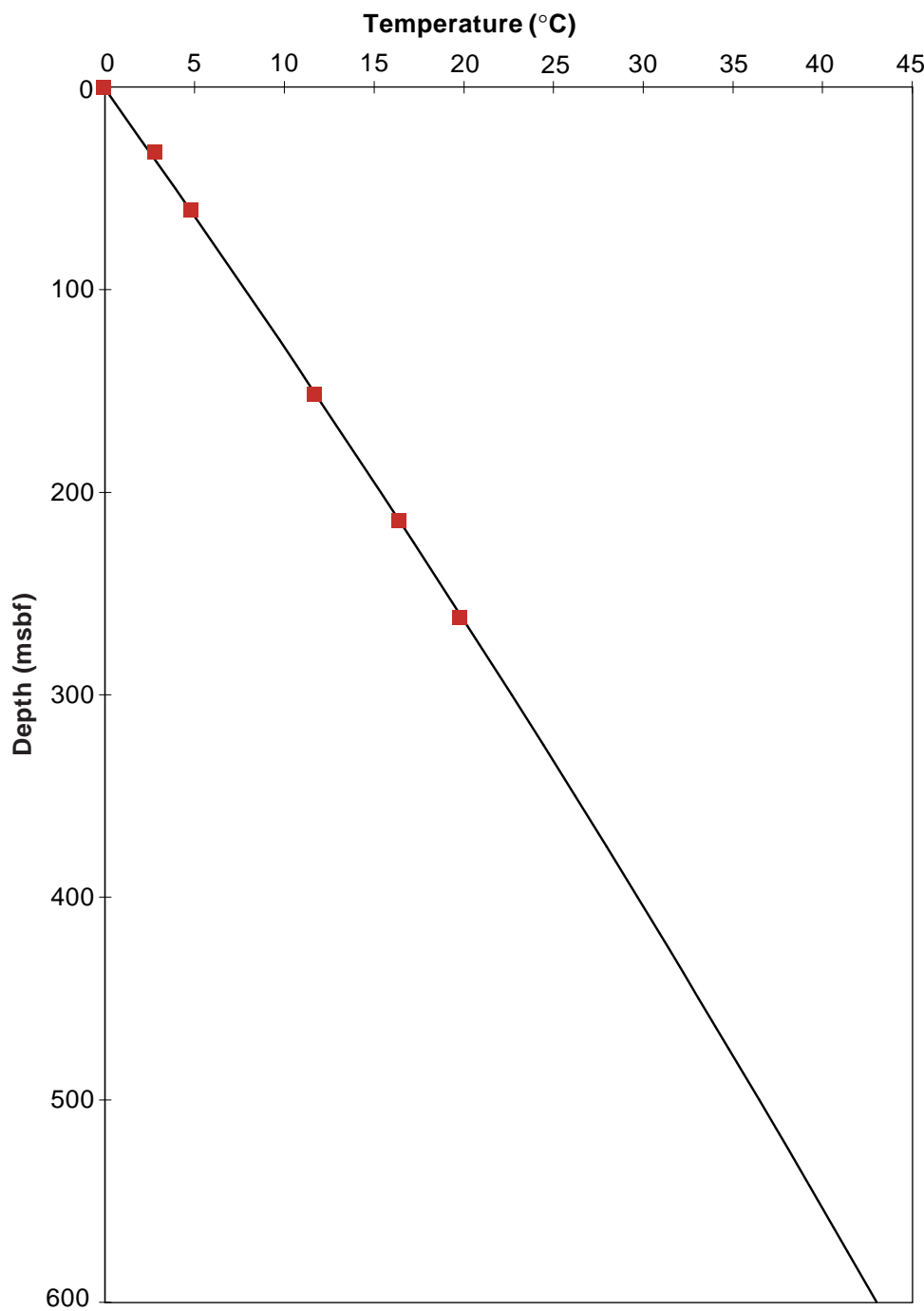


Figure F42. Graphic summary of downhole logging operations at Hole 1096C. Seafloor was picked on the basis of the step in natural gamma activity at the sediment/water boundary as measured during the GHMT run.

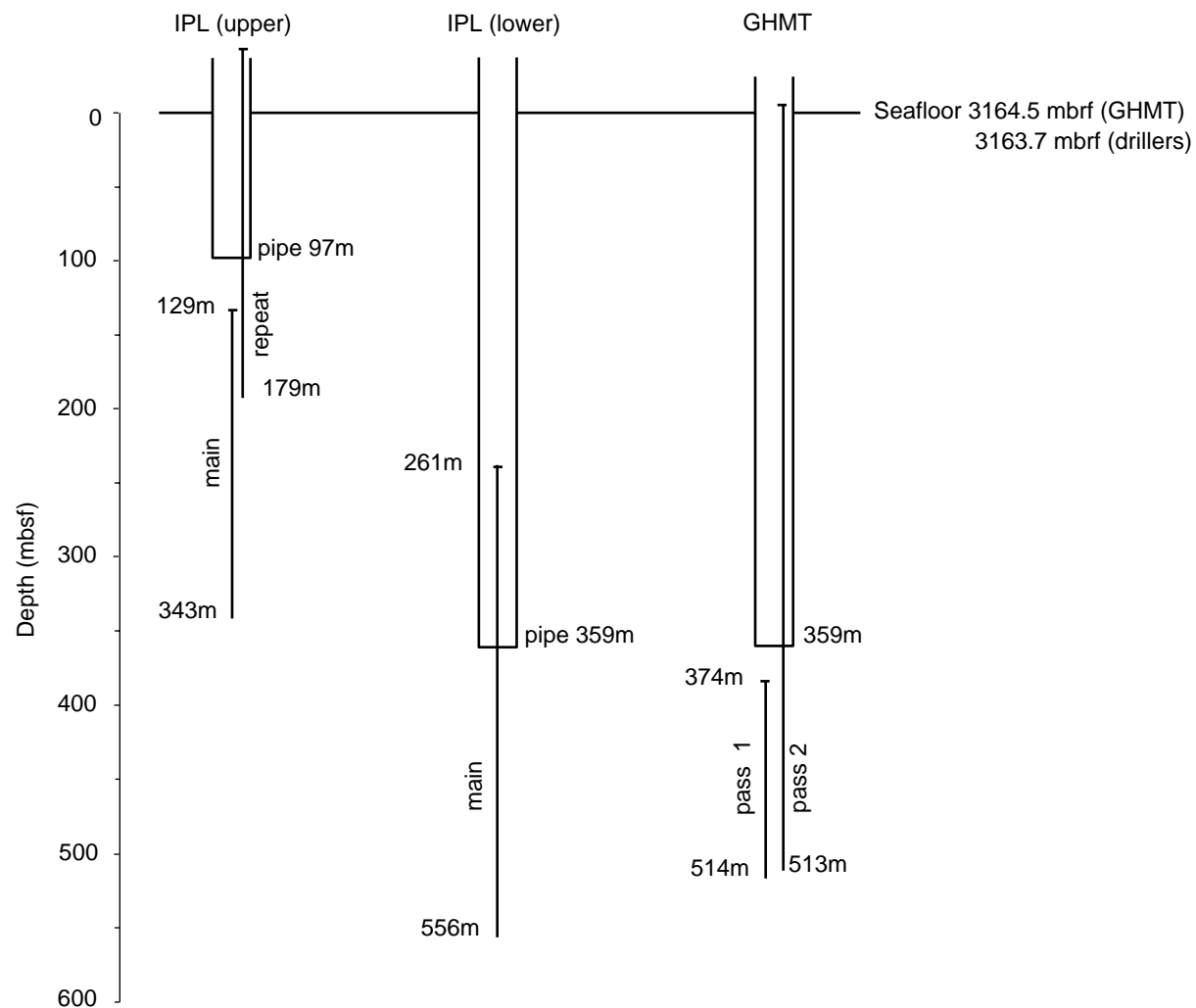


Figure F43. Downhole logs of hole diameter, total natural gamma (HSGR), bulk density (RHOM), porosity (APLC), total natural gamma from GHMT (SGR), and magnetic susceptibility (RMGS) from Hole 1096C, with core measurements of bulk density and porosity (index properties). Depth adjustments have been applied to bring all logs to a common measurement position below the seafloor.

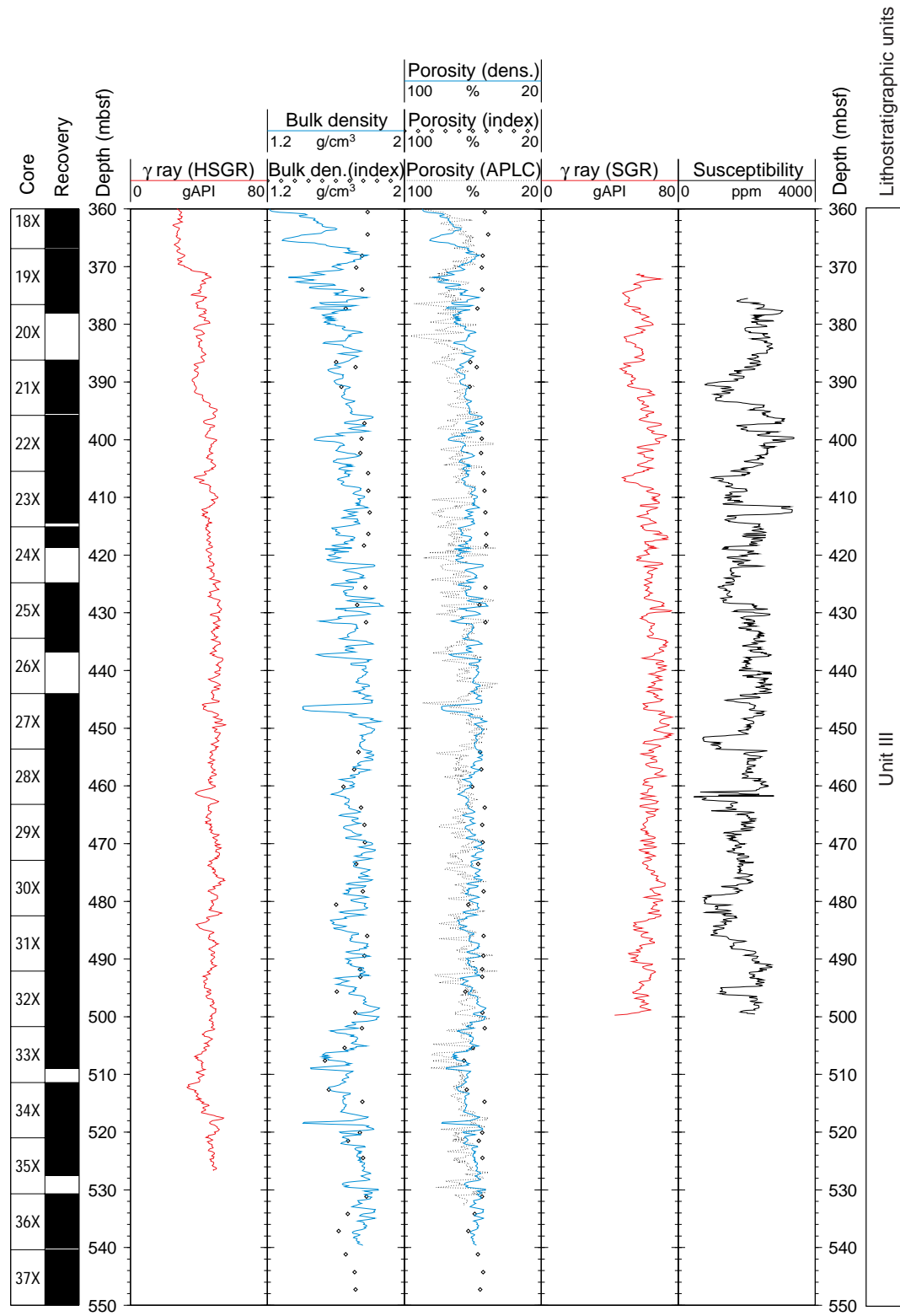


Figure F44. Gamma-ray logs in Hole 1096C from the IPLT (HSGR) and GHMT (SGR) tool strings, corrected for the attenuation caused by the pipe and BHA. Core MST natural gamma from Holes 1096A, 1096B, and 1096C is also plotted.

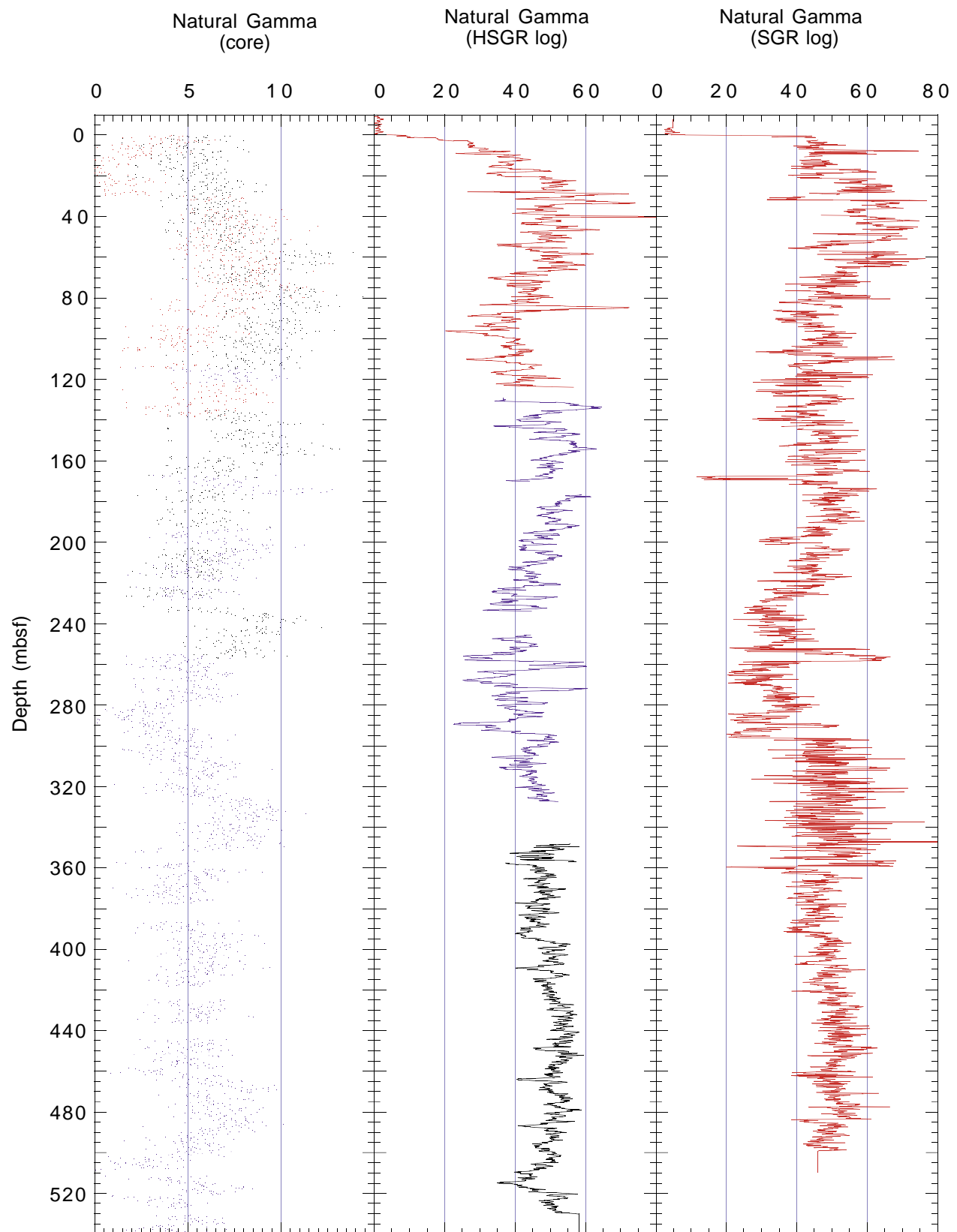


Figure F45. Downhole logs of uranium, potassium, thorium/potassium ratio (from the HNGS natural gamma tool), photoelectric effect (from the HLDS lithodensity tool), and magnetic susceptibility (from the GHMT tool) in Hole 1096C. A guide to interpretation is given beneath, and example A is discussed in the text. Depth adjustments have been applied to bring all logs to a common measurement position below the seafloor. Plag. = plagioclase, montm. = montmorillonite.

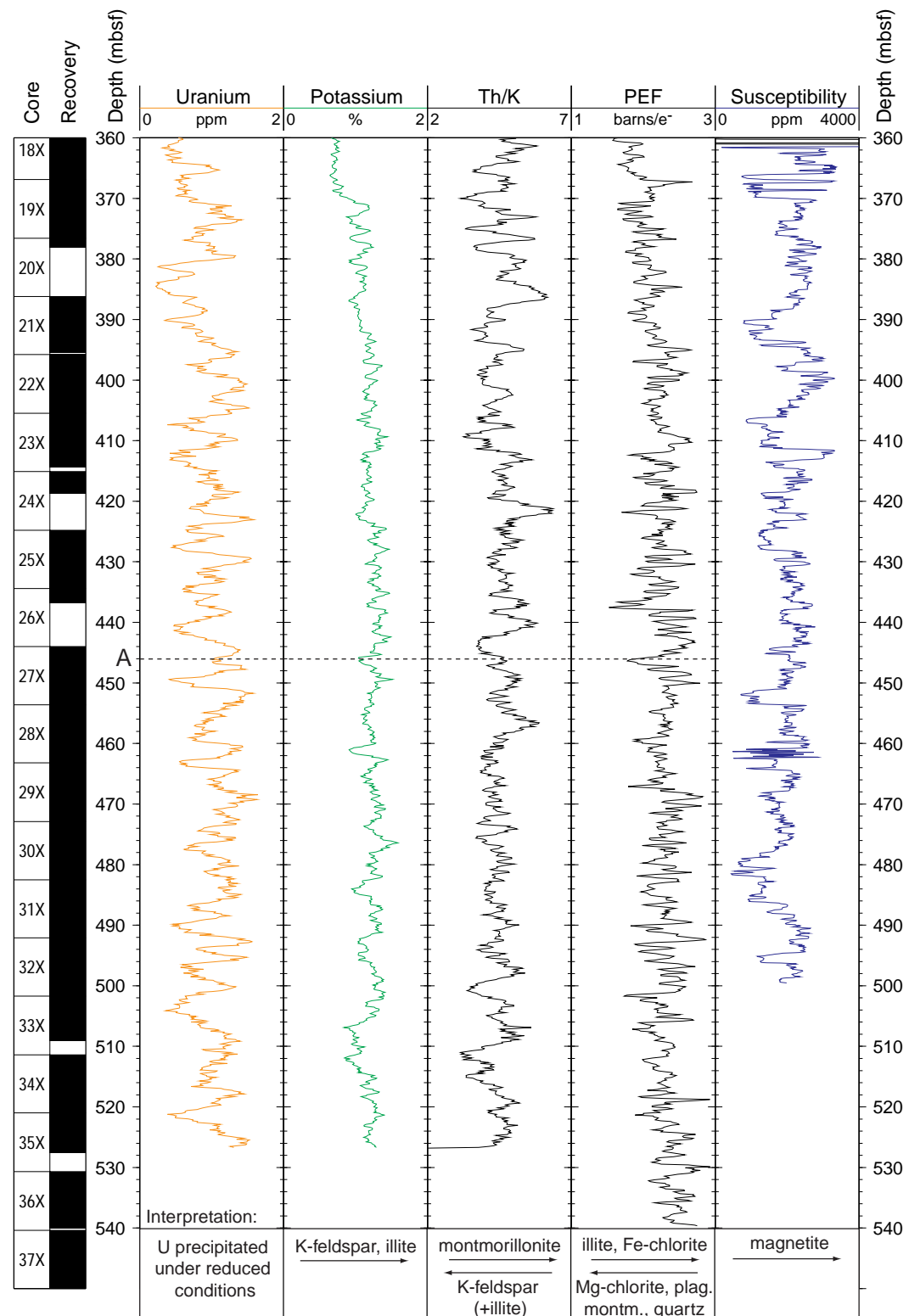


Figure F46. PEF vs. potassium for the interval 360–525 mbsf in Hole 1096C. Both logs were corrected for sediment porosity. The mineral fields are from the Schlumberger chart and represent the positions if that mineral composed 100% of the sediment.

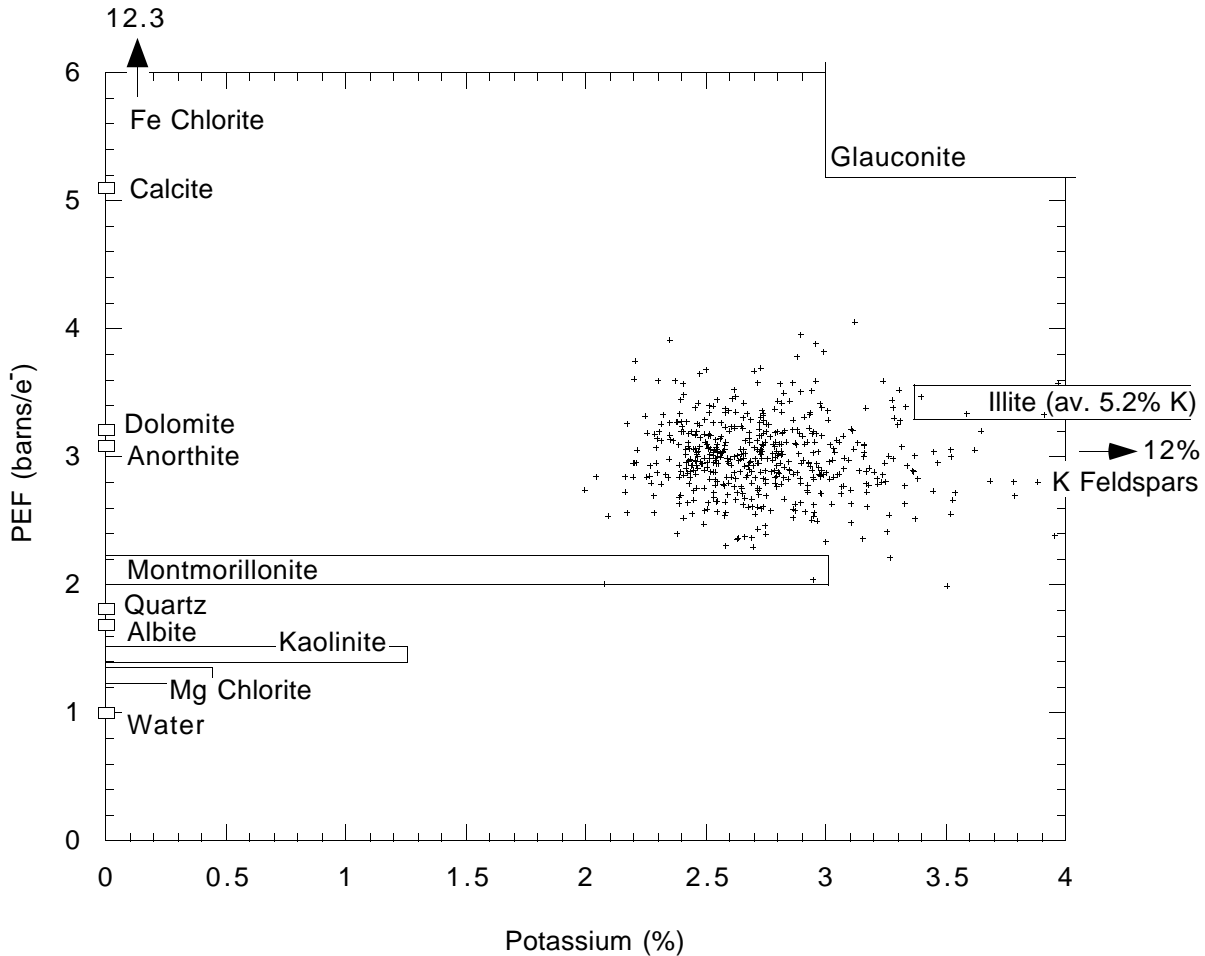


Figure F47. Polarity stratigraphy in Hole 1096C from the GHMT tool string. A. Magnetic field anomaly (total field less 43,300 nT, the Earth's field at the surface), with the modeled pipe effect. B. The field anomaly corrected for the pipe effect. C. Susceptibility (RMGS) converted to an induction in the borehole. D. The field anomaly resulting from the remanent magnetization, calculated by subtracting the induction anomaly from the pipe-corrected total field anomaly (normal polarity corresponds to negative values). E. Polarity.

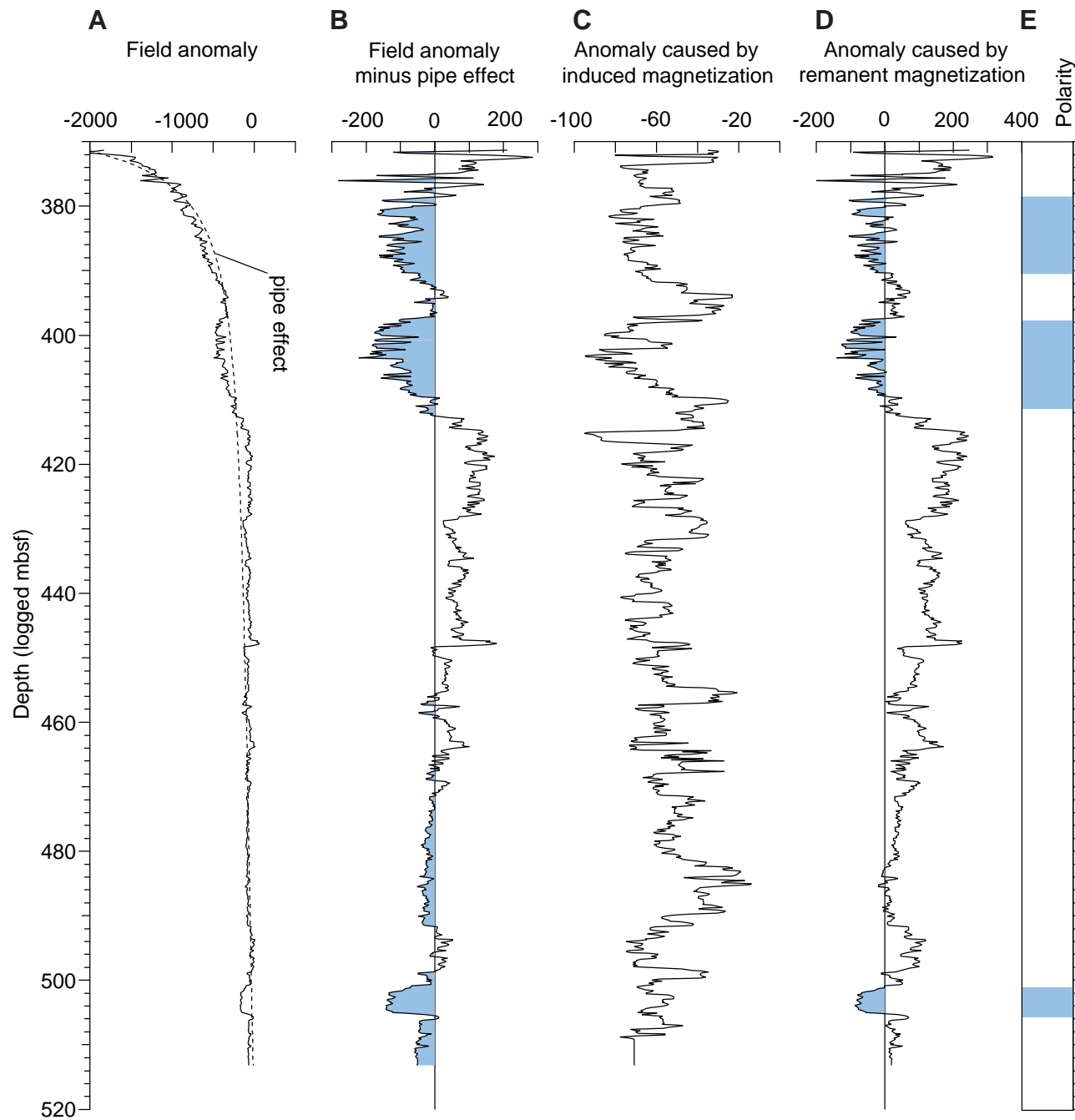


Figure F48. Temperature log from Hole 1096C, taken during the lower IPLT run. See text for discussion and compare with Figure F41, p. 80.

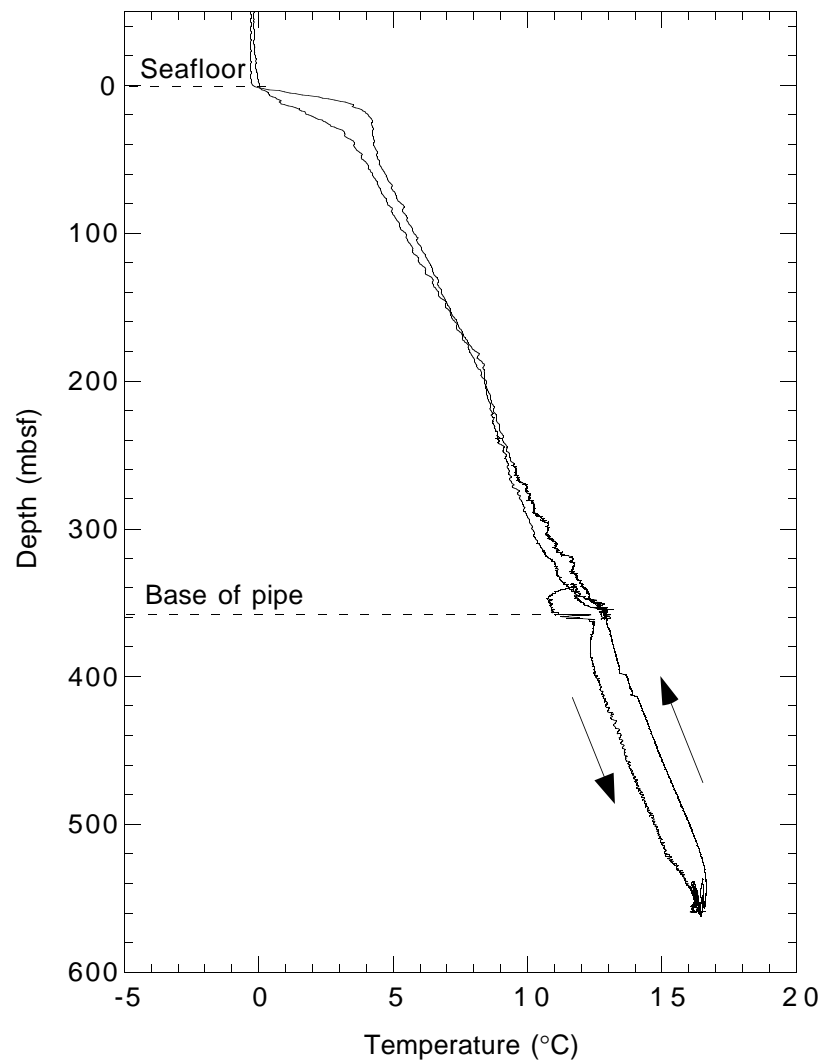


Figure F49. Visual correlation of chromaticity parameter a^* , magnetic susceptibility, GRAPE density, and natural gamma radiation data. Note the cyclic pattern. The symbols I and ? = negative correlation and no correlation, respectively. Composite depths are preliminary (see “[Composite Depths](#),” p. 23, in the “Explanatory Notes” chapter).

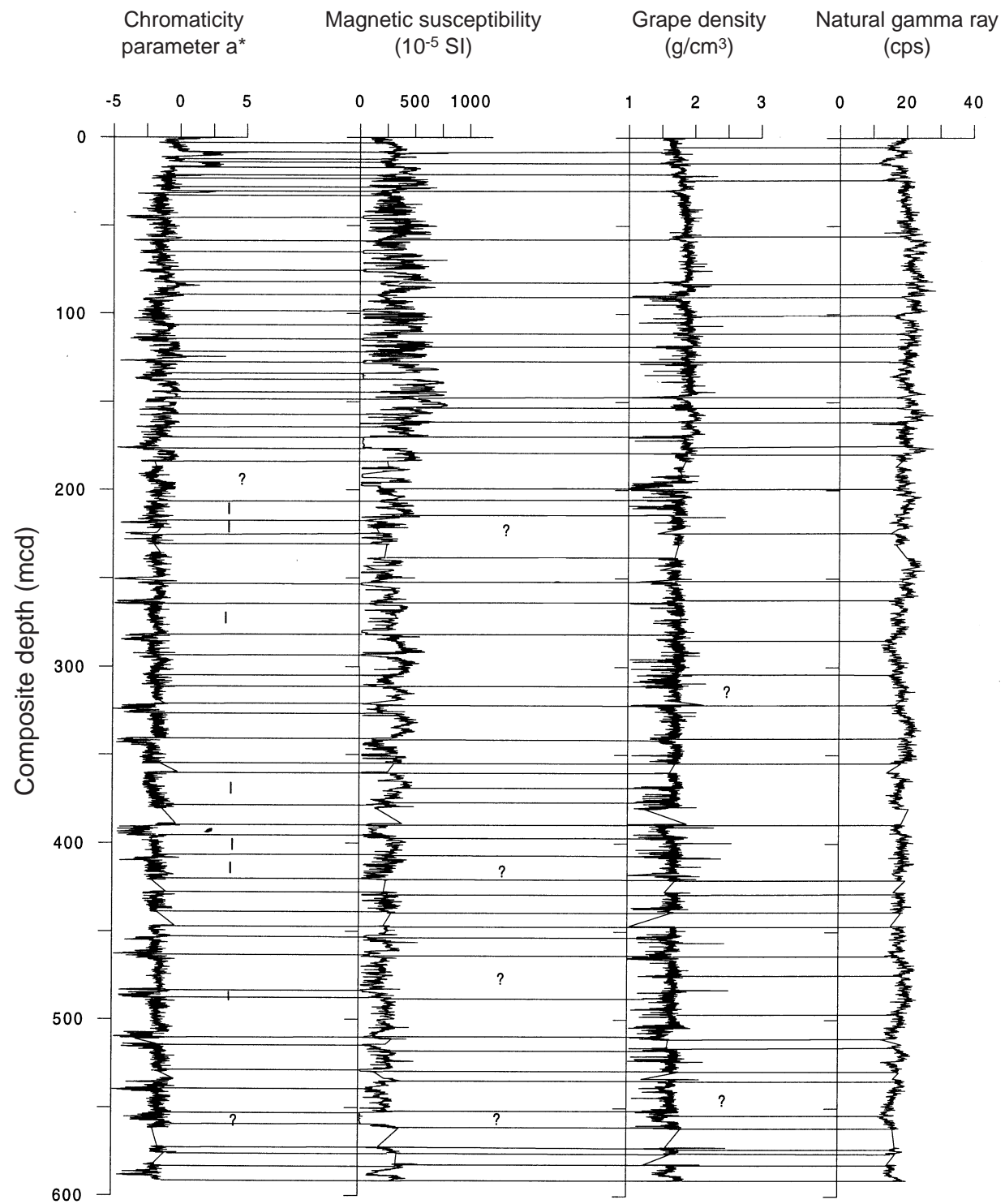


Figure F50. Magnetic susceptibility and chromaticity parameter a^* data from Site 1096 on the mcd scale. Lines for Holes 1096B (dotted) and 1096C (dashed) have been horizontally offset with respect to the line for Hole 1096A (solid) for better display; therefore, values given on the horizontal scale are true values only for Hole 1096A.

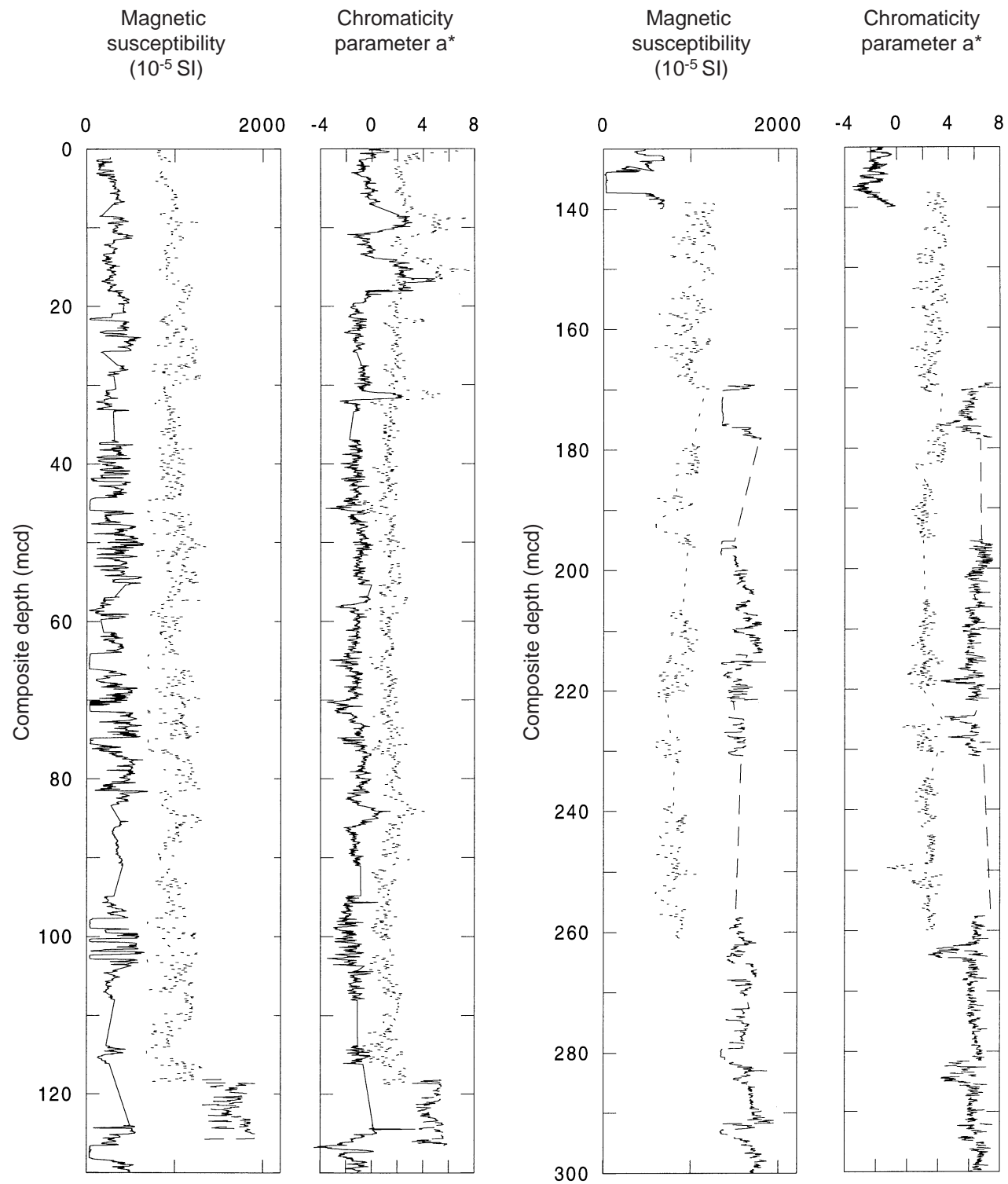


Figure F51. Depth offsets of the Site 1096 mcd scale relative to mbsf depth, illustrating the growth of the composite depth. Crosses = Hole 1096A, circles = Hole 1096B, squares = Hole 1096C.

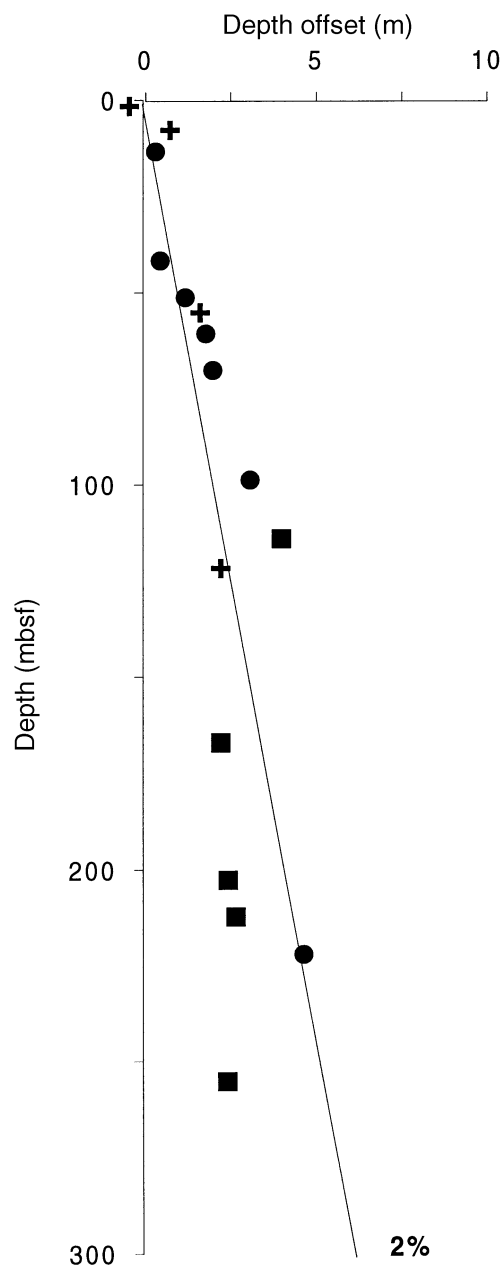


Figure F52. Spliced records of magnetic susceptibility and GRAPE density data for Site 1096. Tie points for forming the splice are given in Table T32, p. 140.

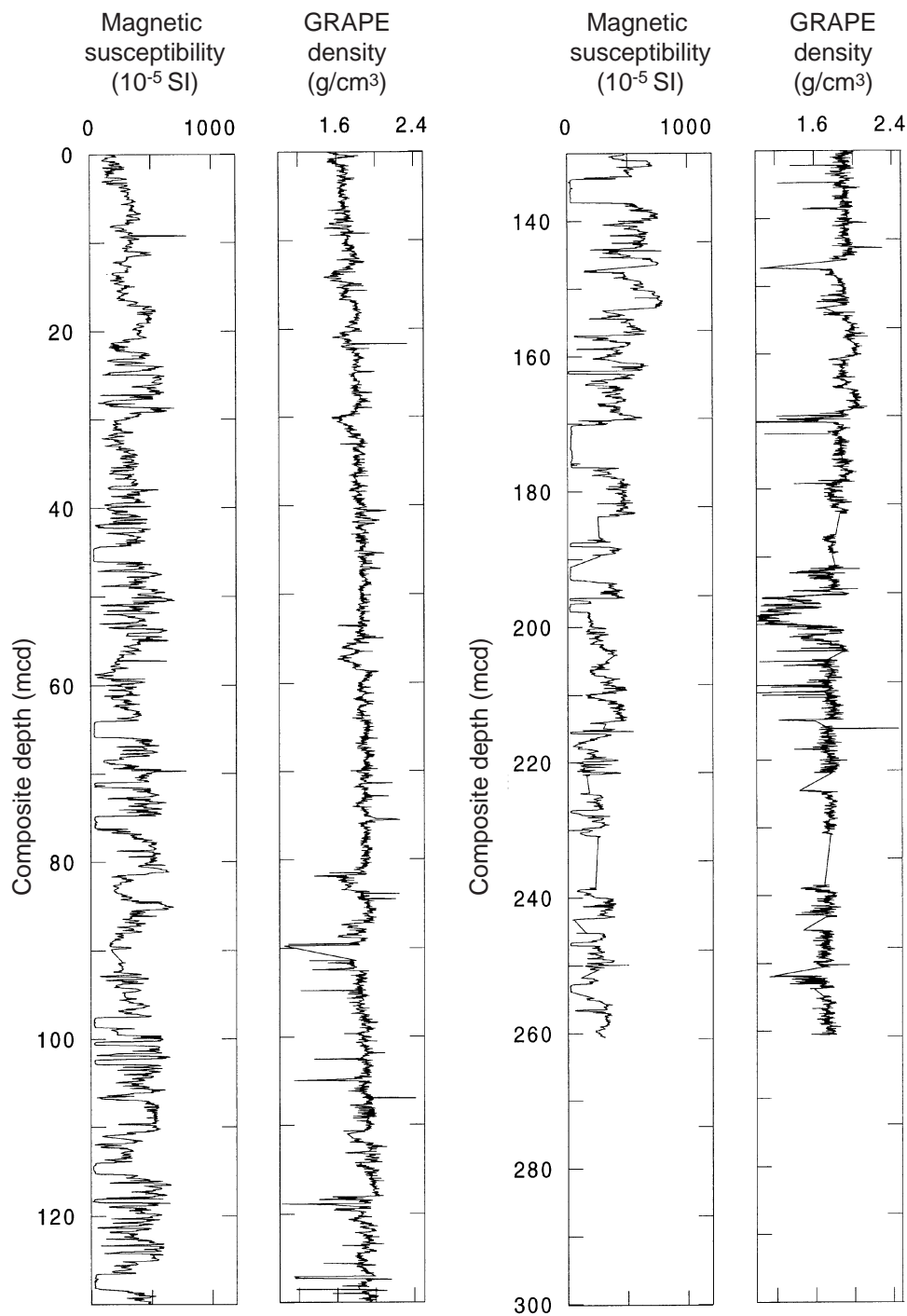


Figure F53. Depth-age relationship for Site 1096 on the basis of geomagnetic reversals (X), biostratigraphic diatom ranges (dark bars), and radiolarian datums (circles). Paleomagnetic data were drawn from shipboard analysis of cores. Intervals of diatom datums are marked with a dark bar indicating the distance between the samples used to define the FO or LO interval. In labels showing species identity, B = first occurrence, T = last occurrence. Sedimentation rates (underlined) for selected intervals are adjacent to the corresponding curve. Vertical solid arrows = dominant age-diagnostic fossil type (biosiliceous vs. calcareous) for respective intervals of this site. Dashed vertical line below B *F. interfrigidaria* datum interval indicates range of published depths for this datum.

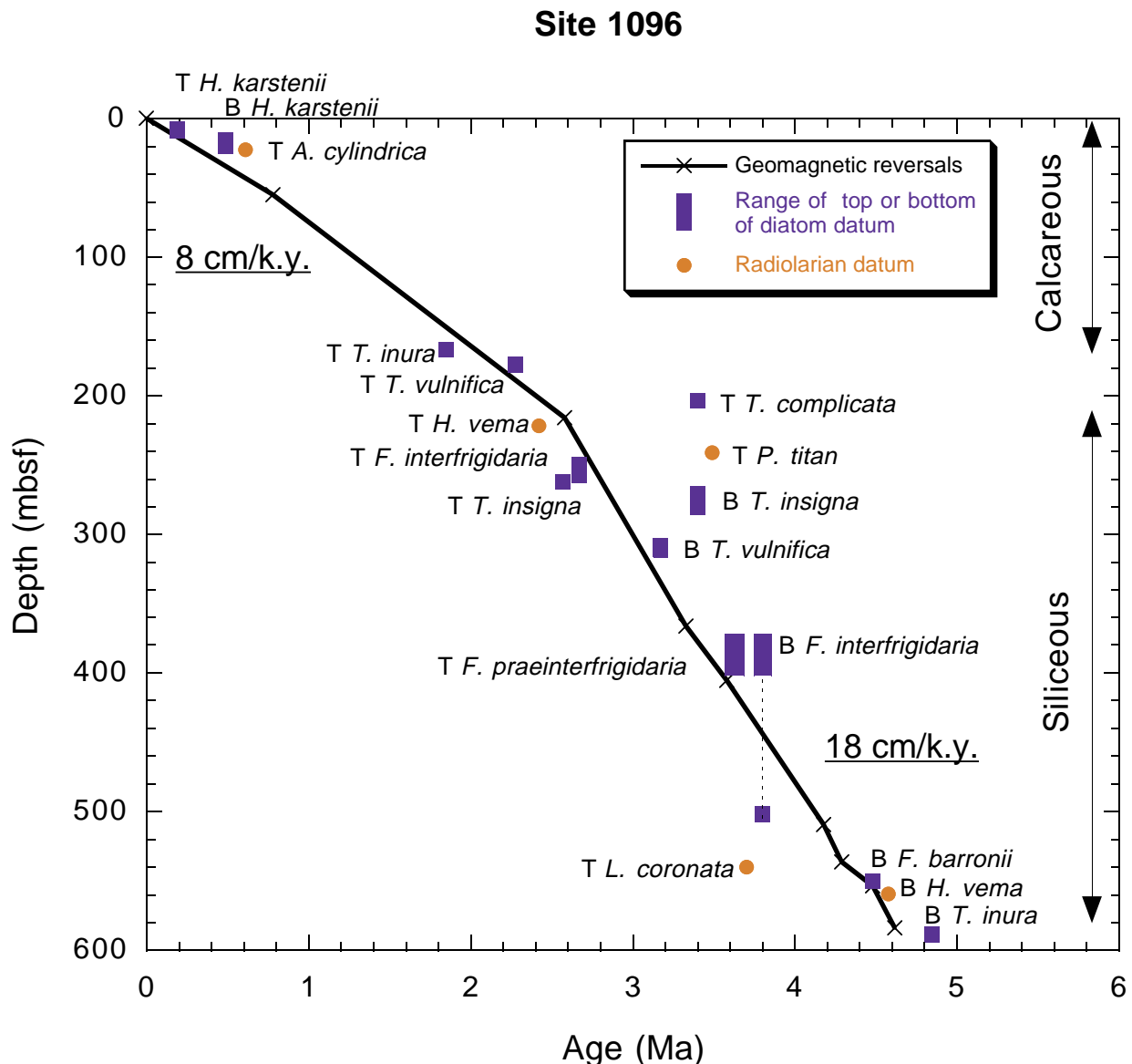


Figure F54. Sedimentation rates vs. depth and age. Age-depth fix points used for calculation are given in Table T34, p. 143.

Site 1096

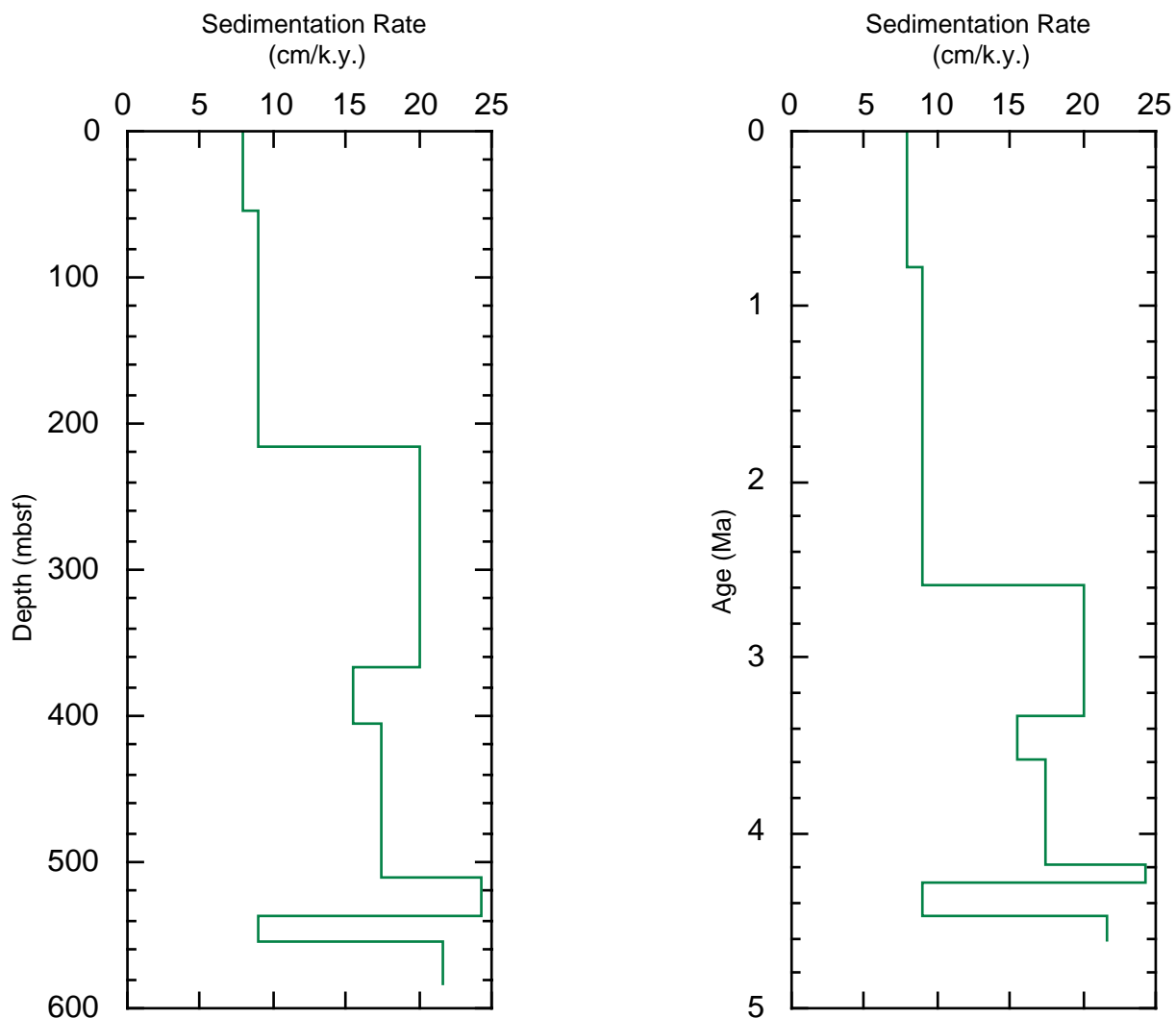


Figure F55. Comparison of MST (smoothed), downhole logging, and index properties densities used for different modeling approaches at Site 1096.

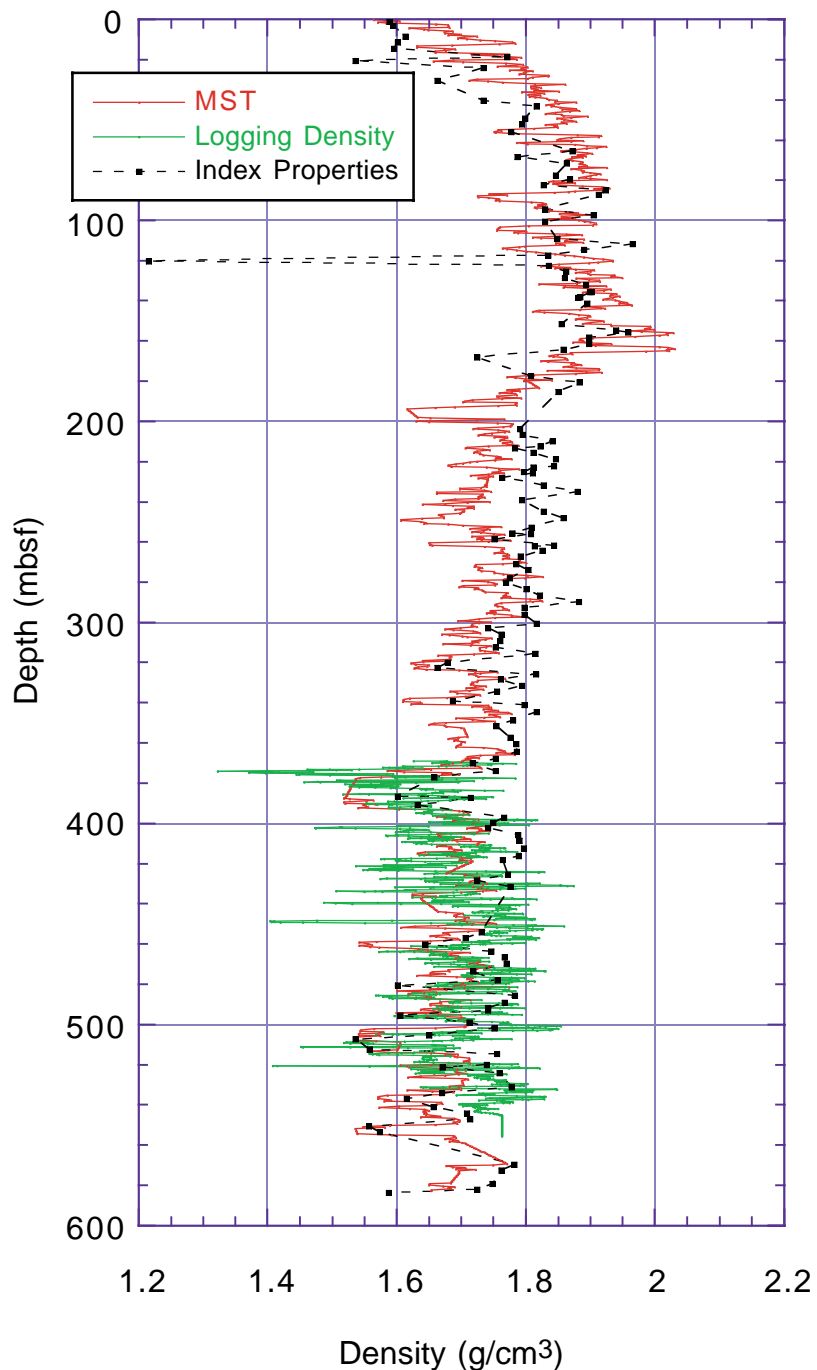


Figure F56. Comparison of MST and PWS *P*-wave velocity used for different modeling approaches at Site 1096.

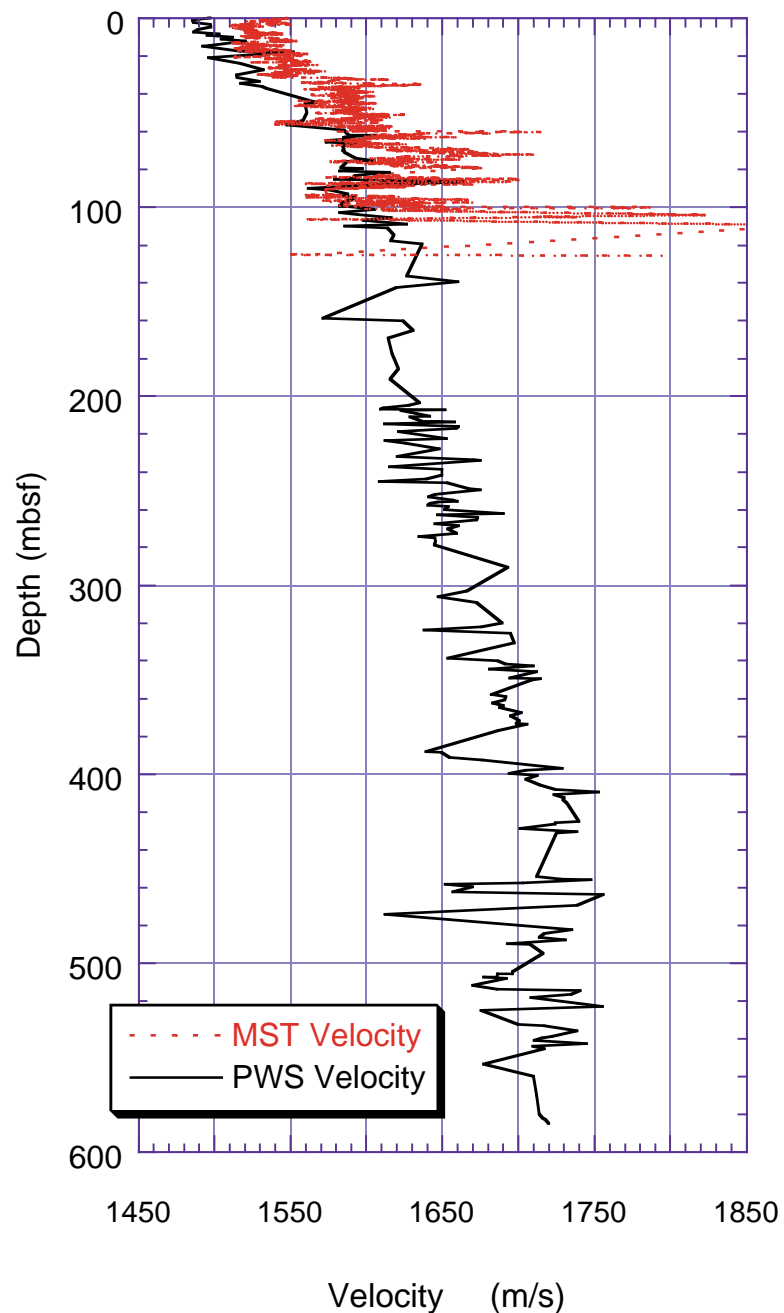


Figure F57. Traveleltime depth models for Site 1096 and comparison with the Site 1095 data and the Carlson approximation.

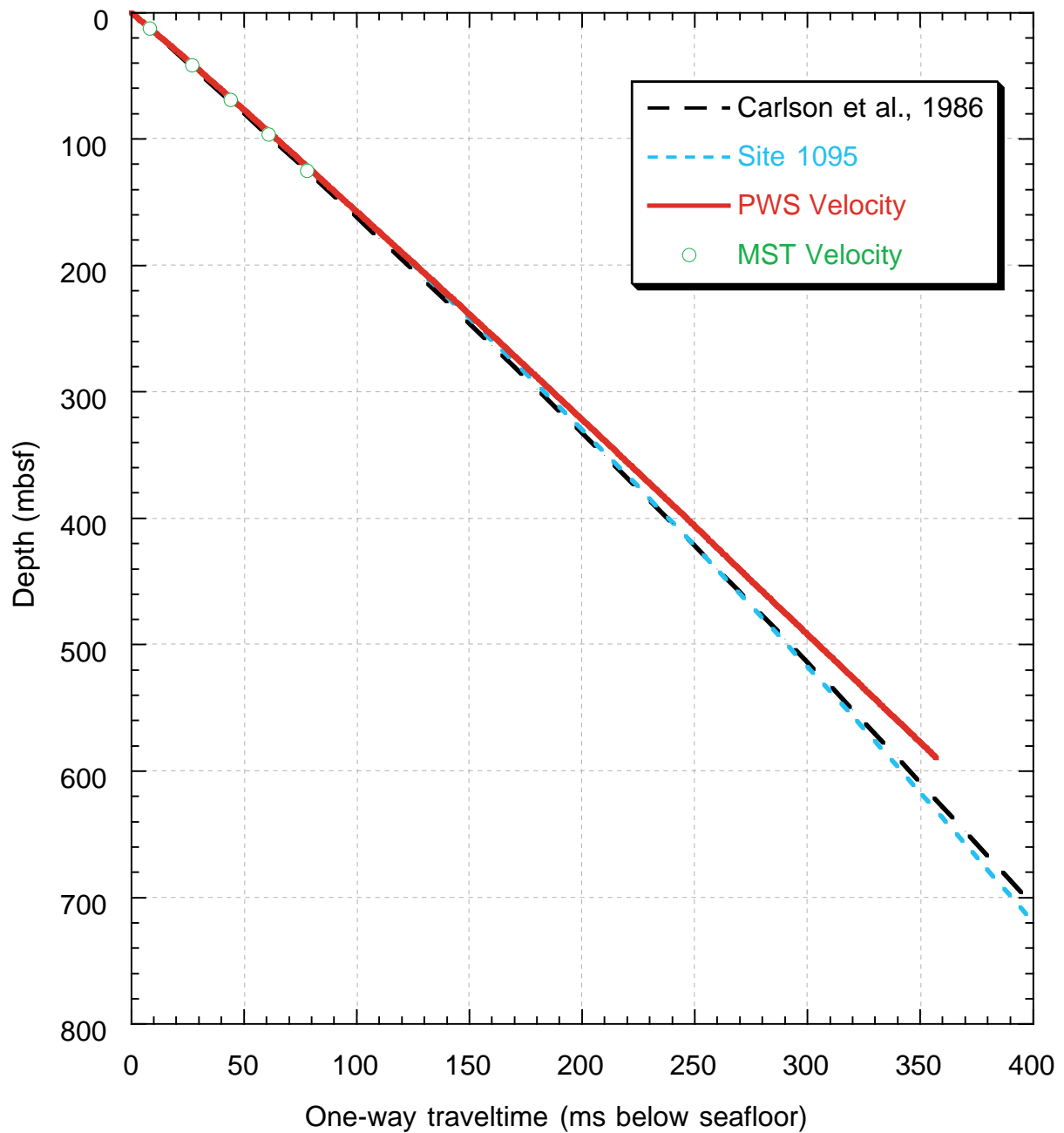


Figure F58. Site 1096 synthetic seismograms and corresponding density/velocity model derived from index properties data and PWS measurements.

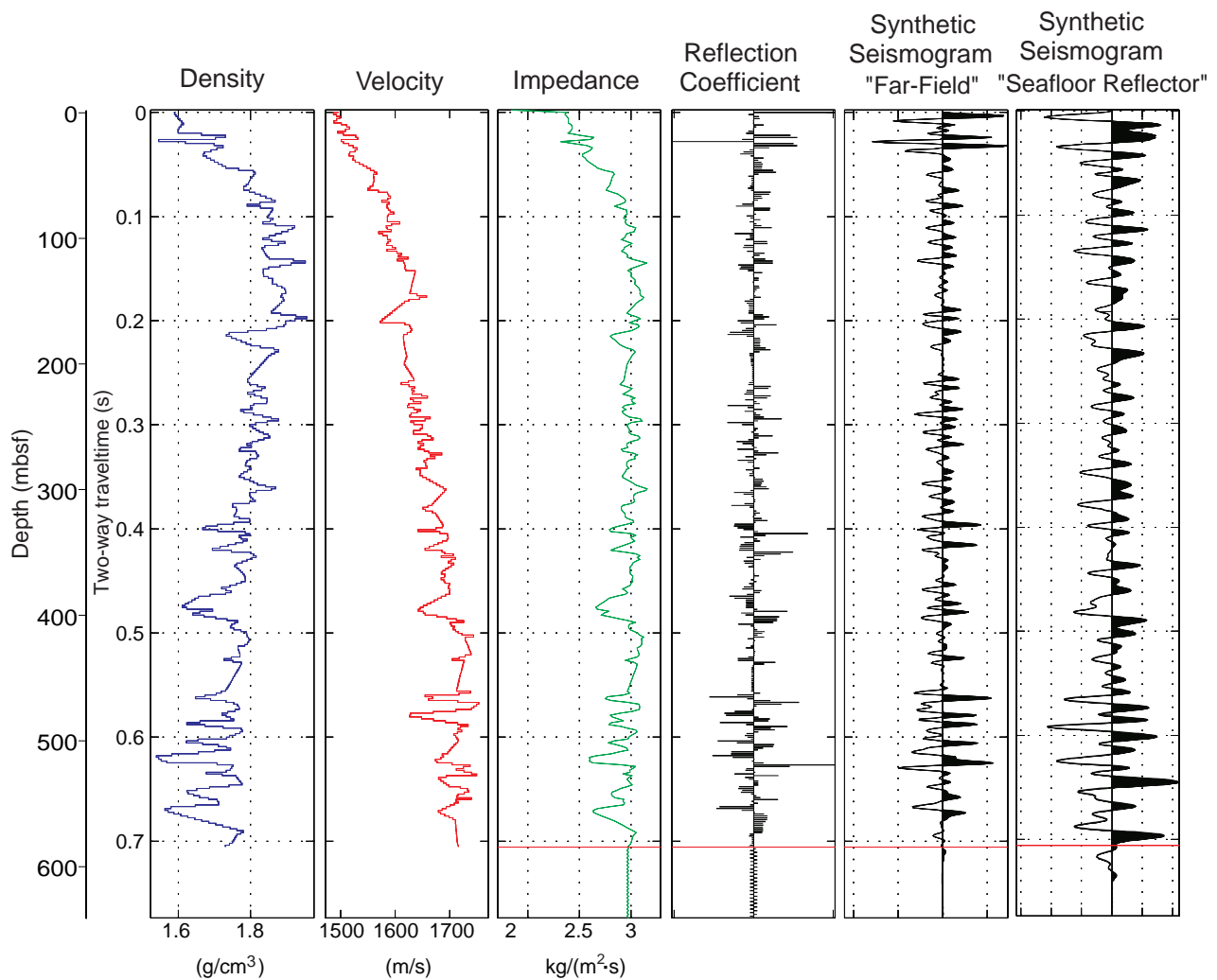


Figure F59. Site 1096 synthetic seismogram (constructed using the far-field wavelet) and field survey traces.

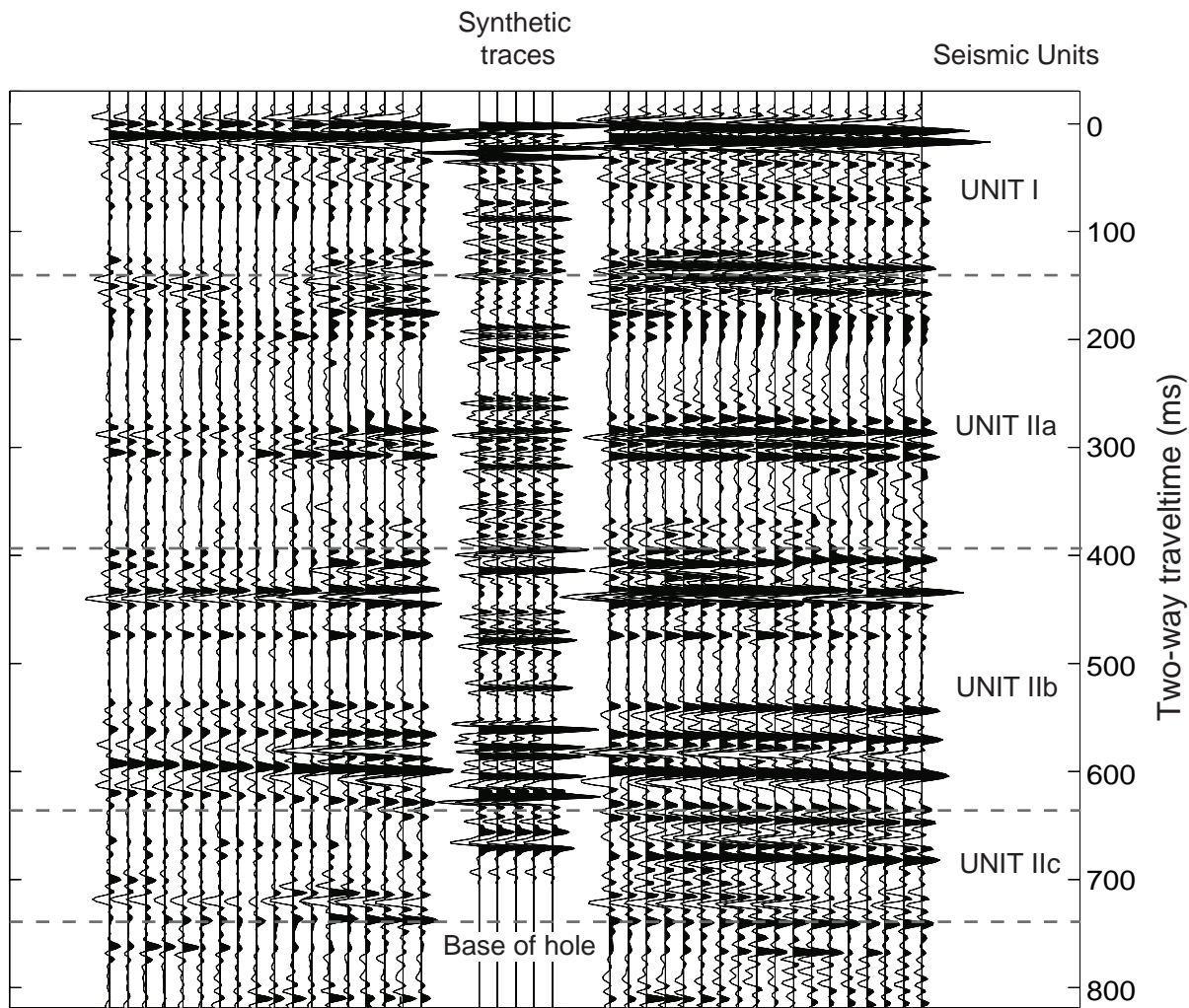


Figure F60. Site 1096 synthetic seismogram (constructed using the seafloor reflection wavelet) and field survey traces.

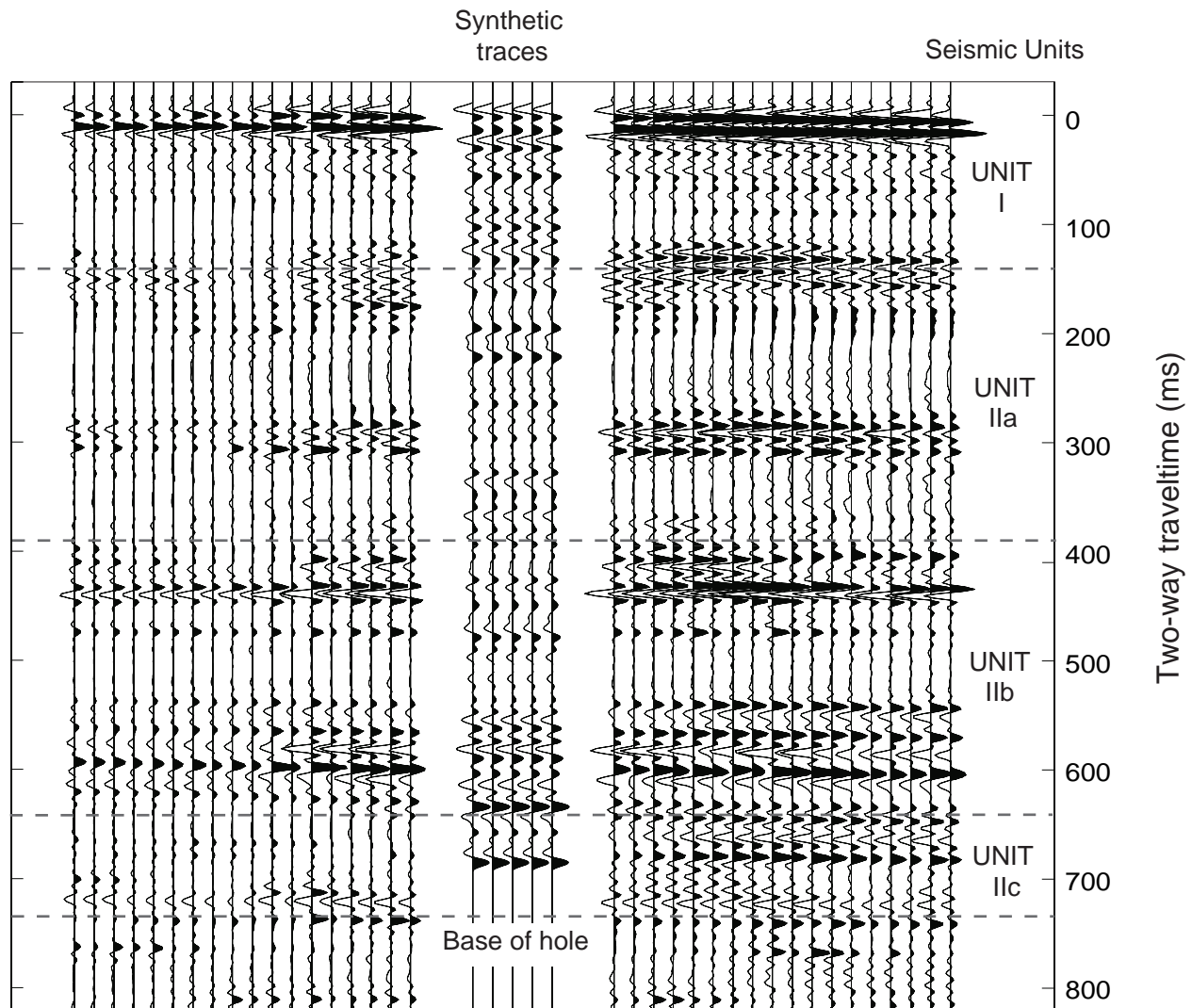


Figure F61. Integration of seismic reflection profile IT92-109 with seismostratigraphic and lithostratigraphic units. BSR = bottom-simulating reflector.

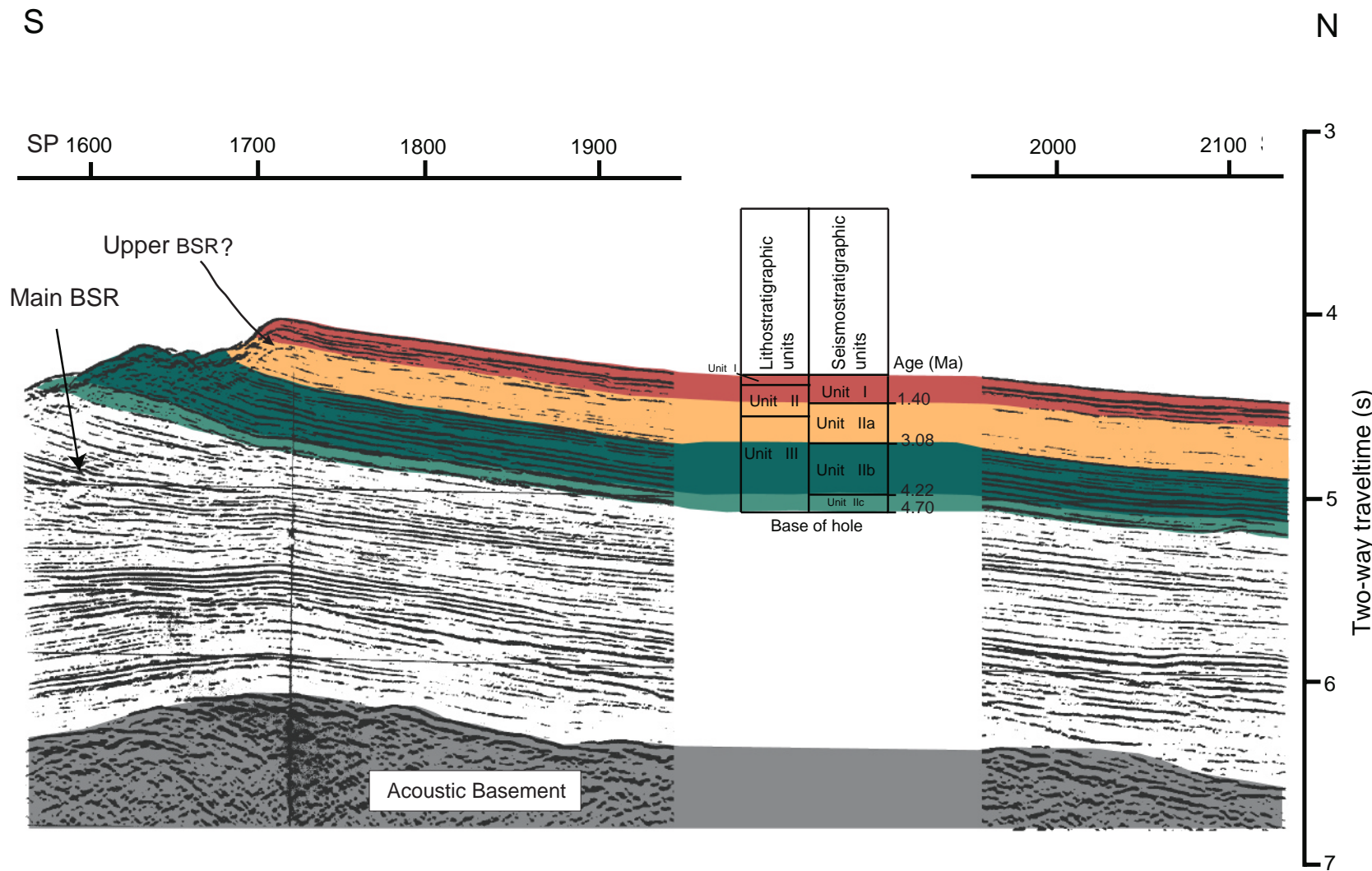


Table T1. Site 1096 coring summary. (See table note.
Continued on next page.)

Table T1 (continued).

Core	Date (1998)	Time (UTC)	Depth (mbsf)	Length cored (m)	Length recovered (m)	Recovery (%)
7X	1 Mar	1200	255.2-260.9	5.7	7.11	124.7
8X	1 Mar	1300	260.9-270.5	9.6	9.83	102.4
9X	1 Mar	1425	270.5-280.0	9.5	9.89	104.1
10X	1 Mar	1555	280.0-289.6	9.6	9.84	102.5
11X	1 Mar	1715	289.6-299.2	9.6	9.98	104.0
12X	1 Mar	1835	299.2-308.8	9.6	9.99	104.1
13X	1 Mar	2000	308.8-318.5	9.7	8.28	85.4
14X	1 Mar	2145	318.5-328.2	9.7	9.89	102.0
15X	1 Mar	2325	328.2-337.9	9.7	9.77	100.7
16X	2 Mar	0055	337.9-347.5	9.6	9.79	102.0
17X	2 Mar	0245	347.5-357.2	9.7	5.41	55.8
18X	2 Mar	0350	357.2-366.9	9.7	9.57	98.7
19X	2 Mar	0505	366.9-376.6	9.7	10.10	104.1
20X	2 Mar	0620	376.6-386.2	9.6	1.56	16.3
21X	2 Mar	0730	386.2-395.8	9.6	9.35	97.4
22X	2 Mar	0905	395.8-405.5	9.7	9.95	102.6
23X	2 Mar	1020	405.5-415.1	9.6	8.93	93.0
24X	2 Mar	1150	415.1-424.8	9.7	3.65	37.6
25X	2 Mar	1325	424.8-434.4	9.6	9.74	101.5
26X	2 Mar	1510	434.4-444.0	9.6	2.42	25.2
27X	2 Mar	1700	444.0-453.6	9.6	9.63	100.3
28X	2 Mar	1835	453.6-463.2	9.6	10.10	105.2
29X	2 Mar	2020	463.2-472.9	9.7	9.99	103.0
30X	2 Mar	2155	472.9-482.5	9.6	9.90	103.1
31X	2 Mar	2320	482.5-492.1	9.6	10.00	104.2
32X	3 Mar	0110	492.1-501.7	9.6	9.74	101.5
33X	3 Mar	0240	501.7-511.4	9.7	7.35	75.8
34X	3 Mar	0410	511.4-521.0	9.6	9.99	104.1
35X	3 Mar	0600	521.0-530.7	9.7	6.54	67.4
36X	3 Mar	0740	530.7-540.4	9.7	9.36	96.5
37X	3 Mar	0905	540.4-550.1	9.7	9.90	102.1
38X	3 Mar	1030	550.1-559.8	9.7	9.32	96.1
39X	3 Mar	1215	559.8-569.4	9.6	0.00	0.0
40X	3 Mar	1355	569.4-579.1	9.7	4.12	42.5
41X	3 Mar	1610	579.1-588.6	9.5	9.74	102.5
42X	3 Mar	1845	588.6-598.1	9.5	0.51	5.4
43X	3 Mar	2250	598.1-607.7	9.6	0.34	3.5
Coring totals:				409.9	344.98	84.2
Drilled:				197.8		
Total:				607.7		

Notes: UTC = Universal Time Coordinated. An expanded version of this coring summary table that includes lengths and depths of sections and sampling comments is included in ASCII format in the **TABLES** directory.

Table T2. Summary of lithostratigraphic units identified at Site 1096.

Unit	Depth (mbsf)	Thickness (m)	Age	Lithology and characteristic features
I	0.0-32.8	32.8	Holocene to late Pleistocene	Laminated and massive, commonly bioturbated dark grayish brown to brown and olive-brown clay and diatom-bearing silty clay
II	32.8-173.0	140.2	late Pleistocene to late Pliocene	Parallel-laminated dark gray to very dark gray silts and mud turbidites with low biogenic content; massive dark gray to dark greenish gray silty clays, commonly with diatoms or foraminifers and ice-rafterd debris
III	173.0-607.7	434.7	late Pliocene to early Pliocene	Fine-grained, thinly laminated, and generally nonbioturbated dark gray and dark greenish gray silty clays; homogenous intensely bioturbated dark greenish gray and greenish gray silty clays

Table T3. The first and last occurrences of diatom species observed at Site 1096 in their stratigraphic order (youngest at the top). (Continued on next page.)

Diatom events	A BKSA95	B BKSA95	C	Hole 1096A	Top depth (mbsf)	Bottom depth (mbsf)
TC <i>Hemidiscus karstenii</i>				0.19	1H-CC<, <2H-4, 127	7.69 13.47
BC <i>Hemidiscus karstenii</i>				0.42	2H-6, 80<, <3H-3, 30	16.00 20.50
T <i>Actinocyclus ingens</i>	0.64	0.64	0.65			
T <i>Fragilariopsis barronii</i>	1.39	1.40	1.30			
T <i>Thalassiosira kolbei</i>	1.85	2.00	2.00			
T <i>Actinocyclus karstenii</i>	1.78-2.90				Base of hole = 140.7 mbsf	
T <i>Thalassiosira inura</i>	1.85	2.50				
T <i>Thalassiosira vulnifica</i>	2.28	2.50	2.30			
T <i>Thalassiosira complicata</i>	3.40	2.50				
T <i>Thalassiosira insignia</i>	2.57	2.63	2.60			
T <i>Fragilariopsis interfrigidaria</i>	2.67	2.63				
B <i>Thalassiosira vulnifica</i>	3.17	3.26				
B <i>Thalassiosira insignia</i>	3.40	3.40				
B <i>Fragilariopsis interfrigidaria</i>	3.80	3.80				
T <i>Fragilariopsis praefrigidaria</i>	3.64	3.80				
B <i>Fragilariopsis barronii</i>	4.48	4.44				
T <i>Cosmiodiscus intersectus</i>		4.89				
T <i>Thalassiosira oliveriana</i> var. <i>sparsa</i>	4.85					
B <i>Thalassiosira inura</i>	4.85	4.92				

Note: Species listed in bold print are used as zonal boundary markers. Ages according to (A) Harwood and Maruyama (1992), (B) Shipboard Scientific Party (1999), and (C) Gersonde and Bár-cena (1998) listed next to each species, where applicable. The interval in which the first/last occurrence was observed and the actual depth (mbsf) shown for all three holes. Datums occur in the cores within the interval listed for each species. T = top/last occurrence datum, B = base/first occurrence datum, BC = base common/first common occurrence datum, TC = top common/last common occurrence datum. BKSA = Berggren et al. (1995). Gray boxes = either an interval drilled but not cored, or an interval not drilled.

Table T3 (continued).

Diatom events	Hole 1096B	Top depth (mbsf)	Bottom depth (mbsf)	Hole 1096C	Top depth (mbsf)	Bottom depth (mbsf)
TC <i>Hemidiscus karstenii</i>	<2H-4, 30		8.60	Base of hole = 607.7 mbsf		
BC <i>Hemidiscus karstenii</i>	3H-1, 140<, 3H-CC	14.7	23.05	Drilled but not cored		
T <i>Actinocyclus ingens</i>					114.0 mbsf	
T <i>Fragilariopsis barronii</i>						
T <i>Thalassiosira kolbei</i>						
T <i>Actinocyclus karstenii</i>	<20H-CC		166.60			
T <i>Thalassiosira inura</i>	<21H-CC		166.80			
T <i>Thalassiosira vulnifica</i>	<23X-3, 70		177.60			
T <i>Thalassiosira complicata</i>	<26X-1, 88		203.80			
T <i>Thalassiosira insignia</i>	<30X-1, 82cm<, <30X-2, 72cm	243.50		<7X-CC		262.26
T <i>Fragilariopsis interfrigidaria</i>	31X-CC<, <32X-CC?	250.3	257.30			
B <i>Thalassiosira vulnifica</i>	29X-CC<	239.7		13X-1, 10<, <13X-2, 80	308.90	311.10
B <i>Thalassiosira insignia</i>	32X-CC<	257.3		8X-CC<, <9X-CC	270.68	280.37
B <i>Fragilariopsis interfrigidaria</i>	Base of hole = 260.6 mbsf			30X-CC<, <31X-CC	482.50	492.10
T <i>Fragilariopsis praefinterfrigidaria</i>				24X-CC<, <25X-2, 19	424.80	426.50
B <i>Fragilariopsis barronii</i>				37X-CC<, <38X-3, 45	550.25	555.00
T <i>Cosmiodiscus intersectus</i>				<36X-CC		540.01
T <i>Thalassiosira oliveriana</i> var. <i>sparsa</i>				40X-CC<, <41X-C	579.10	588.60
B <i>Thalassiosira inura</i>						

Table T4. Split-core paleomagnetic measurements for Hole 1096A before demagnetization (NRM results).

Leg	Site	Hole	Core	Type	Section	Interval (cm)	Depth (mbsf)	Inclination (°)	Declination (°)	Intensity (A/m)	Demagnetization step (mT)	Run #
178	1096	A	1	H	1	10	0.1	-48.85	26.25	1.08E-01	0	5325
178	1096	A	1	H	1	15	0.15	-55.2	24.91	1.20E-01	0	5325
178	1096	A	1	H	1	20	0.2	-56.58	22.14	1.16E-01	0	5325
178	1096	A	1	H	1	25	0.25	-63.52	1.18	1.02E-01	0	5325
178	1096	A	1	H	1	30	0.3	-66	332.1	9.18E-02	0	5325
178	1096	A	1	H	1	35	0.35	-63.75	302.25	8.91E-02	0	5325
178	1096	A	1	H	1	40	0.4	-62.41	296.5	7.13E-02	0	5325
178	1096	A	1	H	1	45	0.45	-59.04	260.18	7.56E-02	0	5325
178	1096	A	1	H	1	50	0.5	-60.11	287.22	9.31E-02	0	5325
178	1096	A	1	H	1	55	0.55	-59.61	5.29	9.35E-02	0	5325
178	1096	A	1	H	1	60	0.6	-58.52	8.5	1.15E-01	0	5325
178	1096	A	1	H	1	65	0.65	-63.02	324.71	1.38E-01	0	5325
178	1096	A	1	H	1	70	0.7	-67.91	9.55	1.77E-01	0	5325
178	1096	A	1	H	1	75	0.75	-60.16	29.41	2.34E-01	0	5325
178	1096	A	1	H	1	80	0.8	-62.59	27.17	2.33E-01	0	5325
178	1096	A	1	H	1	85	0.85	-67.77	33.19	2.50E-01	0	5325
178	1096	A	1	H	1	90	0.9	-62.44	28.15	3.32E-01	0	5325
178	1096	A	1	H	1	95	0.95	-60.9	6.86	3.32E-01	0	5325
178	1096	A	1	H	1	100	1	-67.16	28.15	2.44E-01	0	5325
178	1096	A	1	H	1	105	1.05	-65.34	36.51	2.45E-01	0	5325
178	1096	A	1	H	1	110	1.1	-69.43	30.7	2.38E-01	0	5325
178	1096	A	1	H	1	115	1.15	-64.58	30.4	2.87E-01	0	5325
178	1096	A	1	H	1	120	1.2	-63.4	41.59	2.56E-01	0	5325
178	1096	A	1	H	1	125	1.25	-64.1	38.03	2.78E-01	0	5325
178	1096	A	1	H	1	130	1.3	-62.43	34.57	2.81E-01	0	5325
178	1096	A	1	H	1	135	1.35	-66.46	40.43	2.43E-01	0	5325
178	1096	A	1	H	1	140	1.4	-67.69	22.73	2.06E-01	0	5325
178	1096	A	1	H	2	10	1.6	-72.28	5.66	1.74E-01	0	5328
178	1096	A	1	H	2	15	1.65	-72.35	10.1	1.85E-01	0	5328
178	1096	A	1	H	2	20	1.7	-65.24	358.9	1.94E-01	0	5328
178	1096	A	1	H	2	25	1.75	-62.57	356.64	1.77E-01	0	5328
178	1096	A	1	H	2	30	1.8	-67.88	3.12	1.31E-01	0	5328
178	1096	A	1	H	2	35	1.85	-69.87	341.18	1.03E-01	0	5328
178	1096	A	1	H	2	40	1.9	-59.1	290.63	9.88E-02	0	5328
178	1096	A	1	H	2	45	1.95	-48.89	282.34	1.17E-01	0	5328
178	1096	A	1	H	2	50	2	-46.4	284.21	1.11E-01	0	5328
178	1096	A	1	H	2	55	2.05	-46.42	294.01	1.17E-01	0	5328
178	1096	A	1	H	2	60	2.1	-50.22	318.34	1.28E-01	0	5328
178	1096	A	1	H	2	65	2.15	-59.6	343.43	1.31E-01	0	5328
178	1096	A	1	H	2	70	2.2	-66.96	1.9	1.36E-01	0	5328
178	1096	A	1	H	2	75	2.25	-73.22	1	1.58E-01	0	5328
178	1096	A	1	H	2	80	2.3	-70.63	3.36	1.73E-01	0	5328
178	1096	A	1	H	2	85	2.35	-75.9	6.87	1.57E-01	0	5328
178	1096	A	1	H	2	90	2.4	-82.86	8.56	1.71E-01	0	5328
178	1096	A	1	H	2	95	2.45	-77.55	1.34	2.23E-01	0	5328
178	1096	A	1	H	2	100	2.5	-75.37	320.6	2.31E-01	0	5328
178	1096	A	1	H	2	105	2.55	-68.74	303.32	2.48E-01	0	5328
178	1096	A	1	H	2	110	2.6	-67.73	329.22	2.30E-01	0	5328
178	1096	A	1	H	2	115	2.65	-67.49	335.25	1.91E-01	0	5328
178	1096	A	1	H	2	120	2.7	-76.1	327.47	1.51E-01	0	5328
178	1096	A	1	H	2	125	2.75	-76.55	320.13	1.44E-01	0	5328
178	1096	A	1	H	2	130	2.8	-70.93	310.04	1.43E-01	0	5328
178	1096	A	1	H	2	135	2.85	-70.37	312.46	1.30E-01	0	5328
178	1096	A	1	H	3	10	3.1	-61.83	338.22	1.18E-01	0	5331
178	1096	A	1	H	3	15	3.15	-61.4	348.99	1.64E-01	0	5331
178	1096	A	1	H	3	20	3.2	-60.42	358.91	1.90E-01	0	5331
178	1096	A	1	H	3	25	3.25	-63.77	4.59	1.95E-01	0	5331
178	1096	A	1	H	3	30	3.3	-66.61	10.75	1.80E-01	0	5331
178	1096	A	1	H	3	35	3.35	-66.38	16.43	1.58E-01	0	5331
178	1096	A	1	H	3	40	3.4	-65.73	18.62	1.17E-01	0	5331
178	1096	A	1	H	3	45	3.45	-63.21	18.18	8.02E-02	0	5331
178	1096	A	1	H	3	50	3.5	-59.73	11.56	5.85E-02	0	5331
178	1096	A	1	H	3	55	3.55	-39.39	315.91	5.31E-02	0	5331
178	1096	A	1	H	3	60	3.6	-45.12	326.74	6.67E-02	0	5331
178	1096	A	1	H	3	65	3.65	-50.19	28.07	7.80E-02	0	5331

Note: Only a portion of this table appears here. The complete table is available in ASCII format in the [TABLES](#) directory.

Table T5. Split-core paleomagnetic measurements for Hole 1096A after 10-mT demagnetization.

Leg	Site	Hole	Core	Type	Section	Interval (cm)	Depth (mbsf)	Inclination (°)	Declination (°)	Intensity (A/m)	Demagnetization step (mT)	Run #
178	1096	A	1	H	1	10	0.1	-65.79	39.79	1.14E-01	10	5326
178	1096	A	1	H	1	15	0.15	-66.79	27.02	1.27E-01	10	5326
178	1096	A	1	H	1	20	0.2	-64.88	22.98	1.20E-01	10	5326
178	1096	A	1	H	1	25	0.25	-71.35	0.51	1.06E-01	10	5326
178	1096	A	1	H	1	30	0.3	-71.82	320.01	9.57E-02	10	5326
178	1096	A	1	H	1	35	0.35	-68.55	286.95	9.22E-02	10	5326
178	1096	A	1	H	1	40	0.4	-68.93	277.6	7.71E-02	10	5326
178	1096	A	1	H	1	45	0.45	-60.99	250.16	8.47E-02	10	5326
178	1096	A	1	H	1	50	0.5	-62.91	279.26	9.66E-02	10	5326
178	1096	A	1	H	1	55	0.55	-65.17	3.05	9.29E-02	10	5326
178	1096	A	1	H	1	60	0.6	-63.45	6.96	1.13E-01	10	5326
178	1096	A	1	H	1	65	0.65	-66.19	317.53	1.37E-01	10	5326
178	1096	A	1	H	1	70	0.7	-74.16	6.59	1.78E-01	10	5326
178	1096	A	1	H	1	75	0.75	-65.93	30.09	2.32E-01	10	5326
178	1096	A	1	H	1	80	0.8	-67.63	26.8	2.33E-01	10	5326
178	1096	A	1	H	1	85	0.85	-72.68	35.62	2.52E-01	10	5326
178	1096	A	1	H	1	90	0.9	-67.04	28.91	3.31E-01	10	5326
178	1096	A	1	H	1	95	0.95	-64.79	5.52	3.31E-01	10	5326
178	1096	A	1	H	1	100	1	-70.89	29.89	2.45E-01	10	5326
178	1096	A	1	H	1	105	1.05	-69.12	39.61	2.45E-01	10	5326
178	1096	A	1	H	1	110	1.1	-73.26	33.94	2.39E-01	10	5326
178	1096	A	1	H	1	115	1.15	-69.47	35.06	2.89E-01	10	5326
178	1096	A	1	H	1	120	1.2	-68.08	48.51	2.63E-01	10	5326
178	1096	A	1	H	1	125	1.25	-69.25	44.28	2.86E-01	10	5326
178	1096	A	1	H	1	130	1.3	-68.36	39.49	2.89E-01	10	5326
178	1096	A	1	H	1	135	1.35	-72.54	48.56	2.54E-01	10	5326
178	1096	A	1	H	1	140	1.4	-75.63	29.24	2.16E-01	10	5326
178	1096	A	1	H	2	10	1.6	-79.53	1.76	1.83E-01	10	5329
178	1096	A	1	H	2	15	1.65	-78.87	9.17	1.95E-01	10	5329
178	1096	A	1	H	2	20	1.7	-72.3	358.73	2.00E-01	10	5329
178	1096	A	1	H	2	25	1.75	-70.07	351.89	1.85E-01	10	5329
178	1096	A	1	H	2	30	1.8	-75.04	0.18	1.41E-01	10	5329
178	1096	A	1	H	2	35	1.85	-75.2	333.64	1.12E-01	10	5329
178	1096	A	1	H	2	40	1.9	-61.42	287.72	1.04E-01	10	5329
178	1096	A	1	H	2	45	1.95	-50.69	278.66	1.20E-01	10	5329
178	1096	A	1	H	2	50	2	-50.05	279.75	1.15E-01	10	5329
178	1096	A	1	H	2	55	2.05	-54.23	282.94	1.26E-01	10	5329
178	1096	A	1	H	2	60	2.1	-64.99	297.05	1.50E-01	10	5329
178	1096	A	1	H	2	65	2.15	-73.13	330.6	1.59E-01	10	5329
178	1096	A	1	H	2	70	2.2	-73.9	357.65	1.55E-01	10	5329
178	1096	A	1	H	2	75	2.25	-77.83	355.82	1.69E-01	10	5329
178	1096	A	1	H	2	80	2.3	-74.45	1.69	1.83E-01	10	5329
178	1096	A	1	H	2	85	2.35	-78.42	5.83	1.67E-01	10	5329
178	1096	A	1	H	2	90	2.4	-85.32	6.58	1.79E-01	10	5329
178	1096	A	1	H	2	95	2.45	-80.17	358.39	2.32E-01	10	5329
178	1096	A	1	H	2	100	2.5	-76.21	316.55	2.37E-01	10	5329
178	1096	A	1	H	2	105	2.55	-69.75	298.26	2.52E-01	10	5329
178	1096	A	1	H	2	110	2.6	-72.86	329.1	2.33E-01	10	5329
178	1096	A	1	H	2	115	2.65	-71.02	338.13	1.99E-01	10	5329
178	1096	A	1	H	2	120	2.7	-78.1	316.95	1.57E-01	10	5329
178	1096	A	1	H	2	125	2.75	-78.71	306.01	1.50E-01	10	5329
178	1096	A	1	H	2	130	2.8	-73.34	299.13	1.50E-01	10	5329
178	1096	A	1	H	2	135	2.85	-73.56	301.43	1.37E-01	10	5329
178	1096	A	1	H	3	10	3.1	-65.94	333.3	1.22E-01	10	5332
178	1096	A	1	H	3	15	3.15	-67.05	344.17	1.70E-01	10	5332
178	1096	A	1	H	3	20	3.2	-66.19	356.15	1.98E-01	10	5332
178	1096	A	1	H	3	25	3.25	-69.55	2.04	2.05E-01	10	5332
178	1096	A	1	H	3	30	3.3	-71.74	8.28	1.92E-01	10	5332
178	1096	A	1	H	3	35	3.35	-71.16	15.2	1.68E-01	10	5332
178	1096	A	1	H	3	40	3.4	-71.91	18.76	1.25E-01	10	5332
178	1096	A	1	H	3	45	3.45	-76.37	15.85	8.96E-02	10	5332
178	1096	A	1	H	3	50	3.5	-74.1	7.15	7.21E-02	10	5332
178	1096	A	1	H	3	55	3.55	-53.51	313.31	6.25E-02	10	5332
178	1096	A	1	H	3	60	3.6	-56.35	320.55	7.43E-02	10	5332
178	1096	A	1	H	3	65	3.65	-69.91	33.93	8.50E-02	10	5332
178	1096	A	1	H	3	70	3.7	-69.86	40.71	1.26E-01	10	5332

Note: Only a portion of this table appears here. The complete table is available in ASCII format in the **TABLES** directory.

Table T6. Split-core paleomagnetic measurements for Hole 1096A after 20-mT demagnetization.

Leg	Site	Hole	Core	Type	Section	Interval (cm)	Depth (mbsf)	Inclination (°)	Declination (°)	Intensity (A/m)	Demagnetization step (mT)	Run #
178	1096	A	1	H	1	10	0.1	-68.99	41.27	9.93E-02	20	5327
178	1096	A	1	H	1	15	0.15	-69.2	27.09	1.13E-01	20	5327
178	1096	A	1	H	1	20	0.2	-66.86	22.89	1.08E-01	20	5327
178	1096	A	1	H	1	25	0.25	-73.09	356.81	9.68E-02	20	5327
178	1096	A	1	H	1	30	0.3	-72.61	312.97	8.84E-02	20	5327
178	1096	A	1	H	1	35	0.35	-67.77	281.31	8.60E-02	20	5327
178	1096	A	1	H	1	40	0.4	-68.2	273.09	7.16E-02	20	5327
178	1096	A	1	H	1	45	0.45	-59.01	247.26	8.00E-02	20	5327
178	1096	A	1	H	1	50	0.5	-61.83	274.48	9.05E-02	20	5327
178	1096	A	1	H	1	55	0.55	-66.82	0.64	8.48E-02	20	5327
178	1096	A	1	H	1	60	0.6	-64.99	5.2	1.03E-01	20	5327
178	1096	A	1	H	1	65	0.65	-66.56	314.49	1.27E-01	20	5327
178	1096	A	1	H	1	70	0.7	-75.19	3.62	1.64E-01	20	5327
178	1096	A	1	H	1	75	0.75	-67.26	28.64	2.14E-01	20	5327
178	1096	A	1	H	1	80	0.8	-68.54	25.04	2.16E-01	20	5327
178	1096	A	1	H	1	85	0.85	-73.69	35.63	2.35E-01	20	5327
178	1096	A	1	H	1	90	0.9	-68.12	28.33	3.11E-01	20	5327
178	1096	A	1	H	1	95	0.95	-65.39	4.05	3.12E-01	20	5327
178	1096	A	1	H	1	100	1	-71.82	30.06	2.28E-01	20	5327
178	1096	A	1	H	1	105	1.05	-70.1	40.97	2.28E-01	20	5327
178	1096	A	1	H	1	110	1.1	-74.22	34.64	2.24E-01	20	5327
178	1096	A	1	H	1	115	1.15	-70.6	36.85	2.70E-01	20	5327
178	1096	A	1	H	1	120	1.2	-69.22	50.33	2.47E-01	20	5327
178	1096	A	1	H	1	125	1.25	-70.41	46.72	2.69E-01	20	5327
178	1096	A	1	H	1	130	1.3	-69.76	42.56	2.70E-01	20	5327
178	1096	A	1	H	1	135	1.35	-74.04	51.69	2.36E-01	20	5327
178	1096	A	1	H	1	140	1.4	-77.77	31.1	2.00E-01	20	5327
178	1096	A	1	H	2	10	1.6	-81.24	358.61	1.66E-01	20	5330
178	1096	A	1	H	2	15	1.65	-80.64	6.78	1.78E-01	20	5330
178	1096	A	1	H	2	20	1.7	-74	356.19	1.83E-01	20	5330
178	1096	A	1	H	2	25	1.75	-71.64	348.97	1.68E-01	20	5330
178	1096	A	1	H	2	30	1.8	-76.48	358.02	1.28E-01	20	5330
178	1096	A	1	H	2	35	1.85	-76	326.91	1.02E-01	20	5330
178	1096	A	1	H	2	40	1.9	-59.94	284.95	9.76E-02	20	5330
178	1096	A	1	H	2	45	1.95	-48.77	277.98	1.11E-01	20	5330
178	1096	A	1	H	2	50	2	-48.73	278.98	9.98E-02	20	5330
178	1096	A	1	H	2	55	2.05	-53.66	281.22	1.03E-01	20	5330
178	1096	A	1	H	2	60	2.1	-64.49	293.42	1.20E-01	20	5330
178	1096	A	1	H	2	65	2.15	-73.23	325.45	1.29E-01	20	5330
178	1096	A	1	H	2	70	2.2	-74.42	352.72	1.31E-01	20	5330
178	1096	A	1	H	2	75	2.25	-78.17	351.27	1.52E-01	20	5330
178	1096	A	1	H	2	80	2.3	-74.45	0.3	1.70E-01	20	5330
178	1096	A	1	H	2	85	2.35	-78.43	5.12	1.57E-01	20	5330
178	1096	A	1	H	2	90	2.4	-85.55	5.27	1.69E-01	20	5330
178	1096	A	1	H	2	95	2.45	-80.43	356.62	2.20E-01	20	5330
178	1096	A	1	H	2	100	2.5	-76.18	315.51	2.26E-01	20	5330
178	1096	A	1	H	2	105	2.55	-69.55	298.24	2.38E-01	20	5330
178	1096	A	1	H	2	110	2.6	-73.17	327.28	2.18E-01	20	5330
178	1096	A	1	H	2	115	2.65	-72	336.01	1.85E-01	20	5330
178	1096	A	1	H	2	120	2.7	-78.42	312.54	1.47E-01	20	5330
178	1096	A	1	H	2	125	2.75	-78.67	300.94	1.41E-01	20	5330
178	1096	A	1	H	2	130	2.8	-73.04	295.61	1.41E-01	20	5330
178	1096	A	1	H	2	135	2.85	-73.31	298.02	1.28E-01	20	5330
178	1096	A	1	H	3	10	3.1	-66	332.29	1.14E-01	20	5333
178	1096	A	1	H	3	15	3.15	-67.22	343.21	1.58E-01	20	5333
178	1096	A	1	H	3	20	3.2	-66.39	355.83	1.84E-01	20	5333
178	1096	A	1	H	3	25	3.25	-69.87	1.54	1.91E-01	20	5333
178	1096	A	1	H	3	30	3.3	-72	8.07	1.80E-01	20	5333
178	1096	A	1	H	3	35	3.35	-71.12	15.18	1.56E-01	20	5333
178	1096	A	1	H	3	40	3.4	-71.4	19.21	1.13E-01	20	5333
178	1096	A	1	H	3	45	3.45	-76.24	17.12	7.65E-02	20	5333
178	1096	A	1	H	3	50	3.5	-74.91	5.83	5.87E-02	20	5333
178	1096	A	1	H	3	55	3.55	-53.6	311.19	4.97E-02	20	5333
178	1096	A	1	H	3	60	3.6	-56.23	318.06	5.95E-02	20	5333
178	1096	A	1	H	3	65	3.65	-70.86	33.54	6.78E-02	20	5333
178	1096	A	1	H	3	70	3.7	-70.13	42.23	1.03E-01	20	5333

Note: Only a portion of this table appears here. The complete table is available in ASCII format in the **TABLES** directory.

Table T7. Split-core paleomagnetic measurements for Hole 1096A after processing the results from the 20-mT demagnetization step by removing measurements from drilling-disturbed intervals and measurements made within 10 cm of each core section.

Leg	Site	Hole	Core	Type	Section	Interval (cm)	Depth (mbst)	Inclination (°)	Declination (°)	Intensity (A/m)	Demagnetization step (mT)	Run #
178	1096	A	1	H	1	65	0.65	-66.56	314.49	1.27E-01	20	0
178	1096	A	1	H	1	70	0.7	-75.19	3.62	1.64E-01	20	0
178	1096	A	1	H	1	75	0.75	-67.26	28.64	2.14E-01	20	0
178	1096	A	1	H	1	80	0.8	-68.54	25.04	2.16E-01	20	0
178	1096	A	1	H	1	85	0.85	-73.69	35.63	2.35E-01	20	0
178	1096	A	1	H	1	90	0.9	-68.12	28.33	3.11E-01	20	0
178	1096	A	1	H	1	95	0.95	-65.39	4.05	3.12E-01	20	0
178	1096	A	1	H	1	100	1	-71.82	30.06	2.28E-01	20	0
178	1096	A	1	H	1	105	1.05	-70.1	40.97	2.28E-01	20	0
178	1096	A	1	H	1	110	1.1	-74.22	34.64	2.24E-01	20	0
178	1096	A	1	H	1	115	1.15	-70.6	36.85	2.70E-01	20	0
178	1096	A	1	H	1	120	1.2	-69.22	50.33	2.47E-01	20	0
178	1096	A	1	H	1	125	1.25	-70.41	46.72	2.69E-01	20	0
178	1096	A	1	H	1	130	1.3	-69.76	42.56	2.70E-01	20	0
178	1096	A	1	H	1	135	1.35	-74.04	51.69	2.36E-01	20	0
178	1096	A	1	H	1	140	1.4	-77.77	31.1	2.00E-01	20	0
178	1096	A	1	H	1	145	1.45	-67.2	16.25	1.58E-01	20	0
178	1096	A	1	H	2	25	1.75	-71.64	348.97	1.68E-01	20	0
178	1096	A	1	H	2	30	1.8	-76.48	358.02	1.28E-01	20	0
178	1096	A	1	H	2	35	1.85	-76	326.91	1.02E-01	20	0
178	1096	A	1	H	2	40	1.9	-59.94	284.95	9.76E-02	20	0
178	1096	A	1	H	2	45	1.95	-48.77	277.98	1.11E-01	20	0
178	1096	A	1	H	2	50	2	-48.73	278.98	9.98E-02	20	0
178	1096	A	1	H	2	55	2.05	-53.66	281.22	1.03E-01	20	0
178	1096	A	1	H	2	60	2.1	-64.49	293.42	1.20E-01	20	0
178	1096	A	1	H	2	65	2.15	-73.23	325.45	1.29E-01	20	0
178	1096	A	1	H	2	70	2.2	-74.42	352.72	1.31E-01	20	0
178	1096	A	1	H	2	75	2.25	-78.17	351.27	1.52E-01	20	0
178	1096	A	1	H	2	80	2.3	-74.45	0.3	1.70E-01	20	0
178	1096	A	1	H	2	85	2.35	-78.43	5.12	1.57E-01	20	0
178	1096	A	1	H	2	90	2.4	-85.55	5.27	1.69E-01	20	0
178	1096	A	1	H	2	95	2.45	-80.43	356.62	2.20E-01	20	0
178	1096	A	1	H	2	100	2.5	-76.18	315.51	2.26E-01	20	0
178	1096	A	1	H	2	105	2.55	-69.55	298.24	2.38E-01	20	0
178	1096	A	1	H	3	10	3.1	-66	332.29	1.14E-01	20	0
178	1096	A	1	H	3	15	3.15	-67.22	343.21	1.58E-01	20	0
178	1096	A	1	H	3	20	3.2	-66.39	355.83	1.84E-01	20	0
178	1096	A	1	H	3	25	3.25	-69.87	1.54	1.91E-01	20	0
178	1096	A	1	H	3	30	3.3	-72	8.07	1.80E-01	20	0
178	1096	A	1	H	3	35	3.35	-71.12	15.18	1.56E-01	20	0
178	1096	A	1	H	3	40	3.4	-71.4	19.21	1.13E-01	20	0
178	1096	A	1	H	3	50	3.5	-74.91	5.83	5.87E-02	20	0
178	1096	A	1	H	3	55	3.55	-53.6	311.19	4.97E-02	20	0
178	1096	A	1	H	3	60	3.6	-56.23	318.06	5.95E-02	20	0
178	1096	A	1	H	3	65	3.65	-70.86	33.54	6.78E-02	20	0
178	1096	A	1	H	3	70	3.7	-70.13	42.23	1.03E-01	20	0
178	1096	A	1	H	3	75	3.75	-65.45	23.86	9.32E-02	20	0
178	1096	A	1	H	3	80	3.8	-79.19	2.06	6.91E-02	20	0
178	1096	A	1	H	3	85	3.85	-86.04	290.83	8.48E-02	20	0
178	1096	A	1	H	3	90	3.9	-87.27	355.21	1.32E-01	20	0
178	1096	A	1	H	3	95	3.95	-86.1	12.06	1.64E-01	20	0
178	1096	A	1	H	3	100	4	-85.97	26.34	1.85E-01	20	0
178	1096	A	1	H	3	105	4.05	-81.65	33.17	1.89E-01	20	0
178	1096	A	1	H	3	110	4.1	-81.33	55.89	1.71E-01	20	0
178	1096	A	1	H	3	115	4.15	-82.27	65.05	1.58E-01	20	0
178	1096	A	1	H	3	120	4.2	-85.47	112.07	1.53E-01	20	0
178	1096	A	1	H	3	125	4.25	-85.08	128.27	1.68E-01	20	0
178	1096	A	1	H	3	130	4.3	-86.08	123.12	1.93E-01	20	0
178	1096	A	1	H	3	135	4.35	-88.46	333.33	2.24E-01	20	0
178	1096	A	1	H	3	140	4.4	-83.12	331.09	2.47E-01	20	0
178	1096	A	1	H	3	145	4.45	-70.36	335.19	2.51E-01	20	0
178	1096	A	1	H	4	10	4.6	-67.78	345.63	2.66E-01	20	0
178	1096	A	1	H	4	15	4.65	-72.13	345.22	2.66E-01	20	0
178	1096	A	1	H	4	20	4.7	-71.51	356.59	2.87E-01	20	0

Note: Only a portion of this table appears here. The complete table is available in ASCII format in the [TABLES](#) directory.

Table T8. Split-core paleomagnetic measurements for Hole 1096B before demagnetization (NRM results).

Leg	Site	Hole	Core	Type	Section	Interval (cm)	Depth (mbsf)	Inclination (°)	Declination (°)	Intensity (A/m)	Demagnetization step (mT)	Run #
178	1096	B	1	H	1	10	0.1	-13.7	340.85	8.32E-02	0	5559
178	1096	B	1	H	1	15	0.15	-18.64	338.21	6.28E-02	0	5559
178	1096	B	1	H	1	20	0.2	-44.72	322.06	6.32E-02	0	5559
178	1096	B	1	H	1	25	0.25	-45.4	319.3	9.66E-02	0	5559
178	1096	B	1	H	1	30	0.3	-40.77	324.21	1.15E-01	0	5559
178	1096	B	1	H	1	35	0.35	-54.03	324.36	8.40E-02	0	5559
178	1096	B	1	H	1	40	0.4	-62.81	290.48	7.99E-02	0	5559
178	1096	B	1	H	1	45	0.45	-54.06	242.53	9.47E-02	0	5559
178	1096	B	1	H	1	50	0.5	-46.61	240.2	1.05E-01	0	5559
178	1096	B	1	H	1	55	0.55	-49.84	238.04	9.06E-02	0	5559
178	1096	B	1	H	1	60	0.6	-47.58	229.82	7.65E-02	0	5559
178	1096	B	1	H	1	65	0.65	-33.77	229.11	9.90E-02	0	5559
178	1096	B	1	H	1	70	0.7	-33.84	222.42	1.22E-01	0	5559
178	1096	B	1	H	1	75	0.75	-50.65	231.74	1.43E-01	0	5559
178	1096	B	1	H	1	80	0.8	-66.55	286.78	1.86E-01	0	5559
178	1096	B	1	H	1	85	0.85	-63.37	299.04	2.11E-01	0	5559
178	1096	B	1	H	1	90	0.9	-61.74	306.53	1.95E-01	0	5559
178	1096	B	1	H	1	95	0.95	-66.63	301.08	1.89E-01	0	5559
178	1096	B	1	H	1	100	1	-65.29	294.19	2.63E-01	0	5559
178	1096	B	1	H	1	105	1.05	-63.32	256.91	3.11E-01	0	5559
178	1096	B	1	H	1	110	1.1	-72.35	259.11	3.03E-01	0	5559
178	1096	B	1	H	1	115	1.15	-68.68	335.87	2.39E-01	0	5559
178	1096	B	1	H	1	120	1.2	-64.15	332.91	2.47E-01	0	5559
178	1096	B	1	H	1	125	1.25	-68.39	335.94	2.30E-01	0	5559
178	1096	B	1	H	1	130	1.3	-71.57	325.68	2.50E-01	0	5559
178	1096	B	1	H	1	135	1.35	-62.13	335.29	2.48E-01	0	5559
178	1096	B	1	H	1	140	1.4	-64.85	338.11	2.19E-01	0	5559
178	1096	B	1	H	2	10	1.6	-66.77	7.81	1.89E-01	0	5562
178	1096	B	1	H	2	15	1.65	-64.6	9.71	1.77E-01	0	5562
178	1096	B	1	H	2	20	1.7	-57.33	5.27	1.64E-01	0	5562
178	1096	B	1	H	2	25	1.75	-57.61	0.78	1.48E-01	0	5562
178	1096	B	1	H	2	30	1.8	-60.47	1.65	1.43E-01	0	5562
178	1096	B	1	H	2	35	1.85	-68.14	3.48	1.40E-01	0	5562
178	1096	B	1	H	2	40	1.9	-72.86	357.65	1.47E-01	0	5562
178	1096	B	1	H	2	45	1.95	-68.79	344.12	1.47E-01	0	5562
178	1096	B	1	H	2	50	2	-66.51	353.58	1.17E-01	0	5562
178	1096	B	1	H	2	55	2.05	-74.78	0.12	8.79E-02	0	5562
178	1096	B	1	H	2	60	2.1	-72.42	175.85	8.08E-02	0	5562
178	1096	B	1	H	2	65	2.15	-46.65	178.61	9.63E-02	0	5562
178	1096	B	1	H	2	70	2.2	-33.02	178.69	7.51E-02	0	5562
178	1096	B	1	H	2	75	2.25	3.45	176.82	3.82E-02	0	5562
178	1096	B	1	H	2	80	2.3	78.2	298.67	3.27E-02	0	5562
178	1096	B	1	H	2	85	2.35	30.07	318.03	2.66E-02	0	5562
178	1096	B	1	H	2	90	2.4	-45.89	294.51	4.67E-02	0	5562
178	1096	B	1	H	2	95	2.45	-70.73	281.76	8.45E-02	0	5562
178	1096	B	1	H	2	100	2.5	-72.35	264.29	1.36E-01	0	5562
178	1096	B	1	H	2	105	2.55	-72.44	301.88	1.44E-01	0	5562
178	1096	B	1	H	2	110	2.6	-77.67	320.88	1.32E-01	0	5562
178	1096	B	1	H	2	115	2.65	-80.17	285.31	1.59E-01	0	5562
178	1096	B	1	H	2	120	2.7	-78.41	291.34	1.94E-01	0	5562
178	1096	B	1	H	2	125	2.75	-73.25	201.64	2.02E-01	0	5562
178	1096	B	1	H	2	130	2.8	-64.88	188.53	2.14E-01	0	5562
178	1096	B	1	H	2	135	2.85	-80.98	230.64	1.85E-01	0	5562
178	1096	B	1	H	2	140	2.9	-81.88	332.57	1.56E-01	0	5562
178	1096	B	1	H	3	10	3.1	-68.96	267.46	1.01E-01	0	5565
178	1096	B	1	H	3	15	3.15	-59.66	240.48	7.95E-02	0	5565
178	1096	B	1	H	3	20	3.2	-48.71	206.37	9.45E-02	0	5565
178	1096	B	1	H	3	25	3.25	-58.2	229.83	9.72E-02	0	5565
178	1096	B	1	H	3	30	3.3	-57.22	248	7.91E-02	0	5565
178	1096	B	1	H	3	35	3.35	-55	250.13	7.41E-02	0	5565
178	1096	B	1	H	3	40	3.4	-21.98	331.78	5.91E-02	0	5565
178	1096	B	1	H	3	45	3.45	69.46	261.13	9.62E-02	0	5565
178	1096	B	1	H	3	50	3.5	9.19	200.51	1.47E-01	0	5565
178	1096	B	2	H	1	10	3.9	-4.35	46.09	1.05E-01	0	5568
178	1096	B	2	H	1	15	3.95	20.02	37.58	8.50E-02	0	5568

Note: Only a portion of this table appears here. The complete table is available in ASCII format in the [TABLES](#) directory.

Table T9. Split-core paleomagnetic measurements for Hole 1096B after 10-mT demagnetization.

Leg	Site	Hole	Core	Type	Section	Interval (cm)	Depth (mbsf)	Inclination (°)	Declination (°)	Intensity (A/m)	Demagnetization step (mT)	Run #
178	1096	B	1	H	1	10	0.1	-65.24	311.04	8.92E-02	10	5560
178	1096	B	1	H	1	15	0.15	-71.69	309.42	1.03E-01	10	5560
178	1096	B	1	H	1	20	0.2	-73.76	302.43	1.11E-01	10	5560
178	1096	B	1	H	1	25	0.25	-69.17	302.16	1.30E-01	10	5560
178	1096	B	1	H	1	30	0.3	-62.38	317.29	1.37E-01	10	5560
178	1096	B	1	H	1	35	0.35	-69.34	318.28	1.09E-01	10	5560
178	1096	B	1	H	1	40	0.4	-72.21	269.18	1.06E-01	10	5560
178	1096	B	1	H	1	45	0.45	-60.11	231.16	1.26E-01	10	5560
178	1096	B	1	H	1	50	0.5	-55.61	229.8	1.32E-01	10	5560
178	1096	B	1	H	1	55	0.55	-58.82	228.97	1.14E-01	10	5560
178	1096	B	1	H	1	60	0.6	-55.97	218.22	9.87E-02	10	5560
178	1096	B	1	H	1	65	0.65	-42.82	225.9	1.13E-01	10	5560
178	1096	B	1	H	1	70	0.7	-41.36	219.9	1.33E-01	10	5560
178	1096	B	1	H	1	75	0.75	-54.44	225.84	1.64E-01	10	5560
178	1096	B	1	H	1	80	0.8	-71.4	268.96	2.18E-01	10	5560
178	1096	B	1	H	1	85	0.85	-69.19	288.19	2.41E-01	10	5560
178	1096	B	1	H	1	90	0.9	-68.82	297.09	2.24E-01	10	5560
178	1096	B	1	H	1	95	0.95	-73.08	289.93	2.17E-01	10	5560
178	1096	B	1	H	1	100	1	-70.31	281.58	2.95E-01	10	5560
178	1096	B	1	H	1	105	1.05	-65.41	249.16	3.46E-01	10	5560
178	1096	B	1	H	1	110	1.1	-72.92	247.05	3.40E-01	10	5560
178	1096	B	1	H	1	115	1.15	-73.75	330.03	2.64E-01	10	5560
178	1096	B	1	H	1	120	1.2	-70.52	324.66	2.68E-01	10	5560
178	1096	B	1	H	1	125	1.25	-73.85	329.55	2.56E-01	10	5560
178	1096	B	1	H	1	130	1.3	-77.28	311.43	2.83E-01	10	5560
178	1096	B	1	H	1	135	1.35	-70.67	326.28	2.86E-01	10	5560
178	1096	B	1	H	1	140	1.4	-73.84	328.26	2.61E-01	10	5560
178	1096	B	1	H	2	10	1.6	-76.77	15.96	2.38E-01	10	5563
178	1096	B	1	H	2	15	1.65	-75.88	18.25	2.24E-01	10	5563
178	1096	B	1	H	2	20	1.7	-73.06	13.05	2.10E-01	10	5563
178	1096	B	1	H	2	25	1.75	-73.67	6.24	1.97E-01	10	5563
178	1096	B	1	H	2	30	1.8	-76.91	6.65	1.93E-01	10	5563
178	1096	B	1	H	2	35	1.85	-82.25	9.2	1.95E-01	10	5563
178	1096	B	1	H	2	40	1.9	-85.02	346.96	2.04E-01	10	5563
178	1096	B	1	H	2	45	1.95	-81.05	339.07	2.00E-01	10	5563
178	1096	B	1	H	2	50	2	-78.53	358.04	1.58E-01	10	5563
178	1096	B	1	H	2	55	2.05	-82.4	7.27	1.20E-01	10	5563
178	1096	B	1	H	2	60	2.1	-75.94	178.54	1.02E-01	10	5563
178	1096	B	1	H	2	65	2.15	-53.26	180.73	1.12E-01	10	5563
178	1096	B	1	H	2	70	2.2	-48.28	181.73	9.87E-02	10	5563
178	1096	B	1	H	2	75	2.25	-47.92	185.23	8.91E-02	10	5563
178	1096	B	1	H	2	80	2.3	-62.28	189.2	1.12E-01	10	5563
178	1096	B	1	H	2	85	2.35	-78.39	220.34	1.34E-01	10	5563
178	1096	B	1	H	2	90	2.4	-79.96	267.01	1.49E-01	10	5563
178	1096	B	1	H	2	95	2.45	-81.42	274.85	1.46E-01	10	5563
178	1096	B	1	H	2	100	2.5	-75.58	252.5	1.78E-01	10	5563
178	1096	B	1	H	2	105	2.55	-76.82	294.6	1.78E-01	10	5563
178	1096	B	1	H	2	110	2.6	-81.44	313.53	1.61E-01	10	5563
178	1096	B	1	H	2	115	2.65	-81.31	262.49	1.88E-01	10	5563
178	1096	B	1	H	2	120	2.7	-80.33	278.85	2.25E-01	10	5563
178	1096	B	1	H	2	125	2.75	-74.3	200.41	2.25E-01	10	5563
178	1096	B	1	H	2	130	2.8	-65.27	189.68	2.41E-01	10	5563
178	1096	B	1	H	2	135	2.85	-78.88	216.37	2.21E-01	10	5563
178	1096	B	1	H	2	140	2.9	-86.34	311.6	1.90E-01	10	5563
178	1096	B	1	H	3	10	3.1	-74.3	250.29	1.28E-01	10	5566
178	1096	B	1	H	3	15	3.15	-66.83	228.62	1.07E-01	10	5566
178	1096	B	1	H	3	20	3.2	-56	202.17	1.21E-01	10	5566
178	1096	B	1	H	3	25	3.25	-62.9	215.08	1.32E-01	10	5566
178	1096	B	1	H	3	30	3.3	-66.88	229.99	1.16E-01	10	5566
178	1096	B	1	H	3	35	3.35	-65.03	233.47	1.10E-01	10	5566
178	1096	B	1	H	3	40	3.4	-62.18	316.2	8.05E-02	10	5566
178	1096	B	1	H	3	45	3.45	-9.53	249.76	3.38E-02	10	5566
178	1096	B	1	H	3	50	3.5	-25.59	205.73	1.18E-01	10	5566
178	1096	B	2	H	1	10	3.9	-11.73	49.29	8.68E-02	10	5569
178	1096	B	2	H	1	15	3.95	12.44	41.36	6.00E-02	10	5569
178	1096	B	2	H	1	20	4	4.35	30.67	2.05E-02	10	5569

Note: Only a portion of this table appears here. The complete table is available in ASCII format in the **TABLES** directory.

Table T10. Split-core paleomagnetic measurements for Hole 1096B after 20-mT demagnetization.

Leg	Site	Hole	Core	Type	Section	Interval (cm)	Depth (mbsf)	Inclination (°)	Declination (°)	Intensity (A/m)	Demagnetization step (mT)	Run #
178	1096	B	1	H	1	10	0.1	-68.08	305.17	7.84E-02	20	5561
178	1096	B	1	H	1	15	0.15	-73.72	302.18	9.24E-02	20	5561
178	1096	B	1	H	1	20	0.2	-75.38	296.25	1.00E-01	20	5561
178	1096	B	1	H	1	25	0.25	-70.92	296.41	1.18E-01	20	5561
178	1096	B	1	H	1	30	0.3	-64.78	314	1.24E-01	20	5561
178	1096	B	1	H	1	35	0.35	-70.96	314.49	1.01E-01	20	5561
178	1096	B	1	H	1	40	0.4	-72.42	264.96	9.96E-02	20	5561
178	1096	B	1	H	1	45	0.45	-59.97	229.75	1.18E-01	20	5561
178	1096	B	1	H	1	50	0.5	-55.26	228.07	1.25E-01	20	5561
178	1096	B	1	H	1	55	0.55	-58.48	227.29	1.07E-01	20	5561
178	1096	B	1	H	1	60	0.6	-55.62	216.93	9.26E-02	20	5561
178	1096	B	1	H	1	65	0.65	-42.26	224.46	1.06E-01	20	5561
178	1096	B	1	H	1	70	0.7	-40.82	218.9	1.26E-01	20	5561
178	1096	B	1	H	1	75	0.75	-53.76	224.57	1.55E-01	20	5561
178	1096	B	1	H	1	80	0.8	-71.49	264.22	2.03E-01	20	5561
178	1096	B	1	H	1	85	0.85	-69.6	283.39	2.26E-01	20	5561
178	1096	B	1	H	1	90	0.9	-69.5	293.89	2.09E-01	20	5561
178	1096	B	1	H	1	95	0.95	-73.96	287.15	2.02E-01	20	5561
178	1096	B	1	H	1	100	1	-70.67	278.03	2.76E-01	20	5561
178	1096	B	1	H	1	105	1.05	-64.68	246.64	3.29E-01	20	5561
178	1096	B	1	H	1	110	1.1	-72.33	244.08	3.23E-01	20	5561
178	1096	B	1	H	1	115	1.15	-74.58	329.09	2.48E-01	20	5561
178	1096	B	1	H	1	120	1.2	-71.4	322.56	2.50E-01	20	5561
178	1096	B	1	H	1	125	1.25	-74.88	327.24	2.40E-01	20	5561
178	1096	B	1	H	1	130	1.3	-78.1	307.47	2.67E-01	20	5561
178	1096	B	1	H	1	135	1.35	-71.75	324.43	2.70E-01	20	5561
178	1096	B	1	H	1	140	1.4	-75.12	326.13	2.48E-01	20	5561
178	1096	B	1	H	2	10	1.6	-77.84	18.46	2.21E-01	20	5564
178	1096	B	1	H	2	15	1.65	-77.03	21.21	2.07E-01	20	5564
178	1096	B	1	H	2	20	1.7	-74.43	15	1.94E-01	20	5564
178	1096	B	1	H	2	25	1.75	-75.11	7.78	1.81E-01	20	5564
178	1096	B	1	H	2	30	1.8	-78.33	9.04	1.77E-01	20	5564
178	1096	B	1	H	2	35	1.85	-83.65	13.52	1.79E-01	20	5564
178	1096	B	1	H	2	40	1.9	-86.44	346.04	1.88E-01	20	5564
178	1096	B	1	H	2	45	1.95	-82.47	337.6	1.84E-01	20	5564
178	1096	B	1	H	2	50	2	-79.88	359.62	1.45E-01	20	5564
178	1096	B	1	H	2	55	2.05	-83.95	9.66	1.11E-01	20	5564
178	1096	B	1	H	2	60	2.1	-73.71	178.71	9.61E-02	20	5564
178	1096	B	1	H	2	65	2.15	-51.37	180.22	1.06E-01	20	5564
178	1096	B	1	H	2	70	2.2	-46.47	180.61	8.85E-02	20	5564
178	1096	B	1	H	2	75	2.25	-46.13	183.21	7.42E-02	20	5564
178	1096	B	1	H	2	80	2.3	-59.59	186.09	9.15E-02	20	5564
178	1096	B	1	H	2	85	2.35	-76.82	210.05	1.09E-01	20	5564
178	1096	B	1	H	2	90	2.4	-79.75	252.04	1.24E-01	20	5564
178	1096	B	1	H	2	95	2.45	-80.84	258.89	1.27E-01	20	5564
178	1096	B	1	H	2	100	2.5	-74.7	247.1	1.65E-01	20	5564
178	1096	B	1	H	2	105	2.55	-76.93	290.25	1.67E-01	20	5564
178	1096	B	1	H	2	110	2.6	-81.66	308.66	1.52E-01	20	5564
178	1096	B	1	H	2	115	2.65	-81.11	257.14	1.78E-01	20	5564
178	1096	B	1	H	2	120	2.7	-80.18	274.48	2.15E-01	20	5564
178	1096	B	1	H	2	125	2.75	-73.68	200.52	2.16E-01	20	5564
178	1096	B	1	H	2	130	2.8	-64.74	189.72	2.28E-01	20	5564
178	1096	B	1	H	2	135	2.85	-77.83	213.88	2.07E-01	20	5564
178	1096	B	1	H	2	140	2.9	-87.13	287.37	1.78E-01	20	5564
178	1096	B	1	H	3	10	3.1	-74.04	245.39	1.20E-01	20	5567
178	1096	B	1	H	3	15	3.15	-66.05	224.78	1.00E-01	20	5567
178	1096	B	1	H	3	20	3.2	-54.75	201.03	1.15E-01	20	5567
178	1096	B	1	H	3	25	3.25	-61.76	213.37	1.24E-01	20	5567
178	1096	B	1	H	3	30	3.3	-65.68	225.85	1.07E-01	20	5567
178	1096	B	1	H	3	35	3.35	-63.94	230.11	1.02E-01	20	5567
178	1096	B	1	H	3	40	3.4	-64.8	312.32	7.36E-02	20	5567
178	1096	B	1	H	3	45	3.45	-19.9	247.25	3.28E-02	20	5567
178	1096	B	1	H	3	50	3.5	-27.6	206.6	1.10E-01	20	5567
178	1096	B	2	H	1	10	3.9	-10.38	52.62	7.27E-02	20	5570
178	1096	B	2	H	1	15	3.95	18.08	45.04	4.75E-02	20	5570
178	1096	B	2	H	1	20	4	14.5	31.44	1.07E-02	20	5570

Note: Only a portion of this table appears here. The complete table is available in ASCII format in the **TABLES** directory.

Table T11. Split-core paleomagnetic measurements for Hole 1096B after 30-mT demagnetization.

Leg	Site	Hole	Core	Type	Section	Interval (cm)	Depth (mbsf)	Inclination (°)	Declination (°)	Intensity (A/m)	Demagnetization step (mT)	Run #
178	1096	B	23	X	2	10	175.63	47.54	43.12	8.32E-02	30	5882
178	1096	B	23	X	2	15	175.68	50.18	35.09	5.42E-02	30	5882
178	1096	B	23	X	2	20	175.73	81.18	124.36	6.76E-02	30	5882
178	1096	B	23	X	2	25	175.78	38.45	120.18	1.01E-01	30	5882
178	1096	B	23	X	2	30	175.83	46.81	67.92	6.37E-02	30	5882
178	1096	B	23	X	2	35	175.88	44.45	297.88	7.20E-02	30	5882
178	1096	B	23	X	2	40	175.93	69.25	251.13	7.15E-02	30	5882
178	1096	B	23	X	2	45	175.98	45.13	75.86	9.74E-02	30	5882
178	1096	B	23	X	2	50	176.03	42.84	44.64	1.32E-01	30	5882
178	1096	B	23	X	2	55	176.08	52.28	349.74	1.37E-01	30	5882
178	1096	B	23	X	2	60	176.13	62.47	345.81	1.05E-01	30	5882
178	1096	B	23	X	2	65	176.18	75.76	44.06	8.79E-02	30	5882
178	1096	B	23	X	2	70	176.23	72.3	110.21	8.98E-02	30	5882
178	1096	B	23	X	2	75	176.28	48.76	67.31	1.03E-01	30	5882
178	1096	B	23	X	2	80	176.33	24.34	104.39	5.28E-02	30	5882
178	1096	B	23	X	2	85	176.38	45.44	154.86	2.16E-02	30	5882
178	1096	B	23	X	2	90	176.43	52.49	228.69	9.37E-02	30	5882
178	1096	B	23	X	2	95	176.48	69.19	197.08	9.68E-02	30	5882
178	1096	B	23	X	2	100	176.53	68.56	350.55	6.31E-02	30	5882
178	1096	B	23	X	2	105	176.58	55.99	45.86	5.30E-02	30	5882
178	1096	B	23	X	2	110	176.63	40.71	57.9	6.69E-02	30	5882
178	1096	B	23	X	2	115	176.68	50.13	41	5.73E-02	30	5882
178	1096	B	23	X	2	120	176.73	58.26	352.35	7.66E-02	30	5882
178	1096	B	23	X	2	125	176.78	58.92	91.27	1.02E-01	30	5882
178	1096	B	23	X	3	10	177.03	65.69	314.98	1.10E-01	30	5886
178	1096	B	23	X	3	15	177.08	79.81	308.6	9.89E-02	30	5886
178	1096	B	23	X	3	20	177.13	72.34	261.52	9.32E-02	30	5886
178	1096	B	23	X	3	25	177.18	64.64	163.64	7.79E-02	30	5886
178	1096	B	23	X	3	30	177.23	57.93	173.42	9.10E-02	30	5886
178	1096	B	23	X	3	35	177.28	67.24	162.18	8.72E-02	30	5886
178	1096	B	23	X	3	40	177.33	69.8	310.51	8.30E-02	30	5886
178	1096	B	23	X	3	45	177.38	79.01	32.12	9.73E-02	30	5886
178	1096	B	23	X	3	50	177.43	66.14	120.24	1.24E-01	30	5886
178	1096	B	23	X	3	55	177.48	51.19	96.83	1.38E-01	30	5886
178	1096	B	23	X	3	60	177.53	52.68	2.93	1.40E-01	30	5886
178	1096	B	23	X	3	65	177.58	55.94	272.89	1.60E-01	30	5886
178	1096	B	23	X	3	70	177.63	59.93	194.92	1.45E-01	30	5886
178	1096	B	23	X	3	75	177.68	61.23	87.29	1.20E-01	30	5886
178	1096	B	23	X	3	80	177.73	53.51	1.28	1.23E-01	30	5886
178	1096	B	23	X	3	85	177.78	67.29	347.22	1.05E-01	30	5886
178	1096	B	23	X	3	90	177.83	70.91	66.23	9.73E-02	30	5886
178	1096	B	23	X	3	95	177.88	59.59	44.67	1.12E-01	30	5886
178	1096	B	23	X	3	100	177.93	77.47	197.02	1.03E-01	30	5886
178	1096	B	23	X	3	105	177.98	77.33	83.51	8.83E-02	30	5886
178	1096	B	23	X	3	110	178.03	68.13	31.7	1.02E-01	30	5886
178	1096	B	23	X	3	115	178.08	84.23	172.71	1.03E-01	30	5886
178	1096	B	23	X	3	120	178.13	82.58	342.8	1.03E-01	30	5886
178	1096	B	23	X	3	125	178.18	87.8	23.34	9.48E-02	30	5886
178	1096	B	23	X	3	130	178.23	74.15	55.53	9.68E-02	30	5886
178	1096	B	23	X	3	135	178.28	72.78	22.39	1.16E-01	30	5886
178	1096	B	23	X	3	140	178.33	59.92	357.36	1.30E-01	30	5886
178	1096	B	23	X	4	10	178.53	83.66	101.86	1.32E-01	30	5889
178	1096	B	23	X	4	15	178.58	80.83	127.82	1.49E-01	30	5889
178	1096	B	23	X	4	20	178.63	71.98	61.39	1.46E-01	30	5889
178	1096	B	23	X	4	25	178.68	69.19	11.73	1.25E-01	30	5889
178	1096	B	23	X	4	30	178.73	68.81	309.17	7.74E-02	30	5889
178	1096	B	23	X	4	35	178.78	68.33	292.31	1.04E-01	30	5889
178	1096	B	23	X	4	40	178.83	74.61	300.9	1.45E-01	30	5889
178	1096	B	23	X	4	45	178.88	78.62	296.13	1.46E-01	30	5889
178	1096	B	23	X	4	50	178.93	83.7	204.32	1.31E-01	30	5889
178	1096	B	23	X	4	55	178.98	85.92	55.16	1.08E-01	30	5889
178	1096	B	23	X	4	60	179.03	66.73	329.98	9.69E-02	30	5889
178	1096	B	23	X	4	65	179.08	55.41	303.94	1.20E-01	30	5889
178	1096	B	23	X	4	70	179.13	78.35	308.19	1.24E-01	30	5889
178	1096	B	23	X	4	75	179.18	82.82	130.49	1.30E-01	30	5889
178	1096	B	23	X	4	80	179.23	85.76	55.81	1.27E-01	30	5889

Note: Only a portion of this table appears here. The complete table is available in ASCII format in the **TABLES** directory.

Table T12. Split-core paleomagnetic measurements for Hole 1096B after processing the results from the 20-mT demagnetization step by removing measurements from drilling-disturbed intervals and measurements made within 10 cm of each core section.

Leg	Site	Hole	Core	Type	Section	Interval (cm)	Depth (mbst)	Inclination (°)	Declination (°)	Intensity (A/m)	Demagnetization step (mT)	Run #
178	1096	B	1	H	1	50	0.5	-55.26	228.07	1.25E-01	20	5561
178	1096	B	1	H	1	55	0.55	-58.48	227.29	1.07E-01	20	5561
178	1096	B	1	H	1	60	0.6	-55.62	216.93	9.26E-02	20	5561
178	1096	B	1	H	1	65	0.65	-42.26	224.46	1.06E-01	20	5561
178	1096	B	1	H	1	70	0.7	-40.82	218.9	1.26E-01	20	5561
178	1096	B	1	H	1	75	0.75	-53.76	224.57	1.55E-01	20	5561
178	1096	B	1	H	1	80	0.8	-71.49	264.22	2.03E-01	20	5561
178	1096	B	1	H	1	85	0.85	-69.6	283.39	2.26E-01	20	5561
178	1096	B	1	H	1	90	0.9	-69.5	293.89	2.09E-01	20	5561
178	1096	B	1	H	1	95	0.95	-73.96	287.15	2.02E-01	20	5561
178	1096	B	1	H	1	100	1	-70.67	278.03	2.76E-01	20	5561
178	1096	B	1	H	1	105	1.05	-64.68	246.64	3.29E-01	20	5561
178	1096	B	1	H	1	110	1.1	-72.33	244.08	3.23E-01	20	5561
178	1096	B	1	H	1	115	1.15	-74.58	329.09	2.48E-01	20	5561
178	1096	B	1	H	1	120	1.2	-71.4	322.56	2.50E-01	20	5561
178	1096	B	1	H	1	125	1.25	-74.88	327.24	2.40E-01	20	5561
178	1096	B	1	H	1	130	1.3	-78.1	307.47	2.67E-01	20	5561
178	1096	B	1	H	1	135	1.35	-71.75	324.43	2.70E-01	20	5561
178	1096	B	1	H	1	140	1.4	-75.12	326.13	2.48E-01	20	5561
178	1096	B	1	H	2	10	1.6	-77.84	18.46	2.21E-01	20	5564
178	1096	B	1	H	2	15	1.65	-77.03	21.21	2.07E-01	20	5564
178	1096	B	1	H	2	20	1.7	-74.43	15	1.94E-01	20	5564
178	1096	B	1	H	2	25	1.75	-75.11	7.78	1.81E-01	20	5564
178	1096	B	1	H	2	30	1.8	-78.33	9.04	1.77E-01	20	5564
178	1096	B	1	H	2	35	1.85	-83.65	13.52	1.79E-01	20	5564
178	1096	B	1	H	2	40	1.9	-86.44	346.04	1.88E-01	20	5564
178	1096	B	1	H	2	45	1.95	-82.47	337.6	1.84E-01	20	5564
178	1096	B	1	H	2	50	2	-79.88	359.62	1.45E-01	20	5564
178	1096	B	1	H	2	55	2.05	-83.95	9.66	1.11E-01	20	5564
178	1096	B	1	H	2	60	2.1	-73.71	178.71	9.61E-02	20	5564
178	1096	B	1	H	2	65	2.15	-51.37	180.22	1.06E-01	20	5564
178	1096	B	1	H	2	70	2.2	-46.47	180.61	8.85E-02	20	5564
178	1096	B	1	H	2	75	2.25	-46.13	183.21	7.42E-02	20	5564
178	1096	B	1	H	2	80	2.3	-59.59	186.09	9.15E-02	20	5564
178	1096	B	1	H	2	85	2.35	-76.82	210.05	1.09E-01	20	5564
178	1096	B	1	H	2	90	2.4	-79.75	252.04	1.24E-01	20	5564
178	1096	B	1	H	2	95	2.45	-80.84	258.89	1.27E-01	20	5564
178	1096	B	1	H	2	100	2.5	-74.7	247.1	1.65E-01	20	5564
178	1096	B	1	H	2	105	2.55	-76.93	290.25	1.67E-01	20	5564
178	1096	B	1	H	2	110	2.6	-81.66	308.66	1.52E-01	20	5564
178	1096	B	1	H	2	115	2.65	-81.11	257.14	1.78E-01	20	5564
178	1096	B	1	H	2	120	2.7	-80.18	274.48	2.15E-01	20	5564
178	1096	B	1	H	2	125	2.75	-73.68	200.52	2.16E-01	20	5564
178	1096	B	1	H	2	130	2.8	-64.74	189.72	2.28E-01	20	5564
178	1096	B	1	H	2	135	2.85	-77.83	213.88	2.07E-01	20	5564
178	1096	B	1	H	2	140	2.9	-87.13	287.37	1.78E-01	20	5564
178	1096	B	1	H	3	10	3.1	-74.04	245.39	1.20E-01	20	5567
178	1096	B	1	H	3	15	3.15	-66.05	224.78	1.00E-01	20	5567
178	1096	B	1	H	3	20	3.2	-54.75	201.03	1.15E-01	20	5567
178	1096	B	1	H	3	25	3.25	-61.76	213.37	1.24E-01	20	5567
178	1096	B	1	H	3	30	3.3	-65.68	225.85	1.07E-01	20	5567
178	1096	B	1	H	3	35	3.35	-63.94	230.11	1.02E-01	20	5567
178	1096	B	1	H	3	40	3.4	-64.8	312.32	7.36E-02	20	5567
178	1096	B	1	H	3	45	3.45	-19.9	247.25	3.28E-02	20	5567
178	1096	B	1	H	3	50	3.5	-27.6	206.6	1.10E-01	20	5567
178	1096	B	2	H	1	60	4.4	-68.92	299.17	2.06E-01	20	5570
178	1096	B	2	H	1	65	4.45	-71.83	300.02	2.34E-01	20	5570
178	1096	B	2	H	1	70	4.5	-75.44	277.97	2.29E-01	20	5570
178	1096	B	2	H	1	75	4.55	-73.89	264.22	2.19E-01	20	5570
178	1096	B	2	H	1	80	4.6	-75.78	254.61	2.08E-01	20	5570
178	1096	B	2	H	1	85	4.65	-77.41	253.24	2.13E-01	20	5570
178	1096	B	2	H	1	90	4.7	-77.62	242.77	2.13E-01	20	5570
178	1096	B	2	H	1	95	4.75	-78.28	220.08	2.23E-01	20	5570
178	1096	B	2	H	1	100	4.8	-80.82	213.9	2.28E-01	20	5570

Note: Only a portion of this table appears here. The complete table is available in ASCII format in the [TABLES](#) directory.

Table T13. Split-core paleomagnetic measurements for Hole 1096C before demagnetization (NRM results).

Leg	Site	Hole	Core	Type	Section	Interval (cm)	Depth (mbsf)	Inclination (°)	Declination (°)	Intensity (A/m)	Demagnetization step (mT)	Run #
178	1096	C	1	H	1	10	114.1	75.6	145.03	2.19E-01	0	6152
178	1096	C	1	H	1	15	114.15	65.87	172.89	4.84E-02	0	6152
178	1096	C	1	H	1	20	114.2	77.78	302.45	1.52E-02	0	6152
178	1096	C	1	H	1	25	114.25	64.65	7.87	1.15E-02	0	6152
178	1096	C	1	H	1	30	114.3	55.71	352.34	1.02E-02	0	6152
178	1096	C	1	H	1	35	114.35	51.06	199.7	6.63E-03	0	6152
178	1096	C	1	H	1	40	114.4	36.4	182.24	2.03E-02	0	6152
178	1096	C	1	H	1	45	114.45	56.75	178.58	5.58E-02	0	6152
178	1096	C	1	H	1	50	114.5	66.45	357.74	2.83E-01	0	6152
178	1096	C	1	H	1	55	114.55	73.75	359.84	8.35E-01	0	6152
178	1096	C	1	H	1	60	114.6	85.66	353.63	1.06E+00	0	6152
178	1096	C	1	H	1	65	114.65	84.97	352.91	9.92E-01	0	6152
178	1096	C	1	H	1	70	114.7	81.17	357.85	9.96E-01	0	6152
178	1096	C	1	H	1	75	114.75	80.59	353.63	9.86E-01	0	6152
178	1096	C	1	H	1	80	114.8	79.27	325.05	9.49E-01	0	6152
178	1096	C	1	H	1	85	114.85	84.97	263.13	7.63E-01	0	6152
178	1096	C	1	H	1	90	114.9	87.7	87.7	4.17E-01	0	6152
178	1096	C	1	H	1	95	114.95	82.62	15.39	2.82E-01	0	6152
178	1096	C	1	H	2	10	115.19	78.25	193.14	6.73E-01	0	6156
178	1096	C	1	H	2	15	115.24	75.65	104.28	6.38E-01	0	6156
178	1096	C	1	H	2	20	115.29	77.41	50.7	7.19E-01	0	6156
178	1096	C	1	H	2	25	115.34	83.51	323.58	7.95E-01	0	6156
178	1096	C	1	H	2	30	115.39	81.56	265.94	6.47E-01	0	6156
178	1096	C	1	H	2	35	115.44	82.17	327.79	5.98E-01	0	6156
178	1096	C	1	H	2	40	115.49	78.69	9.17	6.87E-01	0	6156
178	1096	C	1	H	2	45	115.54	77.84	302.51	7.48E-01	0	6156
178	1096	C	1	H	2	50	115.59	79.26	264.15	7.42E-01	0	6156
178	1096	C	1	H	2	55	115.64	87.12	146.94	7.09E-01	0	6156
178	1096	C	1	H	2	60	115.69	81.47	263.18	6.57E-01	0	6156
178	1096	C	1	H	2	65	115.74	82	286.59	7.47E-01	0	6156
178	1096	C	1	H	2	70	115.79	80.92	253.57	8.68E-01	0	6156
178	1096	C	1	H	2	75	115.84	80.04	253.56	8.99E-01	0	6156
178	1096	C	1	H	2	80	115.89	82.51	246.12	9.01E-01	0	6156
178	1096	C	1	H	2	85	115.94	82.57	240.97	8.84E-01	0	6156
178	1096	C	1	H	2	90	115.99	81.77	244.78	8.76E-01	0	6156
178	1096	C	1	H	3	10	116.19	80.62	246.97	8.29E-01	0	6159
178	1096	C	1	H	3	10	116.19	81.55	179.41	2.76E-01	0	6160
178	1096	C	1	H	3	15	116.24	75.29	181.88	2.39E-01	0	6160
178	1096	C	1	H	3	15	116.24	77.51	230.11	6.91E-01	0	6159
178	1096	C	1	H	3	20	116.29	67.05	194.66	1.71E-01	0	6160
178	1096	C	1	H	3	20	116.29	72.5	222.34	4.78E-01	0	6159
178	1096	C	1	H	3	25	116.34	75.47	286.53	3.28E-01	0	6159
178	1096	C	1	H	3	25	116.34	79.57	260.53	1.09E-01	0	6160
178	1096	C	1	H	3	30	116.39	77.73	77	1.97E-01	0	6160
178	1096	C	1	H	3	30	116.39	79.3	18.22	5.86E-01	0	6159
178	1096	C	1	H	3	35	116.44	79.26	133.51	2.65E-01	0	6160
178	1096	C	1	H	3	35	116.44	86.48	250.21	8.01E-01	0	6159
178	1096	C	1	H	3	40	116.49	83.08	103.28	2.40E-01	0	6160
178	1096	C	1	H	3	40	116.49	85.25	240.68	7.50E-01	0	6159
178	1096	C	1	H	3	45	116.54	80.11	50.93	2.34E-01	0	6160
178	1096	C	1	H	3	45	116.54	88	37.45	7.07E-01	0	6159
178	1096	C	1	H	3	50	116.59	84.04	71.75	2.41E-01	0	6160
178	1096	C	1	H	3	50	116.59	88.17	112.43	7.39E-01	0	6159
178	1096	C	1	H	3	55	116.64	81.75	97.69	2.46E-01	0	6160
178	1096	C	1	H	3	55	116.64	86.48	149.65	7.39E-01	0	6159
178	1096	C	1	H	3	60	116.69	85.52	144.41	6.65E-01	0	6159
178	1096	C	1	H	3	65	116.74	70.9	161.16	4.38E-01	0	6159
178	1096	C	1	H	4	10	116.85	78.38	356.77	5.47E-01	0	6163
178	1096	C	1	H	4	15	116.9	72.56	13.25	9.40E-01	0	6163
178	1096	C	1	H	4	20	116.95	79.81	358.51	1.05E+00	0	6163
178	1096	C	1	H	4	25	117	80.16	359.5	1.06E+00	0	6163
178	1096	C	1	H	4	30	117.05	79.52	321.42	1.03E+00	0	6163
178	1096	C	1	H	4	35	117.1	67.24	271.97	7.87E-01	0	6163
178	1096	C	1	H	4	40	117.15	73.28	301.86	4.94E-01	0	6163
178	1096	C	1	H	4	45	117.2	77.35	299.2	2.87E-01	0	6163

Note: Only a portion of this table appears here. The complete table is available in ASCII format in the [TABLES](#) directory.

Table T14. Split-core paleomagnetic measurements for Hole 1096C after 10-mT demagnetization.

Leg	Site	Hole	Core	Type	Section	Interval (cm)	Depth (mbsf)	Inclination (°)	Declination (°)	Intensity (A/m)	Demagnetization step (mT)	Run #
178	1096	C	1	H	1	10	114.1	82.84	179.41	1.30E-02	10	6153
178	1096	C	1	H	1	15	114.15	45.39	192.93	3.87E-03	10	6153
178	1096	C	1	H	1	20	114.2	61.69	232.7	1.09E-03	10	6153
178	1096	C	1	H	1	25	114.25	54.32	351.66	9.84E-04	10	6153
178	1096	C	1	H	1	30	114.3	58.49	338.86	9.32E-04	10	6153
178	1096	C	1	H	1	35	114.35	54.02	241.86	9.19E-04	10	6153
178	1096	C	1	H	1	40	114.4	47.86	205.01	2.89E-03	10	6153
178	1096	C	1	H	1	45	114.45	29.69	200.9	6.78E-03	10	6153
178	1096	C	1	H	1	50	114.5	49.01	358.32	1.52E-02	10	6153
178	1096	C	1	H	1	55	114.55	45.64	16.87	5.51E-02	10	6153
178	1096	C	1	H	1	60	114.6	56.06	38.68	7.83E-02	10	6153
178	1096	C	1	H	1	65	114.65	64.62	39.57	9.43E-02	10	6153
178	1096	C	1	H	1	70	114.7	65.7	24.88	1.06E-01	10	6153
178	1096	C	1	H	1	75	114.75	68.72	11.88	1.05E-01	10	6153
178	1096	C	1	H	1	80	114.8	87.25	101.05	7.50E-02	10	6153
178	1096	C	1	H	1	85	114.85	61.96	161.74	4.18E-02	10	6153
178	1096	C	1	H	1	90	114.9	56.26	357.55	6.10E-03	10	6153
178	1096	C	1	H	1	95	114.95	-19.13	1.04	1.12E-02	10	6153
178	1096	C	1	H	2	10	115.19	52.12	328.14	2.10E-01	10	6157
178	1096	C	1	H	2	15	115.24	58.55	11.71	1.70E-01	10	6157
178	1096	C	1	H	2	20	115.29	46.89	21.29	1.98E-01	10	6157
178	1096	C	1	H	2	25	115.34	45.92	12.67	2.12E-01	10	6157
178	1096	C	1	H	2	30	115.39	55.27	5.23	1.43E-01	10	6157
178	1096	C	1	H	2	35	115.44	61.5	335.32	1.02E-01	10	6157
178	1096	C	1	H	2	40	115.49	48.73	339.45	1.39E-01	10	6157
178	1096	C	1	H	2	45	115.54	63.78	323.09	1.43E-01	10	6157
178	1096	C	1	H	2	50	115.59	79.24	235.78	1.33E-01	10	6157
178	1096	C	1	H	2	55	115.64	80.13	190.64	1.14E-01	10	6157
178	1096	C	1	H	2	60	115.69	74.14	208.56	8.39E-02	10	6157
178	1096	C	1	H	2	65	115.74	80.91	224.17	9.00E-02	10	6157
178	1096	C	1	H	2	70	115.79	73.59	231.31	1.33E-01	10	6157
178	1096	C	1	H	2	75	115.84	68.15	210.87	1.37E-01	10	6157
178	1096	C	1	H	2	80	115.89	71.65	173.31	1.15E-01	10	6157
178	1096	C	1	H	2	85	115.94	73.42	152.5	1.09E-01	10	6157
178	1096	C	1	H	2	90	115.99	74.25	197.42	1.04E-01	10	6157
178	1096	C	1	H	3	10	116.19	68.12	148.78	7.80E-02	10	6161
178	1096	C	1	H	3	15	116.24	61.96	159	8.00E-02	10	6161
178	1096	C	1	H	3	20	116.29	54.17	181.84	6.58E-02	10	6161
178	1096	C	1	H	3	25	116.34	66.22	212	3.60E-02	10	6161
178	1096	C	1	H	3	30	116.39	53.48	139.6	6.44E-02	10	6161
178	1096	C	1	H	3	35	116.44	45.24	137.1	8.45E-02	10	6161
178	1096	C	1	H	3	40	116.49	49.79	92.35	6.55E-02	10	6161
178	1096	C	1	H	3	45	116.54	52.56	54.06	6.48E-02	10	6161
178	1096	C	1	H	3	50	116.59	60.65	64.28	5.98E-02	10	6161
178	1096	C	1	H	3	55	116.64	54.58	76.31	6.78E-02	10	6161
178	1096	C	1	H	4	10	116.85	80.01	20.49	6.67E-02	10	6164
178	1096	C	1	H	4	15	116.9	66.48	13.27	1.36E-01	10	6164
178	1096	C	1	H	4	20	116.95	76.46	340.99	1.73E-01	10	6164
178	1096	C	1	H	4	25	117	77.47	340.29	1.97E-01	10	6164
178	1096	C	1	H	4	30	117.05	76.47	346.63	2.13E-01	10	6164
178	1096	C	1	H	4	35	117.1	66.12	288.09	1.83E-01	10	6164
178	1096	C	1	H	4	40	117.15	72.95	334.41	1.26E-01	10	6164
178	1096	C	1	H	4	45	117.2	73.66	331.82	8.19E-02	10	6164
178	1096	C	1	H	4	50	117.25	71.56	334.97	5.86E-02	10	6164
178	1096	C	1	H	4	55	117.3	81.05	183.28	3.26E-02	10	6164
178	1096	C	1	H	4	60	117.35	64.39	142.86	2.15E-02	10	6164
178	1096	C	1	H	4	65	117.4	60.37	0.35	8.22E-02	10	6164
178	1096	C	1	H	4	70	117.45	69.91	332.12	1.56E-01	10	6164
178	1096	C	1	H	4	75	117.5	74.32	316.51	1.67E-01	10	6164
178	1096	C	1	H	4	80	117.55	78.57	321.11	1.63E-01	10	6164
178	1096	C	1	H	4	85	117.6	85.29	267.15	1.21E-01	10	6164
178	1096	C	1	H	4	90	117.65	80.63	349.26	8.65E-02	10	6164
178	1096	C	1	H	4	95	117.7	72.43	348.67	8.69E-02	10	6164
178	1096	C	1	H	4	100	117.75	76.21	344.94	7.96E-02	10	6164
178	1096	C	1	H	4	105	117.8	82.88	350.08	5.88E-02	10	6164
178	1096	C	1	H	4	110	117.85	83.94	344.14	4.17E-02	10	6164

Note: Only a portion of this table appears here. The complete table is available in ASCII format in the **TABLES** directory.

Table T15. Split-core paleomagnetic measurements for Hole 1096C after 20-mT demagnetization.

Leg	Site	Hole	Core	Type	Section	Interval (cm)	Depth (mbsf)	Inclination (°)	Declination (°)	Intensity (A/m)	Demagnetization step (mT)	Run #
178	1096	C	1	H	1	10	114.1	75.39	1.43	3.74E-03	20	6154
178	1096	C	1	H	1	15	114.15	31.47	184.97	1.13E-03	20	6154
178	1096	C	1	H	1	20	114.2	32.46	201.93	2.81E-04	20	6154
178	1096	C	1	H	1	25	114.25	29.21	288.29	2.58E-04	20	6154
178	1096	C	1	H	1	30	114.3	11.81	256.96	1.92E-04	20	6154
178	1096	C	1	H	1	35	114.35	37.16	239.63	3.06E-04	20	6154
178	1096	C	1	H	1	40	114.4	40.16	217.48	1.36E-03	20	6154
178	1096	C	1	H	1	45	114.45	22.81	210.13	3.29E-03	20	6154
178	1096	C	1	H	1	50	114.5	33.24	4.55	5.93E-03	20	6154
178	1096	C	1	H	1	55	114.55	28.38	28.94	2.27E-02	20	6154
178	1096	C	1	H	1	60	114.6	37.12	51.23	3.35E-02	20	6154
178	1096	C	1	H	1	65	114.65	51.72	56.36	4.20E-02	20	6154
178	1096	C	1	H	1	70	114.7	58.25	38.78	4.76E-02	20	6154
178	1096	C	1	H	1	75	114.75	65.24	24.85	4.54E-02	20	6154
178	1096	C	1	H	1	80	114.8	65.88	149.22	2.85E-02	20	6154
178	1096	C	1	H	1	85	114.85	14.15	160.18	1.68E-02	20	6154
178	1096	C	1	H	1	90	114.9	-62.71	317.79	8.02E-03	20	6154
178	1096	C	1	H	1	95	114.95	-54.01	352.4	1.13E-02	20	6154
178	1096	C	1	H	2	10	115.19	47.86	330.42	1.47E-01	20	6158
178	1096	C	1	H	2	15	115.24	54.37	9.1	1.15E-01	20	6158
178	1096	C	1	H	2	20	115.29	42.12	19.65	1.33E-01	20	6158
178	1096	C	1	H	2	25	115.34	38.93	14.82	1.43E-01	20	6158
178	1096	C	1	H	2	30	115.39	47.19	10.98	9.36E-02	20	6158
178	1096	C	1	H	2	35	115.44	56.24	332.53	6.00E-02	20	6158
178	1096	C	1	H	2	40	115.49	42.44	332.73	8.77E-02	20	6158
178	1096	C	1	H	2	45	115.54	60.91	324.16	8.46E-02	20	6158
178	1096	C	1	H	2	50	115.59	78.08	225.1	8.09E-02	20	6158
178	1096	C	1	H	2	55	115.64	75.32	200.28	6.82E-02	20	6158
178	1096	C	1	H	2	60	115.69	68.78	200.29	4.46E-02	20	6158
178	1096	C	1	H	2	65	115.74	77.1	199.19	4.71E-02	20	6158
178	1096	C	1	H	2	70	115.79	69.8	221.77	7.65E-02	20	6158
178	1096	C	1	H	2	75	115.84	62.57	202.7	8.13E-02	20	6158
178	1096	C	1	H	2	80	115.89	63.37	166.76	6.73E-02	20	6158
178	1096	C	1	H	2	85	115.94	65.42	149.54	6.24E-02	20	6158
178	1096	C	1	H	2	90	115.99	68.16	188.31	5.75E-02	20	6158
178	1096	C	1	H	3	10	116.19	55.91	145.65	4.06E-02	20	6162
178	1096	C	1	H	3	15	116.24	51.98	155.36	4.55E-02	20	6162
178	1096	C	1	H	3	20	116.29	45.97	176.02	3.88E-02	20	6162
178	1096	C	1	H	3	25	116.34	60.14	195.06	1.96E-02	20	6162
178	1096	C	1	H	3	30	116.39	40.5	149.61	4.04E-02	20	6162
178	1096	C	1	H	3	35	116.44	30.9	142.24	5.46E-02	20	6162
178	1096	C	1	H	3	40	116.49	35.93	98.24	3.81E-02	20	6162
178	1096	C	1	H	3	45	116.54	41.41	57.08	3.55E-02	20	6162
178	1096	C	1	H	3	50	116.59	47.46	67.83	2.96E-02	20	6162
178	1096	C	1	H	3	55	116.64	40.71	76.14	3.68E-02	20	6162
178	1096	C	1	H	4	10	116.85	85.95	109.99	2.39E-02	20	6165
178	1096	C	1	H	4	15	116.9	69.52	0.42	5.60E-02	20	6165
178	1096	C	1	H	4	20	116.95	77.22	317.01	8.47E-02	20	6165
178	1096	C	1	H	4	25	117	75.24	286.75	1.02E-01	20	6165
178	1096	C	1	H	4	30	117.05	75.04	312.07	9.77E-02	20	6165
178	1096	C	1	H	4	35	117.1	69.69	324.71	9.84E-02	20	6165
178	1096	C	1	H	4	40	117.15	73.73	340.06	8.55E-02	20	6165
178	1096	C	1	H	4	45	117.2	73.79	325.23	5.94E-02	20	6165
178	1096	C	1	H	4	50	117.25	72.47	328.04	4.30E-02	20	6165
178	1096	C	1	H	4	55	117.3	81.03	188.43	2.35E-02	20	6165
178	1096	C	1	H	4	60	117.35	67.37	135.9	1.50E-02	20	6165
178	1096	C	1	H	4	65	117.4	64.11	1.27	5.78E-02	20	6165
178	1096	C	1	H	4	70	117.45	73.42	323.56	1.10E-01	20	6165
178	1096	C	1	H	4	75	117.5	76.07	302.36	1.19E-01	20	6165
178	1096	C	1	H	4	80	117.55	81.56	296.13	1.13E-01	20	6165
178	1096	C	1	H	4	85	117.6	81.45	217.34	7.72E-02	20	6165
178	1096	C	1	H	4	90	117.65	85.41	329.32	4.76E-02	20	6165
178	1096	C	1	H	4	95	117.7	76.28	345.9	4.54E-02	20	6165
178	1096	C	1	H	4	100	117.75	79.34	336.56	4.13E-02	20	6165
178	1096	C	1	H	4	105	117.8	84.54	330.21	3.05E-02	20	6165
178	1096	C	1	H	4	110	117.85	83.4	344.86	2.15E-02	20	6165

Note: Only a portion of this table appears here. The complete table is available in ASCII format in the **TABLES** directory.

Table T16. Split-core paleomagnetic measurements for Hole 1096C after 30-mT demagnetization.

Leg	Site	Hole	Core	Type	Section	Interval (cm)	Depth (mbsf)	Inclination (°)	Declination (°)	Intensity (A/m)	Demagnetization step (mT)	Run #
178	1096	C	1	H	1	10	114.1	65.31	2	2.09E-03	30	6155
178	1096	C	1	H	1	15	114.15	38.46	179.76	5.52E-04	30	6155
178	1096	C	1	H	1	20	114.2	55.09	213.78	1.59E-04	30	6155
178	1096	C	1	H	1	25	114.25	29.12	289.44	2.30E-04	30	6155
178	1096	C	1	H	1	30	114.3	15.36	250.21	1.31E-04	30	6155
178	1096	C	1	H	1	35	114.35	34.08	223.64	1.78E-04	30	6155
178	1096	C	1	H	1	40	114.4	36.71	216.12	7.96E-04	30	6155
178	1096	C	1	H	1	45	114.45	21.8	209.94	1.91E-03	30	6155
178	1096	C	1	H	1	50	114.5	29.44	9.1	3.43E-03	30	6155
178	1096	C	1	H	1	55	114.55	25.11	28.35	1.32E-02	30	6155
178	1096	C	1	H	1	60	114.6	36.16	47.7	1.98E-02	30	6155
178	1096	C	1	H	1	65	114.65	53.9	52.01	2.58E-02	30	6155
178	1096	C	1	H	1	70	114.7	62.03	34.43	2.95E-02	30	6155
178	1096	C	1	H	1	75	114.75	68.29	12.96	2.82E-02	30	6155
178	1096	C	1	H	1	80	114.8	70.68	172.62	1.75E-02	30	6155
178	1096	C	1	H	1	85	114.85	21.94	174.69	9.06E-03	30	6155
178	1096	C	1	H	1	90	114.9	-49.34	313.56	4.51E-03	30	6155
178	1096	C	1	H	1	95	114.95	-53	356.02	6.16E-03	30	6155
178	1096	C	10	X	2	10	281.6	-51.4	141.33	1.53E-02	30	6327
178	1096	C	10	X	2	15	281.65	-75.94	252.5	8.31E-03	30	6327
178	1096	C	10	X	2	20	281.7	-56.27	12.4	7.75E-03	30	6327
178	1096	C	10	X	2	25	281.75	-62.03	31.65	7.78E-03	30	6327
178	1096	C	10	X	2	30	281.8	-67.68	338.04	8.37E-03	30	6327
178	1096	C	10	X	2	35	281.85	-73.4	324.42	1.22E-02	30	6327
178	1096	C	10	X	2	40	281.9	-62.81	53.75	1.21E-02	30	6327
178	1096	C	10	X	2	45	281.95	-71.3	37.73	1.40E-02	30	6327
178	1096	C	10	X	2	50	282	-70.24	25.38	1.85E-02	30	6327
178	1096	C	10	X	2	55	282.05	-76.34	45.82	1.74E-02	30	6327
178	1096	C	10	X	2	60	282.1	-88.12	160.47	1.73E-02	30	6327
178	1096	C	10	X	2	65	282.15	-84.24	326.65	1.68E-02	30	6327
178	1096	C	10	X	2	70	282.2	-79.1	327.28	1.70E-02	30	6327
178	1096	C	10	X	2	75	282.25	-73.44	83.06	1.83E-02	30	6327
178	1096	C	10	X	2	80	282.3	-60.14	3.33	1.77E-02	30	6327
178	1096	C	10	X	2	85	282.35	-40.3	316.85	1.44E-02	30	6327
178	1096	C	10	X	2	90	282.4	-66.36	253.66	1.16E-02	30	6327
178	1096	C	10	X	2	95	282.45	-83.84	201.82	8.24E-03	30	6327
178	1096	C	10	X	2	100	282.5	-73.96	98.98	3.98E-03	30	6327
178	1096	C	10	X	2	105	282.55	-24.03	170.02	5.02E-03	30	6327
178	1096	C	10	X	2	110	282.6	-64.66	212.3	4.89E-03	30	6327
178	1096	C	10	X	2	115	282.65	-64.94	146.23	7.49E-03	30	6327
178	1096	C	10	X	2	120	282.7	-78.59	115.17	7.91E-03	30	6327
178	1096	C	10	X	2	125	282.75	-14.47	338.51	3.45E-02	30	6327
178	1096	C	10	X	2	130	282.8	-15.21	333.66	2.44E-02	30	6327
178	1096	C	10	X	2	135	282.85	-49.12	341.36	6.07E-03	30	6327
178	1096	C	10	X	2	140	282.9	-34.62	42.63	2.58E-03	30	6327
178	1096	C	10	X	3	10	283.1	-65.47	9.55	3.26E-03	30	6330
178	1096	C	10	X	3	15	283.15	-45.85	335.96	4.27E-03	30	6330
178	1096	C	10	X	3	20	283.2	-58.16	216.56	4.76E-03	30	6330
178	1096	C	10	X	3	25	283.25	-29.69	198.66	1.87E-03	30	6330
178	1096	C	10	X	3	30	283.3	55.8	355.66	1.83E-02	30	6330
178	1096	C	10	X	3	35	283.35	73.75	29.91	2.14E-02	30	6330
178	1096	C	10	X	3	40	283.4	68.74	33.54	1.11E-02	30	6330
178	1096	C	10	X	3	45	283.45	60.35	347.06	1.41E-02	30	6330
178	1096	C	10	X	3	50	283.5	74.89	264.08	3.77E-02	30	6330
178	1096	C	10	X	3	55	283.55	69.78	185.03	4.85E-02	30	6330
178	1096	C	10	X	3	60	283.6	69.66	165.79	4.50E-02	30	6330
178	1096	C	10	X	3	65	283.65	75.92	54.22	3.71E-02	30	6330
178	1096	C	10	X	3	70	283.7	61.5	51.14	4.05E-02	30	6330
178	1096	C	10	X	3	75	283.75	71.9	349.76	4.22E-02	30	6330
178	1096	C	10	X	3	80	283.8	62.99	53.34	5.19E-02	30	6330
178	1096	C	10	X	3	85	283.85	84.53	107.3	4.44E-02	30	6330
178	1096	C	10	X	3	90	283.9	45.28	234.32	5.23E-02	30	6330
178	1096	C	10	X	3	95	283.95	67.6	166.07	4.04E-02	30	6330
178	1096	C	10	X	3	100	284	48.17	119.4	5.75E-02	30	6330
178	1096	C	10	X	3	105	284.05	75.38	135.48	4.06E-02	30	6330
178	1096	C	10	X	3	110	284.1	63.05	29.99	3.99E-02	30	6330

Note: Only a portion of this table appears here. The complete table is available in ASCII format in the **TABLES** directory.

Table T17. Discrete sample NRM and AF demagnetization results for Hole 1096A.

Leg	Site	Hole	Core	Type	Section	Interval (cm)	Depth (mbsf)	Inclination (°)	Declination (°)	Intensity (A/m)	Mx (A·m)	My (A·m)	Mz (A·m)	Demagnetization step (mT)
178	1096	A	1	H	1	71	0.71	-58.54	184.46	1.48E-01	-6.15E-07	-4.80E-08	-1.01E-06	0
178	1096	A	1	H	1	71	0.71	-64.02	186.07	1.47E-01	-5.12E-07	-5.45E-08	-1.06E-06	10
178	1096	A	1	H	1	71	0.71	-64.54	186.01	1.39E-01	-4.75E-07	-5.00E-08	-1.00E-06	20
178	1096	A	1	H	1	71	0.71	-65.06	184.81	1.30E-01	-4.36E-07	-3.67E-08	-9.40E-07	30
178	1096	A	1	H	1	71	0.71	-65.25	184.08	1.21E-01	-4.05E-07	-2.89E-08	-8.80E-07	40
178	1096	A	1	H	1	71	0.71	-65.63	184.62	1.11E-01	-3.64E-07	-2.94E-08	-8.06E-07	50
178	1096	A	1	H	1	71	0.71	-65.78	183.97	1.01E-01	-3.30E-07	-2.28E-08	-7.34E-07	60
178	1096	A	1	H	1	71	0.71	-66.61	185	9.03E-02	-2.86E-07	-2.50E-08	-6.63E-07	70
178	1096	A	1	H	1	134	1.34	-28.98	251.87	1.78E-01	-3.87E-07	-1.18E-06	-6.89E-07	0
178	1096	A	1	H	1	134	1.34	-36.62	262.31	1.70E-01	-1.46E-07	-1.08E-06	-8.10E-07	10
178	1096	A	1	H	1	134	1.34	-36.47	264.34	1.61E-01	-1.02E-07	-1.03E-06	-7.67E-07	20
178	1096	A	1	H	1	134	1.34	-36.51	265.73	1.51E-01	-7.25E-08	-9.71E-07	-7.20E-07	30
178	1096	A	1	H	1	134	1.34	-36.61	266.62	1.42E-01	-5.35E-08	-9.08E-07	-6.75E-07	40
178	1096	A	1	H	1	134	1.34	-37.29	266.83	1.30E-01	-4.56E-08	-8.23E-07	-6.28E-07	50
178	1096	A	1	H	1	134	1.34	-37.1	268.21	1.18E-01	-2.36E-08	-7.55E-07	-5.72E-07	60
178	1096	A	1	H	1	134	1.34	-37.34	268.54	1.07E-01	-1.73E-08	-6.82E-07	-5.20E-07	70
178	1096	A	1	H	2	71	2.21	-78.65	169.52	9.20E-02	-1.42E-07	2.64E-08	-7.22E-07	0
178	1096	A	1	H	2	71	2.21	-82.19	164.46	8.96E-02	-9.38E-08	2.61E-08	-7.11E-07	10
178	1096	A	1	H	2	71	2.21	-82.59	165.55	7.86E-02	-7.86E-08	2.02E-08	-6.24E-07	20
178	1096	A	1	H	2	71	2.21	-82.28	161.25	6.48E-02	-6.60E-08	2.24E-08	-5.14E-07	30
178	1096	A	1	H	2	71	2.21	-81.72	158.14	5.34E-02	-5.71E-08	2.29E-08	-4.23E-07	40
178	1096	A	1	H	2	71	2.21	-81.15	158.73	4.25E-02	-4.87E-08	1.90E-08	-3.36E-07	50
178	1096	A	1	H	2	71	2.21	-80.01	143.82	3.47E-02	-3.89E-08	2.84E-08	-2.73E-07	60
178	1096	A	1	H	2	71	2.21	-79.55	140.44	2.82E-02	-3.16E-08	2.61E-08	-2.22E-07	70
178	1096	A	1	H	2	144	2.94	-62.77	109.67	7.21E-02	-8.88E-08	2.48E-07	-5.13E-07	0
178	1096	A	1	H	2	144	2.94	-65.78	107.05	7.40E-02	-7.12E-08	2.32E-07	-5.40E-07	10
178	1096	A	1	H	2	144	2.94	-65.93	106.01	7.04E-02	-6.33E-08	2.21E-07	-5.14E-07	20
178	1096	A	1	H	2	144	2.94	-66	104.21	6.63E-02	-5.30E-08	2.09E-07	-4.85E-07	30
178	1096	A	1	H	2	144	2.94	-66.32	103.98	6.25E-02	-4.85E-08	1.95E-07	-4.58E-07	40
178	1096	A	1	H	2	144	2.94	-66.46	105.87	5.77E-02	-5.05E-08	1.77E-07	-4.24E-07	50
178	1096	A	1	H	2	144	2.94	-66.86	106.08	5.42E-02	-4.72E-08	1.64E-07	-3.99E-07	60
178	1096	A	1	H	2	144	2.94	-66.25	106.89	4.83E-02	-4.52E-08	1.49E-07	-3.53E-07	70
178	1096	A	1	H	3	71	3.71	-67.53	297.48	1.37E-01	1.93E-07	-3.70E-07	-1.01E-06	0
178	1096	A	1	H	3	71	3.71	-73.08	299.18	1.38E-01	1.56E-07	-2.80E-07	-1.05E-06	10
178	1096	A	1	H	3	71	3.71	-72.95	297.99	1.18E-01	1.30E-07	-2.44E-07	-9.01E-07	20
178	1096	A	1	H	3	71	3.71	-73.57	294.08	9.20E-02	8.49E-08	-1.90E-07	-7.06E-07	30
178	1096	A	1	H	3	71	3.71	-74.27	285.78	6.96E-02	4.11E-08	-1.45E-07	-5.36E-07	40
178	1096	A	1	H	3	71	3.71	-75.65	278.22	5.07E-02	1.44E-08	-9.94E-08	-3.93E-07	50
178	1096	A	1	H	3	71	3.71	-75.34	268.12	3.65E-02	-2.43E-09	-7.38E-08	-2.82E-07	60
178	1096	A	1	H	3	71	3.71	-75.8	263.23	2.67E-02	-6.16E-09	-5.19E-08	-2.07E-07	70
178	1096	A	1	H	3	126	4.26	-83.09	352.44	2.09E-01	1.99E-07	-2.64E-08	-1.66E-06	0
178	1096	A	1	H	3	126	4.26	-85.25	14.57	2.22E-01	1.42E-07	3.70E-08	-1.77E-06	10
178	1096	A	1	H	3	126	4.26	-84.9	12.11	2.11E-01	1.47E-07	3.15E-08	-1.68E-06	20
178	1096	A	1	H	3	126	4.26	-85.09	14.54	1.99E-01	1.32E-07	3.43E-08	-1.59E-06	30
178	1096	A	1	H	3	126	4.26	-85.3	15.62	1.89E-01	1.19E-07	3.33E-08	-1.50E-06	40
178	1096	A	1	H	3	126	4.26	-85.89	21.93	1.74E-01	9.27E-08	3.73E-08	-1.39E-06	50
178	1096	A	1	H	3	126	4.26	-86.3	27.94	1.63E-01	7.42E-08	3.94E-08	-1.30E-06	60
178	1096	A	1	H	3	126	4.26	-86.62	34.42	1.47E-01	5.71E-08	3.91E-08	-1.17E-06	70
178	1096	A	1	H	4	71	5.21	-68.44	265.31	1.11E-01	-2.67E-08	-3.25E-07	-8.25E-07	0
178	1096	A	1	H	4	71	5.21	-72.63	266.55	1.15E-01	-1.65E-08	-2.74E-07	-8.77E-07	10
178	1096	A	1	H	4	71	5.21	-72.3	267.82	1.09E-01	-1.01E-08	-2.65E-07	-8.30E-07	20
178	1096	A	1	H	4	71	5.21	-72.3	266.65	1.02E-01	-1.45E-08	-2.48E-07	-7.78E-07	30
178	1096	A	1	H	4	71	5.21	-72.61	265.42	9.60E-02	-1.83E-08	-2.29E-07	-7.33E-07	40
178	1096	A	1	H	4	71	5.21	-73	262.66	8.83E-02	-2.64E-08	-2.05E-07	-6.76E-07	50
178	1096	A	1	H	4	71	5.21	-73.36	258.89	8.11E-02	-3.58E-08	-1.82E-07	-6.22E-07	60
178	1096	A	1	H	4	71	5.21	-74.04	257.38	7.28E-02	-3.50E-08	-1.56E-07	-5.60E-07	70
178	1096	A	1	H	4	141	5.91	-21.11	163.56	1.23E-01	-8.84E-07	2.61E-07	-3.56E-07	0
178	1096	A	1	H	4	141	5.91	-43.67	151.26	9.40E-02	-4.77E-07	2.62E-07	-5.19E-07	10
178	1096	A	1	H	4	141	5.91	-47.57	147.82	8.57E-02	-3.92E-07	2.46E-07	-5.06E-07	20
178	1096	A	1	H	4	141	5.91	-49.66	144.22	8.13E-02	-3.42E-07	2.46E-07	-4.96E-07	30
178	1096	A	1	H	4	141	5.91	-51.71	141.61	7.76E-02	-3.02E-07	2.39E-07	-4.87E-07	40
178	1096	A	1	H	4	141	5.91	-53.48	138.34	7.50E-02	-2.67E-07	2.37E-07	-4.82E-07	50
178	1096	A	1	H	4	141	5.91	-54.74	135.47	6.86E-02	-2.26E-07	2.22E-07	-4.48E-07	60
178	1096	A	1	H	4	141	5.91	-55.63	132.38	6.25E-02	-1.90E-07	2.09E-07	-4.13E-07	70
178	1096	A	1	H	4	141	5.91	-56.92	134.73	5.76E-02	-1.77E-07	1.79E-07	-3.86E-07	80
178	1096	A	1	H	5	51	6.51	-74.32	241.19	1.09E-01	-1.14E-07	-2.07E-07	-8.43E-07	0

Note: Only a portion of this table appears here. The complete table is available in ASCII format in the **TABLES** directory.

Table T18. Discrete sample NRM and AF demagnetization results for Hole 1096B.

Leg	Site	Hole	Core	Type	Section	Interval (cm)	Depth (mbsf)	Inclination (°)	Declination (°)	Intensity (A/m)	Mx (A·m)	My (A·m)	Mz (A·m)	Demagnetization step (mT)
178	1096	B	13	H	1	89	109.19	66.08	209.2	1.45E-02	-4.11E-08	-2.30E-08	1.06E-07	0
178	1096	B	13	H	1	89	109.19	71.11	181.01	7.74E-03	-2.00E-08	-3.55E-10	5.86E-08	10
178	1096	B	13	H	1	89	109.19	71.94	182.01	6.64E-03	-1.64E-08	-5.78E-10	5.05E-08	20
178	1096	B	13	H	1	89	109.19	73.13	184.89	4.51E-03	-1.04E-08	-8.93E-10	3.45E-08	30
178	1096	B	13	H	1	89	109.19	86.85	328.49	2.61E-03	9.78E-10	-5.99E-10	2.08E-08	40
178	1096	B	13	H	1	89	109.19	66.93	217.18	1.40E-03	-3.51E-09	-2.66E-09	1.03E-08	50
178	1096	B	13	H	1	89	109.19	29.54	188.69	7.85E-04	-5.40E-09	-8.26E-10	3.10E-09	60
178	1096	B	13	H	1	89	109.19	32.73	264.03	5.82E-04	-4.07E-10	-3.89E-09	2.52E-09	70
178	1096	B	13	H	4	133	114.13	82.03	318.41	2.18E-01	1.81E-07	-1.60E-07	1.73E-06	0
178	1096	B	13	H	4	133	114.13	65.28	259.46	1.03E-01	-6.28E-08	-3.37E-07	7.45E-07	10
178	1096	B	13	H	4	133	114.13	64.02	257.58	7.89E-02	-5.94E-08	-2.70E-07	5.67E-07	20
178	1096	B	13	H	4	133	114.13	63.54	255.71	5.41E-02	-4.76E-08	-1.87E-07	3.87E-07	30
178	1096	B	13	H	4	133	114.13	64.31	253.21	3.70E-02	-3.71E-08	-1.23E-07	2.67E-07	40
178	1096	B	13	H	4	133	114.13	60.15	253.98	2.35E-02	-2.58E-08	-8.97E-08	1.63E-07	50
178	1096	B	13	H	4	133	114.13	63	263.46	1.42E-02	-5.89E-09	-5.13E-08	1.01E-07	60
178	1096	B	13	H	4	133	114.13	52.8	247.55	9.06E-03	-1.67E-08	-4.05E-08	5.77E-08	70
178	1096	B	19	H	2	71	152.91	74.61	295	2.25E-01	2.02E-07	-4.34E-07	1.74E-06	0
178	1096	B	19	H	2	71	152.91	66.63	345.65	3.09E-02	9.49E-08	-2.43E-08	2.27E-07	10
178	1096	B	19	H	2	71	152.91	50.55	14.28	1.30E-02	6.43E-08	1.64E-08	8.06E-08	20
178	1096	B	19	H	2	71	152.91	43.42	20.06	7.82E-03	4.27E-08	1.56E-08	4.30E-08	30
178	1096	B	19	H	2	71	152.91	40.53	27.49	5.12E-03	2.76E-08	1.44E-08	2.66E-08	40
178	1096	B	19	H	2	71	152.91	23.28	23.95	2.76E-03	1.86E-08	8.24E-09	8.74E-09	50
178	1096	B	19	H	2	71	152.91	47.61	33.8	1.68E-03	7.54E-09	5.05E-09	9.95E-09	60
178	1096	B	19	H	2	71	152.91	-42.03	25.54	2.55E-03	1.37E-08	6.54E-09	-1.37E-08	70
178	1096	B	19	H	4	71	155.91	62.01	316.71	3.93E-01	1.07E-06	-1.01E-06	2.78E-06	0
178	1096	B	19	H	4	71	155.91	51.98	331.59	1.69E-01	7.34E-07	-3.97E-07	1.07E-06	10
178	1096	B	19	H	4	71	155.91	49.67	334.87	1.20E-01	5.62E-07	-2.64E-07	7.31E-07	20
178	1096	B	19	H	4	71	155.91	48.05	337.62	7.72E-02	3.82E-07	-1.57E-07	4.59E-07	30
178	1096	B	19	H	4	71	155.91	45.98	342.25	4.85E-02	2.57E-07	-8.22E-08	2.79E-07	40
178	1096	B	19	H	4	71	155.91	41.22	345.43	2.61E-02	1.52E-07	-3.95E-08	1.38E-07	50
178	1096	B	19	H	4	71	155.91	35.11	354.83	1.81E-02	1.18E-07	-1.07E-08	8.35E-08	60
178	1096	B	19	H	4	71	155.91	-9.27	0.6	8.35E-03	6.59E-08	6.96E-10	-1.08E-08	70
178	1096	B	20	H	1	81	158.51	69.58	260.92	2.48E-01	-1.09E-07	-6.85E-07	1.86E-06	0
178	1096	B	20	H	1	81	158.51	66.63	227.1	1.24E-01	-2.68E-07	-2.89E-07	9.12E-07	10
178	1096	B	20	H	1	81	158.51	66.72	222.45	9.04E-02	-2.11E-07	-1.93E-07	6.65E-07	20
178	1096	B	20	H	1	81	158.51	67.1	220.61	6.05E-02	-1.43E-07	-1.23E-07	4.46E-07	30
178	1096	B	20	H	1	81	158.51	67.83	217.5	4.13E-02	-9.89E-08	-7.59E-08	3.06E-07	40
178	1096	B	20	H	1	81	158.51	65.56	211.31	2.62E-02	-7.41E-08	-4.50E-08	1.91E-07	50
178	1096	B	20	H	1	81	158.51	70.98	211.57	1.65E-02	-3.66E-08	-2.25E-08	1.24E-07	60
178	1096	B	20	H	1	81	158.51	61.39	229.08	1.02E-02	-2.56E-08	-2.95E-08	7.16E-08	70
178	1096	B	20	H	2	81	160.01	69.5	268.88	3.07E-01	-1.68E-08	-8.60E-07	2.30E-06	0
178	1096	B	20	H	2	81	160.01	68.57	266.19	1.65E-01	-3.21E-08	-4.82E-07	1.23E-06	10
178	1096	B	20	H	2	81	160.01	69.17	266.12	1.23E-01	-2.37E-08	-3.50E-07	9.22E-07	20
178	1096	B	20	H	2	81	160.01	69.77	266.54	8.45E-02	-1.41E-08	-2.33E-07	6.34E-07	30
178	1096	B	20	H	2	81	160.01	70.7	266.46	5.69E-02	-9.28E-09	-1.50E-07	4.30E-07	40
178	1096	B	20	H	2	81	160.01	68.49	264.41	3.61E-02	-1.03E-08	-1.05E-07	2.69E-07	50
178	1096	B	20	H	2	81	160.01	72.2	245.89	2.43E-02	-2.43E-08	-5.43E-08	1.85E-07	60
178	1096	B	20	H	2	81	160.01	65.64	272.07	1.76E-02	2.10E-09	-5.81E-08	1.28E-07	70
178	1096	B	20	H	4	81	163.01	64.15	273.66	1.67E-01	3.73E-08	-5.83E-07	1.21E-06	0
178	1096	B	20	H	4	81	163.01	55.99	254.01	5.67E-02	-6.99E-08	-2.44E-07	3.76E-07	10
178	1096	B	20	H	4	81	163.01	54.19	251.93	3.84E-02	-5.58E-08	-1.71E-07	2.49E-07	20
178	1096	B	20	H	4	81	163.01	54.42	249.35	2.50E-02	-4.11E-08	-1.09E-07	1.63E-07	30
178	1096	B	20	H	4	81	163.01	55.26	244.42	1.69E-02	-3.32E-08	-6.94E-08	1.11E-07	40
178	1096	B	20	H	4	81	163.01	56.49	250.71	1.06E-02	-1.54E-08	-4.40E-08	7.04E-08	50
178	1096	B	20	H	4	81	163.01	57.97	251.06	5.69E-03	-7.84E-09	-2.28E-08	3.86E-08	60
178	1096	B	20	H	4	81	163.01	53.54	245.88	4.71E-03	-9.14E-09	-2.04E-08	3.03E-08	70
178	1096	B	28	X	2	67	224.27	-83.53	335.1	1.11E-02	9.05E-09	-4.20E-09	-8.80E-08	0
178	1096	B	28	X	2	67	224.27	-84.15	333.17	1.03E-02	7.47E-09	-3.78E-09	-8.17E-08	10
178	1096	B	28	X	2	67	224.27	-84.49	325.35	8.60E-03	5.43E-09	-3.75E-09	-6.85E-08	20
178	1096	B	28	X	2	67	224.27	-84.19	350.65	6.38E-03	5.10E-09	-8.40E-10	-5.08E-08	30
178	1096	B	28	X	2	67	224.27	-84.57	314.41	4.61E-03	2.44E-09	-2.50E-09	-3.67E-08	40
178	1096	B	28	X	2	67	224.27	-81.29	339.37	3.04E-03	3.45E-09	-1.30E-09	-2.40E-08	50
178	1096	B	28	X	2	67	224.27	-82.36	354.46	1.85E-03	1.96E-09	-1.90E-10	-1.47E-08	60
178	1096	B	28	X	2	67	224.27	-77.5	242.42	1.08E-03	-8.65E-10	-1.66E-09	-8.42E-09	70

Note: This table is also available in ASCII format in the **TABLES** directory.

Table T19. Discrete sample NRM and AF demagnetization results for Hole 1096C. (See table note. Continued on next page.)

Leg	Site	Hole	Core	Type	Section	Interval (cm)	Depth (mbsf)	Inclination (°)	Declination (°)	Intensity (A/m)	Mx (A·m)	My (A·m)	Mz (A·m)	Demagnetization step (mT)
178	1096	C	1	H	4	84	117.59	83.23	331.53	3.01E-01	2.49E-07	-1.35E-07	2.39E-06	0
178	1096	C	1	H	4	84	117.59	76.58	343.95	9.88E-02	1.76E-07	-5.07E-08	7.69E-07	10
178	1096	C	1	H	4	84	117.59	75.54	349.01	6.89E-02	1.35E-07	-2.62E-08	5.33E-07	20
178	1096	C	1	H	4	84	117.59	76.08	351.8	4.63E-02	8.82E-08	-1.27E-08	3.59E-07	30
178	1096	C	1	H	4	84	117.59	70.8	356.54	3.03E-02	7.96E-08	-4.81E-09	2.29E-07	40
178	1096	C	1	H	4	84	117.59	73	344.74	1.97E-02	4.45E-08	-1.21E-08	1.51E-07	50
178	1096	C	1	H	4	84	117.59	74.04	331.9	1.46E-02	2.84E-08	-1.52E-08	1.13E-07	60
178	1096	C	1	H	4	84	117.59	61.26	3.73	8.04E-03	3.09E-08	2.01E-09	5.64E-08	70
178	1096	C	1	H	5	51	118.76	79.39	103	5.78E-01	-1.92E-07	8.31E-07	4.55E-06	0
178	1096	C	1	H	5	51	118.76	77.82	54.7	1.39E-01	1.35E-07	1.91E-07	1.09E-06	10
178	1096	C	1	H	5	51	118.76	74.04	43.42	8.18E-02	1.31E-07	1.24E-07	6.29E-07	20
178	1096	C	1	H	5	51	118.76	73.26	42.14	5.47E-02	9.35E-08	8.46E-08	4.19E-07	30
178	1096	C	1	H	5	51	118.76	72.14	45.87	3.62E-02	6.19E-08	6.38E-08	2.76E-07	40
178	1096	C	1	H	5	51	118.76	72.76	47.18	2.25E-02	3.63E-08	3.91E-08	1.72E-07	50
178	1096	C	1	H	5	51	118.76	75.18	51.42	1.21E-02	1.55E-08	1.94E-08	9.36E-08	60
178	1096	C	1	H	5	51	118.76	58.19	157.99	1.18E-02	-4.62E-08	1.87E-08	8.04E-08	70
178	1096	C	1	H	6	51	120.26	66.93	97.64	1.14E-01	-4.75E-08	3.54E-07	8.38E-07	0
178	1096	C	1	H	6	51	120.26	45.91	77.57	1.84E-02	2.21E-08	1.00E-07	1.06E-07	10
178	1096	C	1	H	6	51	120.26	32.44	74.93	1.02E-02	1.80E-08	6.68E-08	4.40E-08	20
178	1096	C	1	H	6	51	120.26	30.64	73.05	6.64E-03	1.33E-08	4.37E-08	2.71E-08	30
178	1096	C	1	H	6	51	120.26	29.53	73.86	4.66E-03	9.03E-09	3.12E-08	1.84E-08	40
178	1096	C	1	H	6	51	120.26	26.35	72.64	3.13E-03	6.69E-09	2.14E-08	1.11E-08	50
178	1096	C	1	H	6	51	120.26	24.75	71.37	2.30E-03	5.33E-09	1.58E-08	7.69E-09	60
178	1096	C	1	H	6	51	120.26	27.14	69.52	1.39E-03	3.47E-09	9.30E-09	5.09E-09	70
178	1096	C	2	H	2	61	169.11	44.91	251.56	1.32E-03	-2.36E-09	-7.07E-09	7.43E-09	0
178	1096	C	2	H	2	61	169.11	25.27	221.24	3.27E-04	-1.78E-09	-1.56E-09	1.12E-09	10
178	1096	C	2	H	2	61	169.11	35.45	233.34	1.89E-04	-7.36E-10	-9.89E-10	8.78E-10	20
178	1096	C	2	H	2	61	169.11	45.48	219.26	1.54E-04	-6.70E-10	-5.47E-10	8.79E-10	30
178	1096	C	2	H	2	61	169.11	49.79	219.21	1.20E-04	-4.82E-10	-3.93E-10	7.35E-10	40
178	1096	C	2	H	2	61	169.11	20.68	193.89	4.36E-05	-3.16E-10	-7.83E-11	1.23E-10	50
178	1096	C	2	H	2	61	169.11	40.13	187.01	9.19E-05	-5.58E-10	-6.86E-11	4.74E-10	60
178	1096	C	2	H	2	61	169.11	11.02	183.28	2.47E-05	-1.94E-10	-1.11E-11	3.78E-11	70
178	1096	C	2	H	3	61	170.67	71.8	180.37	5.39E-04	-1.35E-09	-8.78E-12	4.10E-09	0
178	1096	C	2	H	3	61	170.67	15.65	169.04	5.78E-05	-4.37E-10	8.46E-11	1.25E-10	10
178	1096	C	2	H	3	61	170.67	61.58	256.74	7.97E-05	-6.96E-11	-2.95E-10	5.61E-10	20
178	1096	C	2	H	3	61	170.67	44.68	276.38	1.01E-04	6.36E-11	-5.69E-10	5.66E-10	30
178	1096	C	2	H	3	61	170.67	33.31	292.96	8.11E-05	2.11E-10	-4.99E-10	3.56E-10	40
178	1096	C	2	H	3	61	170.67	-54.39	303.76	6.20E-05	1.61E-10	-2.40E-10	-4.03E-10	50
178	1096	C	2	H	3	61	170.67	31.22	317.1	1.89E-04	9.47E-10	-8.81E-10	7.84E-10	60
178	1096	C	2	H	3	61	170.67	-34.27	352.24	2.90E-04	1.90E-09	-2.59E-10	-1.31E-09	70
178	1096	C	2	H	4	61	172.24	67.98	267.86	5.48E-02	-6.13E-09	-1.64E-07	4.06E-07	0
178	1096	C	2	H	4	61	172.24	66.18	261.95	1.92E-02	-8.68E-09	-6.14E-08	1.40E-07	10
178	1096	C	2	H	4	61	172.24	67.4	259.92	8.91E-03	-4.79E-09	-2.70E-08	6.58E-08	20
178	1096	C	2	H	4	61	172.24	71.1	236.36	5.02E-03	-7.21E-09	-1.08E-08	3.80E-08	30
178	1096	C	2	H	4	61	172.24	70.58	252.4	3.27E-03	-2.63E-09	-8.29E-09	2.47E-08	40
178	1096	C	2	H	4	61	172.24	62.72	242.23	2.27E-03	-3.87E-09	-7.36E-09	1.61E-08	50
178	1096	C	2	H	4	61	172.24	68.16	248.61	1.79E-03	-1.94E-09	-4.96E-09	1.33E-08	60
178	1096	C	2	H	4	61	172.24	37.48	24.77	8.52E-04	4.91E-09	2.27E-09	4.15E-09	70
178	1096	C	2	H	5	58	173.79	80.89	229.35	2.63E-03	-2.17E-09	-2.53E-09	2.08E-08	0
178	1096	C	2	H	5	58	173.79	86.13	138.35	4.12E-04	-1.66E-10	1.48E-10	3.29E-09	10
178	1096	C	2	H	5	58	173.79	77.56	123.74	3.28E-04	-3.14E-10	4.70E-10	2.56E-09	20
178	1096	C	2	H	5	58	173.79	70.91	73.44	2.72E-04	2.03E-10	6.83E-10	2.06E-09	30
178	1096	C	2	H	5	58	173.79	65.68	6.34	1.71E-04	5.59E-10	6.21E-11	1.24E-09	40
178	1096	C	2	H	5	58	173.79	7.72	125.68	1.31E-04	-6.07E-08	8.46E-10	1.41E-10	50
178	1096	C	2	H	5	58	173.79	21.13	156.2	1.16E-04	-7.89E-10	3.48E-10	3.33E-10	60
178	1096	C	2	H	5	58	173.79	52.09	199.46	1.64E-04	-7.62E-10	-2.69E-10	1.04E-09	70
178	1096	C	2	H	6	61	175.37	68.94	268.63	9.78E-02	-6.74E-09	-2.81E-07	7.30E-07	0
178	1096	C	2	H	6	61	175.37	62.99	267.5	5.18E-02	-8.22E-09	-1.88E-07	3.69E-07	10
178	1096	C	2	H	6	61	175.37	62.66	267.38	3.96E-02	-6.64E-09	-1.45E-07	2.81E-07	20
178	1096	C	2	H	6	61	175.37	62.23	267.9	2.66E-02	-3.63E-09	-9.90E-08	1.88E-07	30
178	1096	C	2	H	6	61	175.37	62.93	269.01	1.81E-02	-1.14E-09	-6.58E-08	1.29E-07	40
178	1096	C	2	H	6	61	175.37	59.04	267.33	1.13E-02	-2.16E-09	-4.63E-08	7.72E-08	50
178	1096	C	2	H	6	61	175.37	51.98	282.87	5.35E-03	5.87E-09	-2.57E-08	3.37E-08	60
178	1096	C	2	H	6	61	175.37	-41.21	278.91	2.61E-03	2.43E-09	-1.55E-08	-1.38E-08	70
178	1096	C	3	X	6	61	201.11	68.7	327.47	1.68E-01	4.11E-07	-2.62E-07	1.25E-06	0
178	1096	C	3	X	6	61	201.11	70.59	2.77	7.58E-02	2.01E-07	9.75E-09	5.72E-07	10
178	1096	C	3	X	6	61	201.11	71.73	12.26	5.61E-02	1.37E-07	2.99E-08	4.26E-07	20
178	1096	C	3	X	6	61	201.11	71.29	16.39	3.83E-02	9.42E-08	2.77E-08	2.90E-07	30

Table T19 (continued).

Leg	Site	Hole	Core	Type	Section	Interval (cm)	Depth (mbsf)	Inclination (°)	Declination (°)	Intensity (A/m)	Mx (A·m)	My (A·m)	Mz (A·m)	Demagnetization step (mT)
178	1096	C	3	X	6	61	201.11	68.51	17.45	2.72E-02	7.62E-08	2.39E-08	2.03E-07	40
178	1096	C	3	X	6	61	201.11	71.15	23.81	1.77E-02	4.19E-08	1.85E-08	1.34E-07	50
178	1096	C	3	X	6	61	201.11	58.63	22.77	8.32E-03	3.19E-08	1.34E-08	5.68E-08	60
178	1096	C	3	X	6	61	201.11	-10.41	22.13	3.03E-03	2.21E-08	8.99E-09	-4.38E-09	70

Note: This table is also available in ASCII format in the [TABLES](#) directory.

Table T20. Results from the principal component analysis of discrete paleomagnetic samples. (See table notes. Continued on next page.)

Leg	Site	Core	Type	Section	Interval (cm)	Depth (mbsf)	Inclination (°)	Declination (°)	MAD	Length	Devang	Steps	Low	High	Option
178	1096A	1	H	1	134	1.34	-34.2	259.2	1.49	4.43E-01	6.95	4	30	70	FRE
178	1096A	1	H	1	71	0.71	-61.5	182.6	1.56	3.08E-01	4.33	4	40	70	FRE
178	1096A	1	H	2	144	2.94	-65.9	94.9	3.1	1.42E-01	4.34	4	40	70	FRE
178	1096A	1	H	2	71	2.21	-83.3	188.7	0.43	5.06E-01	4.48	4	20	70	FRE
178	1096A	1	H	3	126	4.26	-79.8	355.3	0.46	6.44E-01	6.36	4	20	70	FRE
178	1096A	1	H	3	71	3.71	-71.2	306	0.83	9.18E-01	5.51	4	20	70	FRE
178	1096A	1	H	4	141	5.91	-41.9	149	7.74	1.80E-01	15.85	4	50	80	FRE
178	1096A	1	H	4	71	5.21	-66.7	282.9	0.67	2.96E-01	9.05	4	30	70	FRE
178	1096A	1	H	5	51	6.51	-73	256.3	2.34	3.09E-01	4.07	4	40	80	FRE
178	1096A	1	H	5	71	6.71	-76	285.9	1.92	5.80E-01	2.04	4	40	80	FRE
178	1096A	2	H	2	146	10.66	-57.3	339.9	13.75	3.04E-01	21.46	4	40	80	FRE
178	1096A	2	H	2	71	9.91	-47.7	240.5	5.17	3.18E-01	19.8	4	50	80	FRE
178	1096A	2	H	3	137	12.07	16.5	353.1	10.65	2.25E-01	79.71	4	40	80	FRE
178	1096A	2	H	3	71	11.41	-49.8	277.8	3.22	2.51E-01	14.18	4	40	80	FRE
178	1096A	2	H	4	146	13.66	-73.8	357.4	2.22	1.59E-01	12.68	4	30	80	FRE
178	1096A	2	H	4	71	12.91	-82	183.6	2.14	3.92E-01	5.25	4	40	80	FRE
178	1096A	2	H	5	139	15.09	72.9	170.2	1.3	3.52E-01	10.08	4	30	80	FRE
178	1096A	2	H	5	46	14.16	-72.9	295.2	3.36	1.14E-01	7.8	4	30	80	FRE
178	1096A	2	H	6	144	16.64	-30	216.7	30.63	7.36E-02	48.91	4	50	80	FRE
178	1096A	2	H	6	50	15.7	-53.5	320	5.71	2.66E-01	6.07	4	40	80	FRE
178	1096A	2	H	7	67	17.37	54	238	4.33	1.96E-01	31.46	4	40	80	FRE
178	1096A	3	H	1	145	18.65	-42.5	339.7	2.66	9.49E-01	8.11	4	20	80	FRE
178	1096A	3	H	2	137	20.07	-17.7	319.8	2.54	1.20E-01	7.09	4	30	80	FRE
178	1096A	3	H	2	71	19.41	46.2	295.9	0.63	1.19E+00	1.08	4	20	80	FRE
178	1096A	3	H	3	47	20.67	78.7	240.8	1.54	4.24E-01	7.54	4	20	80	FRE
178	1096A	3	H	4	135	23.05	-41.5	63.1	3.68	2.86E-02	15.29	4	30	80	FRE
178	1096A	3	H	4	71	22.41	-69.4	9.4	11.16	7.49E-02	2.28	4	50	80	FRE
178	1096A	3	H	5	146	24.66	-49.5	83.1	2.06	4.91E-01	15.34	4	40	80	FRE
178	1096A	3	H	5	71	23.91	-27.2	268.3	3.27	1.03E+00	2.67	4	20	80	FRE
178	1096A	4	H	2	141	29.61	29.5	263.5	2.18	4.94E-01	12.42	4	20	80	FRE
178	1096A	4	H	3	141	31.11	-72.3	37.5	1.81	4.03E-01	2.28	4	30	80	FRE
178	1096A	4	H	3	86	30.56	-65.9	33.1	1.1	3.77E-01	7.53	4	20	80	FRE
178	1096A	4	H	4	141	32.61	19.3	343.7	3.72	5.47E-01	18.51	4	20	70	FRE
178	1096A	4	H	4	71	31.91	-66	58.2	1.09	1.25E-01	4.52	4	30	70	FRE
178	1096A	5	H	1	145	37.65	-81.3	94	0.61	7.71E-01	1.36	4	20	70	FRE
178	1096A	5	H	1	71	36.91	-29.2	58.1	4.12	4.26E-01	12.04	4	20	70	FRE
178	1096A	5	H	2	141	39.11	-66.9	59.7	1.6	8.30E-01	5.74	4	30	70	FRE
178	1096A	5	H	2	71	38.41	-78.4	68.8	0.43	2.03E-01	0.34	4	20	70	FRE
178	1096A	5	H	3	141	40.61	-79.6	104.4	0.82	1.10E+00	1.25	4	20	70	FRE
178	1096A	5	H	3	71	39.91	-77.9	126.7	1.94	4.94E-01	4.25	4	20	70	FRE
178	1096A	5	H	4	141	42.11	-60.2	185.6	8.44	5.65E-03	6.13	4	30	70	FRE
178	1096A	5	H	4	71	41.41	-15.7	68.5	2.96	4.21E-02	9.85	4	20	70	FRE
178	1096A	5	H	5	141	43.61	-1.2	65.8	1.03	9.83E-02	7.81	4	20	70	FRE
178	1096A	5	H	5	71	42.91	-82.2	59.3	0.34	1.16E+00	3.4	4	30	60	FRE
178	1096A	5	H	6	141	45.11	80.6	301.2	11.87	1.73E-03	167.65	4	40	70	FRE
178	1096A	5	H	6	70	44.4	60	206.2	32.17	1.86E-03	127.09	4	40	70	FRE
178	1096A	6	H	2	141	48.61	-69.9	335.8	0.78	1.42E+00	3.12	4	20	70	FRE
178	1096A	6	H	2	81	48.01	-73.2	299.1	1.2	7.53E-01	0.52	4	20	70	FRE
178	1096A	6	H	3	141	50.11	-71	21.5	1.27	9.94E-02	2.51	4	20	70	FRE
178	1096A	6	H	3	81	49.51	-74.7	303.9	0.95	2.52E+00	1.54	4	20	70	FRE
178	1096A	6	H	4	141	51.61	-67.1	48	2.53	4.93E-01	1.61	4	30	70	FRE
178	1096A	6	H	4	77	50.97	-69.4	29.6	1.1	1.55E+00	2.22	4	20	70	FRE
178	1096A	6	H	5	141	53.11	-77.6	293.2	1.6	1.55E+00	3.36	4	20	70	FRE
178	1096A	6	H	5	79	52.49	-60.2	6.2	1.65	1.14E+00	7.09	4	20	70	FRE
178	1096A	6	H	6	139	54.59	-73.2	337.6	2.31	5.14E-01	5.31	4	20	70	FRE
178	1096A	6	H	6	79	53.99	-84.6	291.1	1.2	2.21E-01	10.23	4	20	70	FRE
178	1096A	7	H	1	141	56.61	77	278.5	1.08	2.64E-01	3.87	4	30	70	FRE
178	1096A	7	H	1	71	55.91	65.3	290.1	5.13	1.77E-01	8.44	4	20	70	FRE
178	1096A	7	H	2	143	58.13	74.2	234.1	0.53	3.40E-01	1.77	4	20	70	FRE
178	1096A	7	H	2	61	57.31	7.9	216	1.72	5.82E-02	2.07	4	30	70	FRE
178	1096A	7	H	3	141	59.61	57	290.8	2.55	6.76E-01	1.18	4	20	70	FRE
178	1096A	7	H	3	71	58.91	66.1	302.2	3.39	7.23E-01	2.46	4	30	70	FRE
178	1096A	7	H	4	141	61.11	58.5	339.4	2.21	4.52E-01	4.07	4	20	70	FRE
178	1096A	7	H	4	69	60.39	58.5	348.3	7.94	2.90E-01	8	4	40	70	FRE
178	1096A	7	H	6	61	62.81	33.1	177.6	24.3	3.09E-03	86.27	4	40	70	FRE
178	1096A	8	H	1	139	66.09	44.8	2.4	3.32	1.77E-01	12.41	4	20	70	FRE
178	1096A	8	H	2	141	67.61	64.6	332.5	1.07	7.68E-01	4.59	4	20	70	FRE
178	1096A	8	H	2	71	66.91	73.6	312.1	3.55	4.82E-01	8.47	4	40	70	FRE
178	1096A	8	H	3	135	69.05	-4.3	140.2	2.38	8.21E-03	2.58	4	20	70	FRE

Table T20 (continued).

Leg	Site	Core	Type	Section	Interval (cm)	Depth (mbsf)	Inclination (°)	Declination (°)	MAD	Length	Devang	Steps	Low	High	Option
178	1096A	8	H	3	75	68.45	34	298.2	5.34	4.45E-01	7.96	4	20	70	FRE
178	1096A	8	H	4	139	70.59	58.7	17.6	4.91	1.68E-01	8.17	4	40	70	FRE
178	1096A	8	H	4	75	69.95	48.8	343.5	1.53	5.20E-01	4.34	4	20	70	FRE
178	1096A	8	H	5	141	72.11	-5.5	338.7	5.74	4.87E-01	9.14	4	20	70	FRE
178	1096A	8	H	5	77	71.47	60	212	1.64	8.26E-01	4.43	4	20	70	FRE
178	1096A	8	H	6	141	73.66	26.3	232.7	17.04	3.14E-03	106.94	4	40	70	FRE
178	1096A	8	H	6	81	73.06	77.6	292.8	1.44	6.21E-01	0.99	4	20	70	FRE
178	1096A	9	H	2	127	76.97	72.4	9.3	15.95	5.37E-02	80.23	4	40	70	FRE
178	1096A	9	H	2	71	76.41	55	326.5	2.42	1.59E-01	30.92	4	30	70	FRE
178	1096A	9	H	5	141	80.39	62.8	309.7	7.88	2.07E-01	16.88	4	40	70	FRE
178	1096A	9	H	5	69	79.67	32.5	241.9	8.75	1.26E-02	28.43	4	20	70	FRE
178	1096A	9	H	6	131	81.79	6.1	2.4	10.81	5.39E-02	23.41	4	20	70	FRE
178	1096A	9	H	6	71	81.19	77.6	320.2	16.11	1.90E-01	30.33	4	40	70	FRE
178	1096A	9	H	7	99	82.94	79	195.5	0.92	1.41E+00	1.34	4	20	70	FRE
178	1096A	10	H	1	141	85.11	55	328.9	0.53	4.84E-02	8.79	4	30	60	FRE
178	1096A	10	H	1	71	84.41	19	187.8	0.86	1.36E+00	1.26	4	30	70	FRE
178	1096A	10	H	2	145	86.65	5.1	226	0.97	1.12E+00	6.29	4	20	70	FRE
178	1096A	10	H	2	71	85.91	58.7	192.3	3.3	3.37E-01	9.83	4	20	70	FRE
178	1096A	10	H	3	139	88.09	78.4	61.4	2.76	3.04E-01	10.18	4	20	70	FRE
178	1096A	10	H	3	71	87.41	59.6	88.4	3.17	5.26E-01	7.05	4	20	70	FRE
178	1096A	10	H	4	71	88.97	-34.7	325.3	2.9	6.86E-01	8.76	4	20	70	FRE
178	1096A	11	H	6	14	100.84	47.1	156.8	18.86	4.03E-03	52.86	4	40	70	FRE
178	1096A	11	H	6	42	101.12	-7.3	345.9	29.84	3.49E-03	88.41	4	40	70	FRE
178	1096A	11	H	6	44	101.14	-77.3	181.7	11.01	6.01E-04	131.7	4	40	70	FRE
178	1096A	11	H	6	47	101.17	68.9	180.5	31.77	2.85E-03	169.46	4	40	70	FRE
178	1096A	11	H	6	95	101.65	72.2	352.2	0.79	4.45E-01	1.45	4	30	70	FRE
178	1096A	15	H	1	98	132.18	61.1	110.7	11.99	8.68E-03	14.54	4	20	60	FRE
178	1096A	15	H	3	144	135.64	19.2	2.9	19.42	3.80E-03	151.63	4	40	70	FRE
178	1096A	15	H	3	51	134.71	32.2	7.4	26.61	1.84E-03	95.9	4	40	70	FRE
178	1096A	15	H	2	71	133.41	71	339.6	9.94	8.56E-04	85.42	4	40	70	FRE
178	1096A	15	H	4	91	136.61	50.2	323.5	2.93	5.00E-01	3.35	4	20	70	FRE
178	1096A	15	H	5	81	138.01	63.7	32.2	2.48	9.70E-01	4.68	4	20	70	FRE
178	1096B	13	H	1	89	109.19	71.6	168.2	1.47	6.34E-02	8.17	4	20	70	FRE
178	1096B	13	H	4	133	114.13	65.5	259.2	0.48	7.01E-01	3.17	4	20	70	FRE
178	1096B	19	H	2	71	152.91	60	11.6	3.92	1.34E-01	21.58	4	20	70	FRE
178	1096B	19	H	4	71	155.91	52.5	332	1.04	1.16E+00	7.29	4	20	70	FRE
178	1096B	20	H	1	81	158.51	66.7	222.3	1.77	8.03E-01	0.43	4	20	70	FRE
178	1096B	20	H	2	81	160.01	71.1	265.4	1.65	6.70E-01	1.68	4	30	70	FRE
178	1096B	20	H	4	81	163.01	53.8	252.4	0.88	3.37E-01	1.33	4	20	70	FRE
178	1096B	28	X	2	67	224.27	-84.2	331.6	2.51	7.55E-02	1.37	4	20	70	FRE
178	1096C	1	H	4	84	117.59	77.3	347.3	1.69	6.12E-01	2.82	4	20	70	FRE
178	1096C	1	H	5	51	118.76	72.7	40	1.52	4.26E-01	1.52	4	30	60	FRE
178	1096C	1	H	6	51	120.26	33.8	75.9	1.38	8.82E-02	3.88	4	20	70	FRE
178	1096C	2	H	2	61	169.11	52.6	231.7	6.11	1.38E-03	16.93	4	30	70	FRE
178	1096C	2	H	3	61	170.67	51.5	195.7	29.05	2.98E-03	123.09	4	40	70	FRE
178	1096C	2	H	4	61	172.24	64.7	255	5.37	8.62E-02	6.59	4	20	70	FRE
178	1096C	2	H	5	58	173.79	39.1	329.5	32.69	1.72E-03	85.17	4	40	70	FRE
178	1096C	2	H	6	61	175.37	65.6	265.1	1.89	4.03E-01	6.25	4	20	70	FRE
178	1096C	3	X	6	61	201.11	75.2	14.2	1.28	3.80E-01	8.69	4	30	70	FRE

Notes: MAD = maximum angular deviation, Devang = deviation angle (degrees). This table is also available in ASCII format in the [TABLES](#) directory.

Table T21. Depths of geomagnetic reversals in Holes 1096A, 1096B, and 1096C.

Chron	Depth interval (mbsf)			Age (Ma)
	Hole 1096A	Hole 1096B	Hole 1096C	
C1n(o)	54.60-55.40	54.94-54.99	—	0.78
C1r.1n(t)	—	—	—	0.99
C1r.1n(o)	—	—	—	1.07
C2n(t)	—	—	—	1.77
C2n(o)	—	—	—	1.95
C2r.1n(t)	—	—	—	2.14
C2r.1n(o)	—	—	—	2.15
C2An.1n(t)	—	215.35-217.25	215.80-215.90	2.581
C2An.1n(o)	—	—	—	3.04
C2An.2n(t)	—	—	—	3.11
C2An.2n(o)	—	—	—	3.22
C2An.3n(t)	—	—	366.21-367.10	3.33
C2An.3n(o)	—	—	405.15-405.80	3.58
C3n.1n(t)	—	—	507.89-511.55	4.18
C3n.1n(o)	—	—	536.45-536.60	4.29
C3n.2n(t)	—	—	553.60-553.80	4.48
C3n.2n(o)	—	—	583.85-584.05	4.62
C3n.3n(t)	—	—	—	4.8
C3n.3n(o)	—	—	—	4.89
C3n.4n(t)	—	—	—	4.98
C3n.4n(o)	—	—	—	5.23

Notes: Ages after Berggren et al. (1995). (t) = termination, (o) = onset. — = chron not interpreted in this interval.

Table T22. Gas components measured in vacutainer and headspace samples at Site 1096. (Continued on next page.)

Core, section, interval (cm)	Depth (mbsf)	Methane (ppm)	Ethane (ppm)	Propane (ppm)	Iso-butane (ppm)	Iso-pentane (ppm)	Butane (ppm)	Hydrogen sulfide (ppm)
Vacutainer								
178-1096B-								
23X-3, 75-76	176.28	608,000	1,240	23	0	0	0	0
24X-1, 75-76	184.35	1,001,000	2,220	49	0	0	0	28
26X-1, 75-76	203.65	774,000	1,680	40	0	0	0	0
178-1096C-								
8X-6, 75-76	269.15	812,000	1,890	103	0	0	0	0
8X-7, 20-21	270.10	827,000	1,910	101	0	0	0	0
9X-5, 75-76	275.90	773,000	1,790	97	0	0	0	26
10X-3, 75-76	283.75	894,000	2,130	128	0	0	0	17
11X-3, 75-76	293.35	856,000	1,990	132	4	0	0	28
13X-4, 75-76	314.05	874,000	2,250	180	9	0	0	23
14X-4, 75-76	322.64	882,000	2,150	189	11	0	0	28
15X-4, 75-76	333.45	846,000	2,110	190	12	0	0	0
16X-4, 75-76	343.15	758,000	1,900	183	12	0	0	0
17X-3, 75-76	351.25	876,000	2,270	247	17	0	0	0
18X-4, 75-76	362.45	891,000	2,270	262	22	0	0	0
19X-4, 75-76	372.15	888,000	2,240	266	22	0	0	0
21X-5, 75-76	390.96	876,000	2,270	302	26	0	0	33
22X-5, 75-76	402.55	724,000	1,900	259	24	0	0	47
25X-5, 75-76	431.55	911,000	2,520	420	38	3	0	0
27X-4, 75-76	449.15	893,000	2,440	419	37	0	0	24
28X-4, 75-76	458.85	884,000	2,440	475	45	4	0	15
29X-4, 75-76	468.45	946,000	2,800	575	54	5	0	
30X-4, 75-76	478.15	958,000	2,730	559	51	4	0	16
31X-4, 75-76	487.63	883,000	2,590	558	48	5	0	21
32X-4, 75-76	497.23	935,000	2,700	591	51	5	0	0
33X-4, 75-76	506.24	915,000	2,750	663	53	7	8	16
34X-4, 75-76	516.65	903,000	2,740	663	55	6	0	0
36X-4, 75-76	535.95	886,000	2,770	721	54	7	12	24
37X-7, 20-21	549.60	732,000	2,220	586	46	6	10	36
38X-4, 75-76	555.35	782,000	2,370	611	46	6	12	43
41X-4, 75-76	584.35	859,000	2,830	845	57	13	23	0
Headspace								
178-1096A-								
1H-3, 0-5	3.00	3	0	0				
2H-6, 0-5	15.20	7	0	0				
3H-3, 0-5	20.20	7	0	0				
4H-4, 0-5	31.20	6	0	0				
5H-5, 0-5	42.20	178	0	0				
6H-4, 0-5	50.20	3,240	0	0				
7H-4, 0-5	59.70	8,910	4	0				
8H-4, 0-5	69.20	3,060	5	0				
9H-6, 0-5	80.48	37,800	22	0				
10H-4, 0-5	88.26	31,200	23	0				
11H-4, 0-5	97.70	42,000	28	0				
12H-3, 0-5	105.70	14,900	9	0				
13H-2, 0-5	113.47	35,200	23	0				
14H-2, 0-5	123.20	52,800	65	3				
15H-4, 0-5	135.70	90,200	87	3				
178-1096B-								
16H-4, 0-5	139.70	64,000	83	4				
17H-4, 0-5	148.60	116,000	114	4				
19H-4, 0-5	155.20	38,200	48	2				
20H-4, 0-5	162.20	55,500	74	3				
22X-2, 0-5	168.40	65,900	66	2				
23X-3, 0-5	176.93	24,600	41	2				
24-1, 0-5	183.60	500,000	1,481	43				
24-3, 0-5	186.51	33,700	50	2				
26-1, 0-5	202.90	387,000	1,116	20				
26-3, 0-5	205.90	37,800	54	3				
27-2, 0-5	214.00	76,700	97	5				
28-3, 0-5	225.10	60,200	77	6				
29-4, 0-5	236.20	38,600	75	9				
30-4, 0-2	245.80	69,800	96	9				
31-2, 0-5	249.50	115,000	145	14				
32-4, 0-5	255.50	83,500	131	18				

Table T22 (continued).

Core, section, interval (cm)	Depth (mbsf)	Methane (ppm)	Ethane (ppm)	Propane (ppm)	<i>Iso-</i> butane (ppm)	<i>Iso-</i> pentane (ppm)	Butane (ppm)	Hydrogen sulfide (ppm)
178-1096C-								
7X-4, 0-5	259.70	26,400	44	7				
8X-3, 0-5	263.90	58,100	86	11				
9X-5, 0-5	275.15	42,900	82	15				
10X-4, 0-5	284.50	38,200	68	13				
11X-4, 0-5	294.10	41,600	74	17				
12X-4, 0-5	302.43	38,900	64	14				
13X-4, 0-5	313.30	42,000	78	19				
14X-4, 0-5	321.89	46,400	66	12				
15X-4, 0-5	332.70	47,300	81	25				
16X-4, 0-5	342.40	65,700	108	30				
17X-4, 0-5	352.00	66,600	114	37				
18X-4, 0-5	361.70	39,200	72	25				
19X-4, 0-4	371.40	48,800	92	35				
20X-1, 0-5	376.60	33,600	87	40				
21X-5, 0-5	390.21	26,100	47	13				
22X-4, 0-5	400.30	18,000	53	32				
23X-4, 0-5	410.00	39,800	79	39				
24X-2, 0-5	416.60	34,600	82	47				
25X-6, 0-5	432.30	34,400	78	41				
26X-2, 0-5	435.90	41,300	96	57				
27X-3, 0-5	447.00	19,800	52	38				
28X-4, 0-5	458.10	35,500	93	44				
29X-4, 0-5	467.70	45,500	116	65				
30X-4, 0-5	477.40	73,700	207	117				
31X-4, 0-5	486.88	54,600	160	110				
32X-4, 0-5	496.48	54,100	168	118				
33X-4, 0-5	505.49	67,400	164	77				
34X-4, 0-5	515.90	40,500	120	82				
35X-3, 0-5	524.00	28,300	97	76				
36X-4, 0-5	535.20	27,200	87	78				
37X-5, 0-5	546.40	34,100	124	95				
38X-3, 0-5	553.10	22,000	68	50				
40X-2, 0-5	570.90	26,700	91	83				
41X-4, 0-5	583.60	57,600	151	78				
42X-1, 0-5	588.60	31,700	91	68				

Table T23. Analyses of inorganic carbon, total carbon, and sulfur; calculated values of total organic carbon and calcium carbonate at Site 1096. (Continued on next two pages.)

Core, section, interval (cm)	Depth (mbsf)	IC (wt%)	CaCO ₃ (wt%)	TOC (wt%)	TC (wt%)	TS (wt%)
178-1096A-						
1H-1, 139-140	1.39	0.10	0.81			
1H-3, 22-23	3.22	0.10	0.80	0.11	0.20	0.03
1H-5, 87-88	6.87	0.10	0.80			
2H-1, 95-96	8.65	0.05	0.41			
2H-3, 84-85	11.54	0.13	1.09	0.15	0.28	0.03
2H-5, 98-99	14.68	0.05	0.41			
3H-1, 142-143	18.62	0.16	1.30			
3H-3, 44-45	20.64	0.06	0.50	0.04	0.10	0.00
3H-5, 116-117	24.36	0.10	0.81			
4H-3, 81-82	30.51	0.05	0.44	0.04	0.09	0.00
5H-1, 125-126	37.45	0.11	0.91			
5H-3, 133-135	40.53	0.13	1.10	0.15	0.29	0.00
5H-5, 133-135	43.53	0.17	1.40			
6H-1, 139-141	47.09	0.20	1.66			
6H-3, 77-79	49.47	0.16	1.30	0.10	0.25	0.00
6H-4, 90-92	51.10	0.14	1.14			
6H-5, 70-73	52.40	0.15	1.27	0.17	0.32	0.00
6H-6, 28-29*	53.48	3.88	32.36			
6H-6, 52-56	53.72	0.06	0.48			
7H-1, 45-46*	55.65	0.37	3.05			
7H-1, 102-103	56.22	0.04	0.32			
7H-3, 106-107	59.26	0.23	1.90	0.12	0.35	0.00
7H-5, 16-17	61.36	0.17	1.41			
7H-7, 10-11	63.30	0.18	1.54			
8H-1, 92-93	65.62	0.14	1.19			
8H-3, 92-93	68.62	0.19	1.56	0.13	0.32	0.25
8H-5, 92-93	71.62	0.14	1.19			
9H-3, 75-76	77.95	0.08	0.70	0.14	0.22	0.00
9H-5, 75-76	79.73	0.16	1.33			
9H-6, 67-68*	81.15	0.33	2.76			
9H-7, 73-74	82.68	0.04	0.36			
10H-1, 135-136	85.05	0.17	1.41			
10H-2, 46-47*	85.66	3.59	29.89			
10H-3, 75.5-76.5	87.46	0.16	1.31	0.24	0.40	0.00
11H-1, 133-134	94.53	0.09	0.75			
11H-3, 136-137	97.56	0.13	1.06	0.20	0.33	0.00
11H-5, 104-105	100.24	0.13	1.07			
11H-5, 138-139	100.58	0.14	1.17			
14H-1, 83-84	122.53	0.21	1.74	0.15	0.36	0.00
15H-1, 115-116	132.35	0.12	1.00			
15H-2, 117-118	133.87	3.65	30.37			
15H-3, 139-140	135.59	0.13	1.06	0.13	0.25	0.24
15H-5, 108-109	138.28	0.17	1.43			
178-1096B-						
4H-4, 39-40	26.34	3.06	25.53			
4H-7, 44-45	30.89	1.47	12.28			
7H-1, 105-106*	52.35	0.43	3.56			
7H-3, 70-71*	54.94	0.03	0.23			
7H-4, 35-36*	56.09	0.48	4.00			
7H-4, 65-66*	56.39	0.00	0.00			
10H-1, 40-41*	80.20	1.26	10.53			
10H-1, 82-83*	80.62	0.19	1.57			
10H-2, 5-6*	81.35	1.11	9.29			
10H-4, 107-108*	85.37	0.03	0.26			
10H-4, 145-146*	85.75	1.06	8.80			
10H-5, 35-36*	86.15	1.37	11.43			
10H-5, 86-87*	86.66	1.37	11.43			
12H-3, 16-17*	101.96	0.04	0.34			
12H-7, 13-14*	107.93	2.18	18.12			
13H-1, 23-24*	108.53	0.06	0.47			
13H-1, 56-57*	108.86	0.02	0.20			
13H-1, 93-94	109.23	0.16	1.33			

Table T23 (continued).

Core, section, interval (cm)	Depth (mbsf)	IC (wt%)	CaCO ₃ (wt%)	TOC (wt%)	TC (wt%)	TS (wt%)
13H-3, 40-41	111.70	0.14	1.21			
13H-5, 53-54	114.83	0.33	2.73			
16H-1, 40-41	135.60	0.09	0.77	0.14	0.28	0.00
16H-2, 80-81	137.50	0.04	0.34			
16H-3, 40-41	138.60	0.07	0.61	0.16	0.23	0.00
16H-5, 40-41	141.60	0.12	1.02			
17H-1, 70-71	144.80	0.04	0.34			
17H-3, 70-71	147.80	0.04	0.30	0.08	0.12	0.00
19H-1, 100-101	151.70	0.11	0.92			
19H-3, 100-101	154.70	0.14	1.17			
19H-5, 51-52	157.21	0.04	0.33	0.06	0.10	0.00
20H-1, 59-63	158.29	0.13	1.06			
20H-3, 61-62	161.31	0.04	0.30	0.09	0.12	0.00
20H-5, 62-63	164.32	0.16	1.31			
22X-1, 128-129	168.18	0.14	1.18	0.25	0.40	0.00
23X-2, 64-65	176.17	0.04	0.33			
23X-3, 48-49	177.41	0.05	0.41			
23X-5, 47-48	180.40	0.10	0.87	0.24	0.34	0.00
24X-1, 27-28	183.87	0.05	0.46			
24X-3, 27-28	186.78	0.12	0.99			
24X-5, 27-28	189.78	0.04	0.31	0.29	0.32	0.02
27X-1, 80-81	213.30	0.06	0.48			
27X-3, 59-61	216.09	0.03	0.24	0.31	0.33	0.00
28X-1, 85-86	222.95	0.05	0.46			
28X-3, 80-81	225.90	0.05	0.45	0.27	0.33	0.00
29X-1, 11-12	231.81	0.12	1.00			
29X-3, 49-50	235.19	0.14	1.13			
29X-5, 139-140	239.09	0.11	0.89	0.21	0.31	0.00
30X-1, 40-41	241.70	0.14	1.20			
30X-3, 56-57	244.86	0.15	1.26	0.28	0.43	0.01
32X-2, 29-30	252.79					
32X-4, 31-32	255.81					
<hr/>						
178-1096C-						
1H-1, 60-61	114.60	0.23	1.92			
1H-4, 72-73	117.47	0.13	1.07			
1H-6, 71-72	120.46	0.20	1.65			
2H-1, 124-125	168.24	0.13	1.04			
2H-3, 80-81	170.86	0.16	1.36			
2H-5, 90-91	174.11	0.06	0.50			
3X-6, 60-62	201.10	0.04	0.31			
3X-7, 15-16	202.15	0.07	0.55			
4X-1, 137-138	203.97	0.05	0.39			
4X-3, 95-96	206.55	0.10	0.80			
4X-5, 118-119	209.78	0.13	1.10			
5X-1, 10-11	212.30	0.09	0.75			
5X-3, 48-49	215.68	0.02	0.19			
5X-5, 48-49	218.68	0.04	0.34			
6X-3, 28-29	225.08	0.06	0.47			
8X-1, 26-27	261.16	0.05	0.45			
8X-5, 26-27	267.16	0.14	1.17	0.36	0.50	0.05
9X-2, 32-33	271.00	0.14	1.15	0.37	0.51	0.06
10X-1, 42-43	280.42	0.08	0.63			
10X-3, 54-55	283.54	0.11	0.95	0.28	0.39	0.03
10X-5, 70-71	286.70	0.11	0.96			
11X-3, 25-26	292.85	0.10	0.81	0.32	0.41	0.02
12X-4, 57-58	303.00	0.09	0.73	0.37	0.46	0.03
13X-3, 56-57	312.36	0.11	0.94	0.21	0.33	0.04
14X-1, 2-3	318.52	6.14	51.15	0.45	6.59	0.00
14X-5, 50-51	323.89	0.05	0.45	0.41	0.46	0.00
15X-3, 35-36	331.55	0.09	0.71	0.33	0.42	0.03
16X-1, 128-129	339.18	0.06	0.52	0.07	0.13	0.00
16X-5, 81-82	344.71	0.09	0.77	0.60	0.70	0.12
18X-1, 32-34	357.52	0.11	0.88	0.37	0.48	0.53
18X-5, 124-125	364.44	0.08	0.65	0.33	0.41	0.03
19X-3, 24-25	370.14	0.06	0.53	0.48	0.54	0.10
20X-1, 65-66	377.25	0.06	0.54			
21X-2, 8-9	386.54	0.12	1.03	0.55	0.67	0.17
21X-3, 18-19	387.39	3.24	26.97			
21X-5, 65-66	390.86	0.07	0.59			

Table T23 (continued).

Core, section, interval (cm)	Depth (mbsf)	IC (wt%)	CaCO ₃ (wt%)	TOC (wt%)	TC (wt%)	TS (wt%)
22X-3, 103-104	399.83	0.14	1.14	0.40	0.54	0.11
23X-3, 33-34	408.83	0.09	0.75	0.42	0.52	0.04
24X-3, 25-26	418.35	0.09	0.78	0.31	0.40	0.12
25X-3, 84-85	428.64	0.13	1.08	0.46	0.59	0.13
27X-1, 90-91	444.90	0.12	1.01			
27X-3, 90-91	447.90	0.17	1.40	0.41	0.58	0.12
27X-5, 80-81	450.70	0.05	0.42			
28X-3, 57-58	457.17	0.08	0.66	0.44	0.52	0.11
29X-1, 54-55	463.74	0.11	0.95			
29X-3, 55-56	466.75	0.23	1.94	0.47	0.70	0.23
29X-5, 55-56	469.75	0.17	1.39			
29X-6, 80-81	471.50	0.17	1.49			
30X-1, 63-64	473.53	0.15	1.21	0.58	0.72	0.17
30X-6, 17-18	480.57	0.12	1.00	0.17	0.29	0.25
31X-5, 113-114	489.51	0.07	0.61	0.50	0.57	0.08
31X-7, 40-41	491.78	0.07	0.60			
32X-1, 97-98	493.07	0.12	1.04	0.53	0.65	0.24
32X-3, 56-57	495.66	0.04	0.39			
32X-5, 130-131	499.28	0.17	1.40	0.39	0.56	0.24
33X-1, 27-28	501.97	0.12	1.04			
33X-3, 141-142	505.40	0.12	1.04	0.04	0.17	0.00
33X-5, 58-59	507.57	0.04	0.37			
34X-1, 124-125	512.64	0.10	0.82	0.05	0.15	0.00
34X-3, 32-33	514.72	0.06	0.50			
34X-6, 117-118	520.07	0.10	0.85	0.56	0.66	0.18
35X-3, 49-50	524.49	0.12	1.02	0.34	0.46	0.26
36X-1, 48-49	531.18	0.12	1.00			
36X-3, 46-47	534.16	0.05	0.45	0.59	0.65	0.06
36X-5, 43-44	537.13	0.05	0.45			
38X-1, 61-62	550.71	0.11	0.94			
38X-5, 63-64	556.73	0.10	0.80			
40X-1, 37-38	569.77	0.11	0.88			
40X-3, 38-39	572.78	0.16	1.30			

Notes: IC = inorganic carbon, CaCO₃ = calcium carbonate, TOC = total organic carbon, TC = total carbon, TS = total sulfur. * = samples collected in a second round of sampling.

Table T24. Summary of Rock-Eval pyrolysis measurements.

Core, section, interval (cm)	Depth (mbsf)	T _{max}	S ₁	S ₂	S ₃	PI	S ₂ /S ₃	TOC	HI	OI
178-1096C-										
16X-5, 81-82	344.91	596	0.07	0.43	0.31	0.14	1.38	0.29	148	106
21X-2, 8-9	386.54	403	0.20	1.21	0.42	0.14	2.88	0.47	257	89
30X-1, 63-64	473.53	386	0.10	0.71	0.50	0.12	1.42	0.43	165	116
34X-6, 117-118	520.07	398	0.08	0.71	0.34	0.10	2.08	0.40	177	85
36X-3, 46-47	534.16	460	0.09	0.77	0.23	0.10	3.34	0.41	187	56

Notes: Descriptions of the various Rock-Eval pyrolysis parameters are given in "[Organic Geochemistry](#)," p. 16, in the "Explanatory Notes" chapter.

Table T25. Interstitial water analyses for Holes 1096A, 1096B, and 1096C.

Core, section, interval (cm)	Depth (mbsf)	pH	Salinity	Cl ⁻ (mM)	Alkalinity (mM)	NH ₄ ⁺ (mM)	Si(OH) ₄ (mM)	SO ₄ ²⁻ (mM)	Mn ²⁺ (µM)	Fe ²⁺ (µM)	PO ₄ ³⁻ (µM)	F ⁻ (µM)	Ca ²⁺ (mM)	Mg ²⁺ (mM)	K ⁺ (mM)	Sr ²⁺ (µM)
178-1096A-																
1H-2, 145-150	2.95	7.5	35	555	4.48	0.04	0.56	27.0	96.0	0.7	15.1	64.0	12.2	52.6	11.0	91
1H-4, 145-150	5.95	7.8	35	560	4.81	0.08	1.04	26.5	187.2	0.2	13.1	63.6	13.2	51.4	11.2	90
2H-3, 145-150	12.15	7.8	35	566	5.48	0.12	0.54	23.1	194.5	0.2	13.3	55.1	12.1	48.6	10.5	92
2H-5, 145-150	15.15	7.9	35	560	5.62	0.15	0.52	21.0	196.5	0.2	13.9	50.9	12.4	47.7	10.3	90
3H-2, 145-150	20.15	7.9	35	561	5.99	0.15	0.64	17.9	135.5	1.9	10.8	38.6	11.9	48.1	10.5	93
3H-4, 145-150	23.15	7.9	35	564	6.24	0.17	0.76	15.7	124.5	2.4	9.7	35.8	12.7	46.7	10.2	89
4H-2, 145-150	29.65	7.4	34	566	9.34	0.18	0.65	11.8	99.8	2.6	14.5	28.2	11.8	44.0	8.8	95
4H-3, 145-150	31.15	7.8	34	571	6.82	0.18	0.82	11.7	93.2	1.7	12.5	28.3	11.6	44.6	8.6	94
5H-2, 145-150	39.15	8.0	33	563	7.53	0.26	0.87	4.9	52.5	2.0	7.2	19.7	10.6	40.6	7.7	101
5H-4, 145-150	42.15	7.9	33	567	8.15	0.28	0.81	3.0	32.0	1.1	8.3	17.5	10.3	39.7	7.4	105
6H-3, 145-150	50.15	7.9	32	563	7.18	0.31	0.68	1.0	37.2	1.1	7.7	15.9	10.4	36.5	6.6	112
6H-5, 145-150	53.15	7.9	33	566	7.12	0.31	0.73	1.2	41.0	0.6	7.4	14.1	11.0	37.1	6.2	114
7H-3, 145-150	59.65	7.9	32	559	6.73	0.33	0.88	0.0	29.0	1.1	7.0	16.5	11.3	37.4	5.9	116
8H-3, 145-150	69.15	8.0	32	566	5.41	0.42	0.71	0.0	13.0	0.6	3.9	18.3	11.7	35.0	5.8	127
9H-2, 145-150	77.15	7.9	32	560	5.50	0.39	0.46	0.0	34.2	1.1	3.3	19.0	12.7	36.0	5.0	126
10H-3, 145-150	88.15	7.9	32	566	5.08	0.40	0.83	0.0	22.2	0.6	6.0	20.1	13.1	33.8	4.9	136
11H-3, 145-150	97.65	7.8	32	558	4.61	0.53	0.96	0.0	36.0	3.7	4.0	19.2	15.3	33.6	4.6	137
14H-3, 145-150	126.15	8.2	32	557	4.04	0.55	0.37	0.0	9.0	—	2.1	20.6	14.6	31.1	4.5	136
178-1096B-																
1H-1,0-1	0.00	—	—	555	—	0.03	0.12	28.6	—	—	—	—	10.9	55.5	10.9	—
16H-3, 145-150	139.65	7.9	32	558	5.15	0.62	0.49	0.0	16.2	0.3	3.3	19.6	13.5	29.9	3.9	131
19H-3, 145-150	155.15	8.0	—	557	6.59	0.69	0.77	0.0	19.0	0.4	3.7	24.1	14.1	29.3	4.0	133
23X-2, 135-140	176.85	7.8	32	554	7.63	0.89	0.97	2.8	19.5	0.8	3.4	15.9	13.9	30.5	4.1	133
26X-2, 145-150	205.85	8.0	32	554	9.27	1.09	1.04	0.0	17.8	1.0	2.6	13.8	13.9	30.8	4.1	148
29X-3, 145-150	236.15	7.7	32	550	10.42	1.26	0.89	3.4	15.8	2.9	1.4	18.2	13.4	29.1	4.4	145
32X-3, 145-150	255.45	7.9	32	553	10.60	1.73	0.89	2.2	13.0	1.6	1.3	17.0	13.0	28.2	4.2	154
178-1096C-																
9X-4, 140-150	275.05	7.8	32	552	11.20	1.52	0.96	0.0	11.0	1.9	1.3	15.9	14.1	28.7	4.1	157
12X-3, 145-150	302.38	7.8	32	550	10.22	1.79	1.02	3.6	12.5	5.9	1.0	19.9	14.4	30.5	4.1	144
15X-3, 145-150	332.65	7.7	31	544	10.02	1.84	1.15	1.2	14.0	18.3	1.5	15.3	13.9	26.9	4.0	156
18X-3, 145-150	361.65	7.7	31	544	9.98	1.91	1.07	2.6	9.8	10.5	0.9	18.1	13.2	25.8	3.9	158
21X-4, 145-150	390.16	7.9	31	541	10.44	2.16	1.12	0.9	9.8	1.1	1.0	16.7	13.9	23.1	4.0	157
25X-5, 145-150	432.25	7.9	31	538	8.90	2.19	1.01	3.3	9.5	3.1	1.4	21.3	14.2	22.0	4.1	146
28X-3, 140-150	458.00	7.8	31	535	7.87	2.33	1.04	2.2	11.5	2.5	1.0	18.8	14.4	21.3	3.7	150
31X-3, 140-150	486.90	7.8	30	531	7.52	2.26	1.15	1.6	12.5	6.1	0.9	19.8	16.1	19.4	3.8	149
34X-3, 140-150	515.80	7.8	30	527	6.15	1.88	1.08	1.7	11.8	2.3	0.7	19.8	18.5	17.5	3.7	145
37X-4, 140-150	546.30	7.8	30	527	5.64	1.86	1.09	1.3	12.0	0.6	1.0	19.4	20.5	14.9	3.1	145
40X-1, 140-150	570.80	7.8	30	527	4.74	1.75	0.96	2.3	16.0	1.2	0.9	19.4	25.1	13.6	2.7	144

Note: — = no analysis.

Table T26. Relative intensities of selected X-ray diffraction peaks from bulk mineral samples of Site 1096 sediments.

Core, section, interval (cm)	Depth (mbsf)	Chlorite (7 Å)	Quartz (3.34 Å)	Plagioclase (3.19 Å)
178-1096A-				
3H-3, 15-17	20.35	9	100	42
3H-4, 110-112	22.80	11	100	36
5H-4, 85-87	41.55	14	100	39
7H-2, 49-52	57.19	15	100	33
9H-5, 46-47	79.44	13	100	37
14H-3, 60-63	125.30	13	100	37
178-1096B-				
1H-2, 136-139	2.86	11	100	36
13H-4, 66-68	113.46	12	100	38
19H-2, 80-83	153.00	13	100	37
24X-3, 78-80	187.29	10	100	40
27X-2, 109-111	215.09	8	100	38
27X-4, 37-39	217.37	13	100	34
30X-3, 64-68	244.94	14	100	38
178-1096C-				
2H-4, 90-91	172.40	17	100	49
5X-3, 65-67	215.85	6	100	29
8X-3, 14-16	264.04	15	100	40
11X-3, 91-93	293.51	16	100	40
14X-5, 87-89	324.26	13	100	40
17X-2, 83-85	349.83	16	100	54
20X-1, 102-104	377.62	20	100	53
23X-5, 67-70	412.17	13	100	47
26X-1, 58-59	434.98	16	100	38
29X-2, 115-117	465.85	13	100	39
32X-3, 132-134	496.42	15	100	44
35X-3, 69-71	524.69	13	100	45
38X-3, 66-69	553.76	10	100	40
40X-1, 87-89	570.27	14	100	39

Note: Highest selected peak intensity is normalized to 100.

Table T27. Relative intensities of selected X-ray diffraction peaks from clay mineral samples of Site 1096 sediments.

Core, section, interval (cm)	Depth (mbsf)	Glacial/ Interglacial	Chlorite (7 Å)	Illite (5 Å)	Mixed layer (~12 Å)
178-1096A-					
3H-3, 15-17	20.35	I	100	24	60
3H-4, 110-112	22.80	G	100	19	11
5H-4, 85-87	41.55	G	100	18	10
7H-2, 49-52	57.19	G	100	22	7
9H-5, 46-47	79.44	I?	100	21	6
14H-3, 60-63	125.30	G?	100	15	8
178-1096B-					
1H-2, 136-139	2.86	G	100	21	9
13H-4, 66-68	113.46	G	100	13	12
19H-2, 80-83	153.00	G?	100	16	9
24X-3, 78-80	187.29	I?	100	18	31
27X-2, 109-111	215.09	I	100	27	51
27X-4, 37-39	217.37	G	100	20	26
30X-3, 64-68	244.94	G	100	17	10
178-1096C-					
2H-4, 90-91	172.40	?	100	14	9
5X-2, 65-66	214.35	G	100	29	16
5X-3, 65-67	215.85	I	100	36	95
8X-3, 14-16	264.04	G	100	14	10
11X-3, 91-93	293.51	G	100	15	11
14X-5, 87-89	324.26	G	100	13	11
17X-2, 83-85	349.83	G	100	13	17
20X-1, 102-104	377.62	G	100	13	18
23X-5, 67-70	412.17	G?	100	12	15
26X-1, 58-59	434.98	?	100	15	13
29X-2, 115-117	465.85	G	100	16	18
32X-3, 132-134	496.42	I?	100	14	16
35X-3, 69-71	524.69	G?	100	15	17
38X-3, 66-69	553.76	I	100	21	43
40X-1, 87-89	570.27	G	100	12	14

Note: Highest selected peak intensity is normalized to 100.

Table T28. Trace-element chemistry of bulk sediment from Holes 1096A, 1096B, and 1096C.

Core, section, interval (cm)	Depth (mbsf)	Glacial/ Interglacial	Nb (ppm)	Zr (ppm)	Y (ppm)	Sr (ppm)	Rb (ppm)	Zn (ppm)	Cu (ppm)	Ni (ppm)	Cr (ppm)	V (ppm)	Ce (ppm)	Ba (ppm)
178-1096A-														
3H-3,15-17	20.35	I	11	177	31	277	87	119	48	36	45	142	52	1250
3H-4,110-112	22.80	G	11	163	33	259	97	117	27	30	39	152	45	485
5H-4,85-87	41.55	G	13	173	35	262	104	120	24	30	43	156	52	527
7H-2,49-52	57.19	G	14	175	37	271	122	113	25	29	49	154	60	614
9H-5,46-47	79.44	I?	13	174	36	241	120	128	40	33	46	155	62	554
14H-3,60-63	125.30	G?	11	160	34	253	100	121	38	33	39	158	54	540
178-1096B-														
1H-2,136-139	2.86	G	13	171	37	254	112	125	33	28	38	149	59	557
13H-4,66-68	113.46	G	10	159	33	260	92	118	27	27	33	155	46	498
19H-2,80-83	153.00	G?	11	162	33	254	99	127	32	27	32	157	45	512
24X-3,78-80	187.29	I?	10	154	30	268	84	103	20	23	35	156	51	492
27X-2,109-111	215.09	I	11	152	31	239	98	107	17	23	33	136	43	453
27X-4,37-39	217.37	G	11	163	33	260	95	114	17	27	37	151	45	583
30X-3,64-68	244.94	G	10	144	29	221	90	113	22	24	29	134	45	478
178-1096C-														
2H-4,90-91	172.40	?	11	154	31	260	93	126	23	34	29	153	51	502
5X-3,65-67	215.85	I	11	154	31	246	101	108	33	22	33	128	52	537
8X-3,14-16	264.04	G	10	143	29	231	85	109	21	24	31	146	50	506
11X-3,91-93	293.51	G	11	140	28	228	85	102	21	22	26	135	42	495
14X-5,87-89	324.26	G	11	139	26	230	77	95	24	21	25	137	40	470
17X-2,83-85	349.83	G	11	131	23	238	70	98	24	24	25	141	37	488
20X-1,102-104	377.62	G	9	112	21	193	67	88	24	19	26	117	44	443
23X-5,67-70	412.17	G?	10	129	25	234	74	96	25	22	31	137	30	460
26X-1,58-59	434.98	?	11	130	26	224	84	100	28	25	34	134	50	496
29X-2,115-117	465.85	G	10	124	25	211	77	95	29	24	33	130	37	451
32X-3,132-134	496.42	I?	10	124	24	215	76	87	26	20	25	132	38	455
35X-3,69-71	524.69	G?	10	122	24	223	73	94	27	22	30	143	37	423
38X-3,66-69	553.76	I	10	118	20	195	72	87	35	22	25	116	29	437
40X-1,87-89	570.27	G	11	125	25	225	80	97	27	22	28	136	41	478

Table T29. Summary of logging operations at Site 1096.

Task	Start time
Hole preparation	22:50, 3 March 1998
IPLT, upper part of hole	00:30, 4 March 1998
Hole preparation	11:40, 4 March 1998
IPLT, lower part of hole	15:30, 4 March 1998
GHMT, lower part of hole	23:10, 4 March 1998
End of logging operations	09:30, 5 March 1998

Note: IPLT = integrated porosity-lithology tool, GHMT = geological high-sensitivity magnetic tool.

Table T30. Chemical and nuclear parameters for some common minerals.

Mineral	K (average %)	Th (ppm) (approx.)	PEF (barns/e ⁻)	Σf (c.u.)	APS porosity (%)	Density (g/cm ³)
Illite; K _{1-1.5} Al ₄ (Si _{7-6.5} Al _{1-1.5})O ₂₀ (OH) ₈	5.2	6-12	3.03	16.74	~17	2.78
Kaolinite; Al ₄ Si ₄ O ₁₀ (OH) ₈	0.63	18-26	1.49	13.04	~34	2.62
Mg-Chlorite; (Mg,Al) ₆ (Si,Al) ₄ O ₁₀ (OH) ₈			1.39	11.34	~35	2.65
Fe-Chlorite; (Fe,Al) ₆ (Si,Al) ₄ O ₁₀ (OH) ₈			12.36	47.44	~35	3.42
Glauconite; K(R ³⁺ ,R ²⁺) ₂ (Si,Al) ₄ O ₁₀ (OH) ₂	4.5	2-8	4.79	20.89		2.85
Montmorillonite; (Ca,Na) ₇ (Al,Mg,Fe) ₄ (Si,Al) ₈ O ₂₀ (OH) ₄ (H ₂ O) _n	0.22	10-24	1.63	8.1	~60	2.63
Quartz; SiO ₂	0	0	1.81	4.55		2.65
Calcite; CaCO ₃	0	0	5.08	7.08		2.71
Plagioclase (Albite); NaAlSiO ₃			1.7	7.5	~2	2.59
Plagioclase (Anorthite); CaAl ₂ Si ₂ O ₈			3.1	7.2		2.74
K-feldspar; KAlSi ₃ O ₈	13	9	2.9	16		2.52

Table T31. Depth offsets of the Site 1096 mcd scale relative to mbsf depth. (Continued on next page.)

Core	Depth (mbsf)	Depth (mcd)	Offset (m)
178-1096A-			
1H	1.54	1.06	-0.48
2H	7.76	8.48	0.72
3H	17.26	17.98	0.72
4H	26.76	27.48	0.72
5H	36.26	36.98	0.72
6H	45.76	46.48	0.72
7H	55.26	56.86	1.6
8H	64.76	66.36	1.6
9H	74.26	75.86	1.6
10H	83.76	85.36	1.6
11H	93.26	94.86	1.6
12H	102.76	104.36	1.6
13H	112.26	113.86	1.6
14H	121.76	123.96	2.2
15H	131.26	132.86	1.6
178-1096B-			
1H	0.04	0.04	0
2H	3.86	3.86	0
3H	13.36	13.64	0.28
4H	22.86	23.14	0.28
5H	32.36	32.64	0.28
6H	41.86	42.28	0.42
7H	51.36	52.52	1.16
8H	60.86	62.62	1.76
9H	70.36	72.32	1.96
10H	79.86	81.82	1.96
11H	89.36	91.32	1.96
12H	98.86	101.92	3.06
13H	108.36	111.42	3.06
16H	135.26	138.32	3.06
17H	144.16	147.22	3.06
18H	150.16	153.22	3.06
19H	150.76	153.82	3.06
20H	157.76	160.82	3.06
23H	175.58	178.64	3.06
24H	183.66	186.72	3.06
26H	202.96	206.02	3.06
27H	212.56	215.62	3.06
28H	222.16	226.78	4.62
29X	234.76	238.48	3.72
30X	241.36	245.08	3.72
31X	248.06	251.78	3.72
32X	251.06	254.78	3.72
178-1096C-			
1H	114.06	118.03	3.97
2H	167.06	169.26	2.2
3X	193.06	195.26	2.2
4X	202.66	205.08	2.42
5X	212.26	214.9	2.64
6X	221.86	224.5	2.64
7X	255.26	257.66	2.4
8X	260.96	263.58	2.62
9X	270.74	273.36	2.62
10X	280.06	282.68	2.62
11X	289.66	292.28	2.62
12X	299.49	302.11	2.62
13X	308.86	311.48	2.62
14X	318.56	321.18	2.62
15X	328.26	330.88	2.62
16X	337.96	340.58	2.62
17X	347.56	350.18	2.62
18X	357.26	359.88	2.62
19X	366.96	369.58	2.62
20X	376.66	379.28	2.62
21X	386.26	388.88	2.62
22X	395.86	398.48	2.62

Table T31 (continued).

Core	Depth (mbsf)	Depth (mcd)	Offset (m)
23X	405.56	408.18	2.62
24X	415.16	417.78	2.62
25X	424.86	427.48	2.62
26X	434.46	437.08	2.62
27X	444.06	446.68	2.62
28X	453.66	456.28	2.62
29X	463.26	465.88	2.62
30X	472.96	475.58	2.62
31X	482.56	485.18	2.62
32X	492.16	494.78	2.62
33X	501.76	504.38	2.62
34X	511.46	514.08	2.62
35X	521.06	523.68	2.62
36X	530.76	533.38	2.62
37X	540.46	543.08	2.62
38X	550.16	552.78	2.62
40X	569.46	572.08	2.62
41X	579.16	581.78	2.62
42X	588.62	591.24	2.62

Note: To shift from one scale to another, add (or subtract) the offset values to the mbsf depths. The depths are from the bottom of each section.

Table T32. Spliced cores for Holes 1096A, 1096B, and 1096C. (Continued on next page.)

Hole, core, section, interval (cm)	Depth (mbsf)	Depth (mcd)		Hole, core, section, interval (cm)	Depth (mbsf)	Depth (mcd)
1096B-1H-1, 144	1.44	1.44	Tie	1096A-1H-2, 42	1.92	1.44
1096A-1H-6, 48	7.48	7.00	Tie	1096B-2H-3, 20	7.00	7.00
1096B-2H-5, 142	11.16	11.16	Tie	1096A-2H-2, 124	10.44	11.16
1096A-2H-5, 104	14.74	15.46	Tie	1096B-3H-2, 38	15.18	15.46
1096B-3H-7, 16	22.46	22.74	Tie	1096A-3H-4, 32	22.02	22.74
1096A-3H-5, 40	23.60	24.32	Tie	1096B-4H-1, 124	24.04	24.32
1096B-4H-8, 28	31.73	32.01	Tie	1096A-4H-4, 8.5	31.29	32.01
1096A-4H-4, 106	32.26	32.98	Tie	1096B-5H-1, 40	32.70	32.98
1096B-5H-7, 8	41.38	41.66	Tie	1096A-5H-4, 24	40.94	41.66
1096A-5H-6, 6	43.76	44.48	Tie	1096B-6H-2, 76	44.06	44.48
1096B-6H-7, 36	51.16	51.58	Tie	1096A-6H-4, 66	50.86	51.58
1096A-6H-5, 106	52.76	53.48	Tie	1096B-7H-1, 102	52.32	53.48
1096B-7H-7, 58	60.82	61.98	Tie	1096A-7H-4, 68	60.38	61.98
1096A-7H-6, 22	62.42	64.02	Tie	1096B-8H-1, 146	62.26	64.02
1096B-8H-7, 26	70.06	71.82	Tie	1096A-8H-4, 102	70.22	71.82
1096A-8H-6, 68	72.88	74.48	Tie	1096B-9H-2, 72	72.52	74.48
1096B-9H-7, 48	79.78	81.74	Append	1096B-10H-1, 0	79.80	81.76
1096B-10H-6, 78	88.08	90.04	Append	1096B-11H-1, 0	89.30	91.26
1096B-11H-6, 46	97.26	99.22	Tie	1096A-11H-3, 142	97.62	99.22
1096A-11H-6, 104	101.74	103.34	Tie	1096B-12H-1, 148	100.28	103.34
1096B-12H-7, 18	107.98	111.04	Append	1096B-13H-1, 0	108.30	111.36
1096B-13H-5, 70	115.00	118.06	Tie	1096C-1H-1, 8.5	114.09	118.06
1096C-1H-6, 68	120.43	124.40	Tie	1096A-14H-1, 50	122.20	124.40
1096A-14H-7, 48	131.18	133.38	Tie	1096A-15H-1, 58	131.78	133.38
1096A-15H-4, 112	136.82	138.42	Tie	1096B-16H-1, 16	135.36	138.42
1096B-16H-6, 78	143.48	146.54	Append	1096B-17H-1, 0	144.10	147.16
1096B-17H-4, 112	149.72	152.78	Append	1096B-18H-1, 0	150.10	153.16
1096B-18H-1, 18	150.28	153.34	Append	1096B-19H-1, 0	150.70	153.76
1096B-19H-5, 70	157.40	160.46	Append	1096B-20H-1, 0	157.70	160.76
1096B-20H-6, 106	166.26	169.32	Tie	1096C-2H-1, 12	167.12	169.32
1096C-2H-7, 28	176.54	178.74	Tie	1096B-23H-2, 18	175.68	178.74
1096B-23H-5, 74	180.64	183.70	Append	1096B-24H-1, 0	183.60	186.66
1096B-24H-7, 30	192.63	195.69	Tie	1096C-3X-1, 48.5	193.49	195.69
1096C-3X-6, 142	201.92	204.12	Append	1096C-4X-1, 0	202.60	205.02
1096C-4X-7, 70	211.80	214.22	Append	1096C-5X-1, 0	212.20	214.84
1096C-5X-5, 112	219.32	221.96	Append	1096C-6X-1, 0	221.80	224.44
1096C-6X-5, 66	228.46	231.10	Append	1096B-29X-1, 0	231.70	235.42
1096B-29X-6, 34	239.54	243.26	Append	1096B-30X-1, 0	241.30	245.02
1096B-30X-4, 104	246.84	250.56	Append	1096B-31X-1, 0	248.00	251.72
1096B-31X-2, 60	250.10	253.82	Append	1096B-32X-1, 0	251.00	254.72
1096B-32X-5, 40	256.86	260.58	Tie	1096C-7X-2, 148	258.18	260.58
1096C-7X-5, 46	261.66	264.06	Tie	1096C-8X-1, 54	261.44	264.06
1096C-8X-7, 38	270.28	272.90	Append	1096C-9X-1, 0	269.18	271.80
1096C-9X-8, 102	279.95	282.57	Append	1096C-10X-1, 0	280.00	282.62
1096C-10X-7, 88	289.38	292.00	Append	1096C-11X-1, 0	289.60	292.22
1096C-11X-7, 44	299.04	301.66	Append	1096C-12X-1, 0	297.93	300.55
1096C-12X-8, 30	308.73	311.35	Append	1096C-13X-1, 0	308.80	311.42
1096C-13X-6, 34	316.64	319.26	Append	1096C-14X-1, 0	318.50	321.12
1096C-14X-8, 58	327.97	330.59	Append	1096C-15X-1, 0	328.20	330.82
1096C-15X-7, 36	337.56	340.18	Append	1096C-16X-1, 0	337.90	340.52
1096C-16X-7, 34	347.24	349.86	Append	1096C-17X-1, 0	347.50	350.12
1096C-17X-4, 42	352.42	355.04	Append	1096C-18X-1, 0	357.20	359.82
1096C-18X-7, 62	366.23	368.85	Append	1096C-19X-1, 0	366.90	369.52
1096C-19X-7, 32	376.22	378.84	Append	1096C-20X-1, 0	376.60	379.22
1096C-20X-1, 134	377.94	380.56	Append	1096C-21X-1, 0	386.20	388.82
1096C-21X-8, 28	394.99	397.61	Append	1096C-22X-1, 0	395.80	398.42
1096C-22X-7, 40	405.20	407.82	Append	1096C-23X-1, 0	405.50	408.12
1096C-23X-6, 112	414.12	416.74	Append	1096C-24X-1, 0	415.10	417.72
1096C-24X-3, 28	418.38	421.00	Append	1096C-25X-1, 0	424.80	427.42
1096C-25X-7, 38	434.18	436.80	Append	1096C-26X-1, 0	434.40	437.02
1096C-26X-2, 66	436.56	439.18	Append	1096C-27X-1, 0	444.00	446.62
1096C-27X-7, 40	453.30	455.92	Append	1096C-28X-1, 0	453.60	456.22
1096C-28X-7, 34	462.74	465.36	Append	1096C-29X-1, 0	463.20	465.82
1096C-29X-7, 40	472.60	475.22	Append	1096C-30X-1, 0	472.90	475.52
1096C-30X-7, 40	482.30	484.92	Append	1096C-31X-1, 0	482.50	485.12
1096C-31X-7, 44	491.82	494.44	Append	1096C-32X-1, 0	492.10	494.72
1096C-32X-7, 36	501.34	503.96	Append	1096C-33X-1, 0	501.70	504.32
1096C-33X-6, 64	508.63	511.25	Append	1096C-34X-1, 0	511.40	514.02

Table T32 (continued).

Hole, core, section, interval (cm)	Depth (mbsf)	Depth (mcd)		Hole, core, section, interval (cm)	Depth (mbsf)	Depth (mcd)
1096C-34X-7, 30	520.62	523.24	Append	1096C-35X-1, 0	521.00	523.62
1096C-35X-5, 20	527.20	529.82	Append	1096C-36X-1, 0	530.70	533.32
1096C-36X-7, 46	539.66	542.28	Append	1096C-37X-1, 0	540.40	543.02
1096C-37X-7, 30	549.70	552.32	Append	1096C-38X-1, 0	550.10	552.72
1096C-38X-6, 144	559.04	561.66	Append	1096C-40X-1, 0	569.40	572.02
1096C-40X-3, 72	573.12	575.74	Append	1096C-41X-1, 0	579.10	581.72
1096C-41X-7, 34	588.44	591.06				

Table T33. Depths of geomagnetic polarity transitions and diatom and radiolarian datum events in Holes 1096A, 1096B, and 1096C.

Events	Depth (mbsf)			Averaged depth (mbsf)	Published age (Ma)
	Hole 1096A	Hole 1096B	Hole 1096C		
Polarity boundary					
C1n(o)	54.60-55.40	54.94-54.99		54.96	0.78
C2An.1n(t)		215.35-217.25	215.80-215.90	215.85	2.58
C2An.3n(t)			366.21-367.10	366.65	3.33
C2An.3n(o)			405.15-405.80	405.48	3.58
C3n.1n(t)			507.89-511.55	509.70	4.18
C3n.1n(o)			536.45-536.60	536.52	4.29
C3n.2n(t)			553.60-553.80	553.70	4.48
C3n.2n(o)			583.85-584.05	583.95	4.62
Diatom events					
T <i>H. karstenii</i>	7.69-13.47	<8.6		8.15	0.19
B <i>H. karstenii</i>	16-20.5			18.25	0.49
T <i>T. inura</i>		<166.8			1.85
T <i>T. vulnifica</i>		<177.6			2.28
T <i>T. complicata</i>		<203.8			3.4 (2.5)
T <i>T. insignia</i>			<262.26		2.57 (2.63)
T <i>F. interfrigidaria</i>		250.3-257.3		253.80	2.67 (2.63)
B <i>T. vulnifica</i>			308.9-311.1	310.00	3.17 (3.26)
B <i>T. insignia</i>			270.68-280.37	275.53	3.40
B <i>F. interfrigidaria</i>			482.5-492.1	487.30	3.80
T <i>F. praeinterfrigidida</i>			424.8-426.5	425.65	3.64
B <i>F. barronii</i>			550.25-555.0	552.62	4.48
B <i>T. inura</i>			579.1-588.6	583.85	4.85
Radiolarian events					
T <i>A. cylindrica</i>	13.3-22.8			18.05	0.61
T <i>H. vema</i>			212.2-221.8	217.00	2.42
T <i>P. titan</i>			231.7-241.3	236.50	3.49
T <i>L. coronata</i>			530.7-540.4	535.55	3.71
B <i>H. vema</i>			559.8-569.4	564.60	4.58

Notes: See “**Biostratigraphy**,” p. 9, in the “Explanatory Notes” chapter, for age references. T = top/last occurrence, B = base/first occurrence, gray areas = no recovery.

Table T34. Depths of geomagnetic reversals used to calculate sedimentation rates for Site 1096.

Depth (mbsf)	SR (cm/k.y.)	Age (Ma)	Comments
0.00		0.00	Top of sedimentary section
	7.0		
54.96		0.78	C1n(o)
	8.9		
215.85		2.581	C2An.1n(t)
	20.1		
366.65		3.33	C2An.3n(t)
	15.5		
405.48		3.58	C2An.3n(o)
	17.4		
509.70		4.18	C3n.1n(t)
	24.4		
536.52		4.29	C3n.1n(o)
	9.0		
553.70		4.48	C3n.2n(t)
	21.6		
583.95		4.62	C3n.2n(o)

Note: SR = sedimentation rate.

Table T35. Two-way traveltime (TWT) and depth to base of seismic units at Site 1096.

Seismic Unit	TWT (ms)	Depth (mbsf)	Age (Ma)
Unit I	140.6	110	1.4
Subunit IIa	394	316.5	3.08
Subunit IIb	631.6	519	4.22
Base of hole	732	607	

Note: Ages according to magnetic reversal identifications (Table [T33](#), p. 142).